

AD-A258 861

DOCUMENTATION PAGE

Form Approved
OMB No. 0704-0168

2. REPORT DATE 1992		3. REPORT TYPE AND DATES COVERED DISSERTATION	
4. TITLE AND SUBTITLE An Experimental Study of the Driving Mechanism and Control of the Unsteady Shock Induced Turbulent Separation in a MACH 5 Compression Corner Flow		5. FUNDING NUMBERS	
6. AUTHOR(S) William B. McClure, Captain		8. PERFORMING ORGANIZATION REPORT NUMBER AFIT/CI/CIA-92-011D	
7. PERFORMING ORGANIZATION NAME(S) AND ADDRESS(ES) AFIT Student Attending: University of Texas		10. SPONSORING MONITORING AGENCY REPORT NUMBER	
9. SPONSORING MONITORING AGENCY NAME(S) AND ADDRESS(ES) AFIT/CI Wright-Patterson AFB OH 45433-6583		12. DISTRIBUTION CODE	
11. SUPPLEMENTARY NOTES		13. ABSTRACT	
14. STATEMENT OF RESPONSIBILITY Approved for Public Release IAW 190-1 Distributed Unlimited ERNEST A. HAYGOOD, Captain, USAF Executive Officer		15. NUMBER OF PAGES 250	
17. SECURITY CLASSIFICATION OF ABSTRACT		16. PRICE CODE	
17. SECURITY CLASSIFICATION OF ABSTRACT	18. SECURITY CLASSIFICATION OF THIS PAGE	19. SECURITY CLASSIFICATION OF ABSTRACT	20. LIMITATION OF ABSTRACT

DTIC
ELECTE
DEC 08 1992
S E D

GENERAL INSTRUCTIONS FOR COMPLETING SF 298

The Report Documentation Page (RDP) is used in announcing and cataloging reports. It is important that this information be consistent with the rest of the report, particularly the cover and title page. Instructions for filling in each block of the form follow. It is important to **stay within the lines to meet optical scanning requirements.**

Block 1. Agency Use Only (Leave Blank)

Block 2. Report Date. Full publication date including day, month, and year, if available (e.g. 1 Jan 88). Must cite at least the year.

Block 3. Type of Report and Dates Covered. State whether report is interim, final, etc. If applicable, enter inclusive report dates (e.g. 10 Jun 87 - 30 Jun 88).

Block 4. Title and Subtitle. A title is taken from the part of the report that provides the most meaningful and complete information. When a report is prepared in more than one volume, repeat the primary title, add volume number, and include subtitle for the specific volume. On classified documents enter the title classification in parentheses.

Block 5. Funding Numbers. To include contract and grant numbers; may include program element number(s), project number(s), task number(s), and work unit number(s). Use the following labels:

C - Contract	PR - Project
G - Grant	TA - Task
PE - Program Element	WU - Work Unit Accession No.

Block 6. Author(s). Name(s) of person(s) responsible for writing the report, performing the research, or credited with the content of the report. If editor or compiler, this should follow the name(s).

Block 7. Performing Organization Name(s) and Address(es). Self-explanatory.

Block 8. Performing Organization Report Number. Enter the unique alphanumeric report number(s) assigned by the organization performing the report.

Block 9. Sponsoring/Monitoring Agency Name(s) and Address(es). Self-explanatory.

Block 10. Sponsoring/Monitoring Agency Report Number. (If known)

Block 11. Supplementary Notes. Enter information not included elsewhere such as: Prepared in cooperation with...; Trans. of ..., To be published in When a report is revised, include a statement whether the new report supersedes or supplements the older report.

Block 12a. Distribution/Availability Statement.

Denote public availability or limitation. Cite any availability to the public. Enter additional limitations or special markings in all capitals (e.g. NOFORN, REL, ITAR)

DOD - See DoDD 5230.24, "Distribution Statements on Technical Documents."

DOE - See authorities

NASA - See Handbook NHB 2200.2.

NTIS - Leave blank.

Block 12b. Distribution Code.

DOD - DOD - Leave blank

DOE - DOE - Enter DOE distribution categories from the Standard Distribution for Unclassified Scientific and Technical Reports

NASA - NASA - Leave blank

NTIS - NTIS - Leave blank.

Block 13. Abstract. Include a brief (Maximum 200 words) factual summary of the most significant information contained in the report.

Block 14. Subject Terms. Keywords or phrases identifying major subjects in the report.

Block 15. Number of Pages. Enter the total number of pages.

Block 16. Price Code. Enter appropriate price code (NTIS only).

Blocks 17. - 19. Security Classifications. Self-explanatory. Enter U.S. Security Classification in accordance with U.S. Security Regulations (i.e., UNCLASSIFIED). If form contains classified information, stamp classification on the top and bottom of the page.

Block 20. Limitation of Abstract. This block must be completed to assign a limitation to the abstract. Enter either UL (unlimited) or SAR (same as report). An entry in this block is necessary if the abstract is to be limited. If blank, the abstract is assumed to be unlimited.

**AN EXPERIMENTAL STUDY OF THE DRIVING MECHANISM
AND CONTROL OF THE UNSTEADY SHOCK INDUCED
TURBULENT SEPARATION IN A MACH 5**

COMPRESSION CORNER FLOW

Accession For	
NTIS CRA&I	<input checked="" type="checkbox"/>
DTIC TAB	<input type="checkbox"/>
Unannounced	<input type="checkbox"/>
Justification	
By	
Distribution /	
Availability Codes	
Dist	Avail and/or Special
A-1	

**APPROVED BY
DISSERTATION COMMITTEE:**

DS Delling

R.W. WILZ

Michael E. ...

G. F. Carey

David G. ...

012200

92-31011



276PS

Copyright

by

William Berton McClure

1992

To Diane, Rick, and Rob

**AN EXPERIMENTAL STUDY OF THE DRIVING MECHANISM
AND CONTROL OF THE UNSTEADY SHOCK INDUCED
TURBULENT SEPARATION IN A MACH 5
COMPRESSION CORNER FLOW**

by

WILLIAM BERTON McCLURE, B.S., M.S.E.

DISSERTATION

**Presented to the Faculty of the Graduate School of
The University of Texas at Austin
in Partial Fulfillment
of the Requirements
for the Degree of**

DOCTOR OF PHILOSOPHY

THE UNIVERSITY OF TEXAS AT AUSTIN

August 1992

Acknowledgements

The author would like to express his heartfelt thanks to all of the people who have made this work not only interesting, but enjoyable. I am grateful to my supervisor, David S. Dolling, for his guidance and much-used open door policy. The suggestions and insights provided by the committee members are also appreciated and acknowledged. Thanks to the wind tunnel technical staff, Edward Zihlman, Mark Allen, and Frank Wise, and to Joe Edgar for his work in building the models. Thanks also to Frank Marentic of the 3M Company for providing the riblet material. The many discussions with members of "The Bull Pen" - Rich Gramann, Richard Shau, Mehmet Erengil, and Leon Brusniak - are gratefully acknowledged. Finally, I would like to thank my family for their moral support and assistance during this program.

The author was funded during this program through the United States Air Force Institute of Technology. Additional support was provided by NASA Headquarters (Grant NAGW964) and by ARO (Grant DAALO3-91-G-0023). These sources of support are gratefully acknowledged.

August 1992.

**AN EXPERIMENTAL STUDY OF THE DRIVING MECHANISM
AND CONTROL OF THE UNSTEADY SHOCK INDUCED
TURBULENT SEPARATION IN A MACH 5
COMPRESSION CORNER FLOW**

Publication No. _____

**William Berton McClure, Ph.D.
The University of Texas at Austin, 1992**

Supervisor: David S. Dolling

This experimental study has examined the unsteady flowfield associated with the shock-induced separation of a turbulent boundary layer. The interaction was generated by a 28° unswept compression corner in a Mach 5 airstream. Perturbations were made to the interaction to better understand the mechanism responsible for the separation shock dynamics, as well as to demonstrate a method of controlling the shock motion. High frequency wall pressure measurements were used to track the time-dependent position of the separation shock. Conventional and fluctuating pitot pressure measurements were used to quantify the spatial mean and time-dependent extent of the baseline and altered interactions.

Modification of the baseline interaction focused on two regions of the

flowfield. Riblets and a boundary layer manipulator were separately introduced upstream of the interaction to alter the near-wall and outer region of the incoming boundary layer, respectively. Suction was applied through a slot in the face of the compression corner to alter the interaction downstream of the separation line.

Local motion of the separation shock is associated with a characteristic signature in the wall pressure fluctuations beneath the incoming turbulent boundary layer. This signature approaches the separation shock at a speed equal to 75% of the freestream velocity, is coincident with the shock foot at the time of its motion, and continues downstream after passing beneath the shock. The shape of this signature is dependent only on whether the local shock motion is upstream or downstream.

Fluctuating pitot pressure measurements made within the incoming boundary layer indicate that the maximum boundary layer interface crossing frequency is about five times that of the maximum separation shock zero crossing frequency. Power spectra from these pitot pressure data exhibit an increased role of low frequency (< 2 kHz) fluctuations in the overall variance of the signal. This frequency range closely matches the dominant frequencies found in wall pressure fluctuations beneath the separation shock. Such fluctuations are not evident in the wall pressure or freestream pitot pressure measurements taken upstream of the interaction.

Motion and location of the separated shear layer is found to be correlated with that of the separation shock such that the overall separation bubble exhibits a "breathing" motion. As shown for the first time from the results of this study, the motion of the downstream limit of this bubble predominantly lags that of the upstream limit, independent of the direction of

the bubble motion (inflating or collapsing). Motion of both the separation shock and shear layer seem to be secondary responses to primary, but undetermined, changes to the flowfield. Evidence of the shear layer motion is found at least as far downstream as 3.5 times the thickness of the incoming turbulent boundary layer.

No correlation was found between the dynamics of the separation shock and the size of the separation bubble. No changes were observed in either the separation shock motion or the overall interaction due to alteration of the near-wall fluctuations of the incoming boundary layer.

In all, these data suggest that the separation shock motion and associated flowfield unsteadiness is primarily driven by fluctuations in the outer two-thirds of the incoming turbulent boundary layer.

Of the control techniques applied, only the boundary layer manipulator reduced the overall separation bubble size, as well as decreased the range and strength of the separation shock. This was primarily attributed to changes to the inviscid flowfield and a resulting weakening of the compression corner interaction. Nonetheless, this is the first demonstration of altering the motion of the separation shock in a favorable manner.

Table of Contents

Section	Page
List of Tables	xiii
List of Figures	xiv
Nomenclature	xxii
1 Introduction	1
1.1 Motivation	1
1.2 Objective of Current Work	4
2 Literature Review	8
2.1 'Time-Independent' Compression Corner Studies	9
2.2 Studies of the Unsteady Interaction	12
2.2.1 Surface Pressure Studies	12
2.2.2 Flowfield Studies	17
2.2.3 Additional Relevant Studies	19
2.2.4 Summary	21
2.3 Suggested Driving Mechanisms	22
2.4 Interaction Control Efforts	27
2.5 Relevant Boundary Layer Modification Techniques	31
2.6 Summary	33
3 Experimental Program	35
3.1 Wind Tunnel	35
3.2 Compression Corner	36
3.3 Instrumentation Plugs	38
3.4 Probes	38
3.4.1 Probe Drive and Mount	38

3.4.2	Pitot Probes	39
3.4.3	Pitot Rake	41
3.5	Suction System	41
3.6	Boundary Layer Manipulators	42
3.7	Riblets	43
3.8	Instrumentation	43
3.8.1	Pressure Transducers	43
3.8.2	Signal Conditioning	46
3.8.3	Data Acquisition Hardware	47
3.9	Calibration and Noise	47
3.10	Flow Visualization	48
3.11	Upstream Flow Conditions	49
4	Analysis Techniques	54
4.1	Basic Statistical and Time Series Analysis	54
4.2	Event Detection Methods	59
4.2.1	Probability Distribution Technique	59
4.2.2	VITA Technique	61
4.3	Conditional Data Analysis	64
5	Baseline Compression Corner Interaction	72
5.1	Flow Features Upstream of the Corner	72
5.1.1	Surface Flow Visualization	72
5.1.2	Fluctuating Surface Pressures	73
5.1.2.1	Streamwise Development of Interaction	74
5.1.2.2	Modified Ensemble-Averaging Analysis	78
5.1.3	Correlations with Upstream Pitot Pressure Fluctuations	82

5.2	Flowfield Downstream of the Corner	87
5.2.1	Mean Pitot Pressure Profiles	87
5.2.2	Fluctuating Pitot Pressure Results	88
5.2.2.1	Frozen Pitot Pressure Profiles	91
5.2.2.2	Pitot Pressure Events	93
5.3	Summary	96
6	Downstream Perturbations	98
6.1	Effect of Slot and Suction	98
6.1.1	Surface Flow Visualization	100
6.1.2	Interaction Upstream of the Corner	101
6.1.3	Flowfield Downstream of the Corner	105
6.2	Effect of End Fences	107
6.2.1	Surface Flow Visualization	108
6.2.2	Interaction Upstream of the Corner	108
6.3	Summary	109
7	Upstream Perturbations	110
7.1	Boundary Layer Manipulators	110
7.1.1	Surface Flow Visualization	111
7.1.2	Fluctuating Surface Pressure Upstream of the Corner	112
7.1.3	Separated Shear Layer Motion	115
7.2	Effect of BLM on Incoming Flowfield	116
7.2.1	Fluctuating Surface Pressure Measurements	116
7.2.2	Mean Pitot Pressure Measurements	117
7.2.3	Fluctuating Pitot Pressure Measurements	120
7.3	Riblets	125
7.4	Summary	127

8	Flowfield and Driving Mechanism	128
8.1	Flow Structure	128
8.2	Driving Mechanism	130
9	Conclusions	135
	Appendix	140
	References	242
	Vita	251

List of Tables

Table	Title	Page
Table 3-1	Pressure Transducer Specifications	45
Table 3-2	Incoming Flow Conditions	50
Table 3-3	Undisturbed Boundary Layer Parameters	53
Table 6-1	Comparison of the Effects of Slot-Alone and Slot-with Suction on L_{UI}	102
Table 6-2	Effect of Geometry Change on Limits of Separation Shock Motion	103
Table 7-1	Effect of BLM on Limits of Separation Shock Motion	114
Table 7-2	Wave/Wake Angle Downstream of BLM as Determined from Pitot Pressure Surveys	118

List of Figures

Figure	Title	Page
Figure 1-1	Potential Shock Wave/Boundary Layer Interaction Locations on a Hypersonic Vehicle (Jackson et al [1987])	140
Figure 2-1	Model of a Mach 3, 24° Compression Corner Interaction Flowfield (Settles et al [1976])	141
Figure 2-2	Comparison of Computational and Experimental Surface Quantities in a Mach 3, 24° Compression Corner SWTBLI (Horstman et al [1977])	142
Figure 2-3	Comparison of Computational and Experimental Velocity Profiles in a Mach 3, 24° Compression Corner SWTBLI (Horstman et al [1977])	143
Figure 2-4	Comparison of Computational and Experimental Surface Quantities in a Mach 3, 24° Compression Corner SWTBLI (Wilcox [1990])	144
Figure 2-5	Time-Varying Wall Pressure Signal Upstream of a Supersonic Forward Facing Step (Kistler [1964])	145
Figure 2-6	Ensemble-Averaged Pressure Distributions (Erengil and Dolling [1991a])	146

Figure 2-7	Hot-wire RMS Voltage Profiles in a Mach 3 Turbulent Boundary Layer with and without Riblets (Robinson [1988])	147
Figure 2-8	Effect of Boundary Layer Manipulators on Freestream Interface in Incompressible Flow (Chang and Blackwelder [1990])	148
Figure 3-1	Test Section Floor	149
Figure 3-2	28° Compression Corner Model	150
Figure 3-3	Fluctuating Pitot Pressure Probes	151
Figure 3-4	Boundary Layer Manipulators and Struts	152
Figure 3-5	Incoming Boundary Layer Velocity Profile Fit to Law of the Wall/Law of the Wake	153
Figure 3-6	Comparison of Fluctuating Pitot Pressure and Mass Flux Measurements in the Undisturbed Boundary Layer	154
Figure 4-1	Boxcar Conversion Technique	155
Figure 4-2	Shock Motion from Boxcar Signal	156
Figure 4-3	Variable-Window Ensemble Averaging	157
Figure 4-4	Development of Event Relative Timing Analysis Histogram for a Rise-Rise Event Edge Pair	159
Figure 4-5	Example of ERTA Applied to Separation Shock Motion	160
Figure 5-1	Surface Flow Visualization of Baseline Configuration Using Kerosene-Lampblack Technique	162

Figure 5-2	Surface Pressure Signals Beneath the Translating Separation Shock	163
Figure 5-3	Surface Pressure PDD's Upstream of the Corner	164
Figure 5-4	Streamwise Surface Distributions	165
Figure 5-5	Surface Pressure Power Spectra Beneath the Translating Separation Shock	167
Figure 5-6	Separation Shock Streamwise Distributions	168
Figure 5-7	Comparison of Surface Pressure RMS and Separation Shock Intermittency	169
Figure 5-8	Example of Pseudo-Channel Mapping of Surface Pressure Signals for Ensemble-Averaging	170
Figure 5-9	Pseudo-Channel Ensemble-Averaged Surface Pressure Time Histories for a 3-Channel Upstream Sweep	171
Figure 5-10	Pseudo-Channel Ensemble-Averaged Surface Pressure Time Histories for a 3-Channel Downstream Sweep	173
Figure 5-11	Pseudo-Channel Super Ensemble-Averaged Surface Pressure Time Histories for a 3-Channel Upstream Sweep	175
Figure 5-12	Pseudo-Channel Super Ensemble-Averaged Surface Pressure Time Histories for a 3-Channel Downstream Sweep	177
Figure 5-13	Variation in Pitot Pressure Signals and VITA Transformations within the Incoming Boundary Layer	179

Figure 5-14	Sensitivity of Incoming Boundary Layer Pitot Pressure VITA Signal RMS to Averaging Window Size	180
Figure 5-15	Sensitivity of Incoming Boundary Layer Edge Intermittency to VITA Threshold Multiplier	181
Figure 5-16	Boundary Layer Edge Intermittency	182
Figure 5-17	Boundary Layer Edge Interface Crossing Frequency	183
Figure 5-18	Variation in Upstream Ensemble-Averaged Pitot Pressure Signals with Height Above the Surface	184
Figure 5-19	Normalized Cross-Correlations Between Upstream Boundary Layer Pitot Pressure and Surface Pressure Beneath the Separation Shock	186
Figure 5-20	Normalized Fluctuating Pitot Pressure Power Spectra in the Incoming Boundary Layer	187
Figure 5-21	Pitot Pressure Profiles Above the the Ramp Surface - Baseline Configuration	188
Figure 5-22	Variation in Pitot Pressure Signals at Y = 0.1 inch with Distance From the Ramp Corner	189
Figure 5-23	Variation in Pitot Pressure PDD's at Y = 0.1 inch with Distance From the Ramp Corner	190

Figure 5-24	Variation in Pitot Pressure Signals at X = 0.2 inch with Height Above the Ramp Surface	191
Figure 5-25	Variation in Pitot Pressure PDD's at X = 0.2 inch with Height Above the Ramp Surface	192
Figure 5-26	Frozen Pitot Pressure Profiles -Baseline Configuration	194
Figure 5-27	Shear Layer Zero-Crossing Frequency Downstream of the Corner	195
Figure 5-28	ERTA of Separation Shock/ Shear Layer Motion	196
Figure 5-29	Refined ERTA Histograms of Separation Shock/Shear Layer Motion	198
Figure 6-1	Surface Flow Visualization Using Kerosene-Lampblack Technique a) Slot/No Suction b) Slot/Suction	199
Figure 6-2	Streamwise Surface Distributions	201
Figure 6-3	Separation Shock Streamwise Distributions	202
Figure 6-4	Comparison of Surface Pressure RMS and Separation Shock Intermittency Varying Ramp Face Geometry	203
Figure 6-5	Pitot Pressure Profiles Above the Ramp Surface a) Slot/No Suction b) Slot/Suction	204

Figure 6-6	Variation in Pitot Pressure PDD's at X = 0.2 inch with Height Above the Ramp Surface a) Slot/No Suction b) Slot/Suction	206
Figure 6-7	Frozen Pitot Pressure Profiles a) Slot/No Suction b) Slot/Suction	208
Figure 6-8	ERTA Histograms - Slot/No Suction - Slot/Suction	210
Figure 6-9	Surface Flow Visualization Using Kerosene-Lampblack Technique -Baseline/No Side Fences	212
Figure 6-10	Streamwise Surface Distributions -Effect of End Fences	213
Figure 6-11	Streamwise Surface Distributions -Effect of End Fences (with offset)	214
Figure 6-12	Separation Shock Streamwise Distributions -Effect of End Fences (with offset)	215
Figure 6-13	Surface Pressure RMS Distributions Varying Shock-Generating Geometry (Tran [1987])	216
Figure 7-1	Layout of Compression Corner with Boundary Layer Manipulator	217
Figure 7-2	Surface Flow Visualization Using Kerosene-Lampblack Technique w/ Boundary Layer Manipulator	218

Figure 7-3	Surface Pressure Signals Beneath the Translating Separation Shock (15° BLM)	219
Figure 7-4	Surface Pressure Signals Beneath the Translating Separation Shock (35° BLM)	220
Figure 7-5	Surface Pressure PDD's Upstream of the Corner - 15° BLM	221
Figure 7-6	Surface Pressure PDD's Upstream of the Corner - 35° BLM	222
Figure 7-7	Streamwise Surface Distributions -Effect of BLM	223
Figure 7-8	Separation Shock Streamwise Distributions -Effect of BLM	224
Figure 7-9	Surface Pressure Power Spectra in the 15° BLM/Compression Corner Interaction	225
Figure 7-10	Surface Pressure Power Spectra in the 35° BLM/Compression Corner Interaction	226
Figure 7-11	ERTA Histograms - 15° BLM	227
Figure 7-12	Surface Pressure Power Spectra Downstream of the 15° BLM Trailing Edge	228
Figure 7-13	Comparison of Surface Pressure RMS with and without BLM	229
Figure 7-14	Pitot Pressure Profiles a) Undisturbed Boundary Layer b) 15° BLM c) 35° BLM	230

Figure 7-15	Spanwise Variation of Pitot Pressure Profiles; $X_{blm} = 1.28$ inches - 15° BLM	233
Figure 7-16	Pitot Pressure Statistical Moments with and without BLM	234
Figure 7-17	Normalized Pitot Pressure RMS Distributions in Boundary Layer with and without BLM	235
Figure 7-18	Normalized Pitot Pressure Power Spectra; $X_{blm} = 1.25$ inches	236
Figure 7-19	Pitot Pressure Cross Correlations $X_{blm} = 1.25$ inches	237
Figure 7-20	Pitot Pressure Coherence Spectra $X_{blm} = 1.25$ inches	238
Figure 7-21	Streamwise Surface Distributions -Effect of Riblets	239
Figure 7-22	Separation Shock Streamwise Distributions -Effect of Riblets	240
Figure 8-1	Comparison of Event Histograms	241

NOMENCLATURE

C_f	skin friction coefficient
f	frequency
f_c	separation shock zero-crossing frequency
f_i	boundary layer edge interface-crossing frequency
f_s	sampling frequency
$G_{xx}(f)$	power spectral density coefficients
H	boundary layer shape factor (δ^*/θ)
h	riblet height (trough-to-peak)
h^+	riblet height in wall coordinates ($\equiv \frac{hu_\tau}{v_w}$)
L	streamwise distance to the corner
M	Mach number
\dot{m}_{nd}	non-dimensional mass flow rate ($\frac{Q}{\rho U_\infty \theta}$)
N	Number of occurrences
P	wall pressure
\bar{P}_w	mean wall pressure
P_0	total pressure in the settling chamber
P_t	pitot pressure
P_{TH1}	first pressure threshold
P_{TH2}	second pressure threshold
Q	slot mass flow rate per unit width of the slot
Re	Reynolds number
RMS	root-mean square of perturbation from mean
R_{xy}	normalized cross-correlation coefficient
s	spanwise riblet spacing (peak-to-peak)

s^+	spanwise riblet spacing in wall coordinates ($\equiv \frac{su_\tau}{v_w}$)
T_0	total temperature in the settling chamber
T_{TH}	VITA signal threshold
T_{st}	time averaging window for short term variance for the VITA technique
t	time
U	mean streamwise velocity
UI	point of upstream influence
u	streamwise velocity
u^+	dimensionless velocity, u/u_τ
u_τ	friction velocity, $\sqrt{\frac{\tau_w}{\rho_{wall}}}$
X	streamwise coordinate relative to ramp corner line (positive in the downstream direction)
X_{blm}	streamwise distance from the BLM trailing edge (positive downstream)
Y	normal coordinate measured relative to tunnel floor or the ramp face
y^+	normalized boundary layer coordinate, Yu_τ/ν
α	compression ramp angle
α_3	skewness coefficient
α_4	flatness coefficient
γ	separation shock intermittency
γ_{xy}^2	coherence coefficient
δ^*	boundary layer displacement thickness
δ_0	incoming boundary layer velocity thickness ($.99 U_\infty$)
δ_1	incoming boundary layer mass flux thickness ($.99 (\rho U)_\infty$)

ζ	minimum separation distance between two transducers (0.115 inch/0.292 cm)
θ	boundary layer momentum deficit thickness
μ	time-averaged value
ν	kinematic viscosity
Π	boundary layer wake strength parameter
ρ	density
σ	standard deviation
σ^2	variance
σ_{st}^2	short term variance
τ	cross-correlation time delay or ensemble-averaged reference time
τ_w	wall shear stress
Ω_{edge}	boundary layer edge intermittency

Abbreviations:

BFSL	best fit straight line
BLM	boundary layer manipulator
'C'	corner line
d/s	downstream
du	downstream-to-upstream shock turnaround
FS	full scale
kHz	kilohertz
PDD	amplitude probability density distribution
'S'	separation line
S/NS	slot configuration without suction
S/S	slot configuration with suction

UI	upstream influence
ud	upstream-to-downstream shock turnaround
u/s	upstream
VITA	Variable Interval Time Averaging

Subscripts:

shock	separation shock
SL	shear layer
SS	separation shock
T	trigger channel/signal
wo	upstream undisturbed wall conditions
∞	freestream

Chapter 1

Introduction

1.1 Motivation

The mid-1980's saw a renewed interest in hypersonic flight. Motivated by the achievements of the American Space Transportation System (Space Shuttle), society looked to the technical community for a more advanced and flexible successor - an "aerospace plane" - capable of beginning and ending flight in a manner similar to conventional aircraft. Such a vehicle promised much to commercial economies through high speed international travel between Western Europe, North America, and the Far East. This technology would also provide the military with rapid, flexible reconnaissance and force projection. Significant advances in avionics, materials, and simulation capability over those used to design, construct, and fly the Space Shuttle have led some to believe that a hypersonic demonstration vehicle, the Defense Advanced Research Projects Agency (DARPA) X-30, could be flown as early as 1992.

Among the most critical technical challenges for hypersonic vehicle aerodynamicist is the accurate prediction of the intensity and frequency of aeroacoustic loads (Jackson *et al.* [1987]). The challenge is magnified when

these loads are considered in conjunction with the extreme surface temperatures from compression and frictional heating by the freestream and boundary layer, as well as propulsion system exhaust. The largest aeroacoustic loads are expected to be generated in regions of shock-induced separation (Zorumski [1987]), as might occur at engine inlets, wing-body junctions, and control surfaces (Fig 1-1). The need to fly at relatively low altitudes to provide sufficient air for the propulsion system means that these interactions will involve turbulent boundary layers.

Current ground test facilities are incapable of simulating most of the projected X-30 flight environment, so the vehicle design will rely heavily on numerical predictions. The accuracy of these predictions depends on a correct physical model of the flow, which must in turn be validated against suitable experimental data. In the case of shock wave/turbulent boundary layer interactions (SWTBLI's), most of the experimental studies against which numerical results have been evaluated have been of interactions involving simple shock systems and geometries, such as impinging shocks, cylinders, blunt fins, sharp fins, swept and unswept compression corners. While current algorithms adequately predict features in many of these interactions, 15 years of effort has failed to produce acceptable comparisons with experimental mean surface pressure distributions and velocity profiles for the separated unswept compression corner interaction (Wilcox [1990]). Efforts to reduce these discrepancies have

focused primarily on improvements of the turbulence model used in the Reynolds-averaged Navier-Stokes equations, with the most recent emphasis placed on multiscale models (Wilcox [1990], Goldberg [1991]).

At the same time that these improvements in computational ability have been obtained, recent experimental evidence indicates that the separated compression corner SWTBLI is highly unsteady. The term "unsteady" is used here not to refer to the unsteadiness of the incoming turbulent boundary layer, but (following Tran [1987]) to a state where the characteristic time scale is significantly larger than the reference scale, δ/U_∞ , and/or the spatial excursions are considerably larger than the characteristic length scale, δ . As discussed in Chapter 2, this unsteadiness is not primarily the result of turbulence amplification by the shock wave - which might be predicted by turbulence models - but of a moving separation shock wave/compression system, distinct from the shock found in the inviscid field. Improvements in the ability to predict mean flowfield features are therefore overshadowed by the fact that the time-independent numerical solution which matches these features does not accurately reflect the true time- dependent nature of the interaction. Given the critical status of predicting and designing for X-30 aeroacoustic loads, it would seem that the physical model used to predict SWTBLI's must be reexamined to account for this unsteadiness.

Unfortunately, what causes the shock to move is not yet known. Further, studies of some other shock separated flows (e.g. blunt fin SWTBLI's (Dolling and Brusniak [1991]), incident oblique shock SWTBLI (Hayashi *et al.* [1989])) exhibit the same kind of unsteadiness as found in the unswept compression corner interaction. Hence, even in cases where numerical predictions of the SWTBLI flowfield have been quite successful, some of the important physical processes and features are still not correctly modeled.

There exists a need to develop a physical model which explains the mechanism driving the motion of the separation shock. Additionally, from a design perspective, there is a need to minimize the dynamic loading caused by the moving shock. Such may be accomplished through designs which eliminate or minimize the interaction. But, where this is not possible, a method of control - preferably passive in nature - could be used.

1.2 Objectives of the Current Study

The current study is part of a larger ongoing effort at the University of Texas at Austin to understand the dynamics of unsteady separated SWTBLI's. While the investigation reported here focuses on the interaction generated by an unswept compression corner, parallel investigations are being made for interactions involving swept compression corners (Dolling *et al.* [1991], Erengil and Dolling [1992]), cylinders (Dolling and Brusniak [1991]), and sharp fins

(Gibson and Dolling [1991], Schmisser and Dolling [1992]) with the goal of developing a unified model which will account for the similarities and differences observed in the various separation shock motions. The specific objectives of the current work were to:

- a. to gain a better understanding of the mechanism(s) driving the separation shock motion in a turbulent compression corner interaction, and
- b. to demonstrate a method(s) of influencing and/or controlling the separation shock motion, frequency, and/or strength.

These objectives are closely linked and, as such, were pursued concurrently by examining the sensitivity of a baseline, highly separated unswept compression corner interaction to quantified perturbations.

Answers were sought to the following specific questions:

- a. What role does the flow downstream of the traditional surface separation line play in determining the dynamics of the separation shock?
- b. What role does the incoming turbulent boundary layer play in the separation shock motion?

Several types of perturbation were applied to the baseline interaction to aid in answering these questions:

- a. modification of the separation bubble/reattachment point by suction applied

near reattachment,

- b. modification of the separation bubble size by removal of end fences,
- c. modification of the outer region of the incoming boundary layer by a boundary layer manipulator, and
- d. modification of the near-wall region of the incoming boundary layer by riblets.

The investigation was experimental in nature, using both fluctuating surface and pitot pressure measurements to quantify the time-dependent flowfield behavior. Simultaneous data acquisition allowed determination of global changes and correlation of linked phenomena. Re-examination of the baseline interaction, as well as results of the perturbation studies sheds new light on the overall flowfield while pointing to those regions of the interaction to which the separation shock motion is most sensitive.

Chapter 2 sets the context of the current study by reviewing the body of previous work directly related to this investigation. Additionally, Chapter 2 briefly discusses the background for the perturbation techniques which were applied. Chapter 3 describes the experimental program, and is followed by a discussion of analysis techniques in Chapter 4. Chapters 5, 6, and 7 present a re-examination of the baseline flowfield, the response of the separation shock to perturbations downstream of the separation line, and the response of the

separation shock to modifications to the incoming flowfield, respectively. In light of these findings, Chapter 8 discusses implications of the interaction unsteadiness for further study of this flowfield. It also summarizes some ideas on the mechanism responsible for the motion of the separation shock. The results of the study are summarized in Chapter 9.

Chapter 2

Literature Review

The purpose of this chapter is to examine previous research directly related to the current work. The first section reviews the results from studies of turbulent, highly separated unswept compression corner interactions which have ignored - or treated as being of secondary importance - time varying features of the interaction. This is followed by the results of experimental investigations showing the dominant unsteady nature of this class of interactions, the impact of this unsteadiness on the interpretation of "mean" flow data, and suggested mechanisms which drive the unsteadiness. The focus is then shifted to a review of efforts to control the interaction, which have primarily consisted of active techniques (i.e., fluid injection or removal) to minimize or eliminate the shock-induced separation. The chapter concludes with a brief review of some passive techniques to modify the character of a turbulent boundary layer.

For insight into the general topic of shock wave/boundary layer interactions, the reader is referred to other works. An excellent review of early shock wave turbulent boundary layer interactions has been written by Green [1970]. More recent reviews, though heavily biased toward three-dimensional interactions, have been compiled by Settles and Dolling [1986,1990]. Finally,

Dolling [1990] provides a general overview of the flow unsteadiness associated with shock-induced turbulent boundary layer separation.

2.1 'Time-Independent' Compression Corner Studies

Turbulent compression corner interactions have been the subject of experimental study since the early 1950's (Drougge [1953]). Much of the early work focused on examining the role of various parameters (i.e., Reynolds number, Mach number, ramp angle/pressure rise) on the propagation of the inviscid shock influence upstream of the corner. This "upstream influence" was usually determined from surface flow visualization and/or surface pressure measurements. Among the findings for interactions where separation occurred was the apparent existence of a "free interaction." This concept, put forward by Chapman, Kuehn, and Larson [1958], suggests that when the extent of separation is large, the interaction upstream (and possibly for some distance downstream) of the separation point is independent of the shock-producing geometry. Law [1974] observed this feature in the almost-constant boundary layer separation angle for compression corner angles greater than that necessary to force separation. Similarly, Settles *et al.* [1979] found that surface pressure distributions for several ramp angles upstream of and through the separation point could be collapsed reasonably well by shifting the streamwise location of the distributions to make the initial pressure rises coincident.

One of the most complete pictures of the highly separated compression corner interaction has come from the experimental work of Settles *et al.* [1976, 1979] at the Gas Dynamics Laboratory of Princeton University. This interaction was generated by a 24 degree ramp in a Mach 3 flow. In addition to surface measurements, extensive pitot pressure, static pressure, total temperature, and Preston tube measurements were made to develop a model of the flowfield (Fig 2-1). All data were obtained using conventional probing techniques. This model shows an initial compression which turns the external flow through 10 degrees, followed by an additional compression wave system nearer the corner to complete the remaining turning at reattachment. Streamlines calculated from experimental data reveal a distorted vortex centered above the corner. Also of particular interest is the large distance required for the sonic line to return to the near-wall region of the ramp boundary layer. This feature would allow disturbances originating well up the ramp face to propagate upstream of the corner (from $X/\delta = 5$ to $X/\delta = -2$ for Settles' study).

Special attention was paid to documenting the quality of the flow in this experiment. Aerodynamic fences were attached to the ramp sides to isolate the interaction from the tunnel side walls. Spanwise two-dimensionality was checked using transverse surface pressure measurements and surface flow visualization. Though the latter technique indicated a nodal pattern (Settles *et al.* [1979]), the

authors concluded that any three-dimensional perturbations were minor. Selig [1988] has recently reviewed similar work done in the Princeton facility and found the surface patterns for this interaction to be non-unique. He too concluded, however, that this discrepancy did not "seriously compromise" his study of the interaction unsteadiness. Settles *et al.* checked for flow unsteadiness using microsecond spark shadowgrams, but found only "minor motions and ripples" which were of no greater extent than 0.1δ.

These measurements and resulting model have been subsequently and extensively used for comparison with numerical predictions. Early efforts using algorithms which successfully computed unseparated compression corner interactions failed for this highly separated flow (Horstman *et al.* [1977], Viegas and Horstman [1979]). As is shown in Fig 2-2, although several different turbulence models were employed, no numerical model adequately predicted the separation point or the surface pressure distribution under the separated region. Further, the predicted outgoing boundary layer had a slower recovery than was measured (Fig 2-3). In the decade following this work, some improvement occurred. Wilcox [1990], for instance, applied his multiscale turbulence model to obtain superior results (Fig 2-4), which he attributed to the models "more physically realistic description of the Reynolds stress tensor."

To this author's knowledge, all of the computational efforts involving the

highly separated interaction generated by a compression corner have neither considered nor predicted any unsteadiness of the flow. Experiments by Dolling and Murphy [1983], however, have shown Settles' 24 degree corner interaction to be strongly time dependent. The results of their study are discussed in the following section.

2.2 Studies of the Unsteady Interaction

2.2.1 Surface Pressure Studies

Qualitative indications of the unsteadiness of shock- induced turbulent boundary layer separation have been available from the earliest studies, usually in the form of direct observation of the resulting wave system (i.e., shadowgraph or Schlieren images). One of the earliest efforts to obtain quantitative data of such an interaction - - if not the earliest -- was carried out by Kistler [1964], who made fluctuating surface pressure measurements upstream of a forward facing step at Mach 3 and 4.5. Within the separated region near the step face, Kistler observed the surface pressure time history to be that of "a normal turbulence signal (i.e., as a finite bandwidth white noise.)" Convective velocities of turbulent eddies in this region, obtained from cross-correlations of surface pressure measurements, were in the same direction and of nearly the same magnitude as the freestream, leading Kistler to conclude that the pressure fluctuations here were driven by the

"turbulent activity in the free shear layer near the dividing streamline." Near the separation point (as implied by the rapid rise in the mean surface pressure distribution), however, he found the surface pressure signal to exhibit an "on-off" behavior (Fig. 2-5) -- a pattern which is now recognized as characteristic of unsteady shock-induced turbulent boundary layer separation. The frequency of this switching was significantly below that characterizing the incoming boundary layer, U/δ .

Time-dependent investigations of a number of compression corner interactions were carried out by several teams in the Mach 3 facility at the Princeton University Gas Dynamics Laboratory in the 1980's. Dolling and Murphy [1982] made single point high frequency surface pressure measurements throughout the highly separated 24 degree corner interaction of Settles, from upstream of separation through the inviscid pressure rise on the ramp surface. While their mean distributions agreed reasonably well with those obtained by Settles et al, they found the time histories near separation to be like Kistler's - a turbulent signal with the mean value switching between two distinct levels. This behavior was attributed to a "highly unsteady shock wave structure undergoing streamwise excursions," the position of which ranged from the upstream influence line to the separation line as deduced from mean surface measurements. This finding disagrees with the shadowgram-based conclusion of Settles, and is

probably due to the optical integration of the density gradients across a spanwise non-uniform interaction masking the unsteadiness. The motion of the shock wave produced a maximum in the surface pressure root-mean-square (RMS) distribution when normalized by the local mean pressure. A second, smaller peak was also noted near the mean reattachment line, though the time histories showed no switching behavior. Dolling and Or [1985] expanded on this work by performing investigations of 8 degree and 12 degree (unseparated), 16 degree (incipient separation), and 20 degree (separated) compression corner interactions. Similar intermittent behavior was found in all but the weakest interaction, though the size of the intermittent region increased with interaction strength.

Simultaneous multi-channel fluctuating surface pressure data were obtained by Muck *et al.* [1988] for the 16, 20, and 24 degree interactions. Their review of streamwise time history plots showed that the wave structure observed by Dolling and Murphy was a "single sharp shock." Further, spanwise measurements indicated that for all of the ramp angles tested the shock was not planar, but highly three-dimensional. From these results, the authors inferred that this rippling was caused by incoming turbulent structures. Subsequent work (discussed below) has questioned these conclusions.

The most recent experimental investigations of unsteady compression corner interactions have been carried out in the Mach 5 facility at University of

Texas at Austin, focusing on the highly separated interaction generated by a 28 degree ramp. Complementary studies of Marshall and Dolling [1990] and Erengil and Dolling [1991a] used a larger number of simultaneous surface pressure measurements than in the study of Muck *et al.* (8 versus 4), providing a spatially expanded picture of the interaction at any given instant. Marshall's transducers were aligned in spanwise arrangements to examine the two-dimensionality of the separation shock front and its motion. Shock position relative to a given transducer was determined from the instantaneous surface pressure reading through a two threshold method (TTM). The rationale and mechanics of this method are discussed in Section 4.2.1. Information was combined from all transducers to form a binary or ternary "frame" of the shock foot position at each instant in time. Pattern probabilities were then computed by searching the frame sequences. From these data, Marshall concluded that the instantaneous separation shock front was nominally two-dimensional, though more so when moving downstream. Streamwise deviation of the shock front from a linear shape was found to be only a small fraction of the overall distance traversed by the separation shock.

In contrast to Marshall's transducer orientation, Erengil aligned his transducers with the freestream to examine the separation shock behavior and its influence on the flow under the separated shear layer. He too used a TTM to

determine shock position. "Frozen" surface pressure distributions were obtained by ensemble averaging pressure signals when the separation shock moving in a specified (upstream or downstream) direction crossed a fixed point. The results for the upstream shock motion are presented in Fig 2-6; the downstream results were reported as being similar. Several points are worth noting in this figure. First, the pressure rise associated with the separation shock is much steeper than the mean pressure rise (depicted in the figure as a solid line), and is more consistent with the numerically predicted behavior (Fig 2-2). Second, the strength of the separation shock (as determined from the pressure rise between the first and third data points of each curve) increases with downstream shock position. Third, the initial pressure rise is followed by a gradual rise to the plateau pressure, indicating a compression wave system following the shock. These last two findings conflict with the single-shock model of Muck *et al.* , and are due to the more systematic analysis performed by Erengil. Finally, the pressure rise following the pressure plateau (within 1δ of the corner) is relatively independent of shock position. A detailed examination using time history ensembles shows, in fact, a slight pressure drop in this region as the separation shock moves forward and a slight rise as it moves aft.

Gramann and Dolling [1990] have extended the understanding of this interaction through simultaneously-acquired fluctuating surface pressure

measurements upstream of the corner and on the ramp face. Using cross-correlations of conditionally acquired data sets, the authors were able to establish that the separation shock foot location is coincident with the separation point location. The separation line found in the surface flow visualization corresponds to the downstream limit of the separation shock motion (Gramann [1989]). They also found that the location of the reattachment point on the ramp moves in conjunction with - and in the opposite direction to - the separation point, resulting in an expanding and contracting separation bubble. This finding is consistent with that of Kussoy *et al.* [1987] for the separated flow induced by a shock on a flared body of revolution. The unsteadiness permeates the entire interaction for at least 4δ downstream of the corner, and contributes significantly to the local pressure variance. Finally, no evidence was found of a rapid increase in turbulence intensity across the unsteady separation shock, at least as reflected in the wall pressure fluctuations.

2.2.2 Flowfield Studies

The reader is reminded at this point that all of the previous investigators have based their conclusions upon surface measurements; predominantly, fluctuating pressure data. Few efforts have been made to examine the time-dependent flowfield above the surface, and these have limited their focus to the flow downstream of the corner. Kuntz *et al.* [1987] made laser Doppler

velocimetry (LDV) measurements of the developing boundary layer in 8, 12, 16, 20, and 24 degree compression corners at Mach 2.9. For those interactions with large separation bubbles (20 and 24 degrees), the near-wall region of the outgoing boundary layer was highly retarded but rapidly accelerated with increasing distance along the ramp. This behavior, coupled with large measured Reynolds stresses, led the authors to conclude that large scale turbulent structures existed downstream of the interaction. Also, contrary to Gramann's findings, the "turbulence intensities and Reynolds stress values were significantly increased by the interaction." No spectral analysis seems to have been done by the authors nor were any simultaneous upstream measurements made to characterize the unsteady shock. Without this analysis or these data, the contribution of the large scale unsteadiness could not be separated from the true turbulence in the turbulence measurements, and so the conclusions from Kuntz's study must be considered with caution.

Selig *et al.* [1989] made single hot wire measurements above the compression corner in Settles' 24 degree interaction. They, too, found the downstream turbulence to be amplified. Spectral analysis of the signal downstream of the corner exhibited energy peaks at frequencies an order of magnitude higher than those associated with the separation shock. Coupled with comparisons between the variation of maximum shock oscillation amplitude and

maximum turbulence intensity with increasing interaction pressure rise, the authors found no direct link between the unsteady shock motion or the size of the separated region and the downstream turbulence. As with the previous study, no attempt was made to separate the effects of the moving shock from the local turbulence. Selig also noted that the probability density functions of the downstream mass flux measurements were bimodal, with one peak near the expected inviscid value downstream of the shock and another, lower value representative of flow near the surface. The authors suggested two possible causes of this result. Unsteady streamwise/Taylor-Goertler vortices associated with turning flow on a concave surface might be responsible for exchanging low momentum fluid near the surface with higher momentum fluid above the boundary layer. Conversely, such an exchange may be driven by spanwise vortices, seen in the work of Ardonneau [1984] as a vortex sheet emanating from the foot of the separation shock.

2.2.3 Additional Relevant Studies

Before moving on to a review of possible mechanisms driving the separation shock motion, two additional studies should be mentioned. The first is that of Thomas *et al.* [1991], who examined an unseparated compression corner interaction for non-linear energy spectra transfer due to the shock system. Fluctuating surface pressure measurements were made in the flowfield generated

by a 6 degree wedge model at Mach 1.4. Given that these fluctuations are related to weighted products of local velocities and velocity gradients, the authors took their lead from incompressible transition studies and chose to "model the local spatial change of the pressure fluctuation spectrum as a non-linear system consisting of both a linear and a quadratically non-linear input-output relation." Thus, the basis of their approach only loosely draws on first principles for its origin and may even ignore the true relevant coupling between the fluctuations. Nonetheless, the results of their experiment show the interaction to be dominated by linear mechanisms. There was some evidence that the upstream shock interaction tended to result in three-wave interactions which cascaded energy to lower frequencies, while downstream of the corner the opposite process was found to occur.

The second study was that carried out by Shen *et al.* [1990]. The objective of this experiment was to examine the time-dependent behavior of a supersonic reattaching shear layer uncoupled from the separation process. The interaction was generated by the shear layer of a backward facing step impinging on a 20 degree ramp in a Mach 3 flow. The position of the ramp was adjusted such that the free shear layer developed in the absence of a pressure gradient. From fluctuating surface pressure measurements on the ramp surface, the authors found the reattachment to be highly unsteady, with a behavior very similar to the

separation region in the compression corner flow. Rayleigh scattering used to visualize the instantaneous shock shape confirmed the shock unsteadiness. This optical technique succeeded where the shadowgrams failed because the illumination source is a short-duration (4 nsec) laser pulse focused into a thin sheet perpendicular to the axis of observation. Thus, both spatial and temporal integration of the flowfield structure are greatly reduced. With the laser sheet oriented spanwise and projected near the mean reattachment line, the shock was found to ripple in the manner inferred from fluctuating wall pressure measurements.

2.2.4 Summary

This sub-section has reviewed works which have shown the separated turbulent compression corner interaction to be highly unsteady, beginning at the upstream limit of the separation shock travel and extending as far downstream as experiments have investigated. The mean flowfield model initially developed, and against which numerical predictions have been compared, is only loosely representative of the flow at any given instant. Separation is precipitated by a non-stationary shock upstream of and weaker than the primary inviscid shock, and is closely followed by a compression system which completes the initial pressure rise to a plateau value. The reattachment process is also unsteady and correlates with the location of the separation point, though it is not totally clear

whether the reattachment unsteadiness is solely dependent on that of separation.

2.3 Suggested Driving Mechanisms

Several authors have examined the available data of their time and proposed possible mechanisms responsible for the motion of the separation shock. Kistler [1964] discussed the possibility that the shock motion was in response to acoustic oscillations within the separated region, but argued that such a mechanism was improbable since there was no evidence in the surface pressure time histories of a reasonably periodic signal at the low frequency of the shock motion, nor did Schlieren photographs indicate any well organized pattern within the separated region. As an alternative explanation, Kistler suggested that the shock motion was driven by the response of the dividing streamline surface to random cross-stream distortions. His argument was that, for supersonic flow, a perturbation which would cause an increase in the flow deflection angle would also increase the pressure jump, inducing further separation. This process would cease when "either a new separation bubble is formed ahead of the old one or some other mechanism intervenes." He did not specify whether this distortion was due to upstream or downstream influences.

Andreopoulos and Muck [1987] hypothesized that the incoming boundary layer was the "most likely cause triggering the shock wave oscillation," and that large incoming structures might also explain observed spanwise variations in the

shock wave. Their conclusions are based on three points. First, the frequency of the shock-wave unsteadiness was found to be of the same order as the "bursting frequency" of the incoming boundary layer and independent of the downstream separated flow. Second, the findings of Dolling and Or [1983] showed a common relation between shock intermittency and signal skewness for different shock generating geometries with the same upstream conditions. Finally, the authors found that the shock speed was of the same order as the turbulence fluctuations. This analysis, however, has come under criticism by several authors (Tran [1987], Dolling and Brusniak [1989], Erengil and Dolling [1991b]). Namely:

1. No direct correlations were established between the shock motion and any upstream fluctuations.
2. The single-threshold algorithm which they used to define shock position has been shown by Dolling and Brusniak [1989] to be highly sensitive to turbulence fluctuations and noise. No distinction is made between threshold crossings due to the passage of the separation shock and those due to random fluctuations in the flow or signal. The result is a higher number of shock crossings than actually occur. (These problems have been minimized in later studies using the aforementioned TTM.)
3. Separation shock frequencies in cylinder interactions have shown as great a

dependence on cylinder diameter as on the incoming boundary layer thickness (Dolling and Smith [1989]), which would indicate some influence of downstream conditions on the shock motion.

Tran [1987] demonstrated that in three supersonic separated interactions with the same inviscid shock sweep and overall pressure rise -- but generated by three different geometries -- both the mean and RMS surface pressure distribution could be collapsed by referencing streamwise distances to the inviscid shock position. This result would seem to indicate that the dynamic shock behavior may also follow the "free interaction" behavior discussed in Section 2.1 and perhaps provide support for a theory based on an upstream trigger of the shock motion, but was not considered by Tran. He does conclude, however, "that the inviscid shock strength is the primary governing parameter for most of the interaction," specifically the region upstream of the inviscid shock.

Tran also examined conditional ensemble-averaged time histories of surface pressure signals under the separation shock in a Mach 3, 20 degree compression corner interaction. Triggering events for each ensemble were obtained from the Variable Interval-Time Averaging (VITA) transformation (discussed in Section 4.2.2) of a surface pressure signal just upstream of the interaction. Tran found no correlation between these events -- supposedly representing the passage of large scale turbulent structures -- and the low

frequency pressure pulses generated by the separation shock. From this result he concluded that the incoming structures had, at best, a small influence on the flow unsteadiness. However, Erengil and Dolling [1991b] point out that by triggering on an upstream channel and not on the shock motion itself, correlations with appropriate phenomena may be washed out by averaging with more prevalent but unimportant features.

In their study of a 28 degree compression corner at Mach 5, therefore, Erengil and Dolling triggered ensemble selection on shock passages over a specified transducer. They further constrained the triggering event based on the type of shock motion present: upstream sweep, downstream sweep, upstream-to-downstream turn-around, and downstream-to-upstream turn-around. While the results from the first two event types were somewhat ambiguous, ensembles based on turn-arounds showed distinct time-dependent pressure signals which entered the interaction from upstream and were "coincident with the shock foot at the time of the turn-around." From these results they inferred that at least the shock change of direction was due to the passage of large-scale structures through the interaction from upstream. The cause of the large scale shock sweeps, however, is still unknown.

The results of the numerical study by Keefe and Nixon [1991] also support the idea that the separation shock is primarily driven by fluctuations in

the incoming flow. The authors begin by analyzing the response of a normal shock to perturbations in the incoming flow. Shock position spectra from their model exhibited a rapid roll-off at lower frequencies, eventually flattening out at a relatively low level at the mid and high frequencies. It is this receptivity to low frequency perturbations which, the authors contend, makes the separation shock respond to the "unmeasurable" low-frequency fluctuations in a boundary layer dominated by much higher frequencies. Unfortunately, they offer no physical explanation for this observation, nor do they focus further on the nature of the perturbation.

In contrast to studies focusing on upstream driving mechanisms of the separation shock, several studies have presented evidence suggesting that the driving mechanism is primarily within the interaction itself. From fluctuating surface pressure measurements made upstream of a forward facing step at Mach 2 and 4, Bibko *et al.* [1990] concluded that the shock unsteadiness must be driven by fluctuations in the separated and attachment regions. This was based on zero cross-correlation values between signals upstream of and under the separation shock near the frequency of the shock motion. Cross-correlations with downstream channels, however, did not produce appreciably larger values. Further, their choice of frequency band probably excluded the dominant energy-containing frequencies of the incoming boundary layer, though insufficient data

are reported to calculate this frequency. These shortcomings require that the conclusions of the authors be considered with caution.

Dolling and Brusniak [1991] also used fluctuating surface pressure measurements downstream of the separation shock to investigate the unsteady shock interaction generated by a cylinder at Mach 5. As with Erengil and Dolling [1991b], they obtained ensemble-averaged pressure histories through the interaction by triggering on the separation shock behavior. They too found a correlation between the shock change of direction and a pressure signature which arrived at the foot of the shock at the time of the change. This signature, however, originated in the separated region and propagated upstream.

From the above studies, additional insight has been gained into the flow phenomena surrounding the separation shock unsteadiness. As yet, conclusive proof of the shock driving mechanism has not been found.

2.4 Interaction Control Efforts

The severe consequences of shock-induced separation on the degradation of system performance have prompted investigations of means to prevent or reduce its extent. The majority of these efforts have focused on mass transfer (injection or removal) in the near-wall region. The logic behind such an approach is that the separation is a result of the inability of the low-momentum fluid near the surface to overcome the severe adverse pressure gradient imposed by the

shock. By removing this fluid through suction while pulling higher momentum fluid closer to the wall, or by increasing the near-wall region momentum by tangential blowing, separation can be minimized. Hamed and Shang [1989] provide a survey of these studies as involved to supersonic inlets. Viswanath [1988] has written a more general review, to include related efforts in transonic flows. With one exception, all studies have been concerned with only the mean separation bubble.

Experiments by Grin [1967], Krishnamurthy [1973], Manjunath [1973], and Viswanath *et al.* [1983] applied tangential blowing at the surface either upstream of or within the separated region to reduce the extent of separation. In comparing the merits of location, Viswanath found that blowing downstream of the separation point was a more efficient approach. He tentatively attributes this to the technique's ability to "remove the reattachment point by energizing the dead air region rather than the boundary layer upstream of separation."

Of immediate relevance to the current study are the results of compression corner experiments carried out by Tanner and Gai [1967], Ball and Korkegi [1968], and Ball [1970]. In each, suction was applied at the corner to control the extent of separation. Ball and Korkegi, and Ball examined laminar interactions for Mach numbers between 5.3 and 8.0. They used the low pressure region on the downstream face of the wedge as a vacuum source and varied the amount of

suction by controlling the gap between the upstream surface and the wedge face. The slot was reportedly choked, which prevented the downstream conditions from influencing the separated region. The authors reported that the extent of separation was very sensitive to the amount of suction applied, and that "removal of a small percentage of the boundary layer mass defect is sufficient to collapse the separated flow region."

Tanner and Gai investigated the effect of suction on turbulent compression corner interaction at Mach 1.9 for ramp angles of 8, 12, and 16 degrees. The slot through which suction was applied was formed by lifting the ramp off of the surface, and the amount of suction was controlled by a valve separating the model and a vacuum pump. With the slot present, but without suction being applied, the size of the separation bubble increased 50 - 60% over the baseline (no slot) interaction. Suction decreased the size of the separation bubble and raised the pressure on the wedge surface. For the strongest interaction examined and using a slot height of $1/3\delta$, a suction-per-unit-width of $1.5\rho U_\infty \theta$ was required to eliminate the separated region altogether and provide an essentially inviscid surface pressure distribution.

Few passive methods of separation control have been applied to supersonic shock/boundary layer interactions. Glotov and Korontsvit [1983] were able to reduce the extent of separation in a supersonic cylinder interaction

by placing a needle vertically within the separated region. Subsequent work by Brusniak [1991] indicates that the primary effect of this disturbance is to modify the inviscid wave structure in the freestream, and so addresses a different area of control than the others considered here.

Gartling [1971] studied the ability of flat plate vortex generators to prevent turbulent boundary layer separation in a Mach 4.7, 35 degree compression corner interaction. He found the effectiveness to be limited to a very narrow region directly downstream of the generators. Gartling concluded the mechanism by which separation was reduced to be a coupling between the expansion about the vortex generator body, and the tip and base vortices formed by the generator.

Prior to the current study, only the work of Selig [1988] has addressed the issue of controlling the separation shock dynamics. His interaction was generated by a 24 degree compression corner at Mach 2.9. Periodic blowing normal to the boundary layer-generating surface was applied at various locations within the separation bubble upstream of the corner and at various frequencies near that of the separation shock. Using an "appropriate" amount of blowing and by placing it close enough to the shock foot, the shock periodicity could be forced to match that of the blowing. However, this effect seemed to be somewhat localized since no corresponding behavior was observed in the data downstream of the corner.

Further, variation in blowing frequency had no noticeable effect on the wall-pressure power spectra, nor did blowing effect the bimodal nature of the probability density distributions discussed in section 2.1. From his ability to control the shock motion in this manner, Selig concluded that the separated region must have some influence on the unblown shock unsteadiness, though he did not rule out the role of the incoming coherent structures.

2.5 Relevant Boundary Layer Modification Techniques

A great deal of interest has been recently focused on passive drag reduction devices which have been demonstrated as effective in turbulent boundary layers. Two in particular, riblets and outer layer manipulators, have been the subject of numerous phenomenological studies to optimize their benefits. The mechanism by which they operate, however, is only now becoming understood. It is these mechanisms which the current study seeks to exploit to modify the separation shock motion. As such, this section will limit its scope to those features and studies of immediate relevance. The reader is referred to the recent comprehensive reviews on riblets written by Walsh [1990] and on outer layer manipulators written by Anders [1990] for more general coverage.

Riblets are narrow, small streamwise grooves in the surface on which the boundary layer develops. Their effects, as related to changes in turbulent structure, are limited to the near-wall region, $y^+ < 10-15$ (Walsh [1990]). Only

two supersonic studies have been found in the literature, Robinson [1988] and Gaudet [1989]. Of these, only Robinson obtained dynamic flow field data using hot wire anemometry. Though the data presented were not reduced to velocity measurements (Fig 2-7), they do show that the near-wall RMS hot wire voltage (and presumably RMS velocities) is substantially reduced by the presence of the riblets. This finding is consistent with subsonic measurements.

While riblets influence the near-wall region of the turbulent boundary layer, outer layer manipulators (referred to as boundary layer manipulators (BLM's) in this study) alter the structure of the outer region. These devices are typically plates or thin airfoil sections, and are mounted parallel to the boundary layer-generating surface in the outer half of the boundary layer. Disturbances introduced by the BLM's persist for long distances downstream. It is not clear by what specific mechanism these devices operate, though the two leading arguments center around the solid boundary "plate" effect and the "wake" layer effect. One of the most prominent results of the BLM's is their "dramatic reduction in outer edge intermittency" (Anders [1990]), where intermittency is defined here as the percentage of time the flow at a given point is turbulent. Results of Chang and Blackwelder [1990] also show an associated increase in the interface crossing frequency - "defined as the number of large turbulent eddies passing per unit time." The effect of BLM's on these two parameters are

demonstrated in Fig 2-8, where the open symbols represent the undisturbed boundary layer and the filled symbols represent the flow with the BLM. These plots bear a striking resemblance to the separation shock intermittency and zero-crossing frequency streamwise distributions in the compression corner interaction. BLM's have also been shown to significantly reduce the spanwise size of large structures. Unfortunately, there are no available data on the effect of BLM's in supersonic boundary layers.

2.6 Summary

Three decades of study of separated compression corner SWTBLI's has provided us with a detailed description of the mean flowfield, a model against which the accuracy of current numerical prediction techniques is assessed. Current experimental evidence, however, has shown that the overall interaction is highly unsteady, and that the mean model does not accurately reflect the instantaneous flowfield at any point in time. Insufficient understanding of what controls the interaction unsteadiness prevents us from improving numerical models to reflect this time- dependent nature. While several hypotheses have been offered, no firm evidence has been presented to indicate to what aspects the overall flow unsteadiness is even sensitive to. It is with this background that the current study was undertaken. Specifically, this study seeks to answer the question of how the translating shock motion depends on the incoming boundary

layer and the flowfield downstream of the separation line by means of quantified perturbations. Such insight is required to guide the development of a new or modified to numerical model with which to accurately predict shock wave/boundary layer interactions. Further, a demonstrated method of controlling the separation shock may find direct application in alleviating aeroacoustic loading problems associated with such interactions.

Chapter 3

Experimental Program

3.1 Wind Tunnel

All tests were conducted in the Mach 5 blowdown wind tunnel at the Balcones Research Center (BRC) of the University of Texas at Austin. The test section of the tunnel measures 6 in. wide by 7 in. high and is 12 in. long (15 cm x 18 cm x 30 cm). The facility air supply is provided by a 100 hp (75 kW) Worthington compressor, which fills 140 cubic feet (4 cubic meters) of storage volume at ambient temperature and up to 2550 psia (18 MPa). During a run, the pressure is dropped through a 1.5 in. (4 cm) Dahl valve, driven by a Moore 352 controller, to provide a preset stagnation pressure, which is measured by a Setra Model 204 pressure transducer (0-500 psia, 0-3 MPa). Downstream of the valve, the air is heated by two banks of nichrome wire heaters regulated by a Love Controls 1543 controller to match a desired stagnation temperature, measured by a Type K thermocouple. For typical stagnation conditions used during this program, the air supply provided stable run times of up to 50 seconds.

The test section is modular in nature and is installed just downstream of the nozzle exit. For the work reported here, the ceiling had a 0.51 in. (1.3 cm)

wide slot through which a probe shaft could pass for flowfield surveys. The slot is 6.6 in. (16.8 cm) long and begins 2.9 in. (7.3 cm) downstream of the nozzle/test section junction. The floor (Fig 3-1) has two cavities. The upstream cavity houses a circular instrumentation plug and is set on the tunnel centerline, centered 4.2 in. (10.6 cm) downstream of the nozzle/test section junction. The downstream cavity holds the ramp model, is 3.5 in (8.9 cm) wide, and extends from 6.5 in. to 10.25 in. (16.5 cm to 26 cm) downstream of the nozzle/test section junction. Slots in the bottom of this cavity provided for 0.25 in. (0.64 cm) streamwise motion of the compression corner.

3.2 Compression Corner

The 28 degree unswept compression corner was 4 in. (10.16 cm) wide by 1.875 in. (4.76 cm) high. Model dimensions were chosen to provide both adequate width for interaction two- dimensionality and adequate height such that the inviscid pressure level was reached upstream of the expansion corner. The former condition was confirmed using surface flow visualization. While model design prohibited instrumentation of the ramp face, the latter requirement was inferred from the fact that the length of the current ramp face exceeded that of Gramann [1989] (used in the same facility under similar conditions), where surface pressure measurements established that the inviscid static pressure was reached. Fences 2.5 in. (6.35 cm) high and extending at least 2.5 in. forward of

the corner were used to ensure interaction two-dimensionality, as well as isolating the interaction from the tunnel side-walls. The ramp was made up of three sections (Fig 3-2). The base structure mounted to the test section floor and provided a 3.48 in. x 3 in. x 0.63 in. deep (8.8 cm x 7.6 cm x 1.7 cm) plenum for use during suction runs. The plenum was elevated slightly to provide sufficient material at the model base to mount an O-ring between the model and tunnel floor. A top structure capped the plenum. An interchangeable ramp face spanned the central 3.5 in. (8.9 cm) of the model. This feature was designed to minimize possible differences between interactions caused by small changes in ramp angle, as were observed in the work of Gramann and Dolling [1990]. Measurements of the ramp angle for the two faces (slotted and unslotted) showed less than 0.1 deg. difference. The unslotted face completely sealed the model plenum from the interaction. It was used to obtain baseline data for the current investigation, as well as for comparison with past studies. The second face had a centered 3 in. (7.62 cm) wide slot between 0.266 in. (6.8 mm) and 0.532 in. (13.5 mm) from the corner, as measured along the ramp face. The location of the slot was chosen to coincide with the reattachment zone, as defined by Gramann [1989]. The position of the slot relative to the upstream and downstream limits of reattachment, as well as relative to the reattachment line determined from flow visualization, is shown in the inset to Fig 3-2.

3.3 Instrumentation Plugs

A circular brass instrumentation plug 3.375 in. (8.6 cm) in diameter permitted flexible placement of surface mounted pressure transducers. A line of 26 transducer ports, centered on the plug, were equally spaced at 0.115 in. (0.29 cm) (center-to-center) intervals. While the plug was fully rotatable, the transducer line was only oriented in the streamwise direction for this test program. A second instrumentation plug 1.00 in. (2.54 cm) in diameter was used to mount a single pressure transducer in the nozzle exit, up to 12.0 in. (30.5 cm) upstream of the compression corner.

3.4 Probes

3.4.1 Probe Drive and Mount

The probe drive was built around a Velmex UniSlide with a threaded shaft that provided one inch of travel per 40 turns. The drive was manually operated. For continuous surveys with the conventional pitot probe or the pitot rake, vertical position was measured by a Schaevitz DC-operated linear variable differential transformer (LVDT), Model 6000 HPD, with 6 in. (15.2 cm) of travel. The LVDT had a sensitivity of 3.4 V/in. (1.34 V/cm). Vertical probe position for fluctuating pitot pressure point measurements was performed with a dial gauge accurate to 0.001 in. (0.025 mm). This technique made an additional channel of

the data acquisition system available for fluctuating surface pressure measurements.

3.4.2 Pitot Probes

The conventional pitot probe was of standard design, with a rectangular flat face 0.018 in. high by 0.085 in. wide (0.46 mm by 2.2 mm), and an opening 0.005 in. (0.127 mm) high. Approximately 12 in. (30 cm) of 0.062 in. (1.57 mm) i.d. nylon tubing connected the probe tip to the measuring pressure transducer, Kulite model XCQ-062-50A. Power spectra indicated that this configuration had a frequency response of about 200 Hz. The probe tip extended 1.69 in. (4.3 cm) upstream of the center of the probe shaft.

Three fluctuating pitot probe designs were used (Fig 3-3). Probes of this type have been used extensively to study turbulent structures in a compressible shear layer (Shau [1990]). They provide both adequate frequency response and acceptable interference (away from solid surfaces), and are more rugged in the high-speed flow than hot-wires.

For measurements made above the compression corner face or when only a single fluctuating pitot pressure measurement was required, a single Kulite miniature pressure transducer, model XCQ-062-100A, was mounted in a tapered 0.095 in. (2.4 mm) stainless steel tube (Fig 3-3a). The tip of the transducer protruded upstream 0.05 in. (1.3 mm), which placed it 3.36 in. (8.53 cm) upstream

of the probe shaft center.

Simultaneous measurements of fluctuating pitot pressure were conducted with the probe shown in Fig 3-3b. Two Kulite model XCQ-062-050A miniature pressure transducers were mounted in a manner similar to the single Kulite probe, with centers separated vertically by 0.164 in. (4.2 mm). The probe tip extended 2.89 in. (7.34 cm) forward of the probe shaft center.

The probe shaft used for all but the floor pitot probe was a modification on the design described in Fig 3-14 of Shau [1990]. As the current tests required the probe to extend across the entire test section, the cylindrical portion of the shaft was replaced with 0.375 in. (9.5 mm) diameter Type 316 stainless steel tubing with 0.075 in. (1.9 mm) wall thickness. This reduced the probe deflection at full extension from 0.1 in to 0.07 in. (2.5 mm to 1.8 mm).

A third fluctuating pitot probe (Fig 3-3c) was designed by MacKay [1991] to measure boundary layer fluctuations well upstream of the compression corner. To minimize interference with the compression corner interaction, this probe entered through the tunnel floor and had a shaft of diamond cross-section (13 degree half-angle). The center of the pressure transducer was mounted 1.225 inches (3.11 cm) upstream of the shaft center, and could be placed from 0.2 to 1.4 inches (0.51 to 3.56 cm) above the floor.

3.4.3 Pitot Rake

Spanwise mean pitot pressure profiles were measured using the pitot rake of Shau [1990]. The seven pitot probe tips comprising the rake were of design and size similar to the conventional pitot probe described above, and were spaced (center-to-center) 0.5 in. (1.27 cm) apart. Seven Kulite OEM type CTQH-187-50A pressure transducers were installed in the rake body to improve the frequency response of the measurements. Data were not obtained to specifically determine the frequency response of this set-up, but it is believed to be of the same order as the conventional single pitot probe discussed above.

3.5 Suction System

When suction was applied, mass was removed through the model plenum, out the bottom of the model, through a 1.0 in. (2.54 cm) pipe and 2 in. (5.1 cm) Cashco Ranger QCT valve, and into an evacuated tank. The tank had a volume of 33.42 cubic feet (0.95 cubic meters), and was drawn down to an initial pressure of less than 0.2 psia (1.4 kPa) prior to each suction run. The valve was fit with a 40% trim and was run full open. No attempt was made to control the valve setting during a run. However, data taken during each run indicated uniform and repeatable pressure values in the pipe just below the model. The amount of mass removed is discussed in Chapter 6.

3.6 Boundary Layer Manipulators

The boundary layer manipulators (BLM's) were designed based on studies of subsonic Large-Eddy Break-up (LEBU) devices. They were constructed of 0.053 in. (1.3 mm) thick stainless steel. While significantly thicker than subsonic designs, this thickness was chosen to provide sufficient rigidity for the expected loads. Leading and trailing edges were beveled from above at either 15 or 35 degrees (Figs. 3-4a and b) to avoid a leading edge detached shock wave as well as a reflected shock from the tunnel floor.

The BLM's were mounted on two symmetric half-diamond struts with 20 degree leading and trailing edge angles (Fig 3-4c). The sides of the struts facing the tunnel centerline were parallel to each other and the incoming flow, and separated by a distance of 3.83 in. (9.74 cm). The horizontal cross-section of each strut measured 0.245 in. thick by 1.30 in. long (6.2 mm x 33 mm). Each strut was attached to the tunnel floor by two bolts to prevent turning during tunnel operation. The lower surface of the BLM was located 0.5 in. (1.3 cm) above the tunnel floor.

BLM chord lengths of 0.69, 1.03, and 1.38 inches (17.5, 26.2, and 35 mm) were initially examined. Surface flow visualization studies showed streakline "necking" for the largest BLM, indicating a possible shock wave between the struts, BLM, and floor. No such feature was observed for the other two BLM

designs. Further BLM studies were limited to the 1.03 in. chord model. Results are discussed in Chapter 7.

3.7 Riblets

Riblets are fine streamwise grooves in the boundary layer-generating surface which are used to effect turbulent skin friction. The riblets used in this study were of triangular cross-section, with height (h) and peak-to-peak spacing (s) both equal to 0.006 in. (.15 mm). In terms of wall variables of the current study, these dimensions were $s/s-3/u+/d/s+3 = h/s-3/u+/d/s-3 = 15$. The riblets were similar to those used by Robinson [1988] ($s/s-3/u+/d/s+3 = h/s-3/u+/d/s-3 = 17$), and were provided by the 3M Company already machined into a thin sheet of adhesive-backed vinyl. This manufacturing technique has been shown to provide uniform riblets even at these very small dimensions (Walsh and Lindemann [1984]). The riblet material spanned the width of the tunnel floor and covered 18 in. (45.7 cm) upstream of the instrumentation plug.

3.8 Instrumentation

3.8.1 Pressure Transducers

In addition to the transducers mentioned above, fluctuating surface pressure measurements were made using Kulite model XCQ-062-15A or XCQ-

062-50A miniature pressure transducers. While these transducers had a range 8 to 25 times that necessary to measure the expected pressures, transducers with a more appropriate pressure range have more flexible diaphragms and, hence, a lower natural frequency [Dolling and Brusniak, 1991]. The Kulite XCQ transducers have a fully active four arm Wheatstone bridge atomically bonded to a 0.028 in. (0.71 mm) diameter silicon diaphragm, and each have a temperature compensation unit. Specifications for the transducers, as provided by Kulite Semiconductor Products Inc., are presented in Table 3-1. Each XCQ transducer was fitted with a B-type protective screen which reduced the transducer effective frequency response to about 50 kHz.

Shock tube studies have shown the static calibrations of this type of transducer to be within a few percent of dynamic calibrations (Raman [1974], Chung and Lu [1990]).

Kulite Model	XCQ-062-15A	XCQ-062-50A	XCQ-062-100A	CTQH-187-50A
Rated Pressure (psia)	15	50	100	50
Overpressure (psia)	45	150	300	150
FS Output (mV)	100	100	100	100
Excitation (V DC)	5	5	5	10
Combined Non-linearity and Hysteresis (%FS BFUL)	.5	.5	.5	
Repeatability (%FS)	.1	.1	.1	
Natural Frequency (kHz)	500	600	1000	
Resolution	Infinite	Infinite	Infinite	Infinite
Thermal Zero Shift (%FS/100 deg F)	2	2	2	
Thermal Sensitivity Shift (%/100 deg F)	5	5	5	
Compensated Temperature Range (deg F)	80 to 180	80 to 180	80 to 180	
Operating Temperature Range (deg F)	-65 to 250	-65 to 250	-65 to 250	

**Table 3-1: Pressure Transducer Specifications
[Kulite]**

3.8.2 Signal Conditioning

Kulite pressure transducer outputs were amplified by either an EG&G PARC Model 113, Dynamics Model 7525, or Vishay Measurement Group Model 2311 amplifier. Tests made by Gramann [1989] showed no phase shifting associated with these three models over the sampling rates used. Gains varied from 100 (for pitot measurements downstream of the corner) to 2000 (for surface pressure fluctuations in the undisturbed boundary layer). Amplifier settings were adjusted to provide output within a ± 7 volt range to remain within the limits of the filters.

Following amplification, these signals were low-pass filtered using either an Ithaco Model 4113 or Model 4213 analog filter. These filters provide 3 dB attenuation at the set cutoff frequency, with a roll-off of 80 dB/octave. Cutoff frequencies were set at 50 kHz for sampling rates greater than 100 kHz, and at the next available setting below the Nyquist frequency ($1/2$ the sampling frequency) for sampling frequencies of 100 kHz or lower. The latter choice was driven by aliasing problems when the Nyquist frequency fell within the energy-containing portion of the spectrum.

3.8.3 Data Acquisition Hardware

Preliminary data were obtained using a MASSCOMP 5500 data acquisition system. This system consisted of two 12-bit A/D converters coupled with an eight channel sample-and-hold unit. The A/D's had a range of 0-10 volts, and were operated in a differential mode to minimize signal noise through common mode rejection. Maximum sampling frequency per channel was a function of the number of channels used, but could not exceed 500 kHz for two channels. Most eight- channel runs were accomplished at 100 kHz/channel. Data storage was limited to 800 records, where one record contains 1024 data points.

The majority of data acquisition was done using two LeCroy Model 6810 Waveform Recorders (12 bit A/D converters) with four megabytes of memory each. Sampling rates (per channel) for this system were limited to 5 MHz for two channels or 1 MHz for eight channels. Additionally, the LeCroy system allowed individual tailoring of each channel input voltage range, providing greater A/D resolution without requiring maximum gain from the amplifiers. As with the MASSCOMP system, the LeCroy A/D's were operated in a differential mode.

3.9 Calibration and Noise

Calibration of all probe and surface transducers was carried out daily prior to any run. Pressure transducers were calibrated at low levels using a Heise Model 710A digital pressure gauge with a resolution of .001 psia (6.9 Pa), which

itself was zeroed daily to 25 millitorr (3.3 Pa) against a Hastings Vacuum Gauge. Higher pressure calibrations for pitot surveys were made against a 50 psi (0.35 MPa) Heise dial gauge with a resolution of 0.05 psi (345 Pa). Calibration of the LVDT was made against the dial gauge described in section 3.4.1. Calibration data were least-squares fit to a straight line. Typically four to ten points were used to generate each calibration curve, using only points that were within 1% of their predicted value.

Following each calibration and prior to taking actual data, a simulated run was accomplished with transducers under static load. These data were analyzed and provided noise levels for comparison with measurements from actual runs. Noise levels obtained using this approach ranged from ± 2 to ± 15 A/D counts (out of a possible 4096). Comparison of actual and noise RMS values gave signal-to-noise ratios from 10:1 for measurements in the undisturbed boundary layer to 500:1 for measurements in the separated region, and 200:1 for the fluctuating pitot pressure measurements.

3.10 Flow Visualization

Some surface flow visualization was performed to obtain a global mean picture of several of the interactions. The technique employed a slight variation of that described by Settles and Teng (1982). A fluid paste of finely ground graphite and diesel fuel, with a small amount of kerosene, was applied to the

tunnel floor or ramp surface immediately prior to a run. Surface shear stress during the run spread the mixture over the surface. Low static pressures and high wall temperatures caused most of the fluid to evaporate. The pattern left in the thin layer of graphite was then removed using large sheets of transparent tape and mounted on paper. In this manner, a quick undistorted image of the surface streaks was obtained.

3.11 Upstream Flow Conditions

Nominal flow conditions are presented in Table 3-2. Actual stagnation pressure ranged from 325-335 psia (2.2-2.3 MPa) during the test program, but did not vary by more than 4 psia (.03 MPa) during any given run. The higher pressure settings were necessary to overcome occasional tunnel starting problems. The stagnation temperature varied from 630-645 deg R (350-385 K) during the course of the test, mostly due to seasonal changes in outside temperature. However, variation during a given run did not exceed 2 deg R (1 K).

The incoming boundary layer developed under approximately adiabatic conditions, and transitioned naturally on the tunnel floor. Conventional pitot pressure surveys were made at several streamwise positions within the test section to quantify the character of the incoming boundary layer. The data were reduced assuming a piecewise linear decrease in total temperature across the

boundary layer based on total temperature surveys made by Shau [1991]. Static pressure was assumed constant through the boundary layer.

M_∞	4.95	4.95
U_∞	2540 ft/s	773 m/s
Re_∞	15.3×10^6 /ft	50.2×10^6 /m
P_O	330 psia	2.28 MPa
T_O	640 °R	356 K
$\delta_{.99U_\infty}$	0.59 in	1.51 cm
$\delta_{.99(\rho U)_\infty}$	0.70 in	1.77 cm

Table 3-2: Incoming Flow Conditions

A least-squares fit of the data to the law of the wall/law of the wake was carried out using the method of Sun and Childs [1973] to determine the wall skin friction (C_f) and Coles' wake parameter (Π) (Coles [1956]). Data points below $y^+ = 100$ were discarded prior to curve-fitting because of near-wall interference. Results

of this analysis are presented in Table 3-3, and a typical fit of the data is shown in Fig 3-5. The value of $\delta_{99(\rho U)_\infty}$ (δ_1) just upstream of the baseline compression corner interaction (3.75 inches downstream of the nozzle/test section junction) is used to normalize lengths in the current work.

Based on an empirical correlation of a large database of both equilibrium and nonequilibrium incompressible boundary layers, Das [1987] has obtained the following relationship (also cited in White [1991]) between the non-dimensional pressure gradient and Coles' wake parameter (Π):

$$\frac{\delta^*}{\tau_w} \frac{dp_e}{dx} \approx -0.4 + 0.76 \Pi + 0.42 \Pi^2 \quad (3-1)$$

Bradshaw [1977] indicates that Π is also somewhat dependent on Mach number, particularly for $M > 5$. The wake parameter values in the current study reflect a slight adverse pressure gradient, contrary to the findings of previous investigators who assumed a constant total temperature through the boundary layer. Variation in Π over the surveyed range is felt to be sufficiently small to consider the boundary layer as being in equilibrium. Surveys made by Nordyke [1987] at several spanwise locations indicated that the incoming boundary layer was also nominally two-dimensional.

In addition to the mean flow surveys, fluctuating surface and pitot pressure

measurements of the undisturbed boundary layer were made. The surface measurements were consistent with those of Gramann [1989] for the same flow. Gramann found his results compared favorably with those of other investigators. Skewness and kurtosis values from the pitot pressure data were consistent with hot wire data obtained by Spina [1988] in a Mach 3 boundary layer, and with hot wire measurements made by Shau in the BRC tunnel (Fig. 3-6).

Distance Downstream of Test Section/ Nozzle Junction in. (cm)	2.75 (6.99)	3.75 (9.53)	4.75 (12.07)	5.75 (14.61)
$\delta_{99U_{\infty}}$	0.57 (1.45)	0.59 (1.51)	0.59 (1.51)	0.60 (1.53)
$\delta_{99(\rho U)_{\infty}}$	0.67 (1.71)	0.70 (1.77)	0.70 (1.77)	0.70 (1.79)
δ^*	0.26 (0.66)	0.26 (0.67)	0.27 (0.68)	0.27 (0.70)
θ [x 100]	2.44 (6.21)	2.60 (6.61)	2.58 (6.56)	2.64 (6.71)
Π	0.75	0.78	0.78	0.82
H	10.6	10.2	10.4	10.4
C_f [x 10 ⁴]	7.73	7.74	7.68	7.58

Table 3-3: Undisturbed Boundary Layer Parameters

Chapter 4

Analysis Techniques

This chapter describes analysis techniques used in the current study. The first section explains basic statistical and time series analysis methods applied to wall and pitot pressure signals. Section two focuses on event detection techniques. The chapter concludes with a discussion of conditional analyses based on these events.

4.1 Basic Statistical and Time Series Analysis

Basic statistical quantities were calculated for both wall pressure and pitot pressure signals. These included signal mean, standard deviation, skewness coefficient, and flatness coefficient. The mean value of a signal is computed using the equation:

$$\mu_p = \frac{1}{N} \sum_{i=1}^N p(t_i) \quad (4-1)$$

where $p(t_i)$ is the signal value at time t_i , and N is the number of data points in the sample set. In the current study, mean fluctuating pitot pressure values upstream of the interaction compared very well with pitot pressures obtained using a conventional pitot probe. This was not the case for the flow above the ramp

surface, and is discussed further in Section 5.2.2.1.

The standard deviation (or RMS) of a signal is computed as:

$$\sigma_p = \left[\frac{1}{N-1} \sum_{i=1}^N [p(t_i) - \mu_p]^2 \right]^{1/2} \quad (4-2)$$

Standard deviation is a measure of the width of the amplitude probability density distribution (PDD) about the mean value. Because all contributions to σ_p are positive, it provides no information about any asymmetry of the signal PDD. The signal skewness coefficient, on the other hand, depends only on such asymmetry. It is calculated using the equation:

$$\alpha_3 = \frac{1}{[N-1]\sigma_p^3} \sum_{i=1}^N [p(t_i) - \mu_p]^3 \quad (4-3)$$

The skewness coefficient may take on positive or negative values. A signal with a purely symmetric PDD (such as a Gaussian distribution) would have a skewness coefficient of zero. It is strongly influenced by values far from the mean.

The flatness coefficient (or kurtosis) is computed using the following:

$$\alpha_4 = \frac{1}{[N-1]\sigma_p^4} \sum_{i=1}^N [p(t_i) - \mu_p]^4 \quad (4-4)$$

It is a measure of how frequently a signal takes on values far from the mean. A signal with a Gaussian PDD has a flatness coefficient of 3.0.

Note that both the skewness and flatness coefficients are normalized quantities. This normalization was understood in Section 3.11 when comparing boundary layer characteristics determined by fluctuating pitot probes and hot wires.

Amplitude probability density distributions were computed for each signal. For some data, multiple peaks/modes in the PDD's were used to distinguish specific flow conditions, which is discussed further in Section 4.2.

The time dependent nature of the data was examined using standard time series analysis. With the mean of the signal removed, spectral coefficients were computed using a Fast Fourier Transform. Spectral coefficients are computed following equation (11.102) of Bendat and Piersol [1986]:

$$G_{xx}(f_k) = \frac{2}{n_d N \Delta t} \sum_{i=1}^{n_d} |X_i(f_k)|^2 \quad (4-5)$$

where:

n_d = number of contiguous equal-length records into which the signal is divided (the uncertainty in the spectral coefficients being proportional to $1/n_d$)

N = number of data points in each record

Δt = reciprocal of the sampling frequency

$f_k = \frac{k}{N \Delta t} \quad k = 0, 1, 2, \dots, \frac{N}{2}$

$X_i(f_k)$ = the complex Fourier components of the signal for record i

$$= \Delta t \sum_{n=0}^{N-1} x(t_n) e^{-\frac{j2\pi kn}{N}} \quad (j = \sqrt{-1})$$

$x_i(t_n)$ = signal value at time t_n within record i

The length of each record (N) was fixed throughout most of the study at 1024 points. Frequency resolution was thus set at $1/(1024 \Delta t)$, with the maximum resolvable frequency being the Nyquist frequency. A cosine taper was applied to the first and last 10% of the data in each record to eliminate discontinuities at the record boundaries and suppress the associated distortion of the energy spectra. The number of records in a data set (n_d) varied from 100 to 1024, depending on the number of channels sampled and available data acquisition memory. Statistical moments and spectral coefficients converged using as few as 50 records.

Power spectra show signal energy content in the frequency domain. Frequency is usually plotted as $\log(f)$ along the x-axis. $G_{xx}(f)$ may be plotted dimensionally (with units of psi^2/Hz for the pressure data) as $\log(G_{xx}(f))$ along the y-axis to examine the signal frequency content in an absolute sense. Alternatively, the spectral coefficients may be plotted as $G_{xx}(f) \cdot f/\sigma_p^2$, where the area under the curve between two frequencies (when the frequency axis is plotted

on a logarithmic scale) provides a measure of that band's fractional contribution to the overall signal variance (the total area under the curve being 1).

For some two-channel data, cross-correlations and coherence function spectra were computed. The cross-correlation coefficient for two signals $x(t_i)$ and $y(t_i)$ is a function of the time-delay, τ . Again following Bendat and Piersol [1986], equation (11.137), it is computed from the equation:

$$R_{xy}(\tau) = \frac{1}{\sigma_x \sigma_y [N-\tau]} \sum_{n=1}^{N-\tau} x(t_n) y(t_n + \tau) \quad (\tau=0,1,\dots,m < N) \quad (4-6)$$

where $\tau = r \Delta t$, and x and y represent deviations from their respective signal mean. By normalizing R_{xy} by $\sigma_x \sigma_y$, the range of the resulting measure is constrained between -1 and +1. Normalized cross-correlation values near 1 or -1 indicate that the two signals are very similar. Peaks in the cross-correlation at positive time-delay values indicate by how much time events in the primary signal (x in equation 4-6) lead associated events on the follower signal (y in equation 4-6). Likewise, negative time-delay values reflect a general lag in events occurring in the primary signal. These time-delay values, along with a known streamwise distance separating the corresponding transducers, can be used to calculate broad-band convective velocities of flow structures or features.

Coherence is a measure of the correlation of two signals in the frequency domain. It may be computed by the equation:

$$\gamma_{xy}^2(f_k) = \frac{1}{G_{xx}(f_k) G_{yy}(f_k)} \left| \frac{2}{N \Delta t} X^*(f_k) Y(f_k) \right|^2 \quad (k=0,1,\dots,N/2) \quad (4-7)$$

where:

G_{xx}, G_{yy} = spectral coefficients of x and y

X, Y = Fourier components of x and y

X^* = complex conjugate of X

Coherence takes on values between 0 and 1; the higher the value, the stronger the correlation between the two signals (at the specified frequency). Further description of these quantities can be found in Bendat and Piersol [1986].

4.2 Event Detection Methods

4.2.1 Probability Distribution Technique

Wall pressure signals within the region of separation shock motion were used to determine local shock position and motion using the two-threshold method (TTM) described by Dolling and Brusniak [1989]. The process is described here for completeness, and an example is provided in Figure 4-1. The sketch at the top of Fig.4-1 provides a reference relative to the corner and separation line seen in the surface flow visualization. This technique takes advantage of the Gaussian PDD normally associated with the wall pressure signal

of an undisturbed turbulent boundary layer. To begin, the PDD (Fig. 4-1c) of a wall pressure signal (Fig. 4-1b) is examined for non-zero skewness or multimodal character, thereby distinguishing it from signals which are present upstream of the interaction. If such is found and the value of the (lower) peak falls within a specified tolerance of the expected undisturbed wall pressure, the peak is flagged as the mean "upstream" boundary layer pressure (\bar{P}_{wo}). Pressures in the data set less than this value are used to calculate the "upstream" boundary layer pressure standard deviation (σ_{Pwo}). A threshold can then be established following the general form $P_{TH} = \bar{P}_{wo} + n \sigma_{Pwo}$, where n is chosen to be sufficiently large to avoid confusing most turbulence fluctuations with separation shock motion. A second threshold of similar form is used in the TTM to provide a detection dead-band and hence decrease sensitivity to signal noise or turbulence fluctuations superimposed on the separation shock trace. Next, each sample in the wall pressure signal is compared against the two thresholds: $P_{TH1} = \bar{P}_{wo} + n_1 \sigma_{Pwo}$, $P_{TH2} = \bar{P}_{wo} + n_2 \sigma_{Pwo}$. Values of n_1 and n_2 were chosen in accordance with the results of Dolling and Brusniak as 3 and 6, respectively. When the surface pressure increases and crosses both P_{TH1} , and P_{TH2} , the separation shock is detected moving upstream of the measurement station. Similarly, when the surface pressure drops below P_{TH2} and P_{TH1} , the separation shock is detected moving downstream of the measurement station. For consistency, the shock is

designated as being at the transducer immediately after it crosses P_{TH2} when moving upstream or immediately before crossing P_{TH2} when moving downstream. Using this approach, the raw pressure signal can be converted into an "event-driven" boxcar signal (Fig. 4-1d), which is given a value of 0 when the separation shock is downstream of the transducer and has a value of 1 when it is upstream.

Because of their highly skewed/multi-modal probability density distributions, a similar event detection scheme was applied to fluctuating pitot pressure measurements made downstream of the compression corner.

4.2.2 VITA Technique

Another approach to event detection was applied to the fluctuating pitot pressure signals measured in the incoming boundary layer and the flowfield downstream of the boundary layer manipulators. In this case, an "event" is defined as when the pitot pressure RMS value exceeds some (large) multiple of the freestream RMS level. These events were detected using the Variable Interval Time Averaging (VITA) technique [Blackwelder and Kaplan, 1976]. The analysis begins with the calculation of the signal short term variance:

$$\sigma_{\pi}^2 = \frac{1}{T_{\pi}} \int_{-0.5T_{\pi}}^{+0.5T_{\pi}} P^2(\tau) d\tau - \left[\frac{1}{T_{\pi}} \int_{-0.5T_{\pi}}^{+0.5T_{\pi}} P(\tau) d\tau \right]^2 \quad (4-8)$$

where T_{π} is the averaging window set by the user and $P(\tau)$ is the signal being

analyzed. An event occurs when the short term variance exceeds a user specified threshold (T_{TH}). Integration was performed numerically using Simpson's rule.

Some insight into the choice and effect of T_{st} can be gained through application of the VITA technique to a simple sine wave:

$$P(t) = \sin 2\pi ft$$

After performing the integration, the short term variance is found to be:

$$\sigma_{st}^2(t) = \frac{1}{2} - \frac{1}{4\pi f T_{st}} \cos(4\pi ft) \sin(2\pi f T_{st}) - \left[\frac{1}{T_{st} \pi f} \sin(2\pi ft) \sin(\pi f T_{st}) \right]^2$$

(4-9)

Increasing T_{st} from values much less than $1/f$ to values approaching infinity raises the short term variance value from 0 at all time to 0.5 at all time. A VITA transformation with little or no amplitude variation makes detection of the variation in the raw signal very difficult. Optimizing T_{st} , therefore, must focus on maximizing the range of the signal's short term variance. Such a condition can be interpreted in this example as maximizing the slope of the VITA signal. By appropriate differentiation, the "optimum" T_{st} is determined from the roots of the equation:

$$3B \sin(2\pi B) = \frac{2}{\pi} + \left[2\pi B^2 - \frac{2}{\pi} \right] \cos(2\pi B) \quad (4-10)$$

where $B = fT_{st}$. The only root which gives an averaging window smaller than the period of the signal is $B = 0.558$. Choosing T_{st} smaller than the optimum value produces a marked reduction of the VITA signal for all time. Choosing T_{st} larger than optimum increases the average short term variance value but decreases the VITA signal RMS. In both cases, the range of the VITA signal is reduced and the ability to detect the sine wave becomes more difficult. From these results, the VITA technique may be thought of as a band-pass filter "centered" about a frequency $1/T_{st}$. From this analytic result, it was decided to choose T_{st} for the more general fluctuating pitot pressure signals of the current study based on maximizing the overall RMS of the VITA signal. The specific value varied slightly from signal to signal, and a single representative T_{st} was applied in all analyses.

The next step in event detection using the VITA technique is the establishment of a threshold. Events begin or end when the VITA signal exceeds or falls below this threshold, respectively. The result is a boxcar representation of the signal similar to that obtained from the TTM above. In the current study, T_{TH} was set as a multiple of the average freestream VITA value (0.013 psia^2). Choice of the multiplier was made by examining the sensitivity of boundary layer edge intermittency (Ω_{edge}) (described below) to the threshold multiplier, followed by

visual examination of the resulting events. Morrison *et al.* [1989] determined that the reliability of event detection using the VITA technique was improved if an additional constraint (a "level") was applied to the raw signal. For this study, the end of an event also required that the pitot pressure value be within a given percentage of the freestream pitot pressure. As Selig and Smits [1991] found with their hot wire data, Ω_{edge} was not very sensitive to the "level" threshold. A value of 75% of the freestream pitot pressure was used throughout the current analyses.

4.3 Conditional Data Analyses

Once the raw signals were transformed to the simpler boxcar representations, single channel event statistics were calculated. Event intermittency was determined by dividing the total "event-present" time (boxcar signal = 1) by the total sampling time. Thus, intermittency values could range from 0 to 1 (or 0% to 100%). A measure of event frequency was obtained by taking the reciprocal of the average time interval between successive event starts. This is calculated from the equation:

$$f = \left[\frac{1}{N-1} \sum_{i=1}^{N-1} T_i \right]^{-1} \quad (4-11)$$

where N is the total number of events and T_i is the time interval between rise _{i} and

rise_{*i+1*} in the boxcar signal (as seen in Fig. 4-1d for a wall pressure signal). In reference to the upstream fluctuating pitot pressure, the intermittency represents the boundary layer edge intermittency (Ω_{edge}) and the event frequency the interface crossing frequency (f_i). For the surface pressure measurements, the labels are separation shock intermittency (γ) and zero-crossing frequency (f_c). While Dolling and Brusniak [1989] do show that the maxima in the f_c distribution fall close to the center frequency of the surface pressure power spectrum, the label is not meant to imply that the shock motion exhibits a dominant period of $1/f_c$. Examination of the distribution of event periods by Nordyke [1987], in fact, show the separation shock periods to be highly skewed toward periods significantly shorter than $1/f_c$.

Boxcar signals from simultaneous surface pressure signals were used to define the streamwise position history of the separation shock. Based on the way in which the boxcar signals are nested, a shock passage at given location could be labeled as being part of a shock turn-around or a shock sweep. This is illustrated in Fig. 4-2. Shock passages which begin or end a sweep are also involved in a shock turn-around, unless they are at the end of the measurement field. In the latter case, there exists no way of determining the separation shock motion until it returns to the end- channel.

Conditional ensemble-averaged surface pressure time histories based on

shock position were calculated using the variable-window ensemble-averaging technique of Erengil and Dolling [1991a]. In this procedure (illustrated for two channels in Figure 4-3), a boxcar signal from the triggering channel is searched for a specified condition, such as the passage of the separation shock in the upstream direction (a rise in the boxcar signal). When such an occurrence is found, the data for all channels (trigger and follower channels) are extracted over a given time window about the triggering event (the window is labeled "W" Figs. 4-3a and d). The label "follower channel" is used here to indicate that the ensembles extracted from this channel are based on events of another channel. The time of the triggering event is assigned the value $\tau=0$. Discrete sampling times preceding the triggering event take on values of $\tau<0$, and those following it take on values of $\tau>0$. The ends of the window are set at the mid-points between the triggering event and the previous/following boxcar change-of-state. In the example of Fig. 4-3, ensemble windows begin half-way between the preceding boxcar fall and triggering rise, and end half-way to the following boxcar fall. Varying the window in this manner isolates phenomena associated with the triggering event from those associated with other events. The ensembles from each channel are summed, by τ -register, with ensembles of previously determined like events (Figs. 4-3b and e). The ensembles in these figures are offset for clarity. Final sums are normalized by the number of ensembles in each register,

producing an ensemble-averaged time history for each channel (Figs 4-3c and f). The result is a set of synchronized average wall pressure time histories at various locations which share only the event on the triggering channel.

In a more rudimentary manner, separation shock position was used in conjunction with simultaneous fluctuating pitot pressure measurements to provide "frozen" pitot pressure profiles above the surface of the compression corner. Pitot pressure values were extracted for those periods of time when the separation shock fell between two specified surface transducers, then averaged. By repeating this process at several probe locations and using different surface transducer pairs, "frozen" pitot pressure profiles could be constructed corresponding to a given separation shock position. The results of this analysis are presented in Sections 5.2.2.1 and 6.2.3.

Finally, the relative timing between event edges (rises and falls in the boxcar signal) of two simultaneously acquired data sets was examined. This event relative timing analysis (ERTA) was developed as part of the current study and is based on histograms describing the likelihood of changes-of-state in two different boxcar signals being separated by given time intervals.

Following independent conversion of raw data signals to boxcar signals, the analysis was carried out in a six step process:

- 1) Select two boxcar signals to be compared and assign one to serve as the

trigger signal. Timing of event edges of the follower signal are measured relative to event edges of the trigger channel.

2) Choose an event edge pair of interest. This may be a trigger-signal-rise/follower-signal-rise, or a trigger-signal-rise/follower-signal-fall, etc. The choice of the event edge pair may be suggested by the expected behavior of the flow, though all four possible combinations may be examined if there is no previous information on which to base a choice.

3) Choose an observation window centered on the trigger signal event edge. All follower signal event edges which fall within the observation window contribute to the histogram. Typically, this window is initially set large to establish an "uncorrelated" level, which shows up as a flattening of the histogram. The observation window size is then reduced to focus on the peak in the histogram.

4) Create a single time histogram. Since data are obtained at discrete time intervals, spacing between event pairs can occur only at integer multiples of the sampling period. In this histogram, each integer multiplier represents a class. Define the event edge separation time as $\tau = t_{\text{trigger event edge}} - t_{\text{follower event edge}}$.

5) Create a rolling average histogram. A rolling average of the event frequencies (of occurrence) in 4) are used to resolve the dominant frequency (of the event

pair time separation) and the window (τ_{spread}) about which this frequency is distributed. While increasing the averaging window (within reason) enhanced the peak, it also spread the peak. The averaging window was therefore chosen as the minimum which defined the peak in the histogram. Cutoff for the τ_{spread} was chosen to be the classes at which the frequency distribution leveled out. If no peak was found in the histogram, the event edge pair was determined to be uncorrelated and no further analysis was performed.

6) Obtain the relative significance of the dominant event. Return to 4) and sum all events within τ_{spread} , then normalize by the minimum of either the number of events on the trigger channel or the number of events on the *follower channel*. To be a relevant pairing, the normalized sum must exceed a predetermined value. The value chosen for the current study was 30%.

Figure 4-4 illustrates how an ERTA histogram is created for a rise-rise event edge pair. An example of this analysis is depicted in Figure 4-5 for two boxcar signals from surface pressure transducers beneath the translating separation shock. The trigger signal comes from the upstream transducer. Positive values of τ represent secondary signal event edges preceding those of the trigger signal, and vice versa for negative values of τ . The first pair of figures (Figs 4-5a and b) consider the rise/rise event edge pair, corresponding to an upstream motion of the separation shock. The second pair of figures (Figs 4-5c

and d) consider the fall/fall event edge pair, corresponding to a downstream separation shock motion. Figures 4-5a and c use a very wide timing window to highlight the peaks and uncorrelated level, while Figures 4-5b and d focus on the peaks. As can be seen, the peak in the upstream sweep histogram occurs at a positive time, indicating that rises in the downstream boxcar signal generally precede rises in the upstream boxcar signal. The peak ($0.00 \text{ ms} < \tau < 0.20 \text{ ms}$) represents 37% of the upstream channel rises. This number is very close to that obtained by summing all upstream shock sweeps which include these two channels and dividing by the total number of events on the trigger channel (44%). A convection shock speed of $.06U_{\infty}$ is obtained by dividing the distance between the surface transducers by the time of the peak (0.065 ms), which is consistent with previous findings using different techniques (Dolling *et al.* [1991]). Similar information is found in the downstream sweep histogram, where the primary signal falls generally precede those of the downstream signal. In addition to finding the peak value, this method provides a measure of the distribution of the events about the peak.

It should be emphasized that this example is for event pairs with a previously known relationship. This provides a means of establishing the validity of the technique. Further, this technique depends on a probability distribution of event edge timing and, hence, requires both appropriately defined events and a

sufficiently large sample set to produce a reasonable histogram. Choice of the number of trigger channel events to normalize the class probability is somewhat arbitrary, though probably the most meaningful of the available normalizing values. The class probability must be considered in a relative sense, anyway. The values of separation time are not subjective, and are the important result of the analysis. The overall technique differs from a pure cross-correlation of the boxcar signal (such as done by Shau [1990]) in that it independently examines correlations between event edges (beginnings and endings).

Chapter 5

Baseline Compression Corner Interaction

This chapter examines the baseline compression corner interaction in light of the findings of the current study. Comparisons show that results of this study agree well with those of earlier studies. New insights into the driving mechanism are provided through a modified ensemble-averaging technique. Fluctuating pitot pressure results above the ramp face are presented, and are shown to correlate with the motion of the separation shock. Results of this section are referenced later in comparisons with the results of the perturbation studies reported in Chapters 6 and 7.

5.1 Flow Features Upstream of the Corner

5.1.1 Surface Flow Visualization

A kerosene-lampblack image of the baseline surface features is presented in Figure 5-1. This technique has virtually no frequency response. In an unsteady flow, the resulting features captured in the image are felt to reflect a time-average of the surface shear stress direction. As discussed later in regards to mean pitot pressure measurements, the true time-averaged value may differ from that obtained by a measurement technique with limited frequency response. The

corner line is perpendicular to the freestream and is labeled 'C' in the figure. It is the streamwise origin for all subsequent discussions. The separation line, 'S', is visible immediately upstream of the corner as a region of surface tracer coalescence. The slight curvature in the separation line is consistent with previous studies of highly separated compression corner interactions (Selig [1988]), but is not felt to substantially affect study of the separation shock motion. This is particularly true near the centerline of the model where the curvature is negligible. The separation line is 0.78 inch (1.98 cm., $X/\delta_1 = 1.11$) upstream of the corner at the model centerline, which is closer to the corner than that found by Gramann [1989] in the same facility (0.86 inch). This discrepancy may be associated with slight differences in ramp angle and also to the difficulty of clearly defining the separation line in the surface tracer pattern. The difference falls within the uncertainty of the measurement (0.13 inch, 3.42 mm) for the current study. No reattachment is observed on the ramp surface which is possibly obscured by the joint line on the ramp face.

5.1.2 Fluctuating Surface Pressures

A great deal of the current understanding of the unsteadiness of the separated compression corner interaction in general, and the separation shock in particular, has come from fluctuating surface pressure data. As such, a general examination of the fluctuating surface pressures upstream of the corner is

presented here both to highlight certain features and to show consistency between the current study and previous investigations.

5.1.2.1 Streamwise Development of Interaction

An example of simultaneous surface pressure signals obtained upstream of the compression corner are presented in Fig 5-2. The transducers are aligned in a streamwise row (as indicated in the figure) along the model centerline. Coordinates are referenced to the ramp corner ($X = 0$) and the direction of the freestream (positive). Only one record of data (1024 points) is presented for clarity in each case. The signals are characterized by jumps between regions of low mean, small amplitude fluctuations (state 1), and regions of high mean, large amplitude fluctuations (state 2). State 1 is found as far downstream as 'S', and is quantitatively similar to the wall pressure signal beneath the incoming boundary layer. State 2 is found as far upstream as the upstream influence point (UI) (defined below). Its character varies slightly as the corner is approached. Comparison of the signals in Fig. 5-2 shows that the changes in state at a given location are uniquely related to the states existing at positions both upstream and downstream of that location. Transition from State 1 to State 2 occurs when all downstream locations are already at State 2. Likewise, a transition from State 2 to State 1 occurs only when all upstream locations are already at State 1.

This two-state behavior can also be observed in the signal amplitude

probability density distributions (Fig 5-3). The bimodal nature of the PDD's is particularly evident in curves e, f, and g. For clarity of presentation, the low mode of each distribution has been set to $P = 0.66$ psia, which requires a maximum shift of 0.13 psia to any signal. The similarity of the local distribution about this mode indicates that State 1 is effectively the same for all stations.

The increasing presence of State 2 is reflected in the streamwise distribution of the statistical moments, as shown in Fig 5-4. The mean wall pressure and RMS distribution of the current study (Fig 5-4 a and b, respectively) compare well with the previous results of Erengil and Dolling [1991a]. Mean pressure values have been normalized by the wall pressure value just upstream of the interaction. Surface pressure RMS values have been normalized by the local mean wall pressure. The current data are shifted downstream of the previous results by almost exactly one transducer spacing which is similar to the shift observed by Gramann and Dolling [1990]. The reason for this streamwise shift is not known. The point at which \bar{P}_w first deviates from incoming boundary layer values is commonly called the upstream influence (UI) location, and is located a distance L_{UI} from the corner. Well upstream of this point, the surface pressure skewness and flatness coefficients (Figs 5-4c and d) take on values reflecting the Gaussian-distribution values of the undisturbed incoming boundary layer.

The streamwise extent of the interaction bounded by UI and S is referred

to as the intermittent region due to the nature of the surface pressure signals, and is the region over which the separation shock ranges.

Fig 5-5 shows the variation in surface pressure power spectra with streamwise position. As pointed out in Section 4.1.2, plotting the spectral coefficients as $G(f) \cdot f / \sigma^2$ facilitates determining the extent to which a given frequency range contributes to the overall signal variance. Progression from UI to S is marked by a decrease in the frequency band in which energy is concentrated -- from > 5 kHz upstream of the interaction (not shown) to between 100 and 2000 Hz within the intermittent region -- followed by a return to higher frequencies. The spectra remain broad-band throughout, however, indicating no resonant behavior on the part of the flow.

Separation shock location and motion were determined from simultaneous surface pressure signals using the two threshold method described in Section 4.2.1. The resulting shock intermittency and zero-crossing frequency distributions are presented in Fig 5-6. The location of 'S' correlates with the downstream limit of the separation shock motion. Also, as with the statistical moments, good comparison is found with the results of Erengil and Dolling [1991a]. The intermittency distribution can be fit to a Gaussian probability distribution (Erengil and Dolling [1991a]), indicating that the separation shock position is random about the mean location ($X_{\gamma=0.5}$). The large variability of γ ,

particularly around the middle of the intermittent region, has been noted before by Gramann [1989] and attributed to shortcomings in the two threshold method. However, examination of the RMS distribution (Fig 5-4b), which is independent of the TTM, shows similar scatter. Further, a plot of RMS versus γ (Fig 5-7) shows the repeatability of the correlation between these two variables. This suggests that the character of the separation shock is basically unchanged, despite the small streamwise shift.

Because part of the current study examines the effect of perturbations on the separation shock dynamics -- including the extent of the shock travel-- a less subjective method of quantifying the extent of the separation shock motion than visual examination was required. This was accomplished by fitting the available intermittency data to a Gaussian probability distribution and taking the distance between $X_{\gamma=.03}$ and $X_{\gamma=.97}$. Defined in this way, the baseline interaction extends from $X/\delta_1 = -2.18$ to $X/\delta_1 = -1.21$.

The zero-crossing frequency distribution peaks around $X_{\gamma=.50}$ at a value close to 1 kHz. This quantity is highly sensitive to threshold values in the TTM. Further, it is the reciprocal of the mean of a highly skewed shock period distribution and, hence, should not be confused with an average or dominant frequency of the separation shock. It is used here for comparison with previous work (as in Fig 5- 4d) and the current perturbation studies.

5.1.2.2 Modified Ensemble-Averaging Analysis

Analysis by Erengil and Dolling [1991b] found that changes in direction of the separation shock motion are associated with surface pressure "signatures" which enter the interaction from upstream and are coincident with the shock foot at the time of the turnaround. This result was re-examined as part of the current study to explore the possibility that the signatures were tied to local shock motion (motion at a point) and not necessarily a larger global shock motion.

Fluctuating surface pressures were simultaneously acquired at several streamwise locations (up to 8) at minimum transducer spacing. The shock position relative to each channel location and at each sampled time was determined independently using the TTM. The resulting boxcar signals were then combined to determine the global streamwise shock motion. Every rise in each boxcar signal was determined to be part of a larger upstream shock sweep (traversing 1 to 8 transducers), and labeled with the beginning and end channels for that sweep. Likewise, each fall was assigned to a downstream sweep and appropriately labeled. Global motions were considered exclusive such that an event was assigned only to the largest sweep to which it could belong. Thus, if a rise on channel 3 was part of an upstream sweep from channel 6 to channel 1, it was not also considered separately as part of an upstream sweep from channel 5 to channel 2. During this step, each boxcar event was checked to insure that it

nested appropriately within the boxcar signals of the downstream channels. If it did not, it was labeled as a false shock and flagged to be ignored in further analysis. These false shocks may be due to electronic noise or turbulence fluctuations not caught by the TTM and typically made up less than 0.2% of any data set. The number of upstream and downstream shock sweeps between any two channels were tabulated for later use.

Following determination of shock sweeps, ensemble-averaged surface pressures were generated following the variable-window technique outlined in Section 4.3.1. Here, however, the selection criterion for ensemble extraction was sweep length *alone*, not sweep length *and location* as in the work of Erengil and Dolling. Thus a 3-channel upstream sweep from channel 6 to channel 4 provided ensembles which would be averaged with ensembles extracted for upstream sweeps from channel 3 to channel 1. To account for differences in transducer locations, the signals were phase aligned. The ensembles were mapped to a set of pseudo-channels such that the beginning of the triggering event (i.e. upstream or downstream shock sweep) was mapped to the same pseudo-channel. The remaining channels took on the same position relative to the starting channel as in the true channel arrangement. Additionally, local \bar{P}_{w0} was removed from each ensemble to provide a common reference. An example of this process is illustrated in Fig 5-8.

A shock passage on any channel in the sequence could be used to set the center of the ensemble window. If the channel began or ended the sweep, then the triggering event was also a shock turnaround; if it were an interior channel, the triggering event was a pure sweep. Checks were made to insure that sweeps between any given channel pair did not contribute more than 50% of the total number of ensembles and hence dominate the average. Frequently, this number did not exceed about 30% of the overall ensemble set.

Results of this analysis are presented in Figs 5-9a and b for a 3-channel upstream shock sweep and Figs 5-10a and b for a 3-channel downstream shock sweep. The ensembling window was centered on the second channel in each case, making the triggering event a pure sweep. Comparison of the pseudo-channel ensemble averaged signals in Figs 5-9a and 5-10a reveals a wall pressure signature (labeled 'sig' in the figures) which appears at successively later times with increasing downstream distance. This signature is coincident with the foot of the shock at $\tau = 0$. The peak-to-peak amplitude of the pressure pulse is approximately 0.01 psi (68.9 Pa; $.015 P_{w0}$), and has a duration of between $75\mu s$ and $100\mu s$ ($3.2 - 4.3 \delta_1/U_\infty$) for both types of sweep. The two signatures differ in that the upstream sweep signature is fall-rise-fall while the downstream sweep signature is rise-fall-rise. Tracking the leading peak of these signatures in space and time gives a convection velocity of about $0.75U_\infty$. Changing the triggering

sweep length or the channel on which the ensembling window was centered did not affect the period, amplitude, or speed of the signature.

The results are very similar to those of Erengil and Dolling [1991b] for shock turn-arounds. Failure to find similar signatures for shock sweeps in the previous work is attributed here to an insufficient number of ensembles. Experience from the current study indicates that a minimum of 180 to 200 ensembles are required to bring out the characteristic pulse from the surrounding signal. Erengil and Dolling used only 149 and 161 ensembles in their upstream sweep and downstream sweep analysis, respectively.

The signature characteristics are enhanced further by combining ensemble-averaged signals from several different runs. While individual ensemble-averages from each run were weighted by the number of ensembles used to generate the signal, care was taken to insure that no individual run contributed inordinately to the overall "super-ensemble". Ensemble-averaged signals of this type for the 3-channel sweep cases are presented in Figs 5-11 and 5-12. These figures also show the pressure signature continuing to move downstream even after passing under the shock. The stronger signal associated with the downstream motion is consistent with the finding of Marshall [1989] that "the shock has a more planer character while moving downstream than while moving upstream."

It is concluded from these findings that local shock motion (as defined by the passage of the separation shock over a single transducer) is associated with a distinct wall pressure signature which convects into the interaction from upstream. This signature is coincident with the shock foot at the time of the motion. The character of the pressure signature (fall-rise-fall or rise-fall-rise) is tied to the direction of local shock motion (upstream or downstream, respectively). These signatures are independent of the global shock motion (the streamwise motion of the shock as defined by data from several wall pressure transducers). This finding is contrary to findings of the previous work of Erengil and Dolling [1991b].

5.1.3 Correlations with Upstream Pitot Pressure Fluctuations

A model tying temporal variations in the incoming boundary layer to the motion of the separation shock was suggested by Andreopoulos and Muck [1987], though no data were obtained to support their conclusions directly. As part of the current investigation, fluctuating pitot pressure measurements were made in the incoming boundary layer to characterize its dynamic behavior, both by itself and in conjunction with the separation shock motion.

To evaluate the above model, initial emphasis was placed on quantifying the time-varying position of the interface between the freestream and boundary layer as a function of height above the surface. Single records of pitot pressure

signals at three different heights near the boundary layer edge are shown in Fig 5-13, along with their VITA transformations. Periods of time when the pitot probe is in the low RMS flow of the freestream are clearly distinguishable from the high RMS signals associated with the turbulence of the boundary layer. The periods of high pitot pressure fluctuation are accentuated by the VITA transformation. Thus, the VITA-based algorithm outlined in Section 4.2.2 was used to determine boundary layer edge intermittency and interface surface crossing frequency. Selection of an appropriate averaging window (T_{st}), was based on maximizing the VITA signal RMS. The effect of varying T_{st} on the VITA signal RMS is shown in Fig 5-14 for various probe heights and sampling frequencies. Note that maximum VITA signal RMS values consistently occur for T_{st} between 30 and 50 μs , independent of probe height or sampling frequency. For uniformity, a window of 40 μs was chosen for all subsequent analysis. Following the optimization example of Section 4.2.2 for a sine wave, this value would suggest a disturbance period of about 72 μs , which is very close to the wall pressure signature period found in Section 5.1.2.2.

The VITA threshold was chosen as described in Section 4.1.2. The sensitivity of Ω_{edge} to N_{TH} is plotted in Fig 5-15, where N_{TH} is an integer multiplier of the mean of the freestream VITA transformed signal. From this analysis, a multiplier of 40 was chosen to establish the VITA threshold.

The boundary layer edge intermittency distribution is plotted in Fig 5-16 for locations separated by as much as 10 inches (25.4 cm; $14\delta_1$) in the streamwise direction. The results are consistent for this study, and follow the characteristic Gaussian error function (Hinze [1975]). The data are compared with those of Selig *et al.* [1989] at $M = 2.95$ and the incompressible curve fit of Klebanoff [1954] (also cited in Hinze). The close parallel between the curves of Klebanoff and the current study are felt to reflect appropriate choices of T_{st} and T_{TH} . The associated interface crossing frequency distribution is presented in Fig 5-17. Note that the maximum value of f_i is around 5 kHz, which is significantly higher than the maximum zero-crossing frequency of the separation shock. Event-period histograms for both boundary layer edge and separation shock motion ($\Omega_{edge} \approx f_c \approx 0.50$) exhibited similar skewed (log-normal) shapes. The most probable boundary layer edge period was about 110 μs , while that for the separation shock was about 200 μs . These values translate to most-probable event frequencies of 10 kHz and 6.67 kHz, respectively.

Further attempts to examine linkages between fluctuations in the incoming boundary layer and the separation shock motion were carried out through simultaneous data acquisition of fluctuating pitot pressure 9.28 inches (23.57 cm; $13.3\delta_1$) upstream of the corner and fluctuating wall pressures within the intermittent region. Probe tip positions of $0.33\delta_1)_{local} - 1.31\delta_1)_{local}$ above the wall

were investigated. The streamlined floor-mounted probe was used in this series of experiments to minimize interference with the compression corner interaction. Nonetheless, the interaction did shift upstream distances ranging from 0.1 to 0.5 inch (0.25 to 1.27 cm) from its undisturbed position. Preliminary analysis reported by Gramann and Dolling [1992] determined this shift to be associated with the separation bubble growth and that the shock dynamics were not significantly effected. Subsequent spanwise surface pressure measurements by MacKay [1992] have shown that the interference decreases with spanwise distance from the probe. The work of Gramann and Dolling was expanded on in the current study to include additional pitot pressure measurement locations and further analyses.

The ensemble-averaging technique applied in Section 5.1.2.2 was also used here, but due to the increased streamwise distance between the surface transducers and the pitot probe, a time shift was applied to the pitot pressure ensemble window. The magnitude of this shift was calculated as the distance between the pitot probe tip and the triggering transducer divided by the convective velocity of the surface pressure signature ($.75U_\infty$). Varying this shift from 0.2 to 0.4 ms did not significantly alter the results (Gramann and Dolling [1992]). Local shock motion was used to trigger ensemble extraction. Ensemble-averaged signals are presented in Figs 5-18a-f for an upstream shock sweep and

in Figs 5-18g-l for a downstream shock sweep. These results show no distinct signature as in the upstream surface pressure signals, though for $Y < 0.9\delta_1)_{\text{local}}$ there is a gradual decrease in pitot pressure for an upstream shock motion and a gradual increase in pitot pressure for a downstream shock motion.

Cross-correlations between the pitot pressure signal and a surface pressure signal from beneath the translating shock ($\gamma \approx 0.50$) are presented in Fig 5-19. These show a weak but increasing correlation as the pitot probe tip is placed deeper in the incoming boundary layer. Dividing the streamwise distance separating the measurement stations by the time-delay of peak correlation gives a convective velocity of $0.6U_\infty$ for the lowest probe positions. (The time-delay of the lesser "spike" between the primary peak and $\tau = 0$ in the central four curves (labeled 'sp' in Fig 5-19) gives a convective velocity of $0.99U_\infty$.) Cross-correlations between the pitot pressure signal and the separation shock boxcar signal at these positions showed the raw cross-correlations to be dominated by the effect of the separation shock motion on the wall pressure signal. Examination of the normalized pitot pressure power spectra (Fig. 5-20) reveals an increasing fraction of the overall signal variance to be contained at lower frequencies as the wall is approached. The center of this low frequency band is around 200 Hz, as with the surface pressure spectra beneath the translating separation shock (Fig. 5-5), though a significant amount of the fluctuating pitot pressure variance is still

contained at the higher (> 2 kHz) frequencies.

Additional analyses were carried out during this part of the study seeking a possible correlation between the motion of the separation shock and that of the incoming boundary layer edge. The first used ensemble-averaged VITA transformations of the pitot pressure signal, again triggering on local shock motion. Results from this analysis focussed on correlated occurrences of increased turbulent activity in the incoming flow. The second applied the ERTA technique of Section 4.3, where the event pairs were associated with boundary layer edge and separation shock motions. Neither approach showed any correlation between shock motion and boundary layer edge motion. These findings, coupled with the high value of $(f_i)_{\max}$ (relative to $(f_c)_{\max}$) and the cross-correlation and power spectra results above, give no indication that the separation shock moves in response to the unsteadiness of the freestream/boundary layer interface. It is possible that the pitot pressure measurements were made too far upstream of the interaction, for even the surface pressure signatures were very weak at this station. This point is discussed further in Chapter 8.

5.2 Flowfield Downstream of the Corner

5.2.1 Mean Pitot Pressure Profiles

Mean pitot pressure surveys were made at 8 locations along the ramp face

to examine the time-average flowfield structure downstream of the corner. Surveys were made perpendicular to the ramp face. All surveys extended from the ramp surface, through the interaction, into the incoming freestream. The profiles are presented in Fig 5-21. Curves were generated by averaging pressures and heights over 20 consecutive data points within a vertical window < 0.007 inch (0.18 mm) high. Vertical lines mark the streamwise station at which the profiles were measured. Arrows connect these lines and the associated survey. The profiles are consistent with the model of Settles *et al.* [1976] (Fig 2-1). A region of retarded flow near the ramp surface extends from the corner to $X/\delta_1 = 0.86$, followed by a rapid filling-out of the pitot profile with downstream distance. The outer portion of the flowfield appears to be dominated by a weak shock/compression wave system near the corner, which has coalesced into a single shock by the last survey station. The position and strength of the downstream shock, as judged by the data at $X/\delta_1 = 5.0$, agrees with those obtained from inviscid theory for the current freestream Mach number and compression corner angle. Physical constraints prevented surveying any further downstream.

5.2.2 Fluctuating Pitot Pressure Results

Fluctuating pitot pressures at several locations along and above the surface of the ramp were simultaneously acquired with surface pressures in the

intermittent region. The pitot signals were first examined individually for trends. Fig 5-22 shows 1 record of data at $Y = 0.1$ inch (0.25 cm) for $X = 0.0, 0.2, 0.6, 1.0, 1.5$ and 2.5 inches (0.0, 0.51, 1.52, 2.54, 3.81 and 6.35 cm). Associated amplitude probability density distributions are presented in Fig 5-23. A common characteristic in the PDD's is that they are highly skewed. The most prevalent pitot pressure at this height increases gradually over the region (2 psia to 22 psia), not nearly as rapidly as the pitot profiles of Fig 5-21. Increase in the pitot pressure mean is seen in Fig 5-22 to be due to more frequent high pressure bursts entering the region. For $X \leq 1.0$ inch, the value at which the peak occurs is consistent with the surface pressure value found by Gramann [1989].

The effects of varying height on the character of the pitot pressure signal are shown in Figs 5-24 and 5-25. (Note that Fig 5-25 covers two pages.) These data were obtained at $X = 0.2$ inch (0.51 cm), at heights of 0.1-0.7 inch (0.25-1.78 cm). Three modes (peaks) are distinguishable in the probability density distributions of Fig 5-25. Mode 1 is that discussed in conjunction with Fig 5-23; and is present as high above the ramp surface as $Y = 0.4$ inch for this streamwise location. This mode is found as far downstream as $X = 2.5$ inches at a height of 0.3 inch. Because the value at which the peak occurs does not vary with height above the ramp for a fixed streamwise location, Mode 1 is believed to represent flow conditions beneath the separated shear layer. The streamwise extent to

which this mode was evident indicates that the downstream limit of the unsteady reattachment point is significantly greater than deduced by Gramann [1989] based solely on surface pressure data. It is possible that the conditional ensembling technique used by Gramann may not have been sensitive enough to distinguish flow separation further downstream than $X/\delta_1 = 1.0$ in this interaction.

Mode 2 is characterized by a Gaussian probability density distribution, but with a mean value which increases with both distance downstream and height above the ramp surface. It represents the shear layer as processed by upstream compressions. Mode 3 is the freestream flow, with a mean value of approximately 17 psia (117 kPa) and an RMS value of 0.18 psia (1.24 kPa). Note that the pitot pressure is slightly below that expected for the freestream conditions (21 psia, 146 kPa) due to the 28 degree downward pitch of the probe.

Multi-modal behavior of this type was also observed in the hot-wire data of Selig *et al.* [1989] for a 24 degree compression corner at Mach 3. Locations at which the dual peaks in the PDD were found coincided with locations of largest turbulence intensity. As discussed in Chapter 2, the authors attributed this feature to either streamwise or spanwise vortices. Results from the current study, however, indicate that an alternative explanation lies with the time varying location of the upstream separation point and associated shock.

5.2.2.1 Frozen Pitot Pressure Profiles

Fluctuating pitot pressures above the ramp were studied for possible coupling with the separation shock position upstream of the corner (McClure and Dolling [1991]). This was done by averaging pitot pressure values from a given data set only for those periods of time when the separation shock was located between two specified surface transducers. Conditional pitot pressure values obtained in this manner using the same constraint were plotted with data from other streamwise locations and heights to produce "frozen" profiles. No time shift was made to the ensembling window (as in Section 5.1.2.2) because no prior information was available to provide an appropriate "convective" velocity. If the resultant profiles were not tied to the separation shock position, then the frozen profiles would be the same for different separation shock positions. As can be seen in Fig 5-26, however, such is not the case. These data show that as the shock moves upstream, the pitot profile becomes more retarded, and fills out as the separation shock moves downstream. The match in pitot pressure for all cases very near the corner (the lowest point at $X = 0.0$) and in the freestream (the highest point at $X = 0.2$, $X = 0.6$, and $X = 1.0$ inch) supports the validity of the resulting profiles, as these locations would see different values of pitot pressure only when the separation shock reached the limits of its travel. This breathing behavior of the corner flowfield supports the findings of Kussoy *et al.* [1987] in a

flared cylinder interaction based on conditional laser doppler measurements, and of Gramann and Dolling [1990] from fluctuating surface pressure measurements in a compression corner interaction.

Mean pitot pressure values from Fig 5-21 are also shown in Fig 5-26. The discrepancies between the mean values obtained from the fluctuating pitot pressure probe and the conventional pitot probe prompted further investigation. Three possible explanations were examined. First, because of the way in which the profiles are plotted here, differences in position would show up as differences in pitot pressure. This would appear as a constant offset in the profile (as seen in the freestream results at $X = 0.2$, differences in probe placement for a given ramp position varied by less than $0.04\delta_1$, and so should contribute only slightly to any discrepancy. Second, the diameter of the Kulite tip was 2.5 times that of the conventional probe height. Such a difference might lead to integration of P_t over a larger distance and, hence, contribute to differences in pressure values. This would be particularly true in regions of large gradients. Comparison of mean pitot pressure profiles downstream of the boundary layer manipulator (discussed in Chapter 7), however, showed good agreement even through the gradients of the BLM wake. A third possibility is that the tubing separating the transducer and measurement orifice of the conventional pitot probe may be sensitive to the existence of multiple peaks in the PDD's. The largest discrepancies in Fig 5-26

($Y = 0.3$ inch and $Y = 0.4$ inch) correspond to the largest pressure differences between Modes 1 and 2 (Fig 5-25), with the conventional pitot results clearly favoring the higher peak. The argument is akin to that put forward by Shau and Dolling [1990] for similar differences observed in their study of a compressible shear layer. In that study, differences found in the mean pitot pressure values near the edge of the shear layer were attributed to the "skewness of fluctuating signal."

Interpreting the results of previous investigations in light of the current study suggests that the high turbulence levels found downstream of the corner are, to a great extent, variations due to a flapping turbulent shear layer. The position of the shear layer, in turn, correlates with that of the separation shock upstream of the corner. While it is not possible to fully separate the shear layer motion from the motion due to turbulent flow contained within a single-point measurement, it is clear that fluctuations immediately downstream of the corner are dominated by the former.

5.2.2.2 Pitot Pressure Events

In the same way that the separation shock position upstream of the corner could be deduced from the multi-modal surface pressure signals, relative shear layer position was determined from the multi-modal pitot pressure signals. Here, Mode 1 takes the place of P_{wo} in establishing event thresholds. The resulting

event-boxcar signal, therefore, takes on a value of zero when the shear layer is above the measurement position, and a value of one when the probe is within or above the shear layer. Maximum shear layer zero crossing values from this analysis increased from 3 to 5.5 kHz with distances downstream of the corner (Fig 5-27). The difference between $f_c)_{\max}$ of the separation shock and that of the shear layer is attributed to the turbulent flow superimposed on the flapping of the shear layer, which in turn produces higher frequency oscillations in the shear layer boundary. Note that this value is very close to that found for $\Omega_{\text{edge}})_{\max}$ of the incoming boundary layer.

The timing between the motion of the separation shock and that of the shear layer was studied using the event-relative-timing-analysis (ERTA) described in Section 4.2.2. From the frozen pitot profiles and the breathing model of the corner interaction, the event pairs of interest were the upstream rise-downstream fall and the upstream fall- downstream rise. Upstream boxcar events are associated with the passage of the separation shock over the wall pressure transducer while downstream boxcar events are associated with motion of the bottom of the shear layer across the pitot probe.

The results of this process are illustrated for both event pairings in Fig 5-28. The upstream surface pressure transducer is the same for all cases ($X = -1.165$ inches), as is the height of the pitot probe above the surface ($Y = 0.2$ inch).

Streamwise position of the pitot probe is varied as in Fig 5-22. The rolling average window spanned three points, which equates to $30\ \mu\text{s}$ for the sampling frequency of 100 kHz. Results are based on 128 records of data. Two features are noted. First, the peaks in both event pairings occur at negative time separation, which indicates that the downstream event (shear layer motion) predominantly lags the upstream event (separation shock motion), independent of the direction of shock motion. Thus, while the separation bubble breathes, the position of the upstream limit of the bubble is not uniquely correlated with the position of the bubble's downstream limit. Decreasing clarity of the event relationship with distance downstream of the corner is due to the fact that the motion of the shear layer is part of the breathing bubble. As the shock moves downstream, the reattachment location on the ramp face moves upstream toward the corner and the shear layer moves closer to the ramp face. Examination of ERTA results for the surface transducer located at $X = -1.165$ inches and the pitot probe at $X = 1.0$ or 1.5 inches, but with $Y = 0.1$ inch clearly shows a stronger event-pair relationship than that found in Fig 5-22 for $Y = 0.2$ inch for the same streamwise positions.

The second feature of note is that the time delay at a fixed streamwise location is the same for both event pairs. If the streamwise distance between the measurement stations is divided by this time delay, the resulting velocity is of the

order of the velocity of the incoming freestream. To reduce the uncertainty in this value of velocity, additional data were obtained at 500 kHz. These results are presented in Fig 5-29 for the same transducer positioning as Fig 5-28, but only for the pitot probe located at the corner ($X = 0.0$ inch). Timing of the peaks gives convective velocities of 2697 ft/s (822 m/s; $1.07U_\infty$) for the fall-rise pair, and 2855 ft/s (870 m/s; $1.13U_\infty$) for the rise-fall pair. A possible explanation as to why these velocities are higher than U_∞ is that both events are secondary responses to another primary change in the interaction, with the separation shock motion following primary change closer in time (and perhaps space) than the shear layer motion.

5.3 Summary

Re-examination of the baseline separated compression corner interaction has provided additional insight into the time dependent nature of the interaction; modifying some previous ideas and independently confirming others. Local motion of the separation shock is associated with a signature in wall pressure beneath the incoming boundary layer, which convects into the interaction at $0.75U_\infty$ and is coincident with the shock foot at the time of its motion. The period of this signature is between 75 and 100 μ s, but its shape is dependent on the direction (upstream or downstream) of the shock. Previously, such a signature had only been associated with global shock motions, specifically changes in the

direction of the separation shock. No similar signature was observed in fluctuating pitot pressure measurements made within the incoming boundary layer. Correlations between pitot pressure fluctuations in the incoming boundary layer and wall pressure fluctuations beneath the separation shock motion strengthened with decreasing probe distance from the wall. Pitot pressure power spectra near the wall also had a weak low-frequency content not present higher in the boundary layer. No evidence of a correlation between the motion of the separation shock and position of the boundary layer/freestream interface was found.

The interaction downstream of the corner is strongly correlated with the position of the separation shock. The separated shear layer rises and falls as the separation moves upstream and downstream, respectively, confirming the breathing behavior of the interaction. It is shown here, however, that the motion of the downstream edge of the separation bubble generally lags the motion of the upstream edge (i.e. separation shock). Finally, regions above the ramp face previously noted for high turbulence levels are, in fact, regions dominated by fluctuations associated with the motion of the separated shear layer.

Chapter 6

Downstream Perturbations

The role of the separation bubble in the motion of the separation shock has been argued about by several authors. As part of the current study, perturbations were applied to the separation bubble of the baseline compression corner interaction to investigate possible linkages. Two basic modifications were applied: suction through a slot near the mean reattachment position and alteration/removal of the model side fences.

6.1 Effect of Slot and Suction

The location and type of suction orifice were chosen in an effort to stabilize the point of shear layer reattachment. Data were obtained for the slot configuration without suction (S/NS), as well as for with suction (S/S), to investigate the effect of the geometry change alone. Data were obtained for three (S/NS) "plumbing" configurations: 1) suction plumbing in place but suction inactive, 2) plumbing removed and the exit hole in the model base capped, and 3) filled model plenum. No differences were observed in any data due to these modifications. Tests were also conducted with the slot filled and faired flush with the ramp face. The results from these tests were consistent with those of the no-

slot face, confirming that changing the model face did not change the "global" geometry of the ramp.

Direct measurement of slot mass flow rate was made difficult by several competing factors. First, it was desired to maximize mass flow rate through the slot while keeping the perturbations to the overall flowfield caused by the slot geometry to a minimum. This required a small slot area but high slot velocities (i.e. the slot flow should be choked). Second, the pressure at the slot entrance was expected to be very low (≤ 2 psia), so little pressure difference could be generated to drive the mass flow through the slot. This required that pressure losses in the plumbing system (valve, piping and, if present, flow meter) be minimized. Further, low pressure at the slot entrance limited maximum expected mass flow rates to small values (.016 lbm/sec, 7.1 g/sec). Available mass flow transducers which matched this range had insufficient cross-sectional area and would actually have restricted mass flow. Unknown air density at the measurement station also prohibited use of volumetric flow transducers to determine suction mass flow rate. As an alternative, two independent, indirect techniques were used to measure mass flow through the slot. The first approach used the pressure increase in the vacuum vessel and the total suction-on run time. This technique resulted in a slot mass flow rate of 0.0119 ± 0.0017 lbm/sec. The second method was based on the pressure difference in the pipe beneath the model (suction-on vs suction-off). Slot

mass flow rate computed in this manner was 0.0122 ± 0.0005 lbm/sec, and indicated little variation during the course of a run. Values obtained using these two techniques were very repeatable between runs. They are also lower than the rate that would be calculated assuming the flow to be choked within the slot ($M_{slot} \approx 0.5$), implying that the governing restriction was at the valve. In terms of incoming variables, the slot mass flow represented 3.4% of incoming boundary layer mass flow (per unit width) or 11.3% of the freestream mass flux (per unit area).

6.1.1 Surface Flow Visualization

Kerosene-lampblack surface traces of the interaction for S/NS and S/S are presented in Figures 6-1a and b, respectively. The slot appears as a white band just downstream of the corner. Introduction of the slot places the separation line 1.25 inches upstream of the corner. As with the baseline case (Fig 5-1), there is a slight curvature in the coalescence line, but very little near the model centerline. Application of suction draws the separation line to 0.4 inch from the corner. Curvature of the separation line is also much less pronounced, which suggests that the effects of the suction were two-dimensional. It is clear that insufficient suction was applied to totally remove the separation bubble. Nonetheless, the large differences in the size of these two separation bubbles and the associated changes to the separation shock motion provide insight into the role of the bubble

in driving the motion of the separation shock. These findings are discussed below.

6.1.2 Interaction Upstream of the Corner

Surface pressure measurements were used to quantify the effects of slot and suction on the overall interaction upstream of the corner, with particular attention paid to the dynamics of the separation shock. Examination of surface pressure signals showed characteristics similar to those presented for the baseline configuration in Fig 5-2. Values of both \bar{P}_{w0} and $\sigma_{P_{w0}}$ derived through the interaction were similar to those measured in the baseline interaction.

Streamwise distributions of the normalized surface pressure mean and RMS are presented in Fig 6-2 for both S/NS and S/S. For clarity, symbols represent average values over all runs of a given configuration and within 0.014 inch (0.02 cm) streamwise windows. (Recall that minimum center-to-center transducer spacing is 0.115 inch.) Baseline data and flow visualization separation points are also plotted for reference. The overall data variation about these average values is similar to that shown for the baseline case in Fig 5-4. A one-transducer streamwise shift has been made to some of the data to provide a consistent data base for the curve fits carried out below. The streamwise shifts in the interaction found in the separation line of the surface tracer patterns are reflected in these data as well.

The changes in the mean surface pressure distribution due to the introduction of the slot and suction agree quantitatively with those found by Tanner and Gai [1967] for a 16 degree compression corner at a Mach number of 1.93. The suction slot in that study was formed by raising the ramp vertically above the tunnel floor. Comparisons with the current study are shown in Table 6-1.

	Tanner and Gai	Current Study
Slot height	.17 - .33 δ_0	.21 δ_0
Suction rate $\dot{m}_{\text{nd}} = \frac{Q}{\rho U_{\infty} \theta}$	0.52 - 0.58	0.54
L_{UI} (slot alone) (% of baseline L_{UI})	150 - 160 (initial surface pressure rise)	149 ($\gamma = 0.03$)
L_{UI} (slot + suction) (% of baseline L_{UI})	100 (initial surface pressure rise)	100 ($\gamma = 0.03$)

Table 6-1: Comparison of the Effects of Slot-Alone and Slot-with-Suction on L_{UI}

Q here refers to the mass flow rate per unit width of the slot.

Comparison of all three cases in Fig 6-2 (baseline, S/NS and S/S) clearly shows the increase in magnitude and streamwise extent of the interaction due to the slot. The RMS peak is driven by the dynamic separation shock, and the increase from baseline to S/NS indicates that the separation shock is stronger. The fact that the peak does not decrease between S/NS and S/S implies that this change is driven by the geometry of the slot and not the flowfield between the corner and L_{UT} .

Separation shock intermittency and zero-crossing frequency distributions are presented in Fig 6-3. From the intermittency distributions, comparative length scales of the extremes and extent of the separation shock motion may be determined (Section 5.1.2.1). These data are shown in Table 6-2. The associated curve fits are also shown in Fig 6-3a.

	$\frac{X_1(\gamma=0.03)}{\delta_1}$	$\frac{X_2(\gamma=0.97)}{\delta_1}$	$\frac{X_2-X_1}{\delta_1}$
Baseline	-2.18	-1.21	0.97
Slot	-3.26	-1.70	1.56
Suction	-2.19	-0.17	2.02

Table 6-2: Effect of Geometry Change on Limits of Separation Shock Motion

The effect of suction is seen to linearize the intermittency distribution near the downstream end. A consequence of this effect on the derived lengths in Table 6-2 is to place the downstream limit of the S/S separation shock closer to the corner than it actually is. While the separation lines from flow visualization agree well with the values of X_2/δ_1 for the baseline and slot configurations ($L_s/\delta_1 = 1.11$ and 1.79 respectively), a large discrepancy exists for the suction configuration ($L_s/\delta_1 = 0.57$). Replacing the curve-fit value for X_2/δ_1 with L_s/δ_1 in this case results in a streamwise range of the separation shock of $1.62\delta_1$. This value is very close to that of S/NS, and further suggests the similarity of separation shock motion in these two cases.

A third indicator of the dependence of the separation shock on model geometry (and not on the separation bubble) is presented in Figure 6-4. As in Fig. 5-7, separation shock intermittency has been plotted against normalized surface pressure RMS. Data from the baseline configuration differ distinctly from the slotted configurations (S/NS and S/S). The decrease in γ at which the peak normalized wall pressure RMS occurs is also consistent with a stronger shock. The wall pressure RMS value is driven by both the passage of the separation shock and the turbulent fluctuations downstream of the shock, with the latter contributing more at locations of higher intermittency. The peak value should

therefore be located somewhere downstream of $\gamma = 0.5$. As the shock strength increases, the shock motion will become the dominant influence on the RMS peak and, hence, drive the peak toward $\gamma = 0.5$. This is exactly what is observed in Fig. 6-4 when comparing the results of the baseline and slotted models.

Finally, the shock zero-crossing frequency distribution also exhibits similarities in separation shock behavior between S/NS and S/S. For both cases, $f_{c, \max}$ is about 600 Hz, compared with 1 kHz in the baseline case.

Using the empirical equation developed by Settles *et al.* [1981] for compression corner interactions at Mach 2.95, the change in L_{UI} between the baseline and S/NS is consistent with a two degree increase in the ramp angle. This might be due to an expansion/compression wave system forming at the lips of the slot which would coalesce with and reinforce the primary inviscid shock. As discussed below, however, such structures are not apparent in the pitot profiles above the ramp surface. Alternatively, the slot may locally strengthen the shock system near the corner, resulting in both the higher peak surface pressure RMS and the increase in the streamwise range of the separation shock.

6.1.3 Flowfield Downstream of the Corner

As in the baseline interaction, mean and fluctuating pitot pressure measurements were made in the flowfield downstream of the corner for both S/NS and S/S. Results of conventional pitot probe surveys are presented in Figs

6-5a and b. The location of the slot is shown on the horizontal axis. Comparison of these two figures and Fig 5-21 show changes in the flowfield consistent with those observed in the interaction upstream of the corner. For surveys made at the corner, deviation from baseline data appears between $0.14 \text{ inch} \leq Y \leq 0.94 \text{ inch}$ for S/NS and between $0.06 \text{ inch} \leq Y \leq 0.58 \text{ inch}$.

Note that the profiles of all three configurations relax back to the same shape downstream of the corner. The position and strength of the shock wave at the most downstream survey station is the same for the baseline, S/NS, and S/S. Further, the most downstream baseline and S/S profiles are virtually identical, differing only slightly through the lowest 0.35 inch at $X=3.5 \text{ inch}$. Thus, any changes due to the introduction of the slot, including those to the inviscid shock, are rapidly damped out (in the mean) as the flow moves over the ramp.

Fluctuating pitot pressure signals downstream of the corner for S/NS and S/S exhibit similar characteristics to those found for the baseline. The three modes in the baseline PDD's (Fig 5-25) are also seen in Fig 6-6a for S/NS and Fig 6-6b for S/S, though the spatial development differs as reflected in the flowfield scale changes of Fig 6-5. Pressure values at which the modes occur are also comparable with those found in the baseline interaction. A strong representation of mode 1 is found at $Y=0.4 \text{ inch}$, $X=1.0 \text{ inch}$ for S/NS, and, to a much lesser extent at $Y=0.3 \text{ inch}$, $X=1.0 \text{ inch}$ for S/S. Given the presence and

interpretation of this mode in the S/S PDD's, it is clear that the reattachment point was not stabilized with the amount of suction applied here.

Frozen pitot profiles were generated as for the baseline configuration and are presented in Fig 6-7. Again, the profiles correlate with the separation shock in a manner consistent with the breathing bubble model. Event-relative timing analysis between separation shock motion and shear layer motion was applied with the pitot probe at $X=0$ (Fig 6-8). Peaks for both the rise/fall and fall/rise event edge pairs occur at negative values of τ . As found in the analysis of Section 5.2. , the shear layer motion predominantly lags that of the separation shock. Further, the convective velocity between these event-transitions is of the order of the freestream velocity. Thus, while the scales of the S/NS and S/S interactions vary by a factor of 3 (based on a comparison of $L_{S.}$), the quantities characterizing the flowfield dynamics remain largely unchanged.

6.2 Effects of End Fences

The study of the effect of the fences used to insure two dimensional flow over the ramp was carried out as a sensitivity study of the interaction to fence presence and position. The results, given the findings of Section 6.1, provide further insight into the role of the separation bubble on the motion of the separation shock and, hence, are reported here.

6.2.1 Surface Flow Visualization

Surface tracer patterns were obtained for three fence conditions: extending 3.5 inches forward of the corner, extending 2.5 inches forward of the corner, and off. Results of the first two conditions did not differ and were as shown in Fig 5-1. Removing the fences reduced L_{S^*} from 0.78 inch (baseline) to 0.5 inch (Fig 6-9), which is comparable to L_{S^*} found for S/S. Rippling of the separation line is similar to that found for the other cases. Spillage at the sides of the ramp is evident, though not severe, in the surface tracer patterns.

6.2.2 Interaction Upstream of the Corner

Fluctuating surface pressures were measured upstream of the corner for four fence configuration; those described in Section 6.2.1 and with the fences extending 1.6 inches forward of the corner. Normalized surface pressure mean and RMS streamwise distributions for these cases are presented in Fig 6-10. Differences between the fence-on configuration are within the variation seen for the baseline (Fig 5-4). The location of the fence-off interaction, however, has moved approximately 0.35 inch downstream. This shift compares well with the shift in the separation line of the surface flow visualization. Removing this shift (Fig 6-11) shows that region of the interaction dominated by the separation shock motion to be very similar. The streamwise shock intermittency and zero-crossing frequency distribution (Fig 6-12) support this conclusion.

6.3 Summary

Four different interactions were generated by perturbations downstream of the separation line for the same compression corner. When the slot was not present, $L_{s'}$ differed by a factor of 2, yet the separation shock motion was basically the same. Similarly, with the slot present, $L_{s'}$ differed by a factor of 3 and, again, the motion of the separation shock was basically unchanged. Finally, comparing the two cases with the closest values of $L_{s'}$ (S/S and baseline/no fences) shows distinctly different shock motions. These results indicate that the separation bubble does not play a direct role in the dynamics of the separation shock. If it did, one would expect that these large variations in separation bubble size would directly influence any downstream feedback and, hence, the streamwise extent or frequency of the separation shock.

Based on these findings, it is suggested that the downstream geometry/boundary conditions serve to establish a baseline flowfield with an inherent sensitivity. The motion of the separation shock motion is a result of this flowfield reacting to perturbations of the incoming turbulent flow. This model is supported by the results of Tran [1987] shown in Fig 6-13. Shocks of similar strength and sweep, generated by different geometries, and interacting with the same incoming turbulent boundary layer produce the same streamwise distribution of normalized wall pressure RMS.

Chapter 7

Upstream Perturbations

Dependence of the separation shock motion on the character of the incoming turbulent boundary layer was examined by perturbing specific regions of the incoming boundary layer. Changes in the separation shock motion were quantified using simultaneous fluctuating surface pressure measurements from transducers aligned in the streamwise direction and perpendicular to the ramp corner line. Boundary layer perturbations were quantified in the absence of the compression corner using fluctuating surface pressure measurements, conventional pitot pressure surveys, and fluctuating pitot pressure measurements.

7.1 Boundary Layer Manipulators

A schematic of the test configuration for the boundary layer manipulator (BLM) study is shown in Fig 7-1. BLM's were mounted with their lower surface parallel to and 0.5 inch above the tunnel floor. This placed the BLM at $0.7\delta_1$. The chord length of each BLM was 1.0 inch ($1.4\delta_1$). Both the height and chord length are consistent with those used in incompressible studies of LEBU's to obtain optimum drag reduction. The chord length of each BLM was 1.0 inch ($1.4\delta_1$), Average Mach number at this height was 4.46. The trailing edge of the

BLM was 2.24 inches upstream of the corner. The lower surface of the BLM was flat with the sharp leading and trailing edges beveled from the upper surface at either 15 or 35 degrees. Two angles were tested to distinguish the effects of BLM wake structure from BLM wave structure on the compression corner interaction. This orientation placed the BLM shock wave mostly above the boundary layer.

The first part of this section examines the effect of the BLM on the compression corner interaction, focusing on changes in the motion of the separation shock. The latter part quantifies changes to the mean and dynamic incoming flowfield due to the BLM in the absence of the compression corner.

7.1.1 Surface Flow Visualization

The surface tracer pattern of the compression corner interaction with the 15 degree BLM in place is shown in Fig 7-2. The position of the corner ('C'), separation line ('S'), and BLM trailing edge ('BLMTE') are marked for reference. No disturbances are visible upstream of the corner interaction to suggest a shock system beneath the BLM, nor the introduction of any three dimensional disturbance by the BLM and struts. The separation line itself is nominally two-dimensional and is 0.56 inch upstream of the corner at the model centerline, which less than that for the baseline interaction.

7.1.2 Fluctuating Surface Pressures Upstream of the Corner

As in the baseline (undisturbed) compression interaction, the study of the separation shock motion in the BLM-perturbed interaction begins with a qualitative assessment of the streamwise development in the fluctuation surface pressures. Fig 7-3 and 7-4 present such developments for the 15 degree BLM interaction and 35 degree BLM interaction, respectively. Comparing these figures with those of the baseline (Fig 5-2), three differences are evident. First, while two states (see Section 5.1.2.1) are visible in surface pressure signals d, e, and f of Fig 7-3 and signals f, g, and h of Fig 7-4, the distinction between the states is not as clear as for the baseline signals. Second, noting that the transducer spacing is the same for Figs 5-2, 7-3, and 7-4, the intermittent behavior associated with the translating separation shock is restricted to a smaller streamwise range in the BLM-perturbed interactions. Both of these changes are similar to those observed by Erengil and Dolling [1992] in comparing swept to unswept compression corner interactions. Finally, given that two states can be defined in the surface pressure signal as in the baseline interaction, both \bar{P}_{w0} and $\sigma_{P_{w0}}$ appear higher in the BLM-perturbed interactions, suggesting an inviscid compression due to the BLM. Surface pressure PDD's (Figs 7-5 and 7-6) still exhibit a bimodal shape, but the peaks of the modes are much closer than for the baseline interaction (Fig 5-3). Note that since \bar{P}_{w0} downstream of the BLM may

vary, no shifts are applied to line up the lower modes in the PDD's. PDD's for upstream traces with basically Gaussian shapes have been removed for clarity. Focusing on the lower 'incoming' mode, \bar{P}_{wo} increases by an average of 13% for the 15 degree BLM configuration and 8% for the 35 degree BLM configuration. Additionally, $\sigma_{P_{wo}}$ increases by an average of 120% for the 15 degree BLM configuration and 73% for the 35 degree BLM configuration.

Normalized surface pressure mean and RMS streamwise distributions are presented in Fig 7-7 for both the BLM and the baseline configurations. These clearly show that the BLM delays the onset of the primary pressure rise, decreases the travel of the separation shock and decreases the magnitude of the peak surface pressure RMS, though this last result may result from decreased spatial resolution.

The effect of BLM presence on separation shock intermittency and zero-crossing frequency are presented in Fig 7-8. Interaction lengths derived from curve fitting the shock intermittency data are presented in Table 7-1, though the decrease in spatial resolution makes the resulting numbers less reliable than for the baseline interaction. This discrepancy is highlighted by the difference between L_s/δ_1 (0.80) and X_2/δ_1 (0.66) for the 15 degree BLM interaction. The associated curve fits are shown in Fig 7-8a. The maximum zero-crossing frequency increases by 22% for the 15 degree BLM interaction and by 45% for

the 35 degree BLM interaction.

	$\frac{X_1(\gamma=0.03)}{\delta_1}$	$\frac{X_2(\gamma=0.97)}{\delta_1}$	$\frac{X_2-X_1}{\delta_1}$
15° BLM	-1.28	-0.66	0.62
35° BLM	-1.06	-0.81	0.25

Table 7-1 Effect of BLM on Limits of Separation Shock Motion

Streamwise development of the normalized surface pressure power spectra between the BLM trailing edge and the compression corner (Fig 7-9 for the 15 degree BLM and Fig 7- 10 for the 35 degree BLM) reflects the presence of the translating separation shock. These spectra are based on 256 records of data sampled at 200 kHz. Streamwise locations are the same as for the wall pressure signals in Figs 7-3 and 7-4. Surface pressure variance at the most upstream locations is dominated by high frequency ($2 \text{ kHz} < f$) fluctuations. Beneath the translating separation shock, there is a shift to lower frequencies ($200 \text{ Hz} < f < 10 \text{ kHz}$), as found in the baseline interaction (Fig 5-5). Finally, as the downstream edge of the intermittent region is approached, higher frequency fluctuations once

again dominate the surface pressure variance while the PDD's (Figs 7-5 and 7-6) return to the Gaussian shape characteristic of the fully separated region just upstream of the corner.

7.1.3 Separated Shear Layer Motion

Given the findings of Sections 5.2.2.2 and 6.1.3 showing a relationship between the motion and location of the separation shock and separated shear layer, a similar analysis was carried out here for the 15 degree BLM perturbed flowfield. Fluctuating pitot pressure measurements were made at $X=0$. No frozen pitot profiles were generated, but an event relative timing analysis was performed using separation shock and shear layer boxcar signals. 1024 records of data were obtained at 500 kHz to provide a statistically sufficient number of both types of events with adequate time resolution. Representative results are provided in Fig 7-11 for a surface transducer at $X=-0.825$ inch and the pitot probe at a height $Y=0.10$ inch. Peaks in both the rise-fall and fall-rise histograms are well above the 'uncorrelated' level. The time-delays of the rise/fall peak and fall/rise peak are $-16 \mu s$ and $-12 \mu s$, respectively. As in the undisturbed compression corner interaction, the motion of the downstream edge of the separation bubble lags the motion of the upstream edge (separation shock), irrespective of the direction of motion.

7.2 Effect of BLM on Incoming Flowfield

Having established the ability of the BLM to alter the motion of the separation shock, it remained to be determined how the BLM had altered the incoming flowfield. This section presents results examining such changes in the absence of the compression corner. Fluctuating surface and pitot pressure data, as well as mean pitot pressure surveys were used to quantify these changes.

7.2.1 Fluctuating Surface Pressure Measurements

Figure 7-12 presents normalized wall pressure power spectra at several streamwise locations ($\Delta X = 1\zeta = 0.115$ inch) with and without the 15 degree BLM in place. These spectra were computed from 256 records of data sampled at 200 kHz. The most upstream station is 0.04 inch downstream of the BLM trailing edge station. The spectra obtained in the undisturbed boundary layer are virtually identical, with almost all of the wall pressure variance being contained in frequencies above 2 kHz. By contrast, a low frequency 'bulge' appears in the wall pressure spectra just downstream of the BLM (Fig 7-12b) at $f < 500$ Hz, then rapidly disappear within 0.58 inch (note its absence in Figs 7-12g and h). Also note that the spectra in Figs 7-12g and h are similar to that shown in Fig 7-9a (for the location 0.115 in (1ζ) downstream of that for 7-12h) with the compression corner in place. This suggests that an equilibrium has been reached as indicated by the wall pressure fluctuations prior to the separation shock of the compression

corner interaction.

Fig 7-13 shows the streamwise variation in σ_{P_w} associated with the power spectra of Fig 7-12. Normalization is by the average undisturbed value, which represents the incoming undisturbed boundary layer. It is clear that the redistribution of the variance noted above is accompanied by an increase in the value of the variance itself. The 'outgoing' value of σ_{P_w} is almost twice that of the undisturbed boundary layer (0.023 psia versus 0.012 psia). Though the value of \bar{P}_w is not as reliable, 'outgoing' \bar{P}_w increases by approximately 13%.

These surface pressure data clearly show that the boundary layer entering the compression corner interaction has been altered by the BLM. Most significantly, the level of σ_{P_w} has been increased, which could reflect more vigorous turbulent activity in the boundary layer or that the shock system associated with the BLM has raised the pressure level of the overall flowfield. The distinction of which process is at work was sought through the flowfield data discussed below. In either case, the wall pressure data indicate that some level of equilibrium has been reached prior to the compression corner interaction.

7.2.2 Mean Pitot Pressure Measurements

Pitot pressure surveys were made downstream of the BLM trailing edge to determine its effect on the flowfield, with particular emphasis on mapping the development of the BLM wake and wave structure. Surveys were carried out at

four streamwise stations at the mid-span of the BLM using a single-tip conventional pitot probe. Three flowfields were examined: no BLM (NBLM), 15 degree BLM (BLM15), and 35 degree BLM (BLM35). Additionally, spanwise variation at the NBLM and BLM15 flowfields were examined using the 7-tip pitot rake described in Section 3.4.3.

Streamwise development of the three flowfields are shown in Figs 7-14a-c. The upper dashed lines in Figs 7-14b and c trace the leading-edge and trailing-edge shock waves from the BLM (as deduced from the pitot pressure measurements). The lower dashed line tracks the center of the BLM wake. The angles of these features, as determined using a least-squares linear fit, are summarized in Table 7-2.

	Leading Edge Shock	Trailing Edge Shock	Wake	Turning Angle for L.E. Shock
15° BLM	14.7°	9.3°	0.3°	4.4°
35° BLM	16.0°	8.9°	1.6°	6.0°

**Table 7-2 Wave/Wake Angles Downstream of BLM
as Determined from Pitot Pressure Surveys**

The angle through which the freestream ($M=4.95$) must be turned to generate the observed leading edge shock angle is also included. Pitot pressure jumps across the shock are consistent with this turning. The slight inclination of the wake is consistent with the results of a two-dimensional inviscid shock/expansion analysis for the given BLM geometry using the Mach number at $Y=0.5$ inch in the boundary layer ($M=4.45$).

The two-dimensionality of the BLM15 flowfield may be judged from the pitot rake results presented in Fig 7-15. These data were obtained 1.28 inches downstream of the BLM trailing edge. Because of the rake design, no data could be obtained below $Y=0.2$ inch. Nonetheless, sufficient height is traversed to capture all significant features of the profile and establish that the mean flowfield is nominally two-dimensional. Profile repeatability is particularly good between the five center stations ($Z=\pm 1.0, \pm 0.5, 0.0$ inch). A similar survey 4.0 inches downstream of the BLM trailing edge showed increased discrepancy between the outermost profiles ($Z= \pm 1.5$ inch) and those measured at the other stations, primarily between the lower edge of the wake and the trailing edge shock. The central 2 inches of the flowfield remained two-dimensional.

Examination of these profiles indicates that the BLM (either 15° or 35°) has a negligible effect on the pitot profile beneath the BLM. With exception of the wave structure, there appears little change to the mean flowfield to which the

observed changes in the compression corner separation shock motion may be attributed.

7.2.3 Fluctuating Pitot Pressure Measurements

Fluctuating pitot pressure measurements were made at several streamwise locations downstream of the 15° BLM and in the undisturbed boundary layer to quantify changes in the time-varying properties of the flowfield. Data were obtained using both one- and two-tip probes. The latter are somewhat more intrusive but provide simultaneous multi-point flowfield data through and across the BLM wake.

Figure 7-16 presents distributions of basic statistical moments (mean, standard deviation, skewness and flatness coefficient) of the fluctuating pitot pressure signal. Data are for the 15° BLM flowfield and the undisturbed boundary layer. Streamwise position is measured from the BLM trailing edge location. Data were acquired at 200 kHz or 500 kHz.

Fig 7-16a compares mean pitot pressure values obtained by time-averaging the fluctuating pitot pressure signal with those measured by the conventional pitot probe and presented in Fig 7-14. Agreement between the results of the two methods is generally good, though the mean of the fluctuating data is slightly lower at the upper edge of the interaction. The same type of shift was observed by Shau and Dolling [1990], as mentioned in Section 5.2.2.1. Also

note that, despite the severe gradients in the vicinity of the BLM wake, the mean of the fluctuating pitot pressure measurement agrees well with the value obtained from the conventional probe. This indicates that integration across the larger Kulite tip is not a problem in this study.

Pitot pressure RMS distributions (Fig 7-16b) exhibit decreases of up to 56% within the BLM wake when compared with undisturbed boundary layer values. This decrease in activity persists through the surveyed streamwise range. Normalizing by the local mean pitot pressure largely eliminates this difference (Fig 7-17). Little change in the RMS is seen elsewhere. In contrast, the skewness and flatness coefficients (Figs 7-16c and d, respectively) show greatest sensitivity to the presence of the BLM near the height of the undisturbed boundary layer edge. Here, both coefficients are reduced, suggesting decreased vertical travel of the boundary layer edge. As with the mean pitot profiles, no significant differences are seen in any of the pitot pressure moments at heights beneath the BLM.

Normalized pitot pressure power spectra obtained at a distance 1.3 inches downstream of the BLM trailing edge location are presented in Fig 7-18. For reference, vertical positions of the pitot probe are indicated on the mean pitot pressure profiles at the top of the figure, with symbols referencing specified spectra. The low frequency 'bulge' previously noted in Fig 5-20 is still weakly

present near the wall (Fig 7-18a) and gradually disappears with increasing probe height. No significant differences are seen between the NBLM and BLM15 spectra. Two inches further downstream, the BLM wake flattens the peak in the power spectrum, but results just above or below this point show the change to be highly localized.

As a final effort to quantify changes to the dynamic structure of the incoming flowfield due to the BLM, simultaneous fluctuating pitot pressure measurements were made at several Y-positions downstream of the BLM trailing edge. The probe tips had a fixed vertical separation (ΔY) of 0.16 inch (center-to-center), but no streamwise stagger ($\Delta X=0$). The tips were mounted to a single shaft and traversed as a unit through the flowfield. Data were sampled at 500 kHz to provide adequate timing resolution (2 μ s).

Figure 7-19 shows cross-correlations between pitot pressure signals measured 1.25 inches downstream of the BLM trailing edge location and at several heights above the floor in both NBLM and BLM15 flowfields. Time-averaged pitot pressure values are mapped onto the mean pitot pressure profile at the top of the figure to allow interpretation of the cross-correlation results in reference to mean flowfield features. Marker pairs indicate the vertical position of the probe tips for any given data set. The time-delay was applied to the signal of the probe tip closest to the wall.

For each cross-correlation, the time delay of $R_{xy})_{\max}$ is noted for both NBLM (τ_{UBL}) and BLM15 (τ_{BLM}). This can be used to approximate structure angles in the boundary layer from the equation:

$$\beta = \text{atan}(\Delta Y / U_c \tau) \quad (7-1)$$

where β is the structure angle relative to the freestream direction and U_c is some measure of structure convective velocity. While data from this probe have been found to slightly overestimate structure angles due to the size of the sensing elements, it is reassuring to note in Fig 7-19 that τ_{UBL} remains positive throughout the boundary layer and decreases as the freestream is approached. These characteristics indicate that the structure angle is less than 90° and increases with distance from the wall.

Examination of the differences in cross-correlations due to the presence of the BLM reveals little change for the first three heights (Figs 7-19a-c). Surprisingly, the two cases where the probe spanned the BLM wake (Figs 7-19b and c) produced almost identical cross-correlations as for the undisturbed flowfield. The differences seen in Fig 7-19d can be directly attributed to the fact that the lower tip is in the center of the BLM wake, slowing the local flow and increasing the time difference between a structure passing across the upper probe and its subsequent passage over the lower probe. The negative cross-correlation

observed in Fig 7-19e (noting that the values have been multiplied by -1.0 to place it on the same scale with the other data) is the result of the proximity of the upper probe tip to the BLM trailing edge shock. As the lower probe experiences a local increase in pitot pressure, the BLM trailing edge shock moves downstream, placing the tip of the upper probe upstream of the shock and reducing the measured pitot pressure. Upstream motion of the BLM shock results in an increase in the pitot pressure of the upper probe, and is associated with a decrease in the pitot pressure of the lower probe. Oscillations in the shock position, therefore, dominate the cross-correlation at this height.

The coherence spectra associated with the cross-correlations of Fig 7-19 are presented in Fig 7-20. Again, the biggest differences associated with the introduction of the BLM are seen in Figs 7-20d and e, and are attributed to the phenomena discussed above. The spacing between the probes makes these data insensitive to higher frequencies. However, for the given location in the boundary layer, the coherence spectra should be dominated by the larger scales (Spina [1988]).

In all, introduction of the BLM was found to do little to the dynamics of the downstream flowfield. Of much greater significance was the resulting wave structure which turns and compresses the inviscid flow. A preliminary study performed in the current facility and a more detailed study by Settles *et al.*

[1981] have shown that the scale of this type of interaction depends exponentially on the compression corner angle. The reduction in the compression corner interaction scale and strength brought about by introducing the BLM upstream are consistent with a weaker interaction such as would occur by turning the flow through a smaller angle. Further, the increased 'pre-turning' caused by the 35° BLM, compared to that due to the 15° BLM, results in an even weaker compression corner interaction. This is supported by the results of Fig 7-7.

7.3 Riblets

A separate series of tests was conducted to examine the sensitivity of the compression corner interaction to alteration of the near-wall region of the incoming turbulent boundary layer. For this purpose, an 18 inch streamwise length of riblet film was applied to the tunnel floor just upstream of the compression corner interaction. The test procedure was similar to that used for the BLM study: first quantify changes to the compression corner interaction, then determine what effect the riblets had on the incoming boundary layer/flowfield.

Results of the influence of riblets on the compression corner interaction are presented in Figs 7-20 and 7-21. All riblet data are within experimental repeatability of the baseline (no-riblets) compression corner interaction results. Therefore, the riblets produced no changes to either the wall pressure distribution or the separation shock behavior.

The inspiration for this perturbation study came from the experimental results of Robinson [1988], as described in Section 2.5. In that study, near wall ($0.03 < Y/\delta < 0.16$, $41 < y^+ < 217$) velocity fluctuations were significantly reduced in a Mach 3 turbulent boundary layer ($Re_\theta = 15,000$). The riblet field extended 56δ upstream of the measurement station. The riblets themselves were of the same cross-section and of similar wall-unit dimensions as those used in the current study.

Because of interference between the wall and the pitot probe, data could be obtained no closer than 0.1 inch from the wall (as measured from the center of the transducer). This equates to $Y/\delta_1 = 0.14$ or $y^+ = 218$, and is the extreme limit of the riblet influence as determined by Robinson. No differences were found in either the basic statistical quantities or the power spectra of the pitot measurements. It is assumed that since the riblets in this study had the same cross-sectional geometry and approximately the same wall dimensions as those used by Robinson, suppression of near-wall velocity fluctuations was also present here. The difference in Re_θ between Robinson's flow (15,000) and that of the current study (33,000) is not believed to substantially alter this result, based on Robinson's finding that the effect of riblets on the turbulence quantities in his study were similar to those found in low-speed flows at significantly lower Reynolds numbers.

7.4 Summary

Efforts to effect the motion of the separation shock by perturbation of the incoming/upstream flow met with mixed success. The BLM effectively reduced the travel and strength of the shock wave, while increasing its frequency. Examination of both the mean and fluctuating features of the flowfield downstream of the BLM, however, suggests that this change to the compression corner interaction was brought about by a pre-turning and pre-compressing of the flow upstream of the ramp, resulting in an overall weaker compression corner interaction.

Application of riblets upstream of the corner to modify the compression corner interaction through altering the near-wall turbulent fluctuations had no measurable effect. No direct measurement was made to confirm alteration of the near-wall region of the incoming boundary layer due to instrumentation interference limitations. It is assumed that near-wall velocity fluctuations were suppressed in a manner similar to that observed by Robinson. The results lead to the conclusion that near-wall ($y^+ < 220$) velocity fluctuations are not responsible for the motion of the separation shock wave in the compression corner interaction.

Chapter 8

Flowfield and Driving Mechanism

The purpose of this chapter is to summarize the current understanding of the unsteady, highly separated compression corner interaction based on the findings of the current study. Implications for further study of this type of interaction, experimental and numerical, are discussed. This is followed by a series of thoughts on the mechanisms contributing to the motion of the separation shock.

8.1 Flowfield Structure

From the results of this and previous work, it is clear that the interaction downstream of the separation shock is inseparably tied to the motion of the separation shock. Efforts to numerically predict such flows must take this time dependence into account, or run the risk of modeling a flow which may reproduce specific experimental results (i.e. mean surface pressure or skin friction distributions), yet not accurately predict other important features of the flow because the physical model is incomplete. Experimentalists must also consider the unsteadiness when interpreting measurements. This specifically applies to 'turbulence' measurements made downstream of the ramp corner which do not

distinguish between the large scale unsteadiness of the flow (as reflected in the dynamic behavior of the separation shock and the associated separated shear layer) and fluctuations due to turbulence. Such single point measurements can only lead to incorrect conclusions about turbulence amplification through the interaction.

Results from the current study also suggest limits on the understanding of the flowfield that may be obtained solely from wall pressure measurements. While these measurements may be made in a non-intrusive manner and do track the position of the separation shock, they only weakly indicate the low frequency oscillations found in the near-wall region of the incoming boundary layer, and they fail to indicate the flapping motion of the separated shear layer downstream of the corner. It may be argued that the former feature is the result of a shock/boundary layer interaction set up by the pitot probe. However, similar trends in hot wire data of Shau [1991] for this boundary layer using a probe of significantly different geometry suggest that this is not the case. The bimodal pitot pressure amplitude probability density distributions from this study (and similar mass flux PDD's obtained by Selig [1988]) show the dynamic separation bubble to extend significantly further downstream of the corner than previously deduced using fluctuating surface pressure measurements.

8.2 Driving Mechanism

While no direct tie has been established between the motion of the separation shock and other features of the flow, several observations from the current study suggest a possible division of roles between the incoming boundary layer and the shock-generating geometry. As regards that portion of the flowfield downstream of 'S', the separation shock motion shows no direct dependence on the size of the separation bubble. Further, motion of the separated shear layer is tied to that of the separation shock, but predominantly lags it. These results imply the absence of any feedback mechanism through the flowfield downstream of 'S', at least none beyond the immediate vicinity of the instantaneous separation point. If a disturbance was to propagate upstream from the ramp corner line, its strength would be expected to dissipate with distance as it traveled to the separation shock. A larger separation bubble would therefore be associated with a different shock motion than that associated with a smaller bubble. It would also be expected that the motion of the shear layer above the corner, being closer to the disturbance, would precede that of the separation shock. Neither of these conditions were observed.

Correlations of separation shock motion and incoming boundary layer dynamics generated mixed results. Perturbations to the near wall region of the boundary layer ($y^+ < 200$) had no effect on either the motion of the separation

shock or the overall compression corner interaction. The maximum interface crossing frequency of the boundary layer edge was found to be about five times that of the separation shock maximum zero crossing frequency, but almost equal to the maximum zero crossing frequency of the separated shear layer.

These last results are very similar to those found by Devenport and Simpson [1990] within the unsteady incompressible flowfield upstream of a wing-body junction. In that study, bimodal velocity histograms were observed between

$-0.86 < X/\delta < -0.28$ (as measured from the wing leading edge) near separation, which led the authors to conclude that a region of intermittent backflow was being generated by the recirculation of fluid impinging on the leading edge of the wing. Some of this fluid "comes from the outer intermittent part of the boundary layer," and the instantaneous extent of the backflow is determined by the whether that contribution originated from a low-momentum boundary-layer structure or from the irrotational freestream. The frequency characterizing the intermittent region was 20% of the "typical passage frequency of structures in the outer part of the boundary layer," a relationship nearly identical to that between the maximum shock zero-crossing frequency and maximum interface crossing frequency of the incoming turbulent boundary layer in the current study. Only a fraction of the incoming structures, therefore, were responsible for generating the

backflow "jet". Further, histograms of the period between back-flow to zero-flow transitions in the wing-body interaction exhibit the same log-normal shape found in the histograms of the period between separation shock crossings (Fig 8-1).

While it is unlikely that the unsteady flowfield in the current study is driven by structures impinging on the compression corner and recirculating upstream (Gramann [1989] reported that surface pressure PDD's from the ramp surface were close to Gaussian), a mechanism similar to that at work in the flowfield of Devenport and Simpson may be operating here. The separation shock represents an interface between the flow upstream of the interaction and a region of backflow upstream of the corner. It would thus be a *result* of the flow separation, and not the cause. This idea is also supported by the finding of 'convective' velocities between the motion of the separation shock and that of the separated shear layer being greater than U_∞ . The difference between $\Omega_{\text{edge}})_{\text{max}}$ and $f_c)_{\text{max}}$ is explained as in the above model. Similarities between $\Omega_{\text{edge}})_{\text{max}}$ and the maximum shear layer zero crossing frequency are due to the continued downstream travel of the boundary layer structures within the separated shear layer. No direct correlation was found in this study between the motion of the boundary layer edge and that of the separation shock, but it is possible that the boundary layer measurements were made too far upstream of the interaction.

Correlations between fluctuating pitot pressure measurements in the

incoming boundary layer and fluctuating wall pressure measurements beneath the separation shock increased as the pitot probe approached the wall. A greater portion of the pitot pressure signal variance was composed of low-frequency fluctuations near the wall, and spanned a frequency band consistent with the dominant frequencies of wall pressure power spectra beneath the separation shock.

Fluctuating surface pressures measured upstream of the separation shock also exhibit a characteristic signature which seems to be the 'footprint' of a structure that convects downstream and is coincident with the separation shock foot at the time of its motion. The nature of this signature varies with the type of local shock motion (upstream or downstream).

Together, these results suggest a flow model in which the shock-generating geometry is responsible for setting the strength and orientation of the 'equilibrium' interaction, which is then perturbed by fluctuations in the incoming turbulent boundary layer. Sensitivity to these perturbations must be a function of the 'equilibrium' interaction. While this 'model' is not definitive and represents another change in explaining the primary mechanism responsible for the interaction unsteadiness (Dolling and Murphy [1983], Andreopoulos and Muck [1987], Tran [1987]), it is based on a more thorough examination of the flowfield and benefits from improved conditional analysis techniques which focus on the

motion of the separation shock as the appropriate trigger. Such a model would account for differences observed in shock dynamics within the same incoming boundary layer, but for interactions generated by different geometries.

Chapter 9

Conclusions

This experimental study has examined the unsteady flowfield associated with the shock-induced separation of a turbulent boundary layer. The interaction was generated by a 28° unswept compression corner in a Mach 5 airstream. Perturbations were made to the interaction to better understand the mechanism responsible for the separation shock dynamics, as well as to demonstrate a method of controlling the shock motion. High frequency wall pressure measurements were used to track the time-dependent position of the separation shock. Conventional and fluctuating pitot pressure measurements were used to quantify the spatial mean and time-dependent extent of the baseline and altered interactions.

In light of the specific objectives put forward in Chapter 1, the findings of this study indicate:

- 1) The unsteady motion of the separation shock is most likely due to fluctuations in the outer portion of the incoming turbulent boundary layer ($Y/\delta_1 > 0.3$) acting on an 'equilibrium' interaction set up by the inviscid shock, and not to the feedback of disturbances upstream through the separation bubble.
- 2) The streamwise extent of the separation shock travel and overall separation

bubble can be reduced by a weak pre-compression of the incoming inviscid flow by a flat-plate manipulator.

Modification of the baseline interaction focused on two regions of the flowfield. Riblets and a boundary layer manipulator were separately introduced upstream of the interaction to alter the near-wall and outer region of the incoming boundary layer, respectively. Suction was applied through a slot in the face of the compression corner to alter the interaction downstream of the separation line.

Analyses of the data support the following conclusions:

- 1) Local motion of the separation shock is associated with a characteristic signature found in the ensemble-averaged wall pressure fluctuations beneath the incoming turbulent boundary layer. The signature may be followed in space and time, convecting downstream toward the shock with a velocity of $0.75U_{\infty}$, and is coincident with the separation shock foot at the time of its motion. Signature shape depends on the local shock motion, upstream or downstream. This result differs from the previous finding that such signatures were linked to specific global shock motions. Similar signatures were not found in ensemble-averaged pitot pressure fluctuations measured within the incoming boundary layer, though this may be due to the measurements being made too far upstream of the interaction.
- 2) Maximum zero crossing frequency of the separation shock was about 20% of

the maximum interface crossing frequency of the incoming boundary layer edge. This relation is similar to that found by Devenport and Simpson [1990] between separation bubble oscillations and incoming boundary layer interface crossing frequency in an unsteady incompressible flow upstream of a wing-body junction.

3) Correlations between wall pressures beneath the translating shock and pitot pressure signals within the incoming boundary layer increased significantly with decreasing Y/δ_1 . Further, low frequency fluctuations (< 2 kHz) were found to contribute increasingly to the pitot pressure variance with decreasing Y/δ_1 for $Y/\delta_1 < 1$. The range of these frequencies closely matches those associated with the separation shock.

4) Fluctuating pitot pressure measurements above the ramp surface indicated extensive flapping of the separated shear layer, extending more than $3.5\delta_1$ downstream of the corner. The extent of separation is significantly greater than previously determined using surface pressure measurements. The maximum frequency of this motion is very close to that of the incoming boundary layer interface crossing frequency. The motion and position of the shear layer are found to be related to the motion and position of the separation shock, following the previously determined 'breathing bubble' model. Current data shows, however, that the relation between the location of the upstream and downstream limits of the bubble is not one-to-one, with the motion of the downstream edge

generally lagging that of the upstream edge.

5) Separation shock dynamics are not directly related to the size of the separation bubble (as defined by L_s). Introduction of the slot to the ramp face increased L_s and strengthened the resulting shock. Applying suction through the slot decreased L_s by a factor of three but did not appreciably alter the motion or strength of the separation shock. A similar value of L_s to that found with the suction study was produced by removing the end fences from the no-slot model. The shock dynamics, however, were the same as for the baseline no-slot model with fences. Coupled with the findings in 4), this suggests that the motion of the separation shock is not driven by disturbances which propagate upstream through the separated region. The shock motion may, however, respond to changes immediately downstream of the instantaneous separation point.

6) Using riblets to suppress the near-wall turbulent fluctuations of the incoming turbulent boundary layer had no effect on the separation shock dynamics.

7) Use of a single plate boundary layer manipulator to modify the incoming flowfield significantly reduced the extent of the overall separation bubble and the separation shock travel. However, flowfield surveys downstream of the manipulator showed this change to be due to pre-turning and compression of the inviscid flow, and not to an alteration of the boundary layer dynamics.

Combining these findings with those of previous work, it is most likely

that the motion of the separation shock is driven by fluctuations in the outer portion of the incoming boundary layer ($Y/\delta_1 > 0.3$). Confirmation of this relationship will require continuous, non-intrusive measurements of the boundary layer flow just upstream of the interaction obtained simultaneously with some measure of the separation shock position and motion. The shock-generating geometry is responsible for setting up an 'equilibrium' interaction with an inherent sensitivity to the incoming disturbances. The sensitivity, in turn, is a function of the interaction strength and sweep/curvature.

Appendix

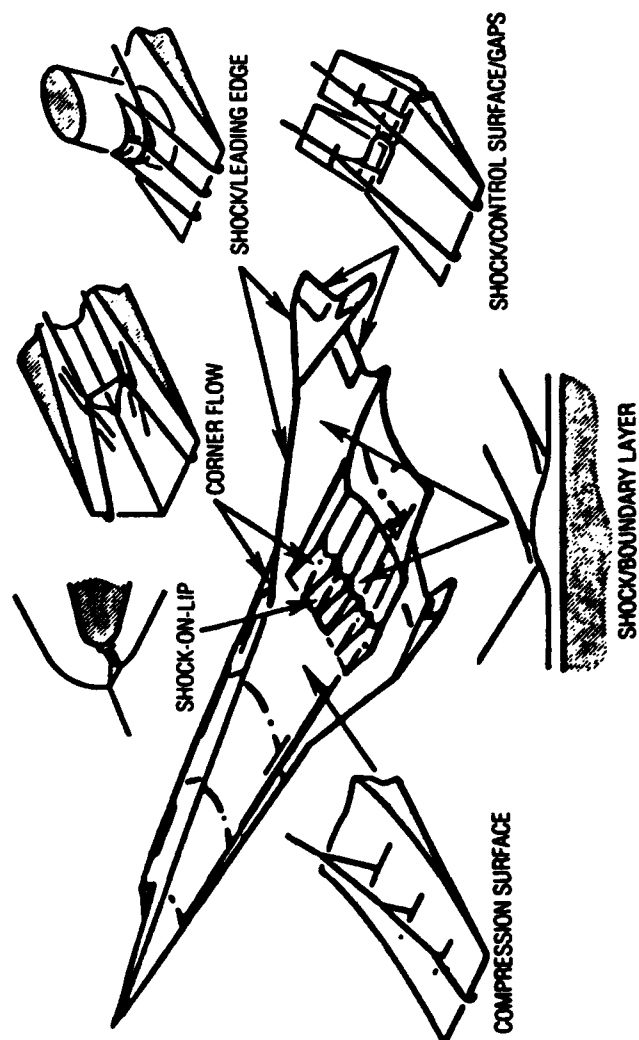


Fig. 1-1: Potential Shock Wave/Boundary Layer Interaction Locations on a Hypersonic Vehicle (Jackson et al [1987])

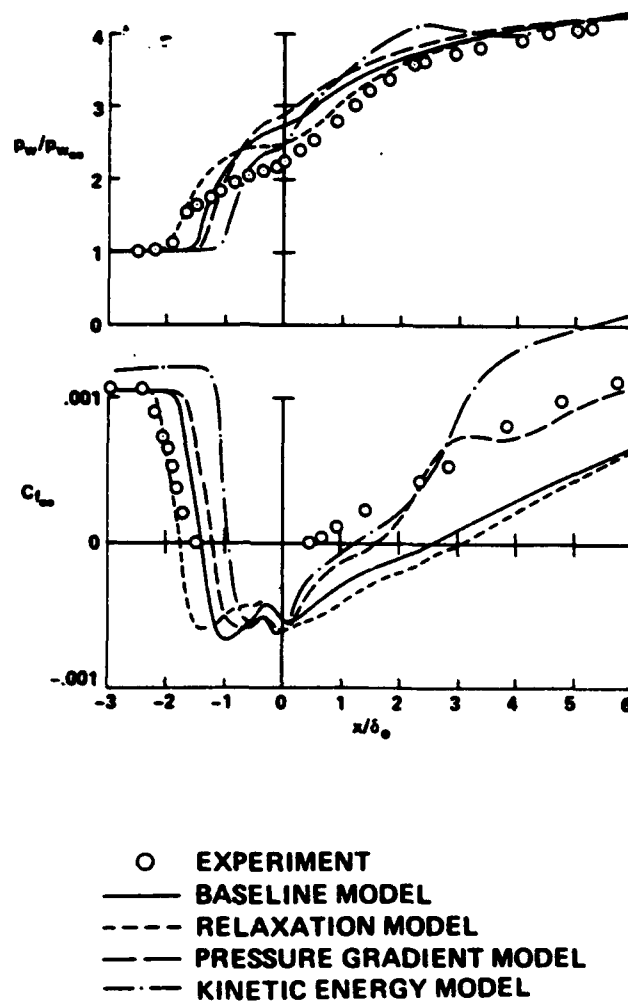


Fig. 2-2: Comparison of Computational and Experimental Surface Quantities in a Mach 3, 24° Compression Corner SWTBLI (Horstman et al [1977])

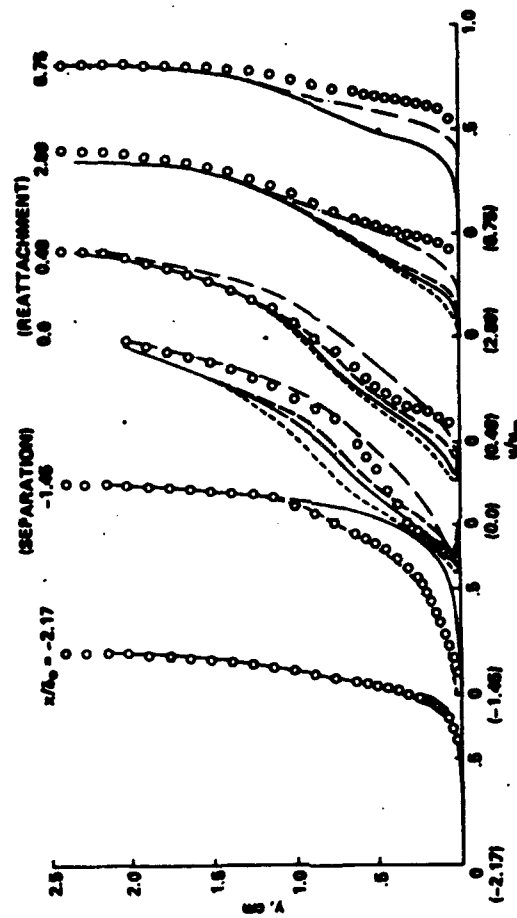


Fig. 2-3: Comparison of Computational and Experimental Velocity Profiles in a Mach 3, 24° Compression Corner SWTBLI (Horstman et al [1977])

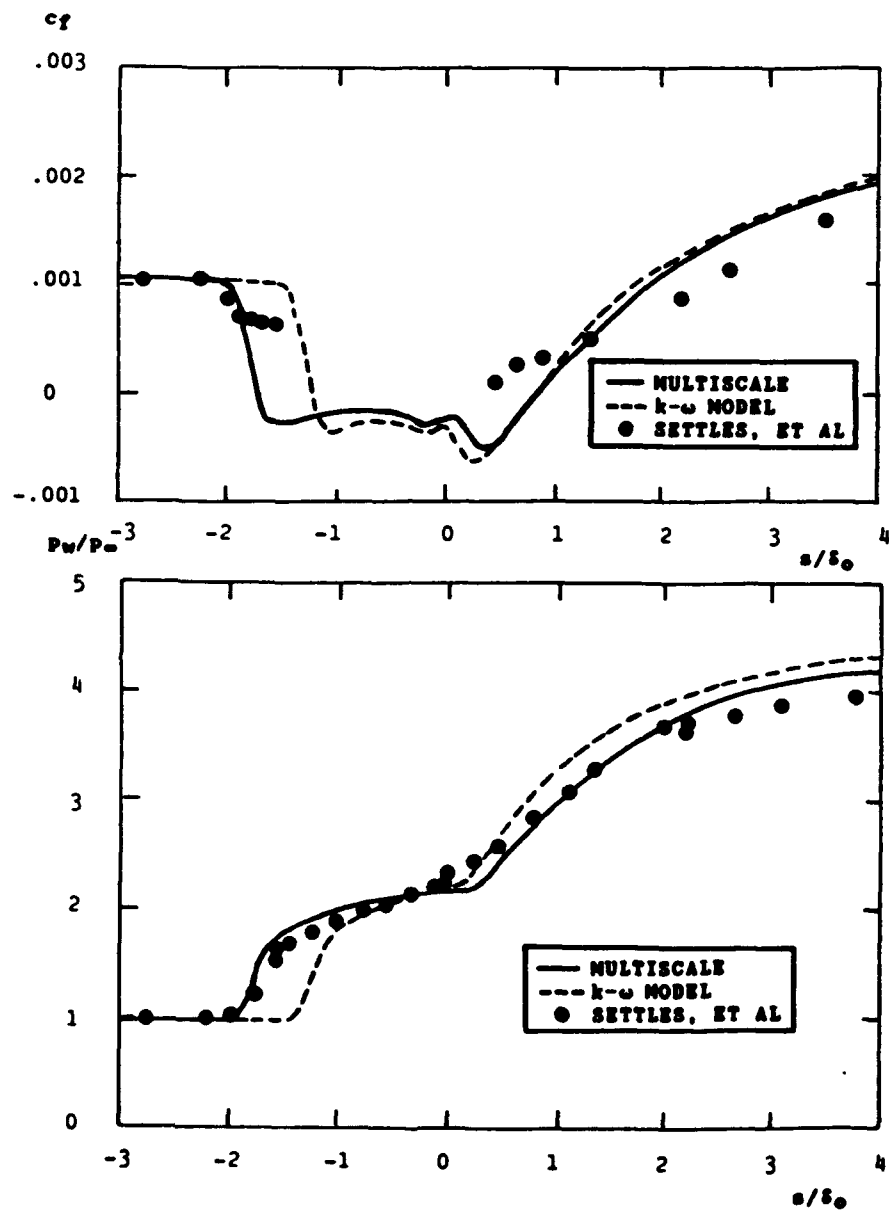
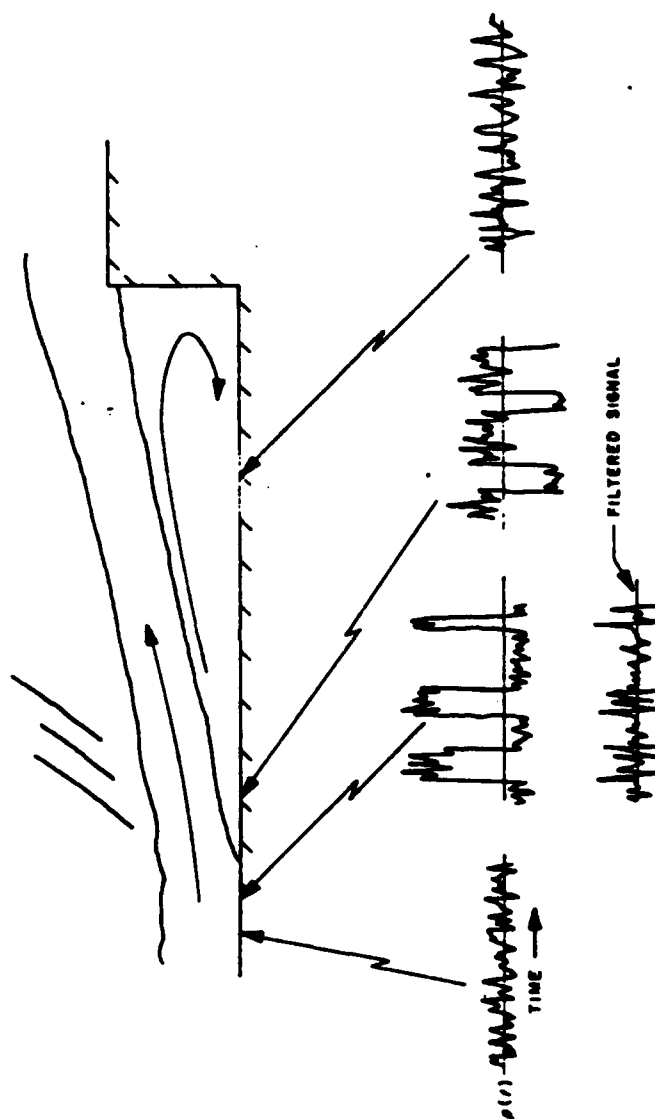
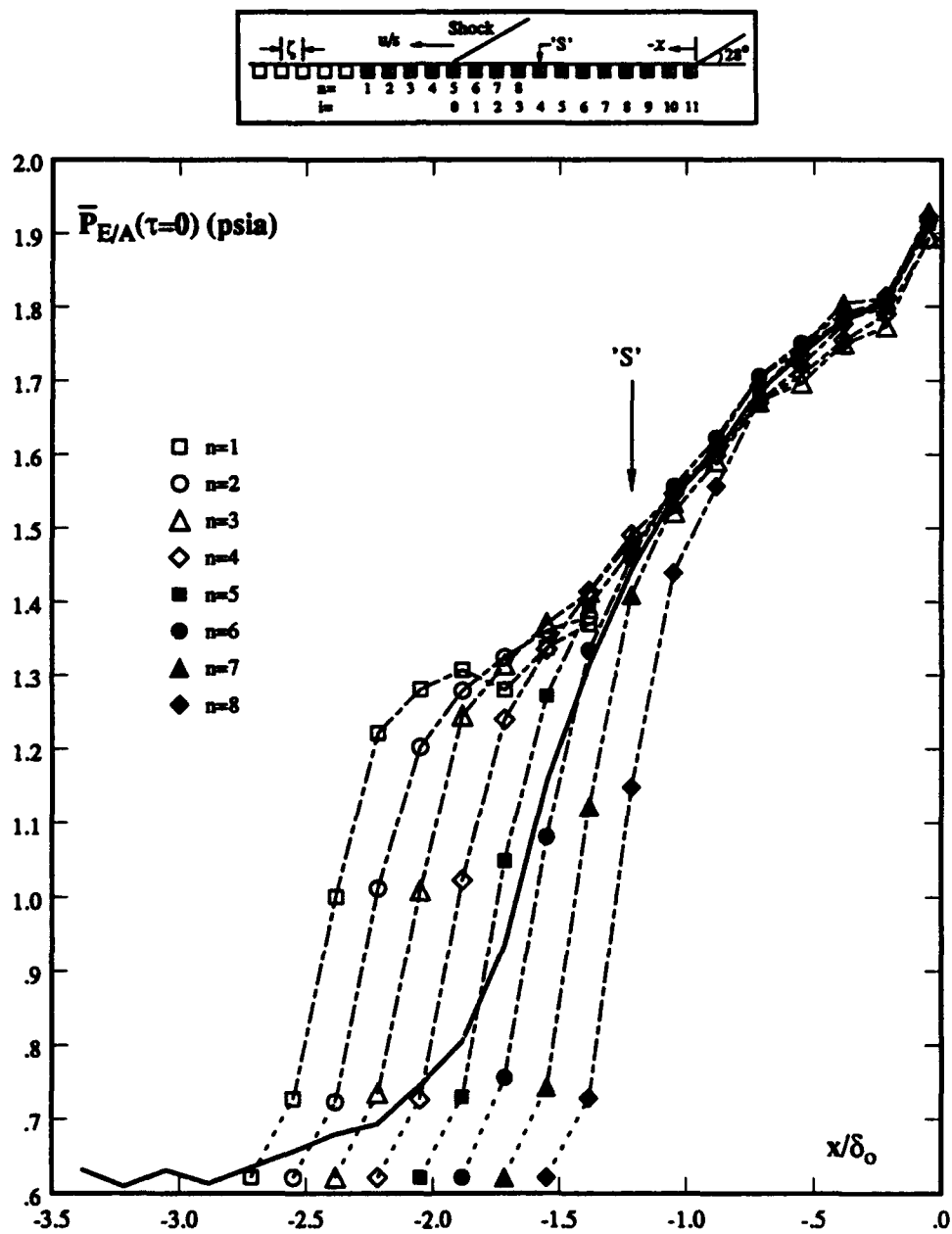


Fig. 2-4: Comparison of Computational and Experimental Surface Quantities in a Mach 3, 24° Compression Corner SWTBLI (Wilcox [1990])



**Fig. 2-5: Time-Varying Wall Pressure Signal
Upstream of a Supersonic Forward Facing Step
(Kistler [1964])**



**Fig. 2-6: Ensemble-averaged Pressure Distributions
(Erengil and Dolling [1991a])**

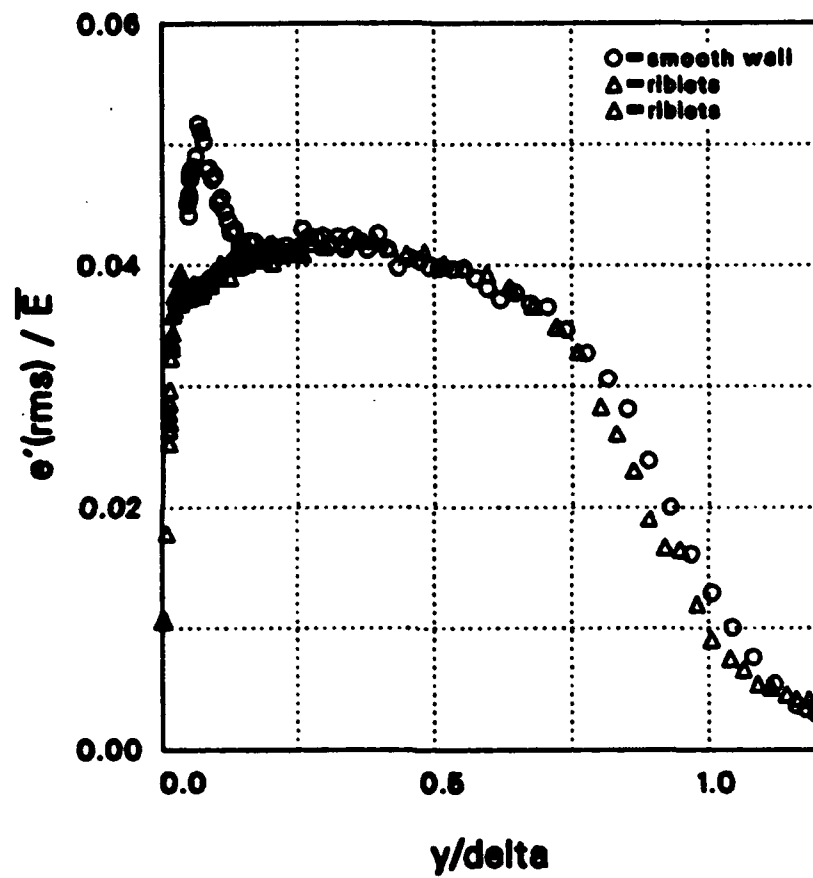


Fig. 2-7: Hot-wire RMS Voltage Profiles in a Mach 3 Turbulent Boundary Layer with and without Riblets (Robinson [1988])

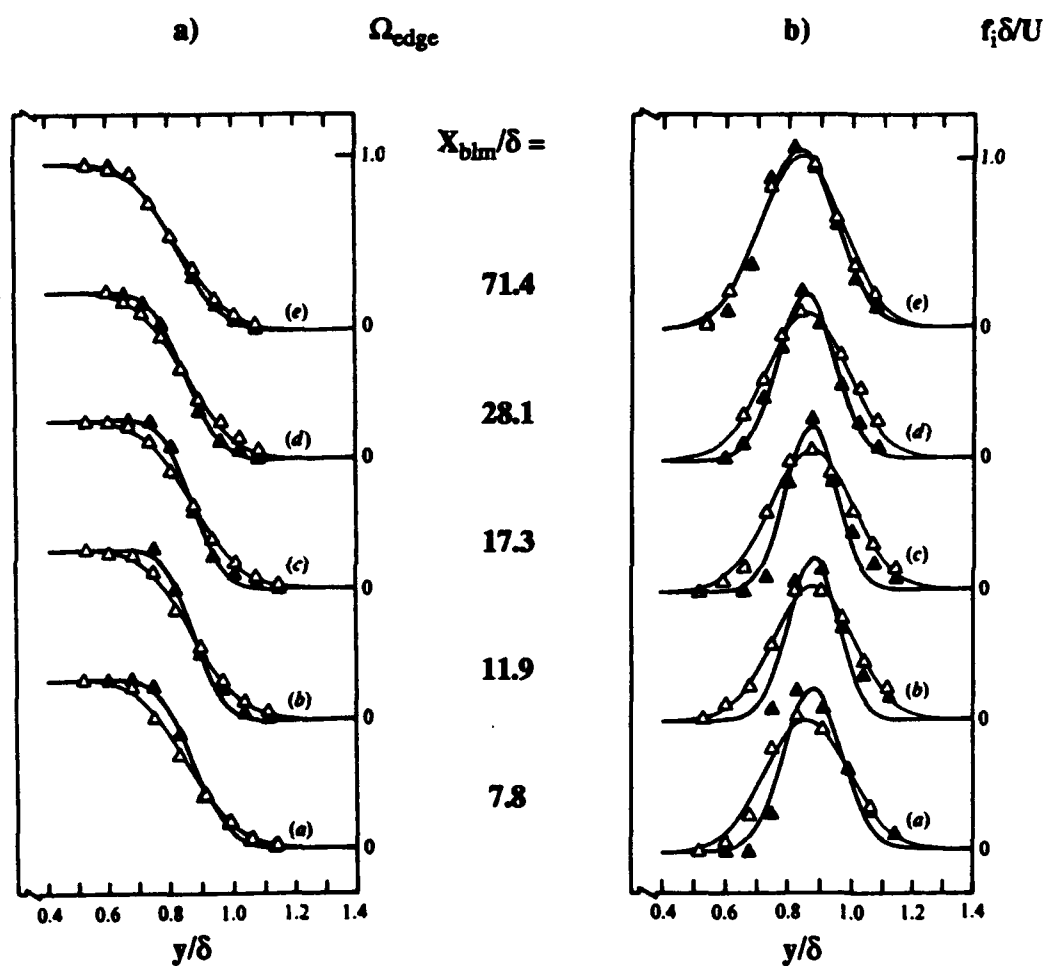


Fig. 2-8: Effect of Boundary Layer Manipulators on Freestream Interface in Incompressible Flow
a) Intermittency
b) Interface Crossing Frequency
 (Open symbols = undisturbed boundary layer)
 (Filled symbols = with manipulators)
 (Chang and Blackwelder [1990])

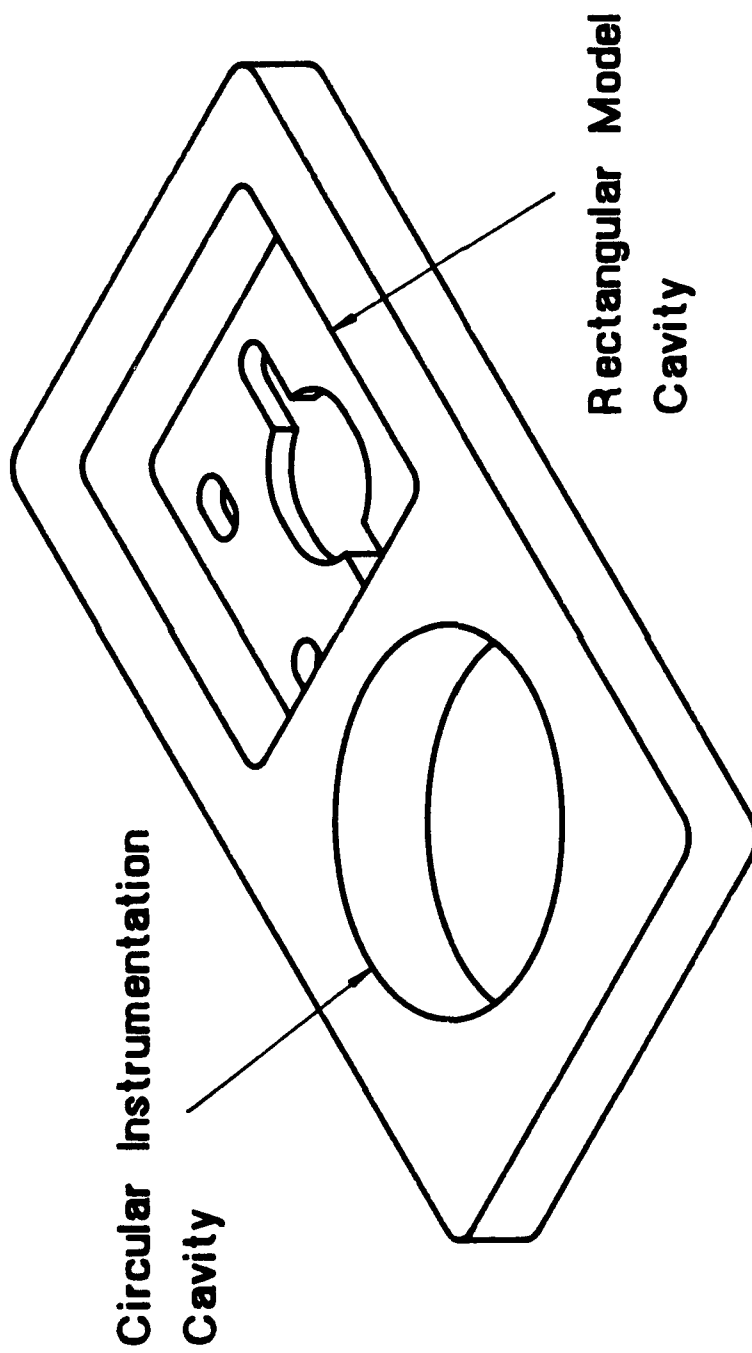
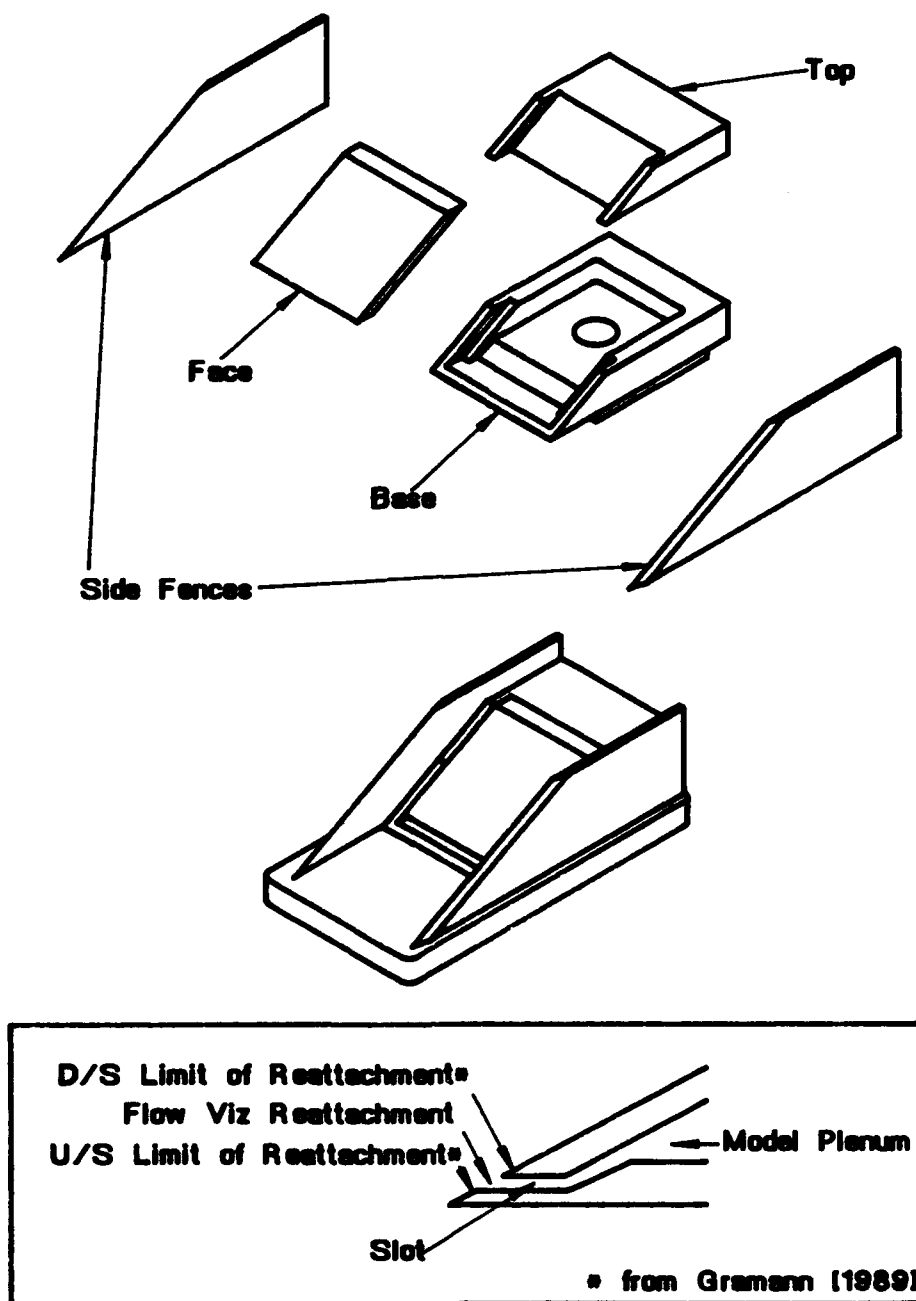


Fig. 3-1: Test Section Floor



**Fig. 3-2: 28-degree Compression
Corner Model**

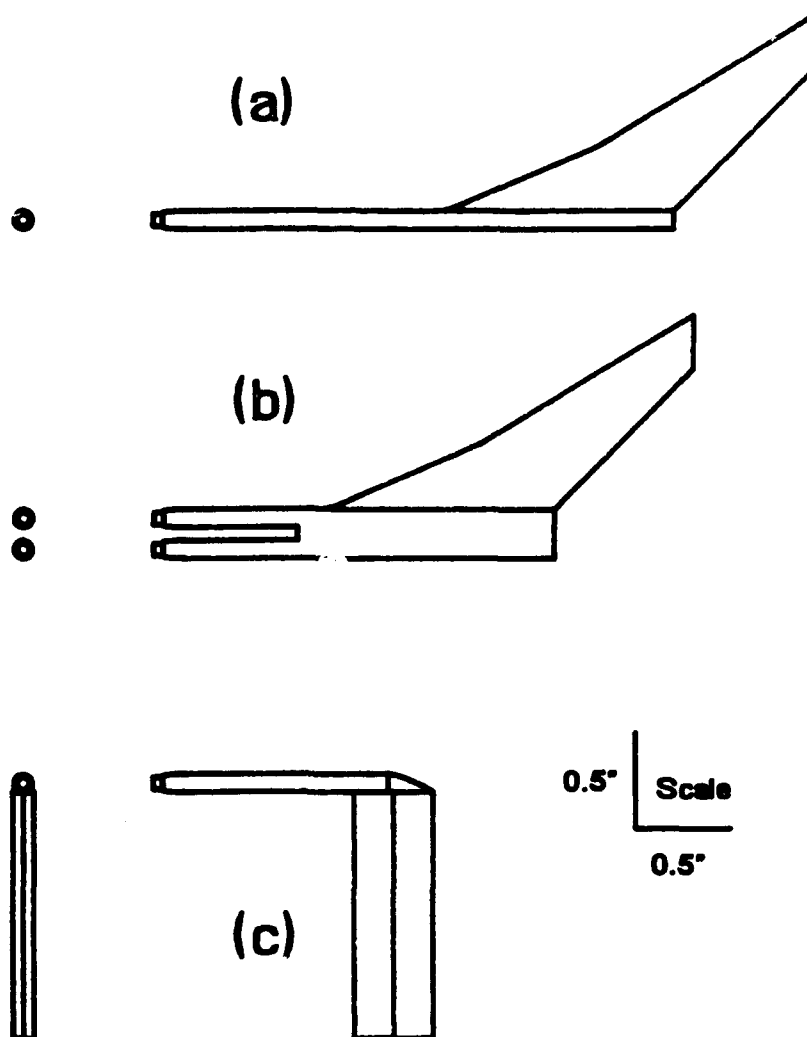


Fig. 3-3: Fluctuating Pitot Probes
(a) Single Ceiling Probe
(b) Double Ceiling Probe
(c) Single Floor Probe

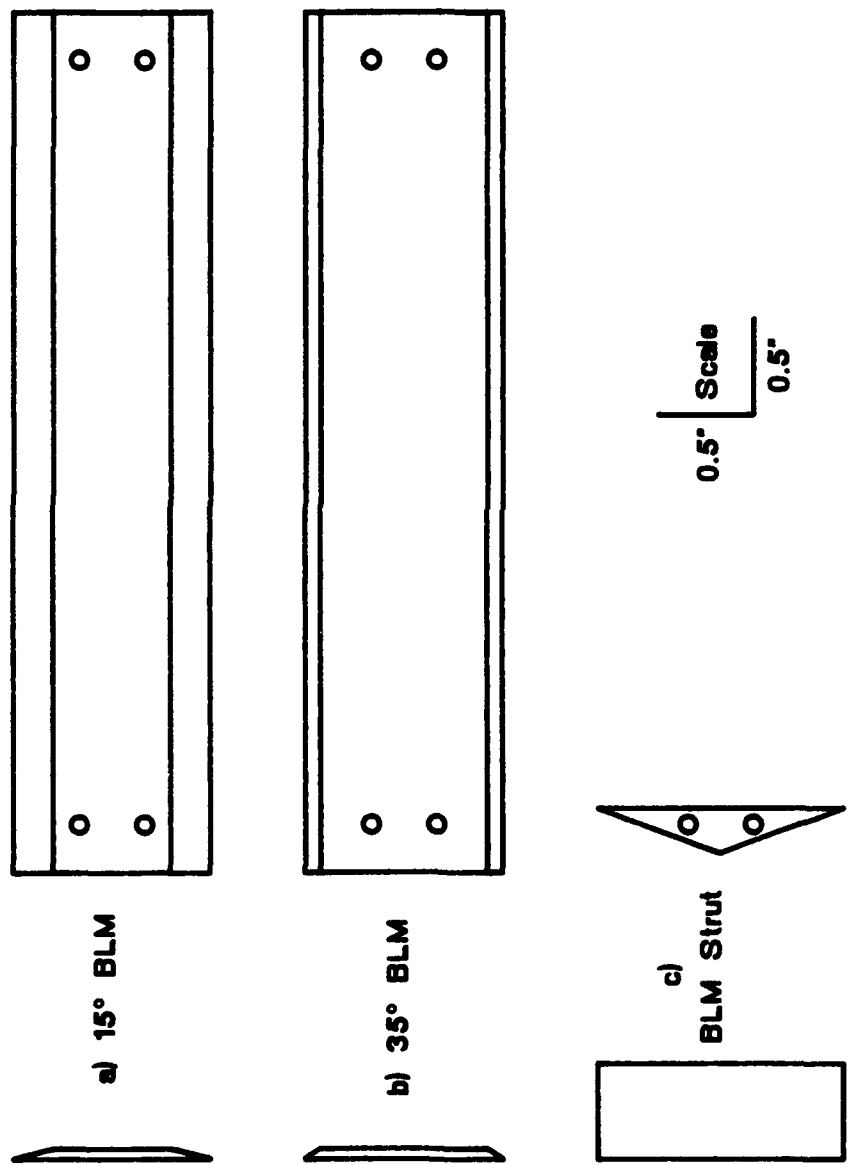
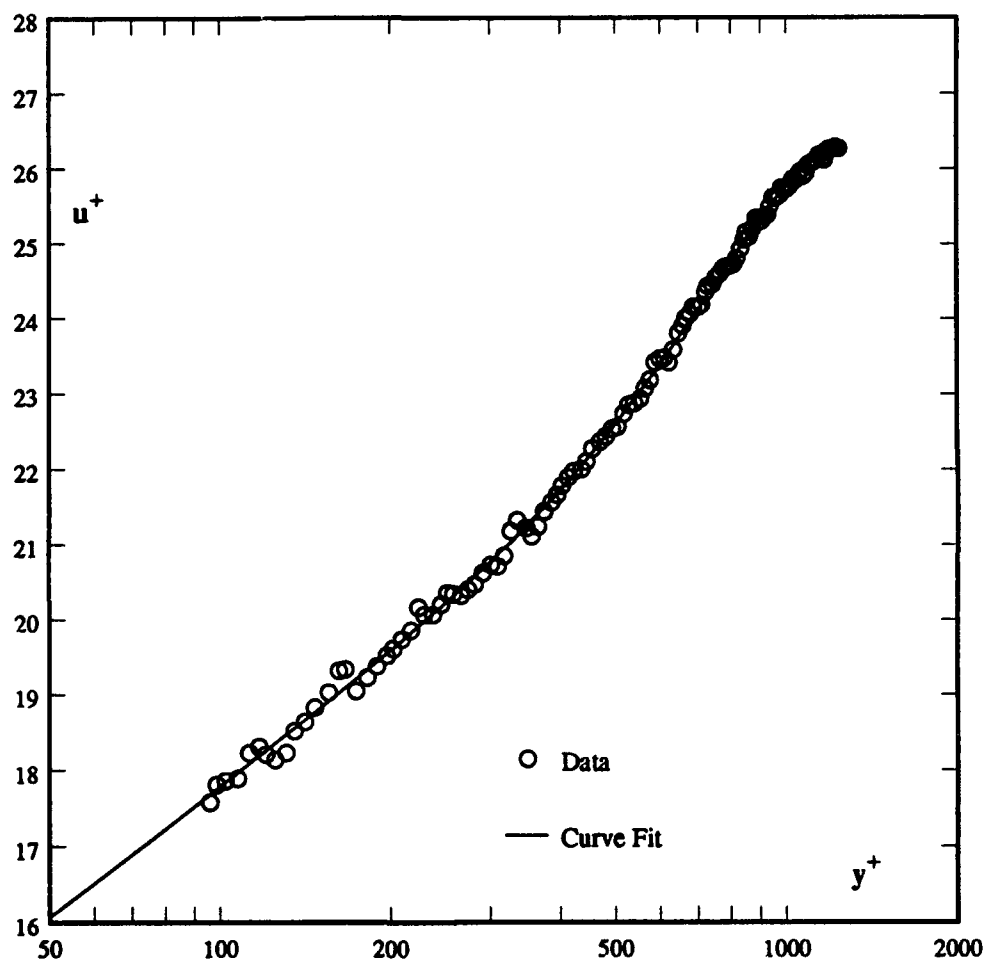


Fig. 3-4: Boundary Layer Manipulators and Struts



**Fig. 3-5: Incoming Boundary Layer Velocity Profile
Fit to Law of the Wall/Law of the Wake**

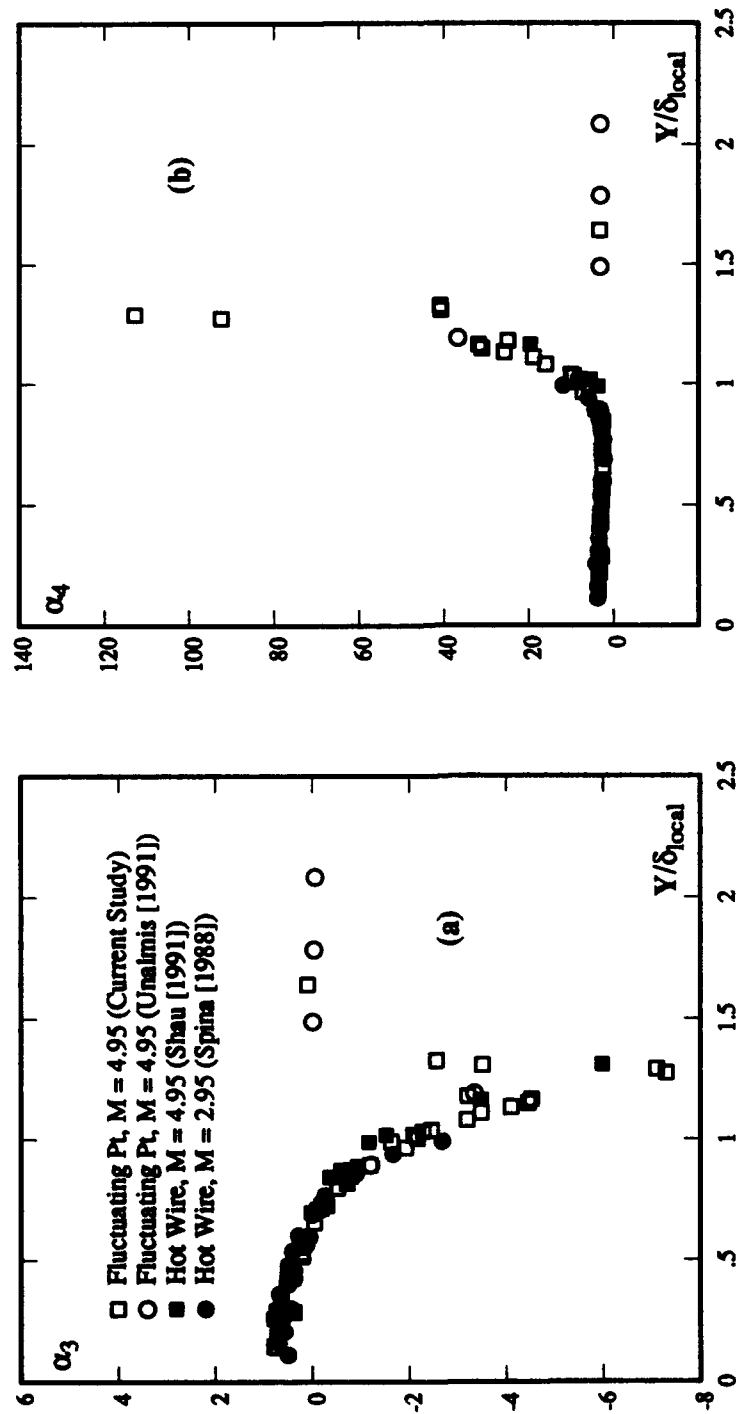


Fig. 3-6: Comparison of Fluctuating Pitot Pressure and Mass Flux Measurements in the Undisturbed Boundary Layer
 a) Skewness Coefficient
 b) Flatness Coefficient

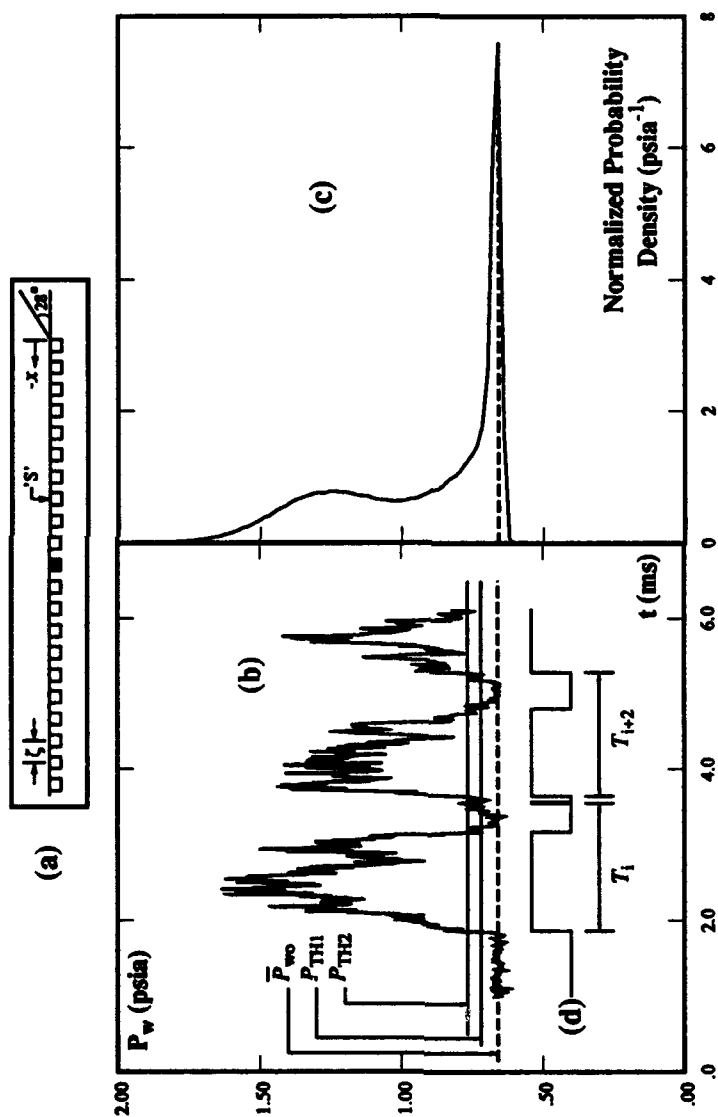


Fig. 4-1: Boxcar Conversion Technique

- (a) Schematic showing transducer position
- (b) One record of wall pressure data within intermittent region
- (c) Wall pressure PDD of 512 records (of which (b) is one)
- (d) Resulting box-car signal for (b)

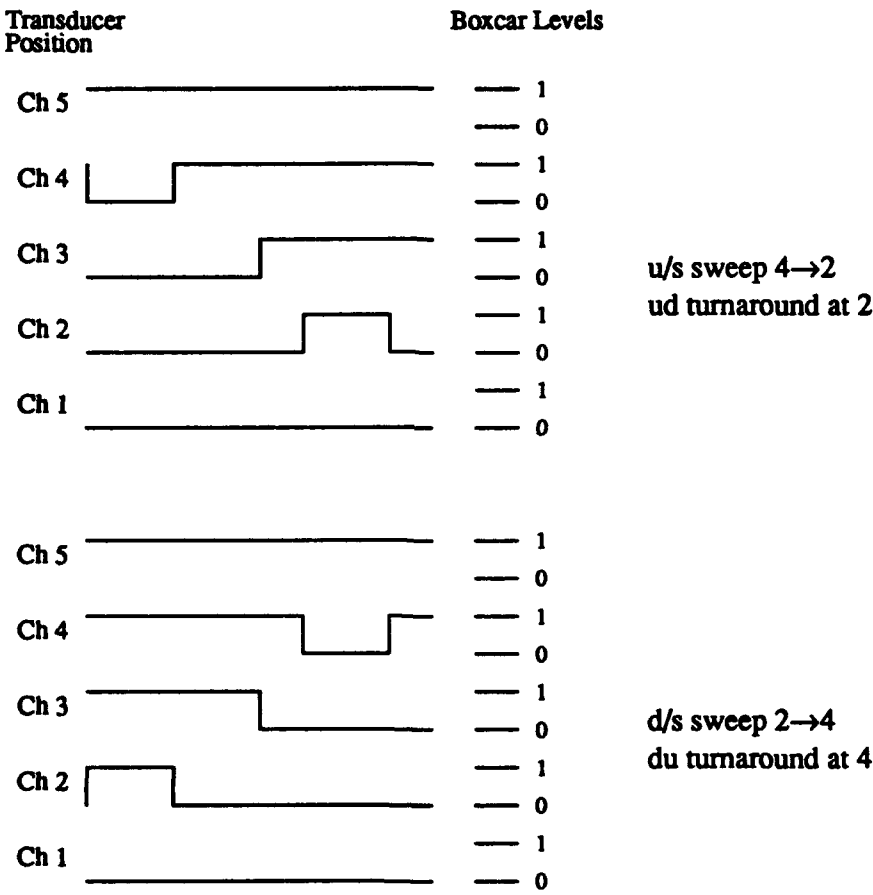
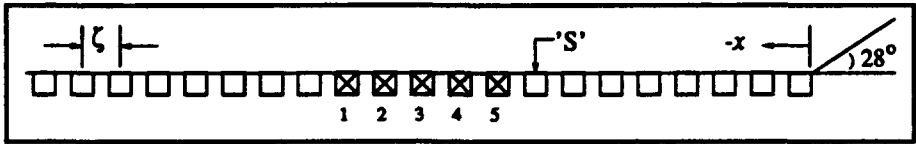


Fig. 4-2: Shock Motion from Boxcar Signal

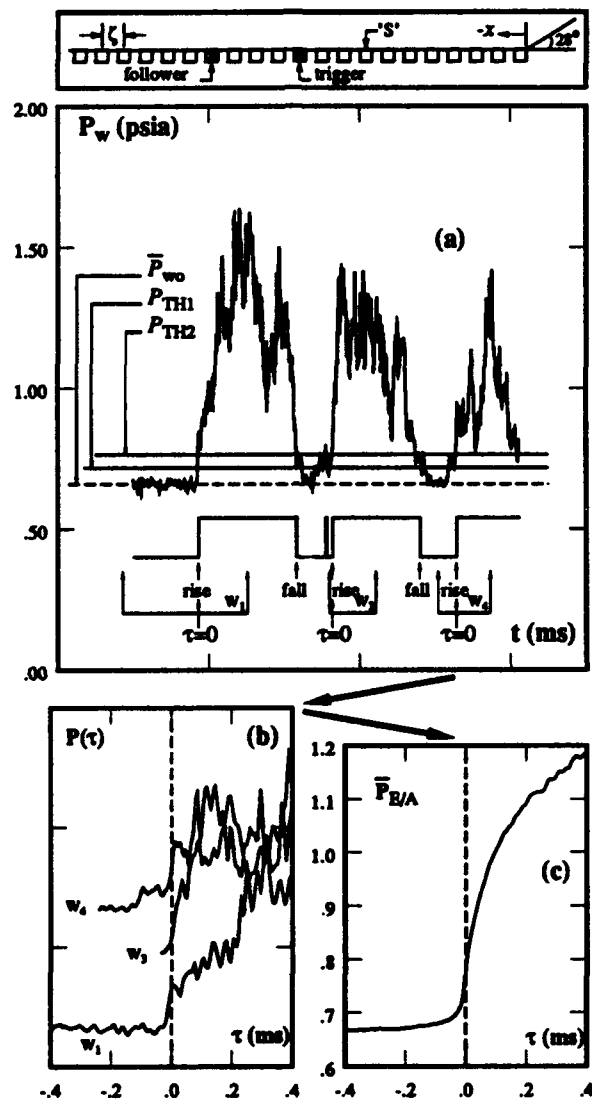


Fig. 4-3 Variable-window ensemble averaging:
(a) Wall Pressure Signal (Trigger channel) [1 record]
(b) Individual Ensembles (Trigger channel) [from (a)]
(c) Ensemble-Average Signal (Trigger channel)
[from entire data set]

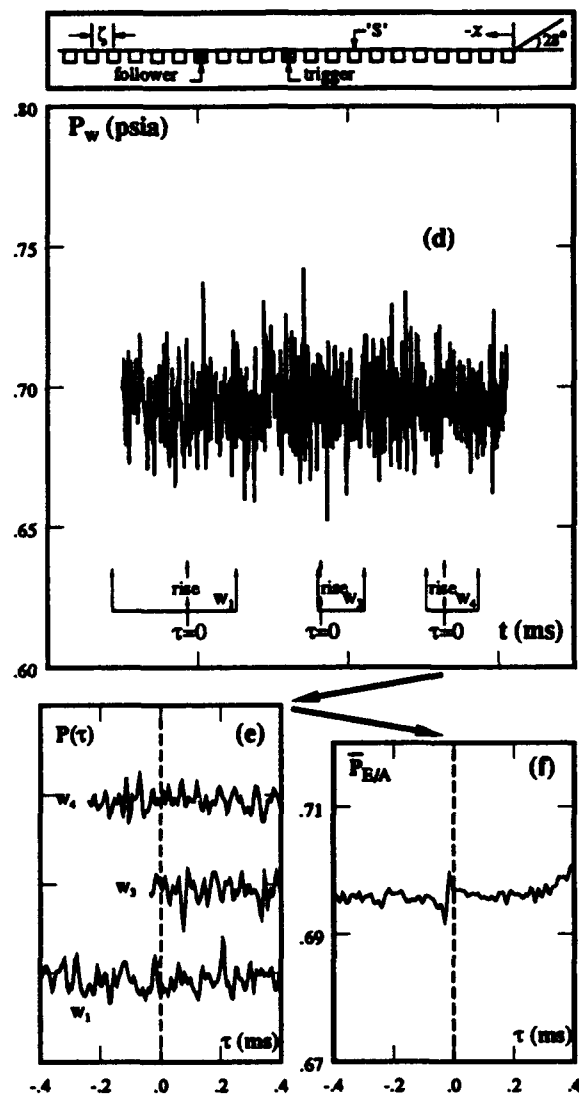


Fig. 4-3 Variable-window ensemble averaging (concluded):
 (d) Wall Pressure Signal (Follower channel) [1 record]
 (e) Individual Ensembles (Follower channel) [from (d)]
 (f) Ensemble-Average Signal (Follower channel)
 [from entire data set]

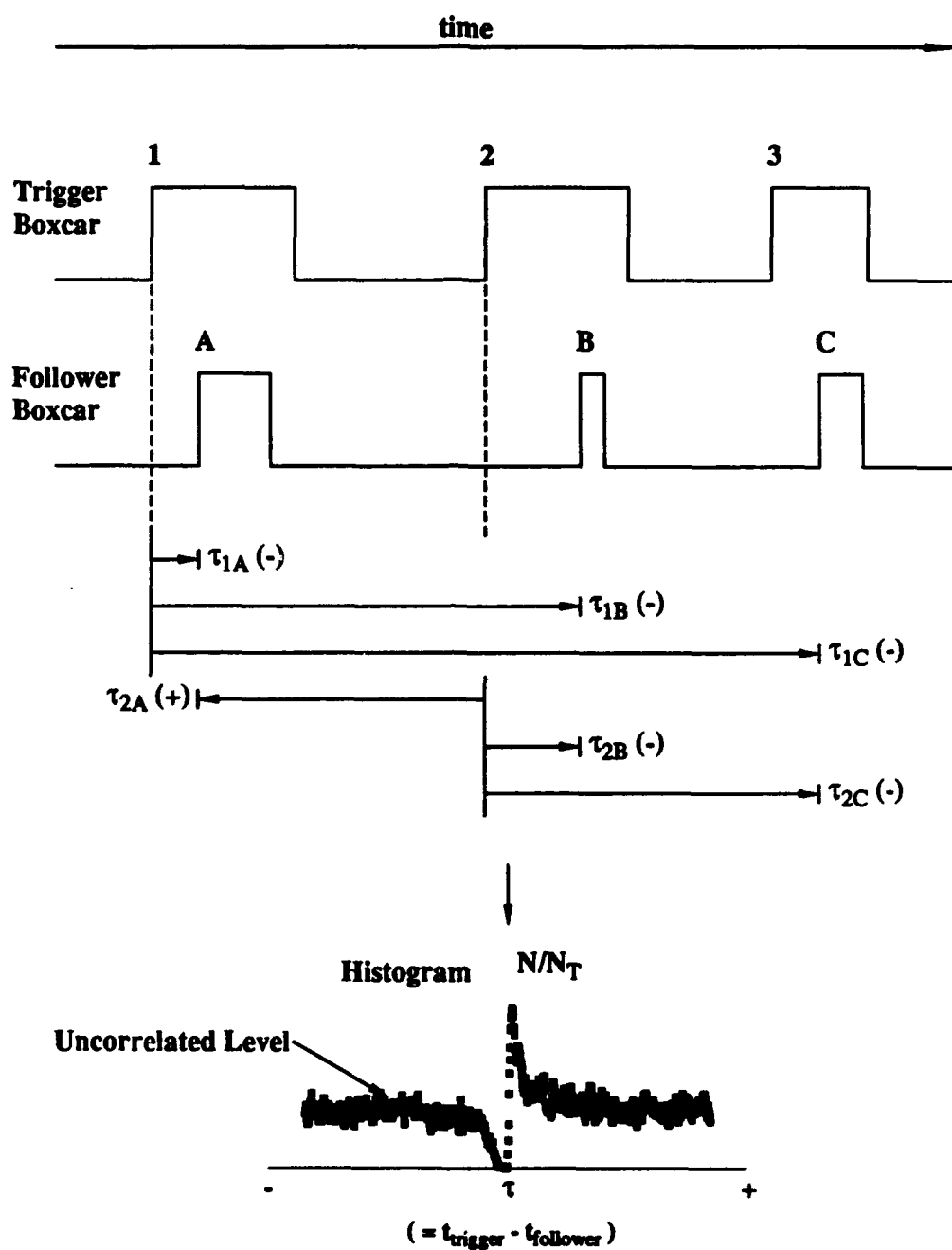


Fig. 4-4: Development of Event Relative Timing Analysis (ERTA) Histogram for a Rise-Rise Event Edge Pair

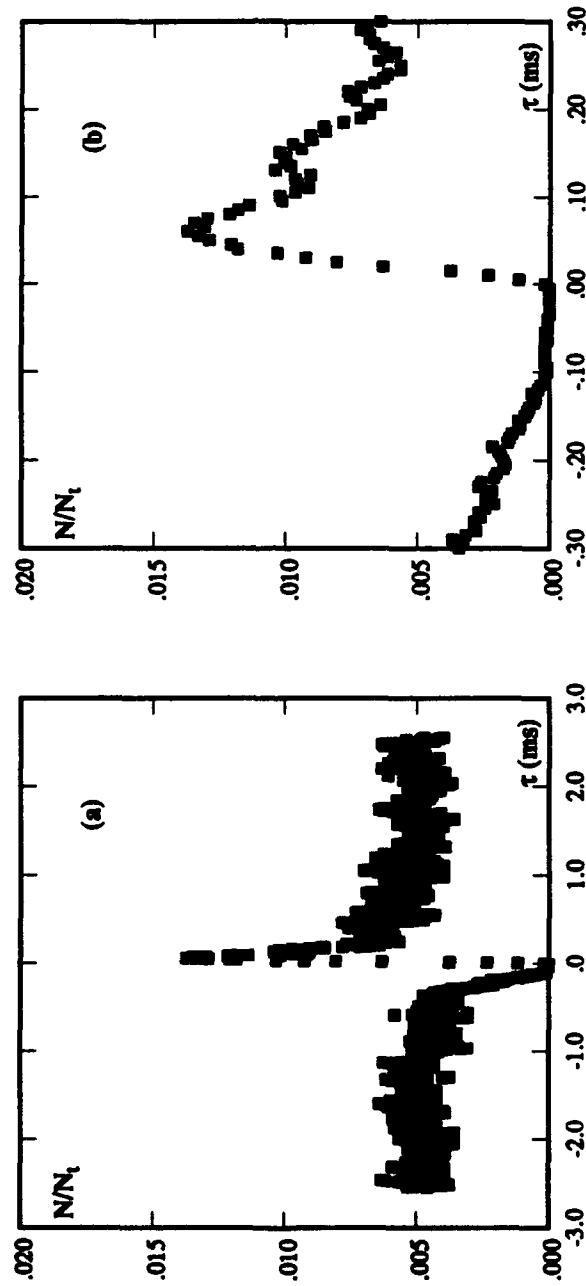


Fig. 4-5: Example of ERTA Applied to Separation Shock Motion:
Event Pair = Rise-Rise (Upstream Sweep)
 (a) Wide Observation Window
 (b) Focussed Observation Window

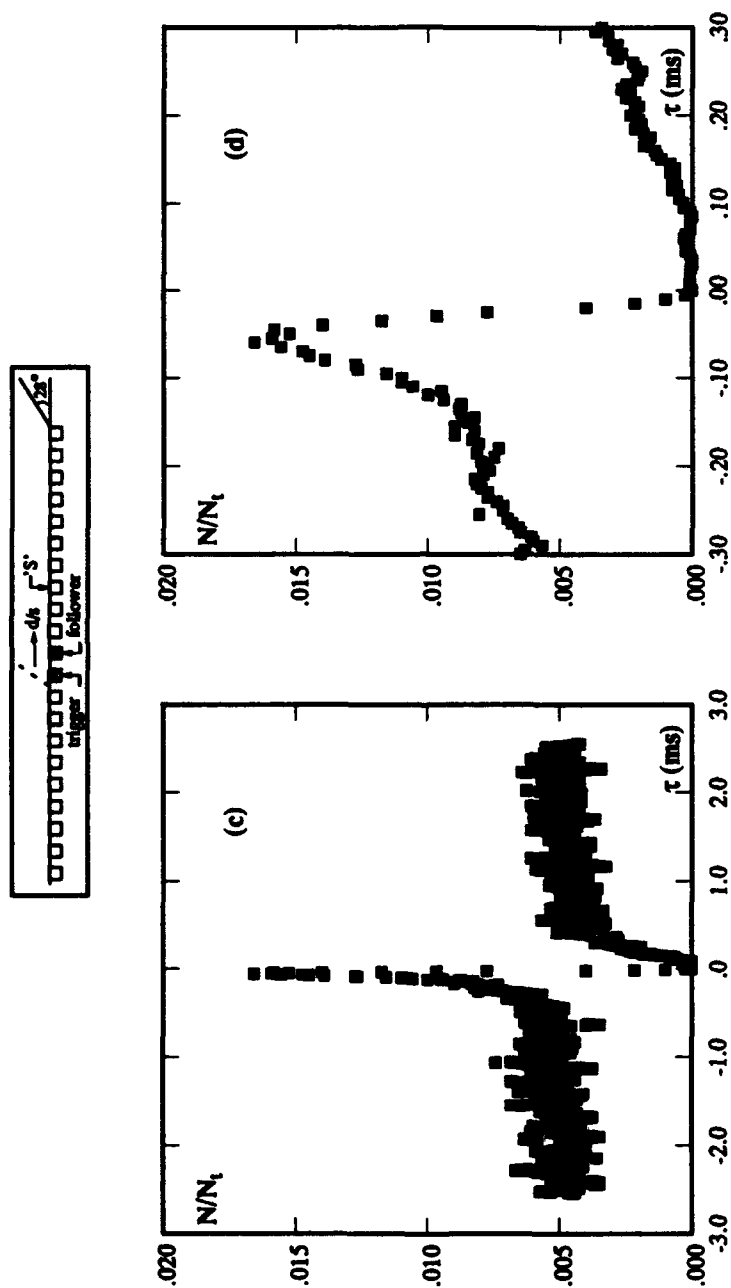


Fig. 4-5: Example of ERTA Applied to Separation Shock Motion (concluded):

Event Pair = Fall-Fall (Downstream Sweep)

(c) Wide Observation Window

(d) Focused Observation Window

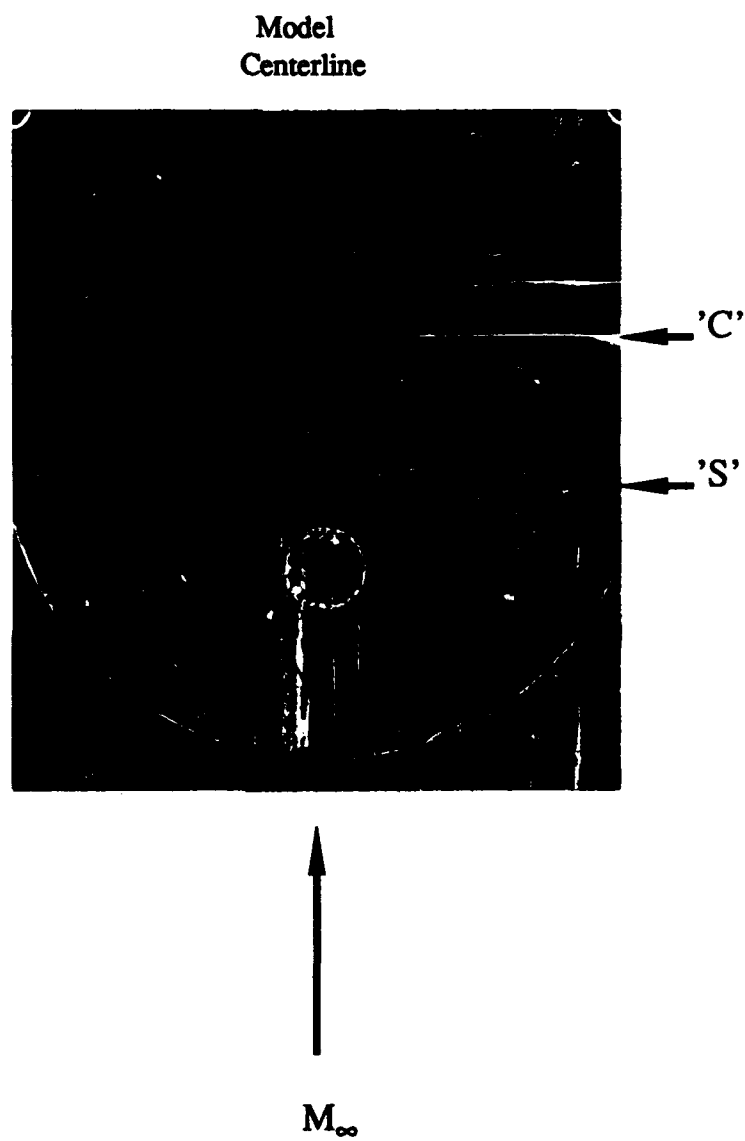
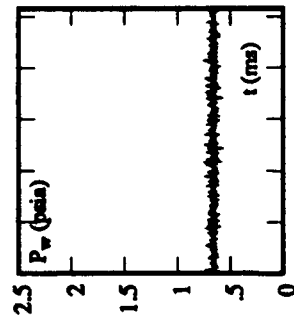
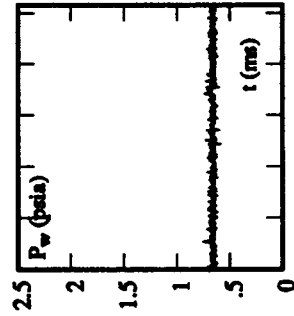


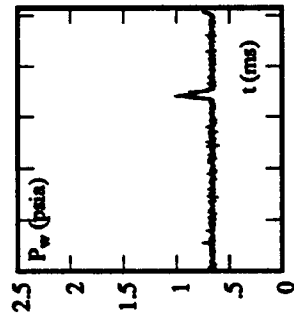
Fig. 5-1: Surface Flow Visualization of Baseline Interaction Using Kerosene-Lampblack Technique



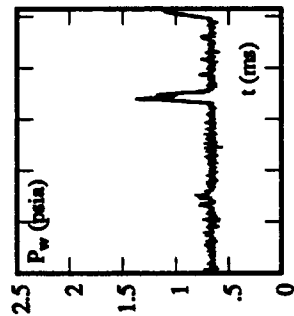
a) $X/\delta_1 = -2.51$



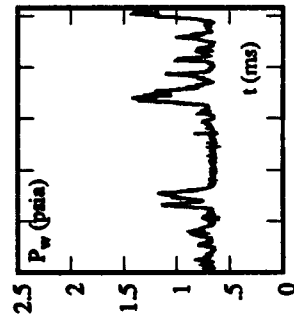
b) $X/\delta_1 = -2.35$



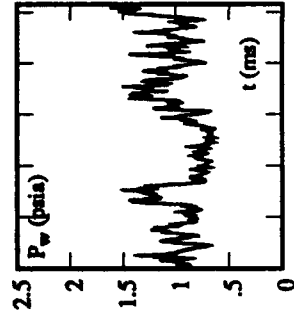
c) $X/\delta_1 = -2.19$



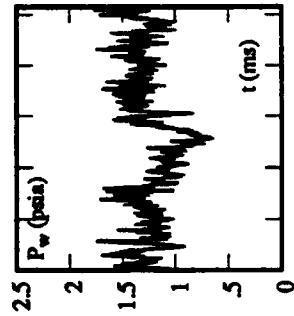
d) $X/\delta_1 = -2.02$



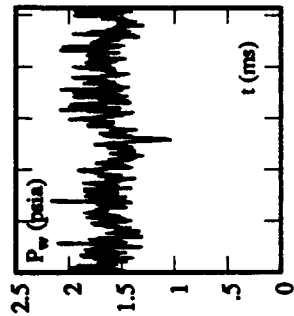
e) $X/\delta_1 = -1.86$



f) $X/\delta_1 = -1.69$



g) $X/\delta_1 = -1.53$



h) $X/\delta_1 = -1.36$

Fig. 5-2: Surface Pressure Signals Beneath the Translating Separation Shock (1-record / 1024 data points)

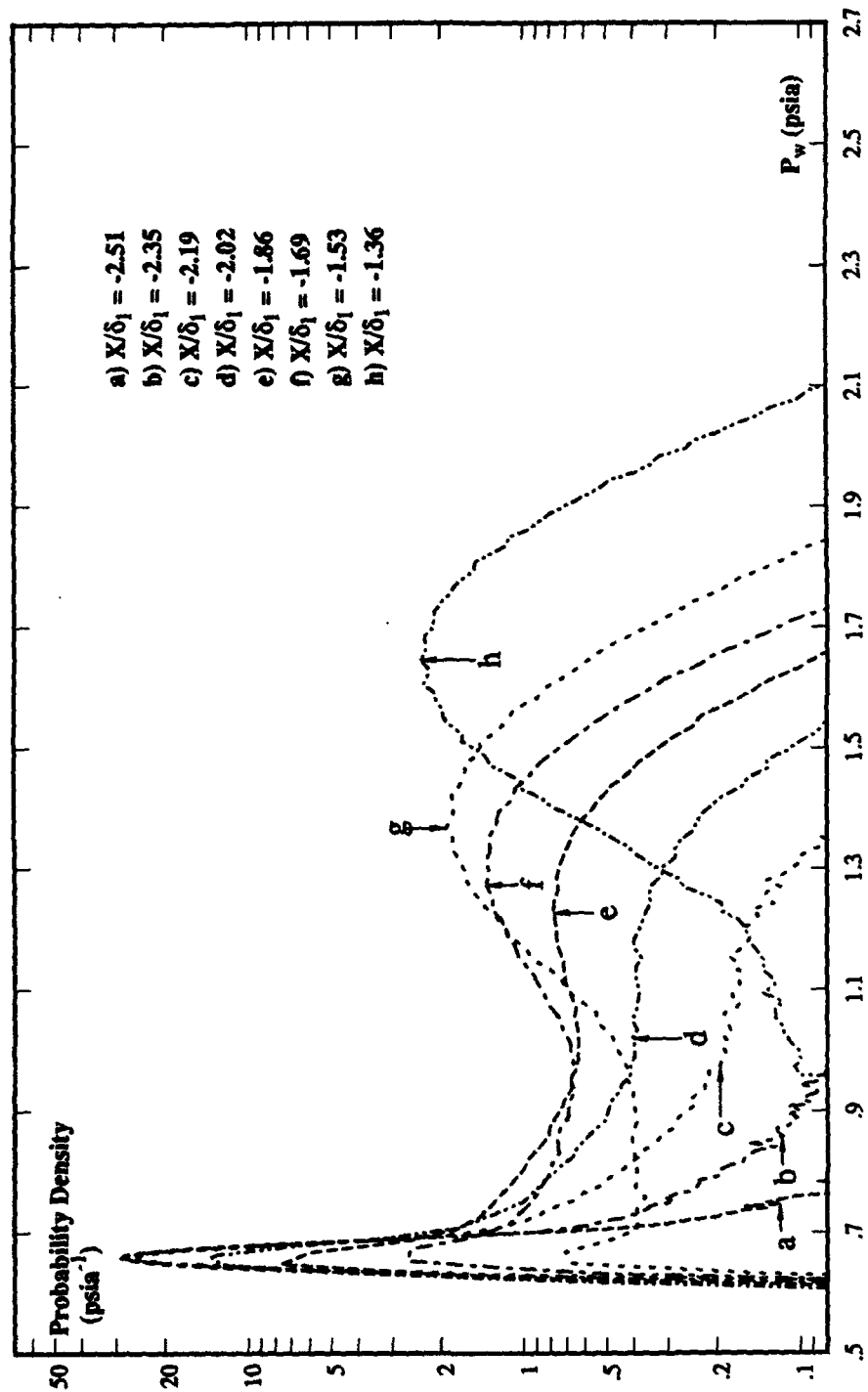


Fig. 5-3: Surface Pressure PDD's Upstream of the Corner

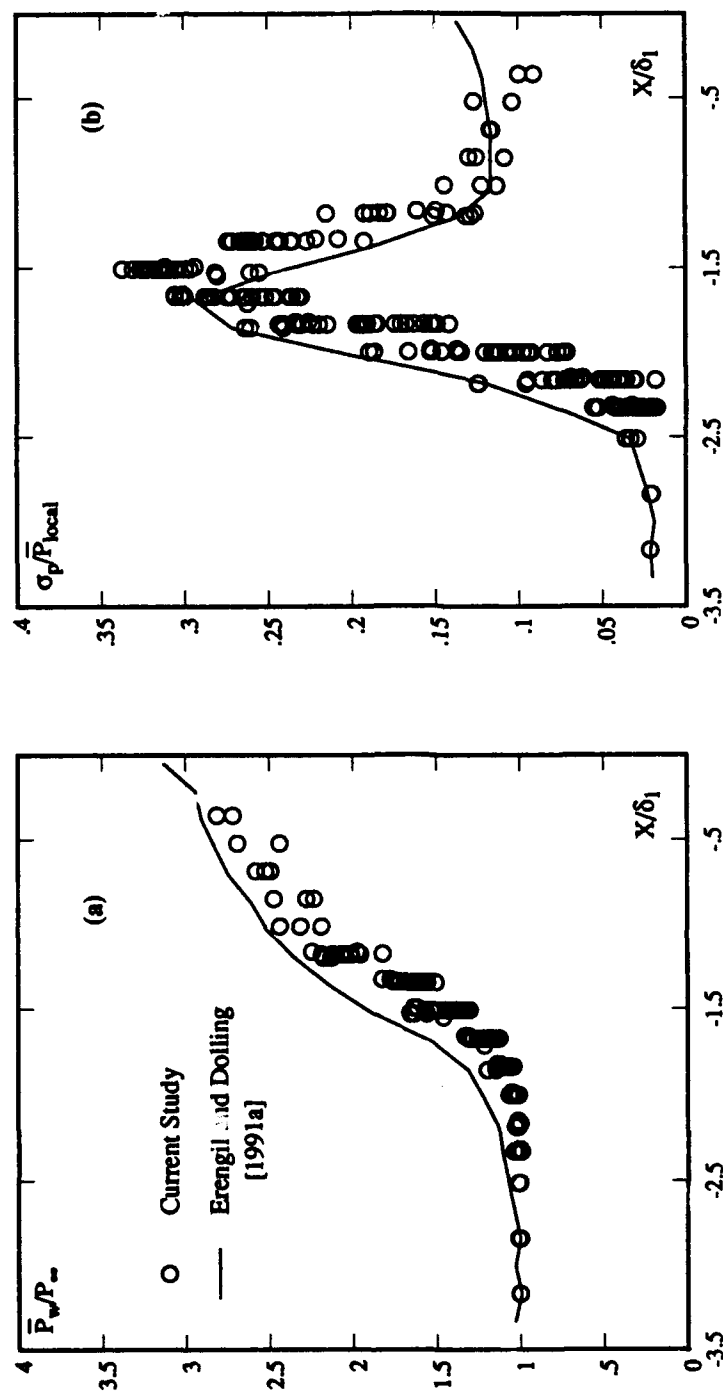


Fig. 5-4: Streamwise Surface Distributions
 a) Normalized Mean Surface Pressure
 b) Normalized Surface Pressure RMS

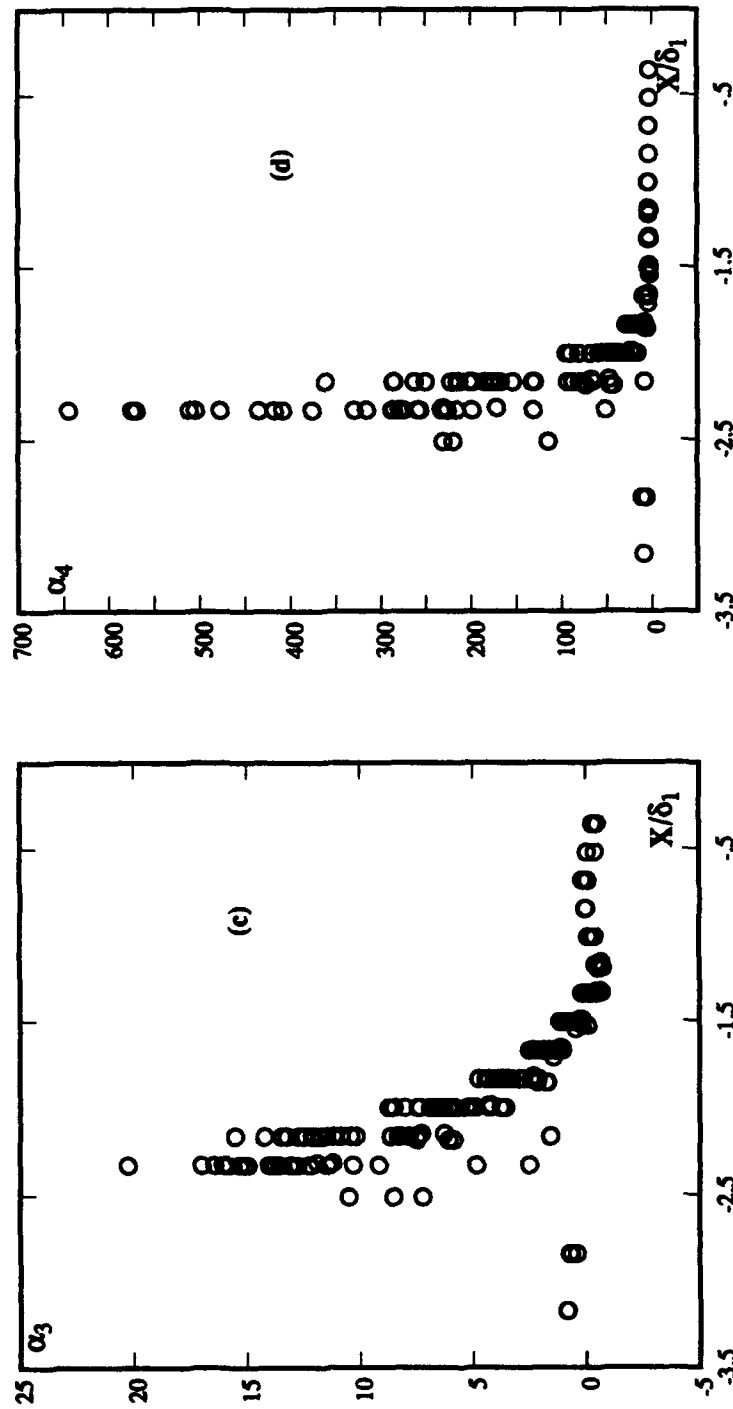


Fig. 5-4: Streamwise Surface Distributions (concluded)

c) Skewness Coefficient

d) Flatness Coefficient

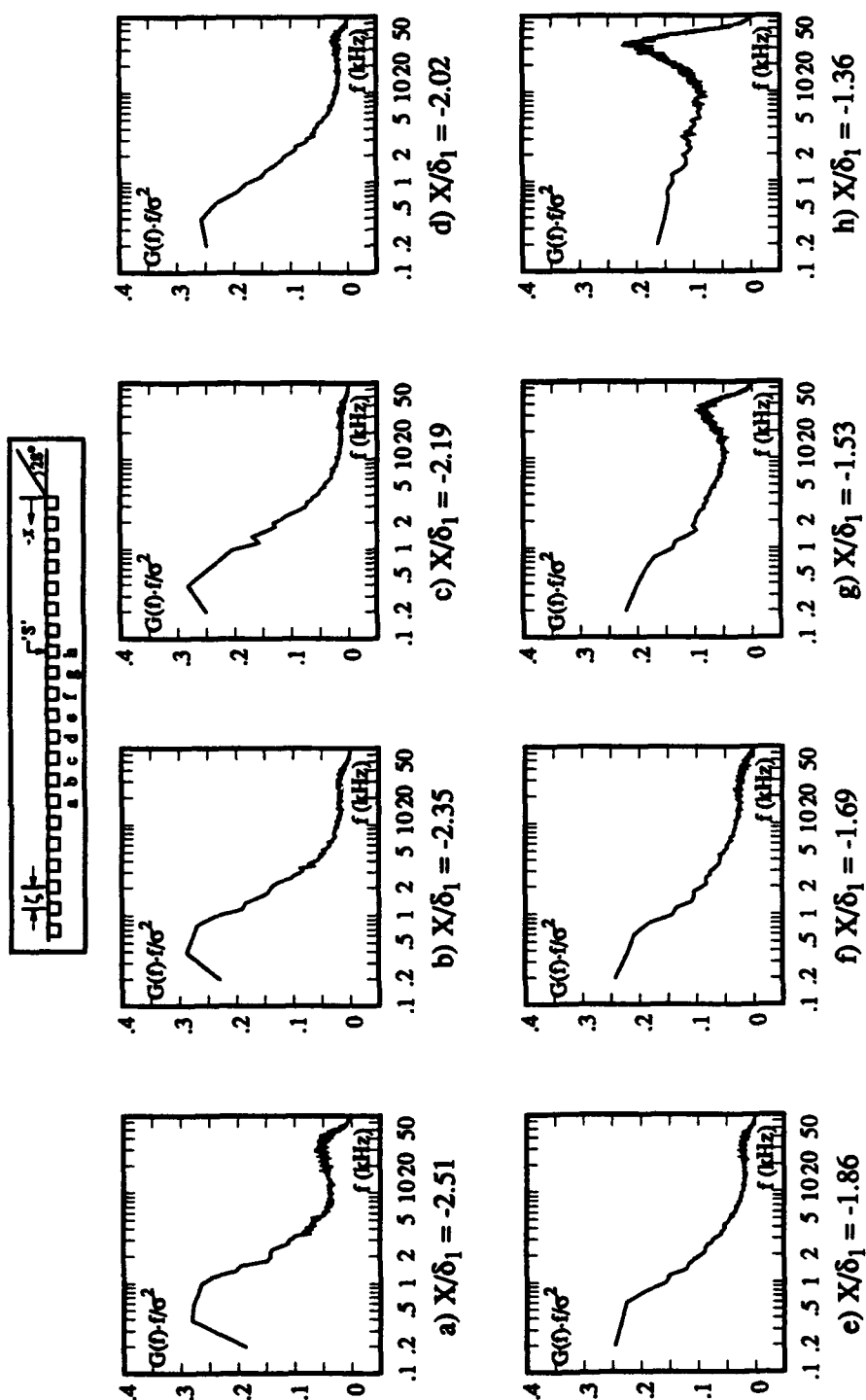


Fig. 5-5: Surface Pressure Power Spectra Beneath the Translating Separation Shock (Sampling Frequency = 200 kHz)

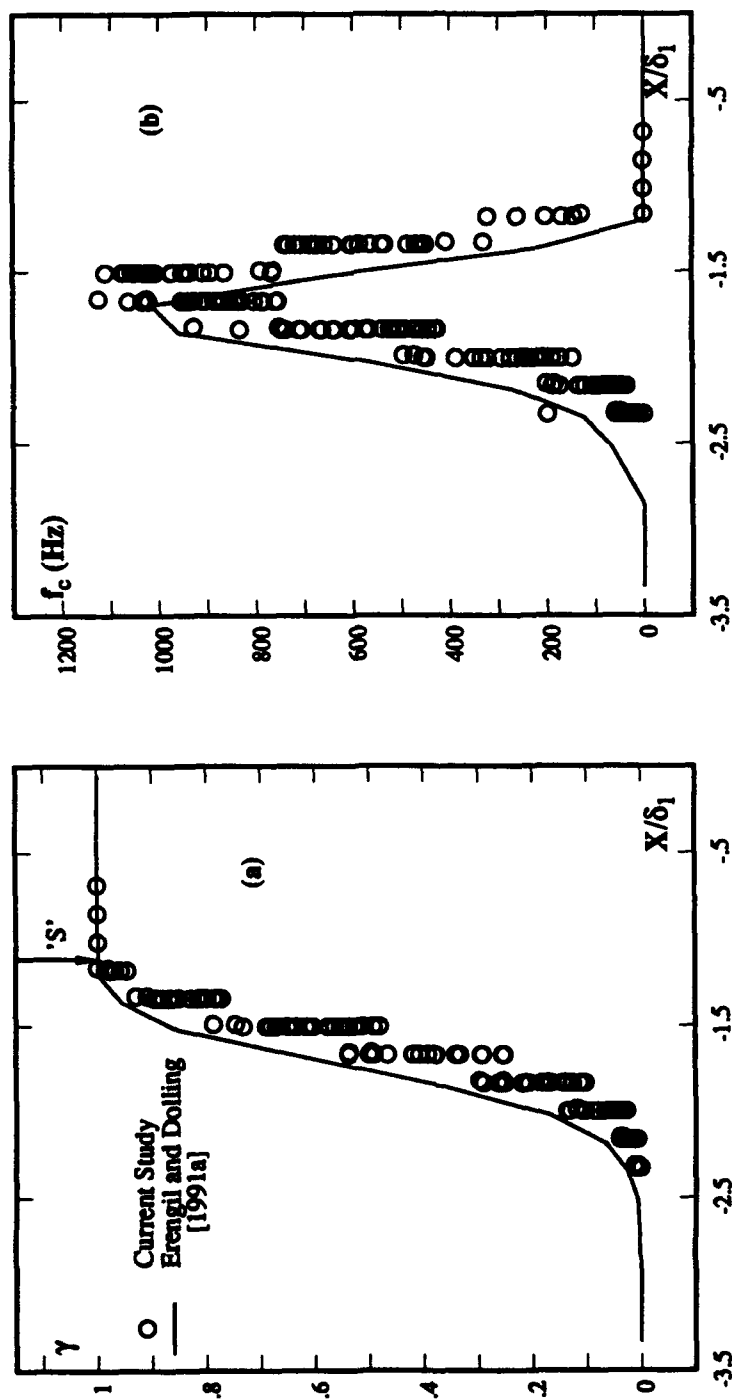


Fig. 5-6: Separation Shock Streamwise Distributions
 a) Intermittency
 b) Zero-Crossing Frequency

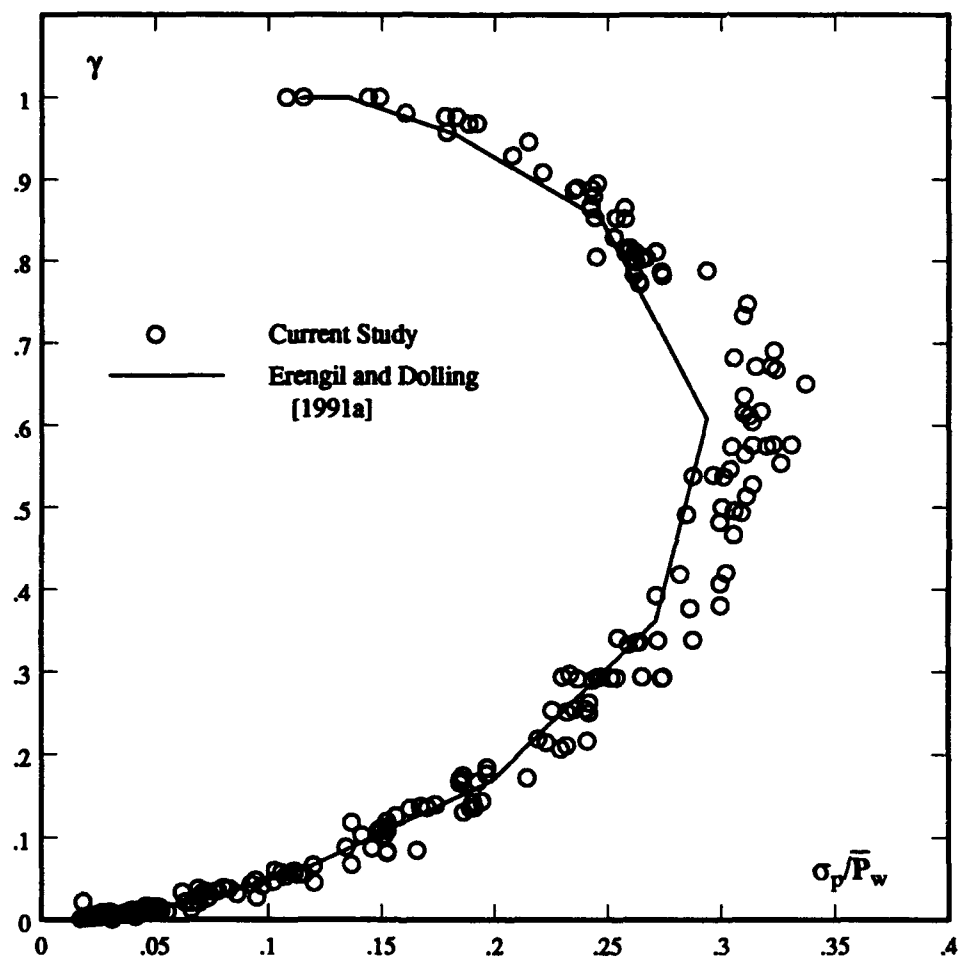


Fig. 5-7: Comparison of Surface Pressure RMS and Separation Shock Intermittency

Trigger Condition: 3-channel Upstream Sweep

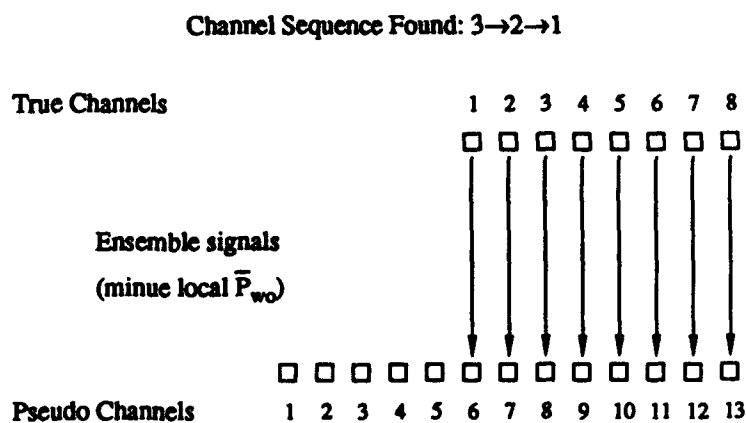
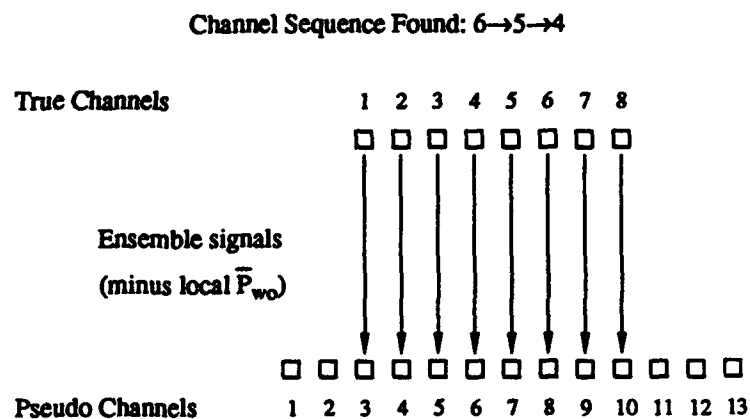


Fig. 5-8: Example of Pseudo-Channel Mapping of Surface Pressure Signals for Ensemble-Averaging

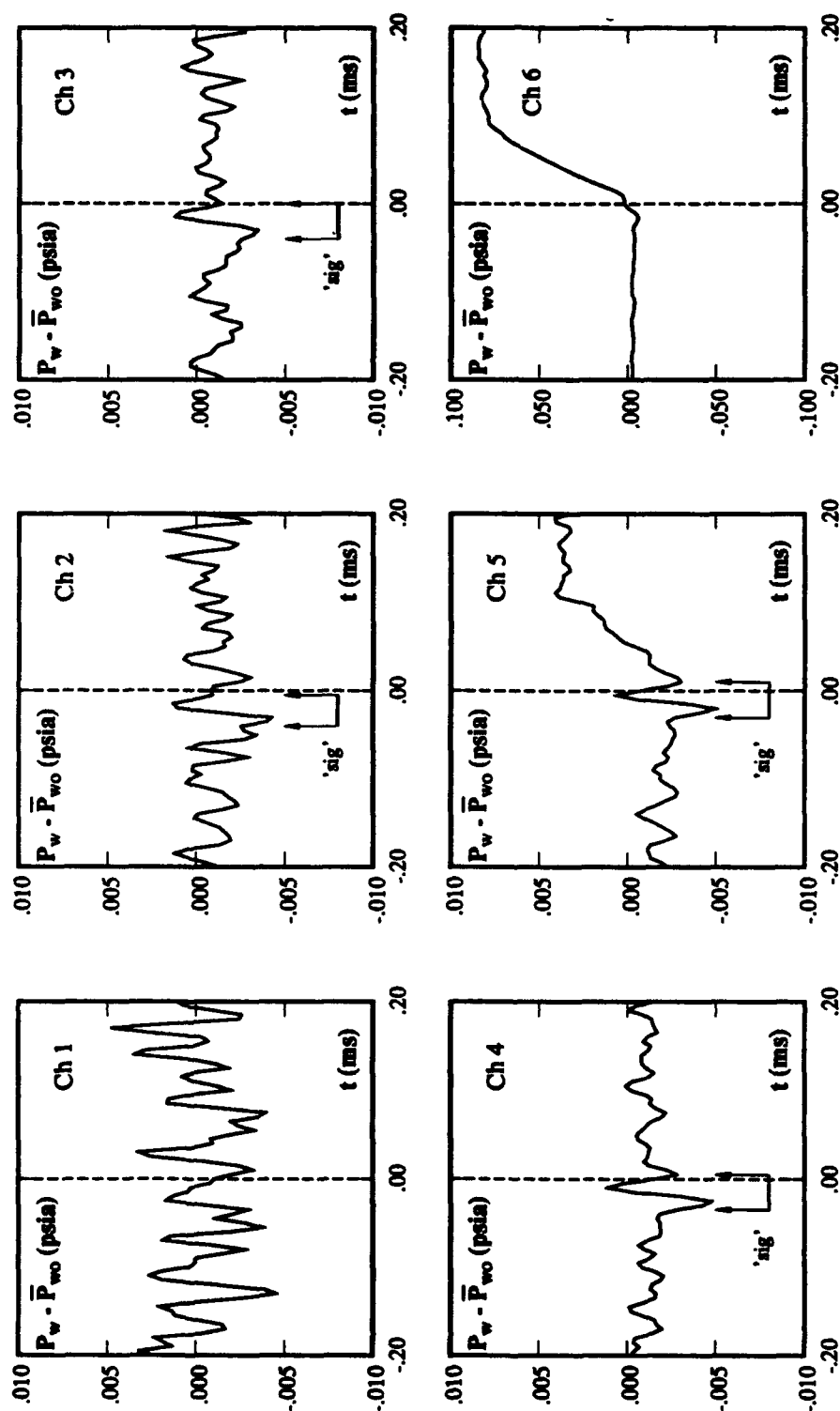


Fig. 5-9: Pseudo-Channel Ensemble-Averaged Surface Pressure Time Histories for a 3-Channel Upstream Sweep (Sweep Channels 8 \rightarrow 7 \rightarrow 6; Trigger on Channel 7)
a) Upstream of the Separation Shock

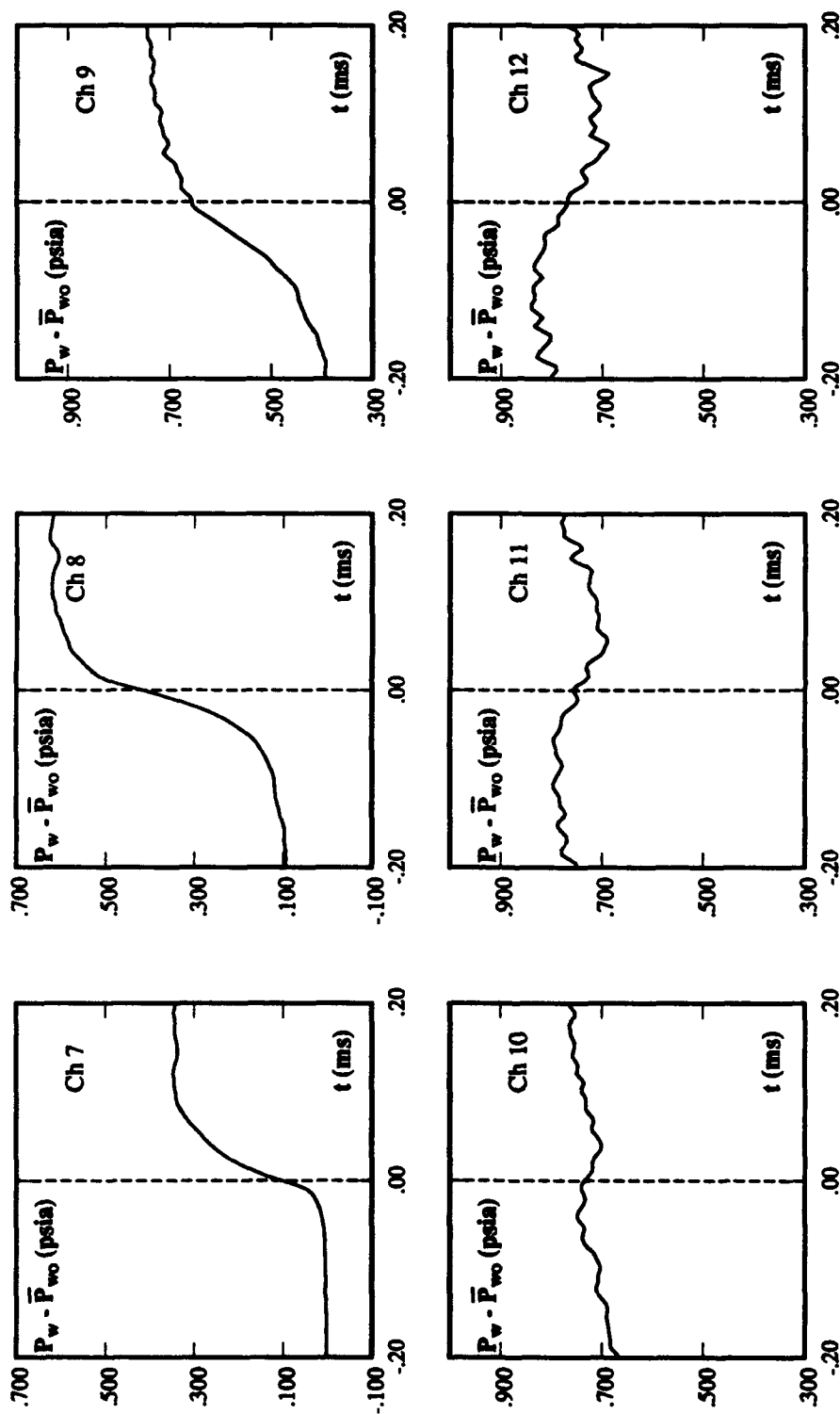


Fig. 5-9: Pseudo-Channel Ensemble-Averaged Surface (concluded)
Pressure Time Histories for a 3-Channel Upstream Sweep
(Sweep Channels 8 \rightarrow 7 \rightarrow 6; Trigger on Channel 7)
b) Downstream of the Separation Shock

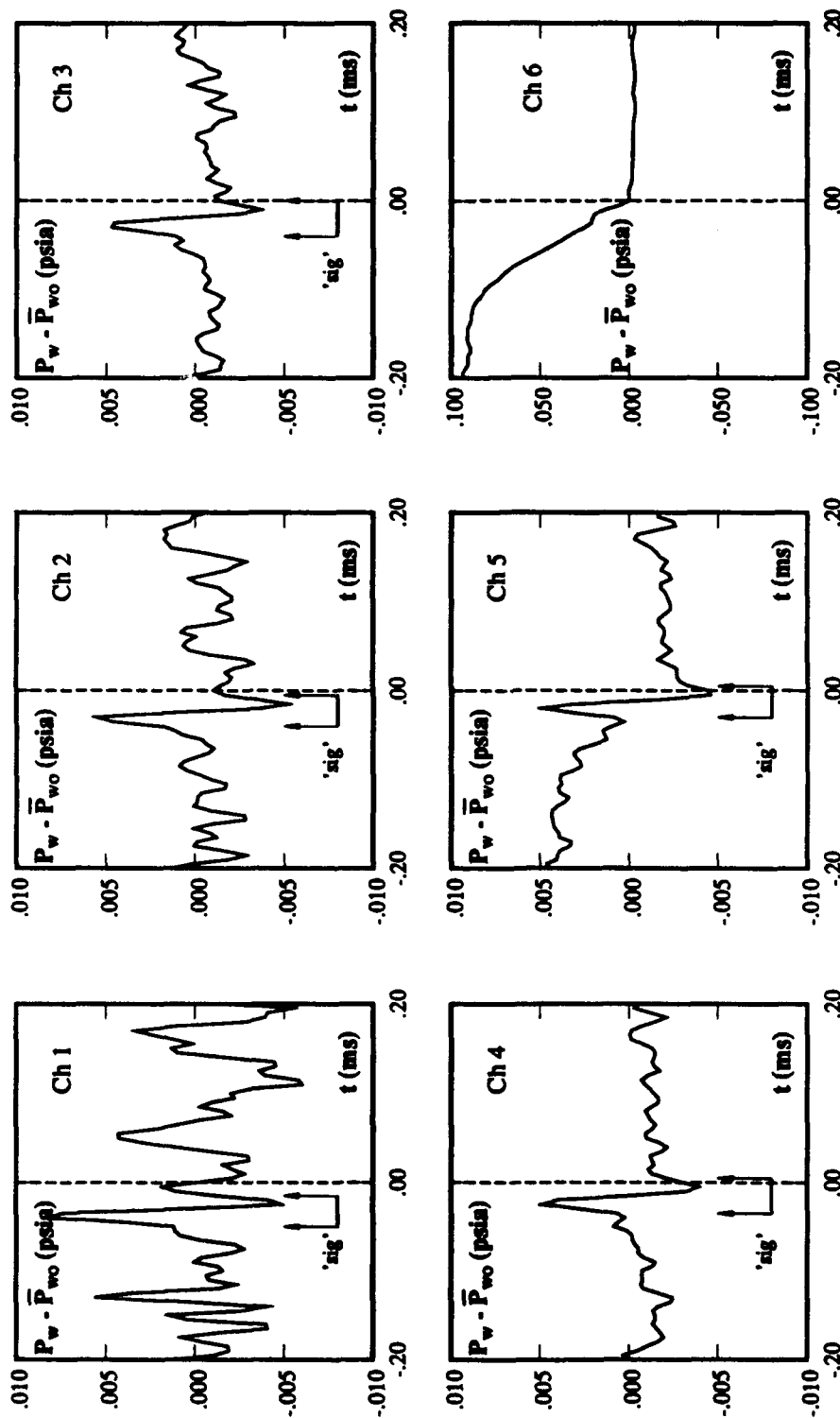


Fig. 5-10: Pseudo-Channel Ensemble-Averaged Surface Pressure Time Histories for a 3-Channel Downstream Sweep (Sweep Channels 6 \rightarrow 7 \rightarrow 8; Trigger on Channel 7)
a) Upstream of the Separation Shock

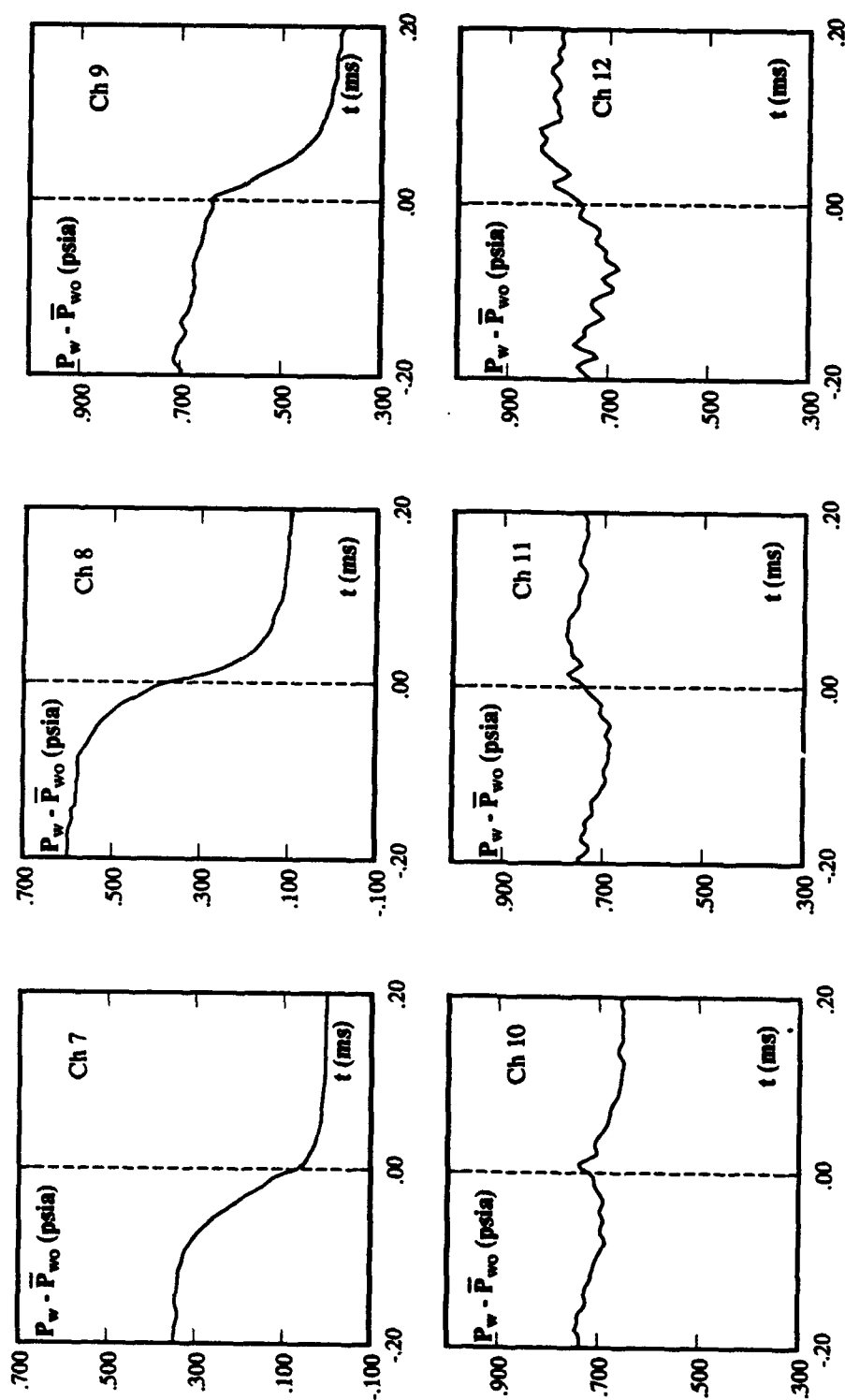


Fig. 5-10: Pseudo-Channel Ensemble-Averaged Surface (concluded)
Pressure Time Histories for a 3-Channel Downstream Sweep
(Sweep Channels 6 \rightarrow 7 \rightarrow 8; Trigger on Channel 7)
b) Downstream of the Separation Shock

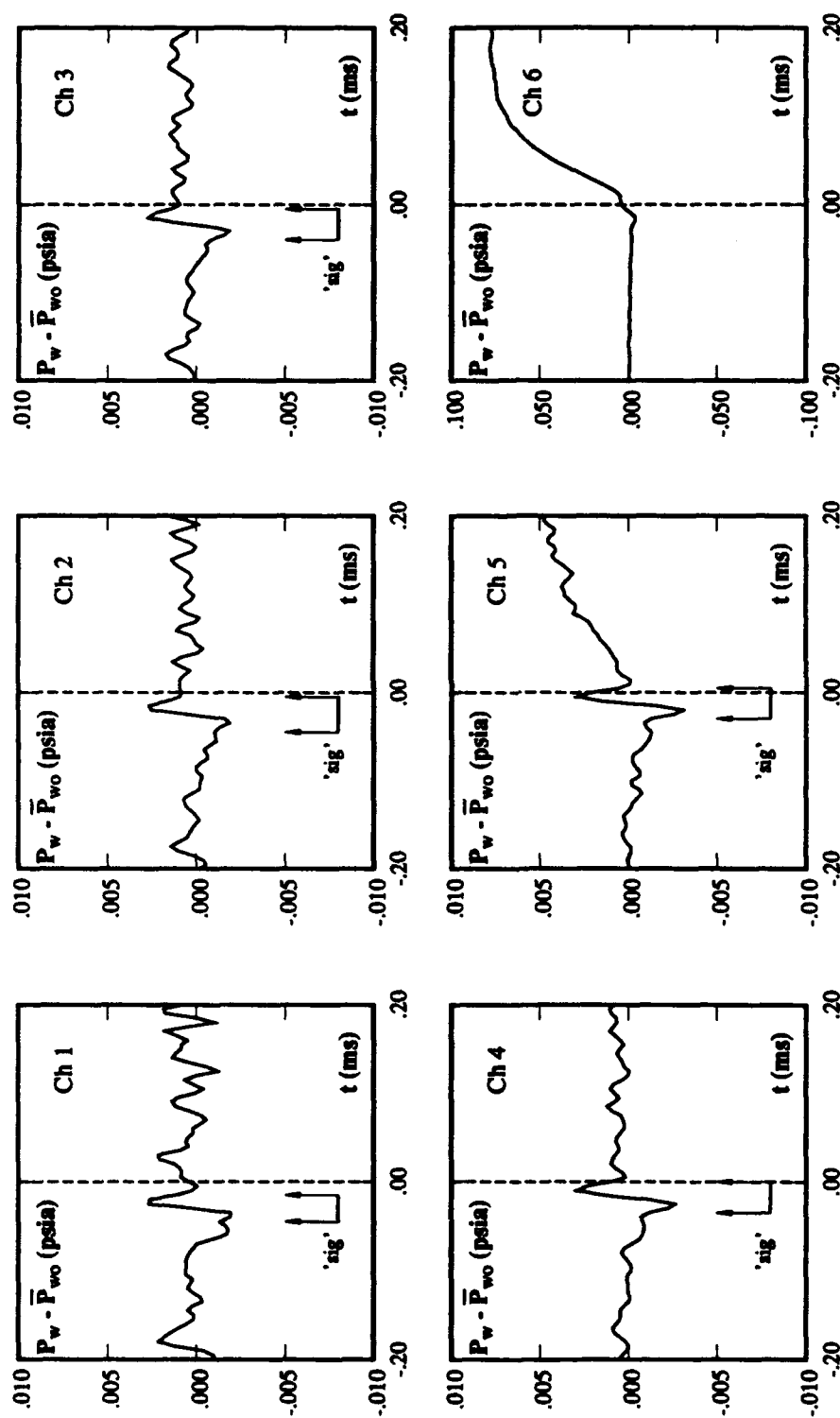


Fig. 5-11: Pseudo-Channel Super Ensemble-Averaged Surface Pressure Time Histories for a 3-Channel Upstream Sweep (Sweep Channels 8 \rightarrow 7 \rightarrow 6; Trigger on Channel 7)
a) Upstream of the Separation Shock

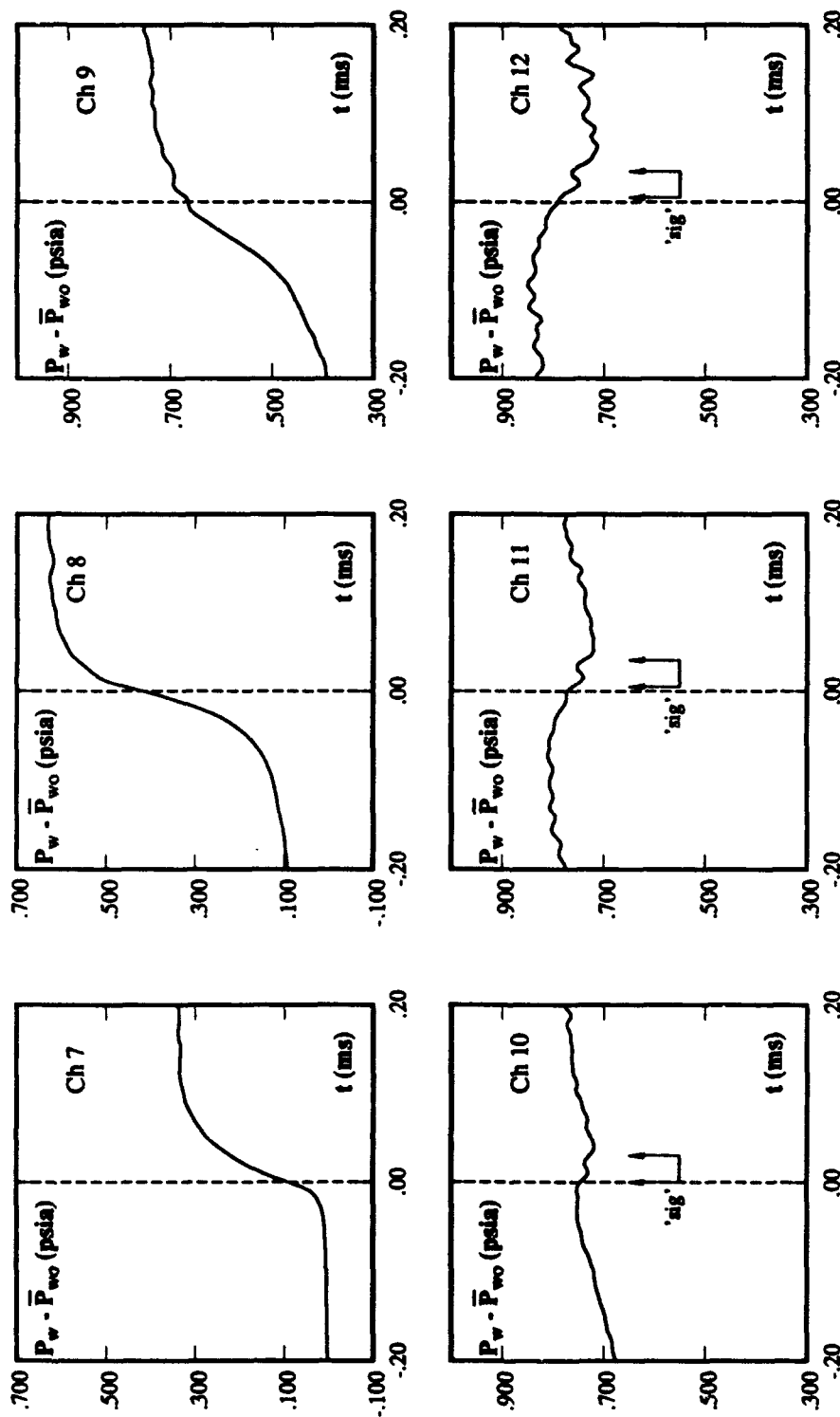


Fig. 5-11: Pseudo-Channel Super Ensemble-Averaged Surface (concluded)
Pressure Time Histories for a 3-Channel Upstream Sweep
(Sweep Channels 8 \rightarrow 7 \rightarrow 6; Trigger on Channel 7)
b) Downstream of the Separation Shock

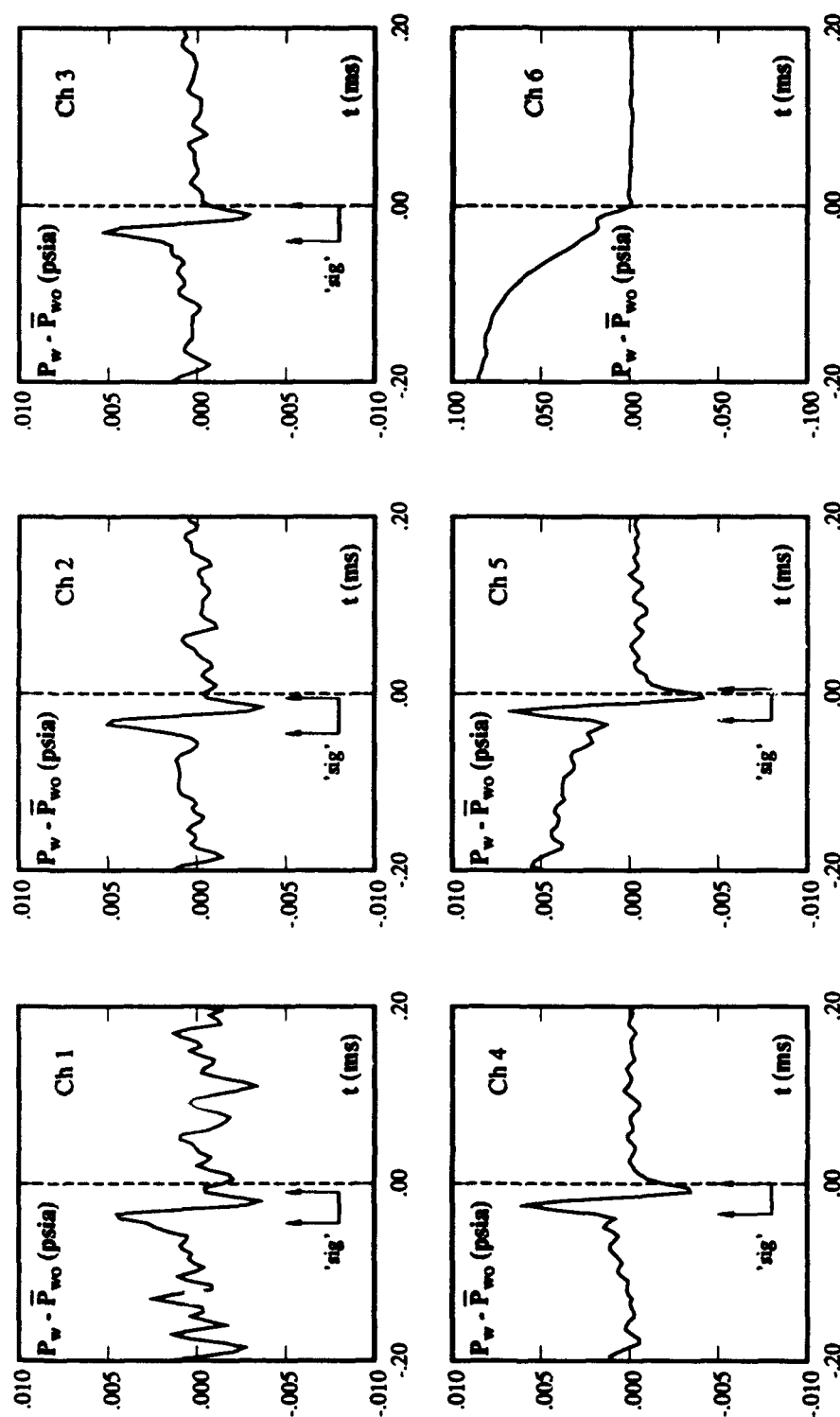


Fig. 5-12: Pseudo-Channel Super Ensemble-Averaged Surface Pressure Time Histories for a 3-Channel Downstream Sweep (Sweep Channels 6 \rightarrow 7 \rightarrow 8; Trigger on Channel 7)
a) Upstream of the Separation Shock

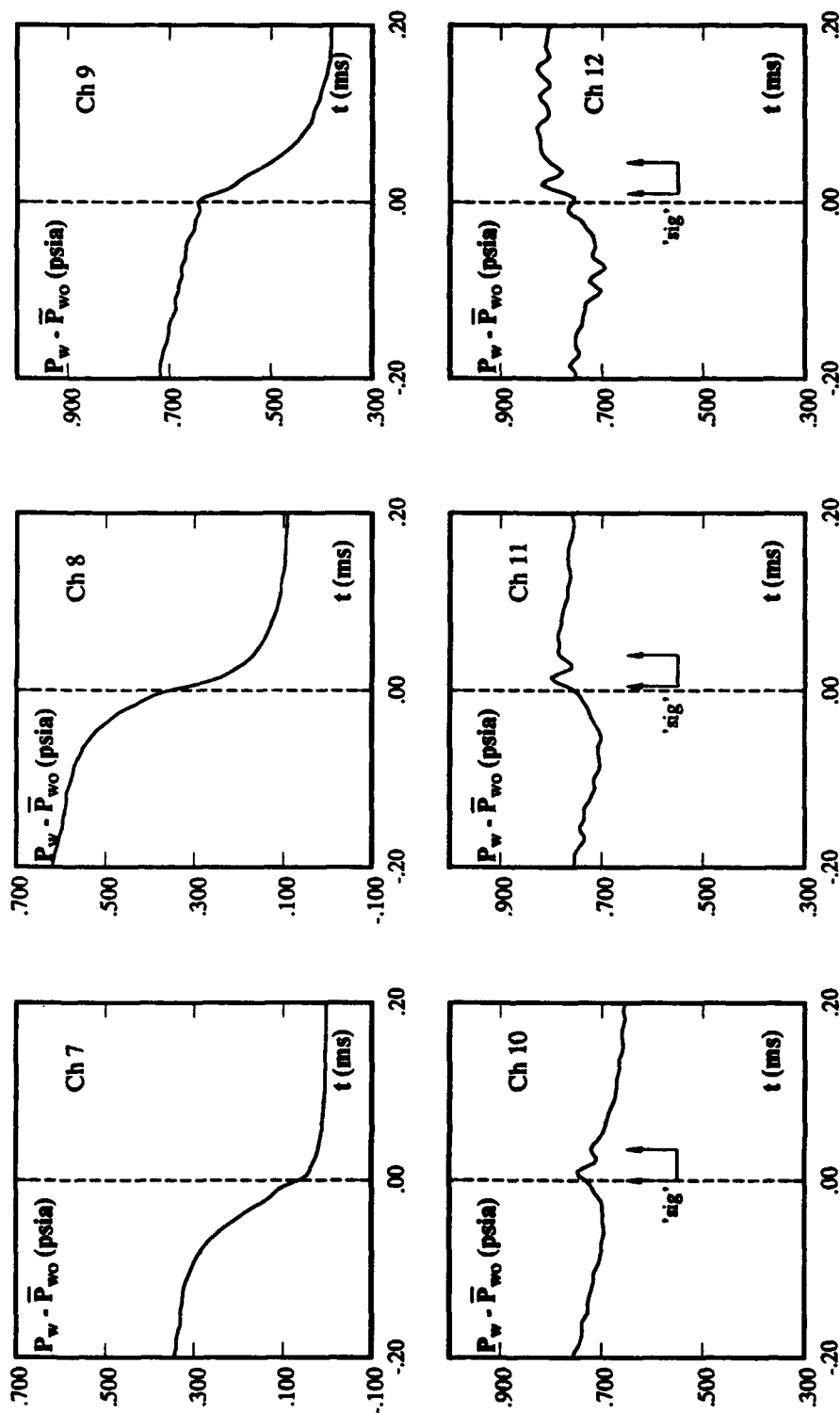


Fig. 5-12: Pseudo-Channel Super Ensemble-Averaged Surface (concluded)
Pressure Time Histories for a 3-Channel Downstream Sweep
(Sweep Channels 6 \rightarrow 7 \rightarrow 8; Trigger on Channel 7)
b) Downstream of the Separation Shock

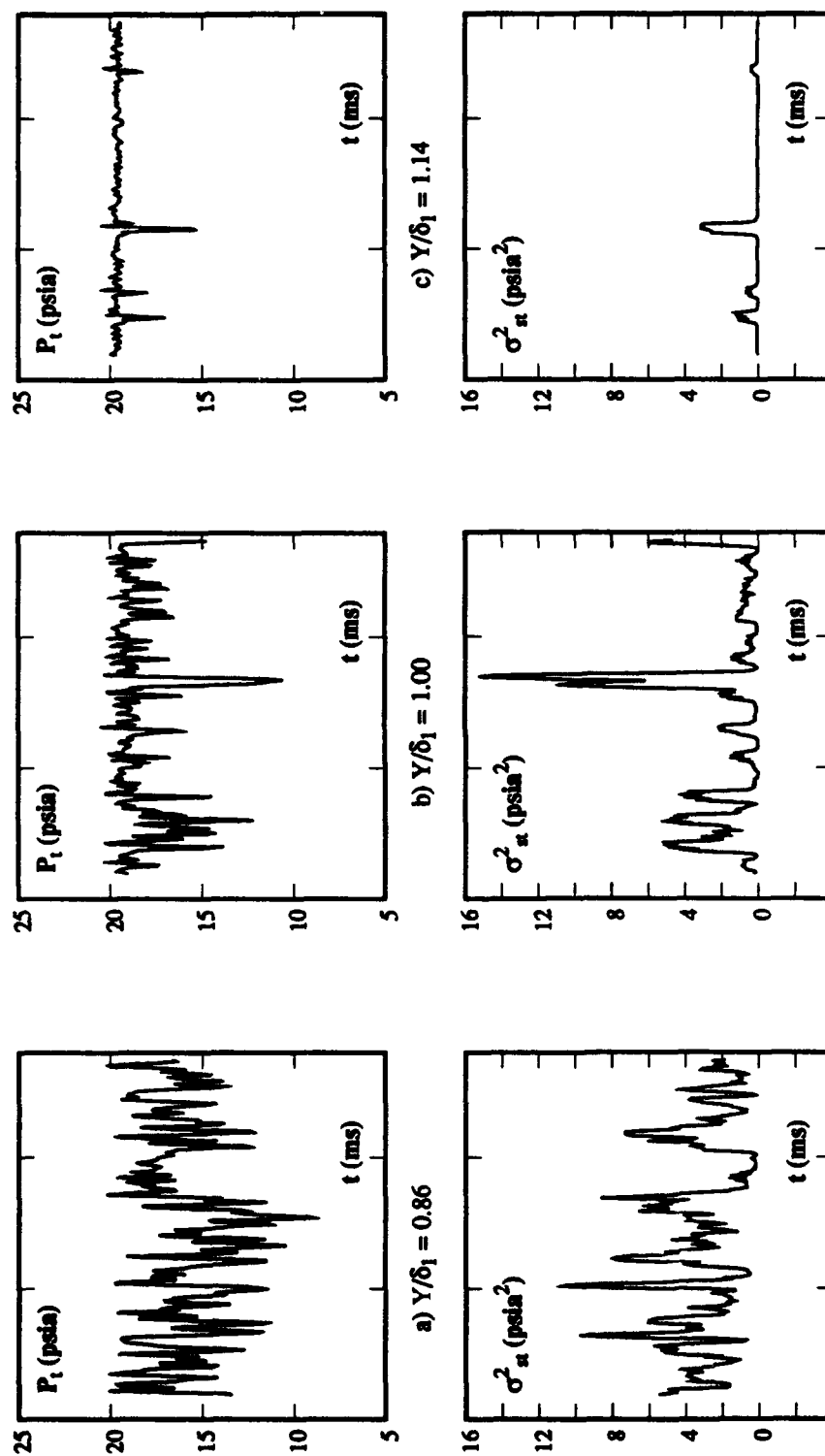


Fig. 5-13: Variation in Pitot Pressure Signals and VITA Transformations within the Incoming Boundary Layer
(Each plot contains 256 points; $T_{st} = 40 \mu s$)

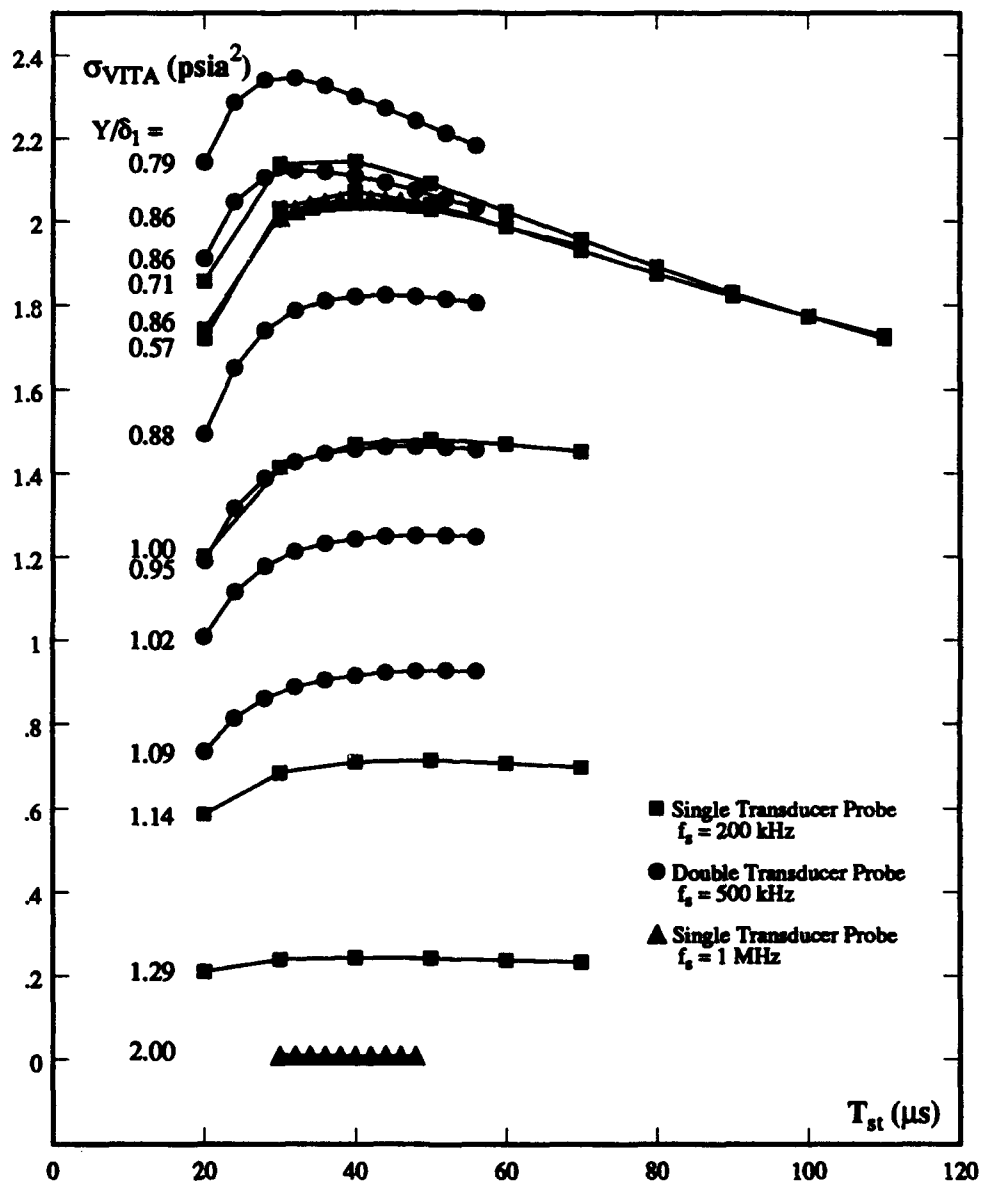
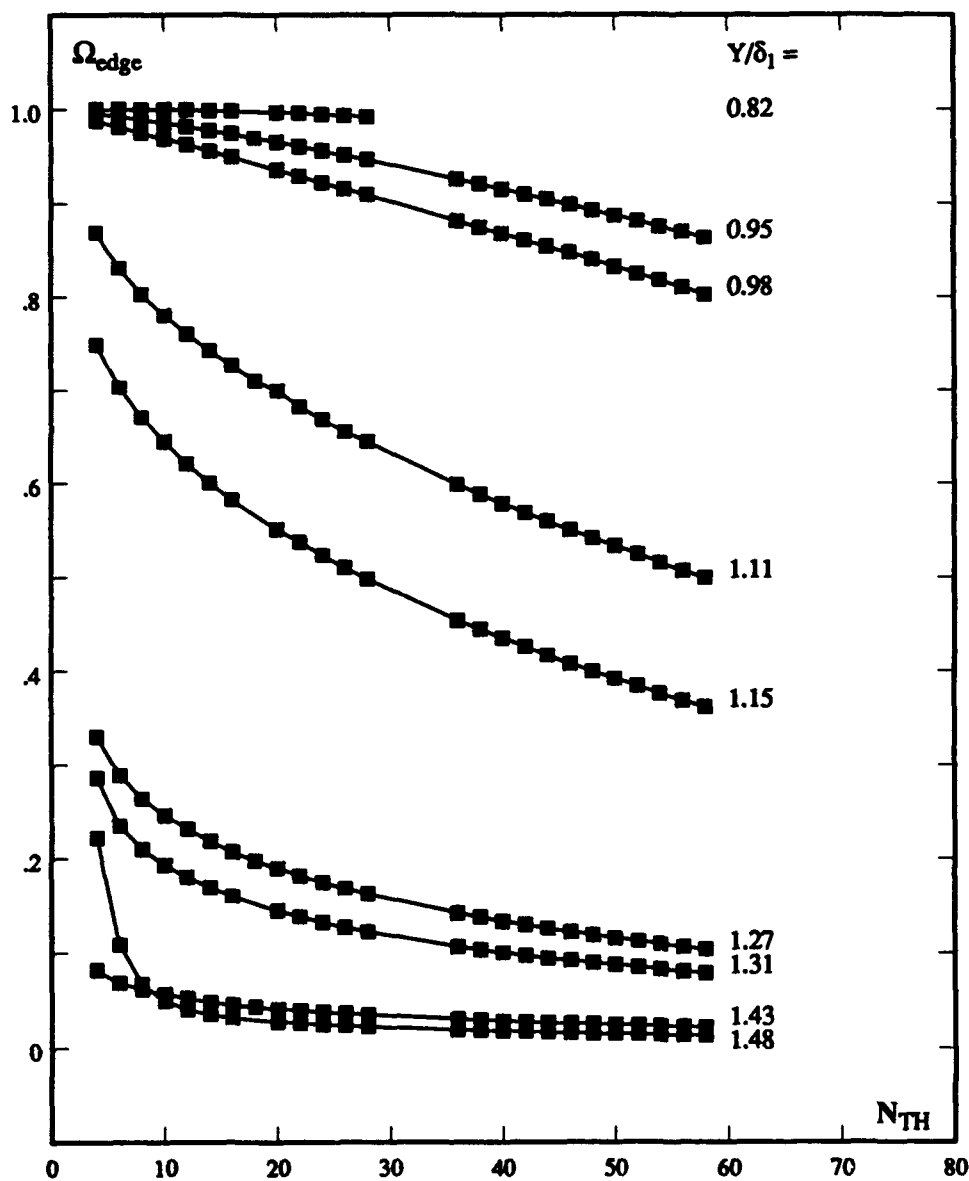


Fig. 5-14: Sensitivity of Incoming Boundary Layer Pitot Pressure VITA Signal RMS to Averaging Window Size



**Fig. 5-15: Sensitivity of Incoming Boundary Layer
Edge Intermittency to VITA
Threshold Multiplier ($T_{\alpha} = 40 \mu s$)**

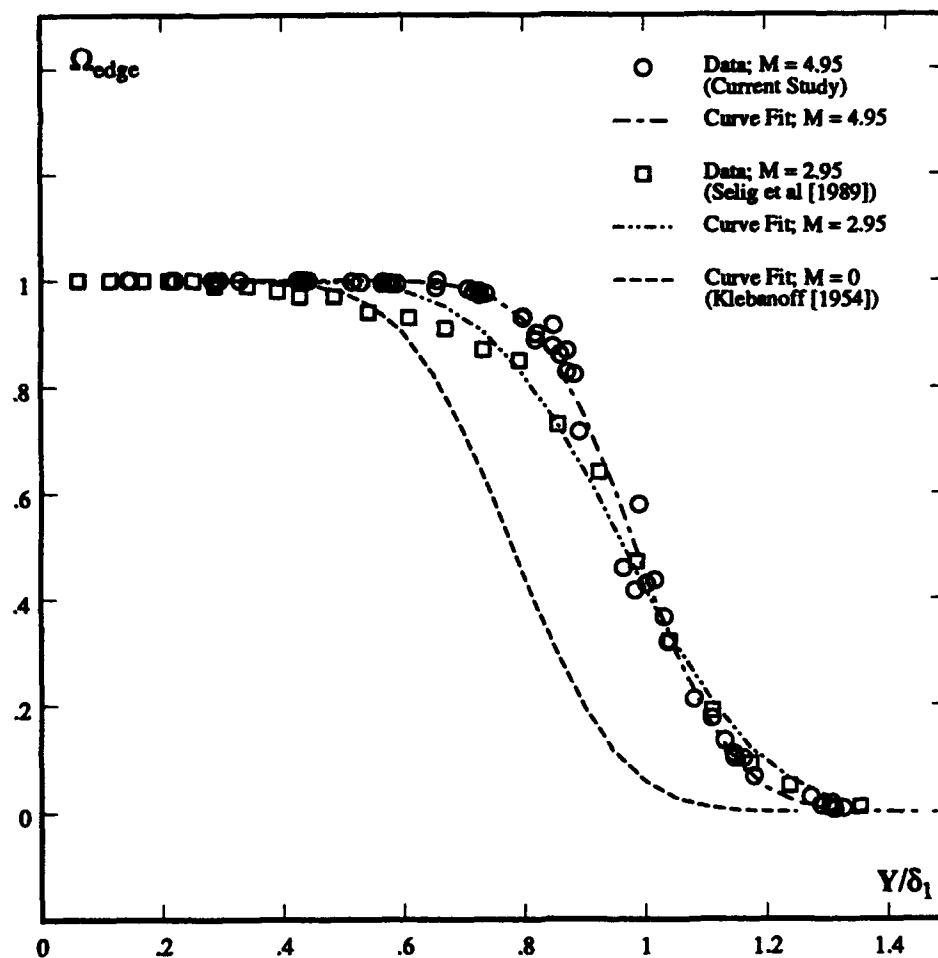
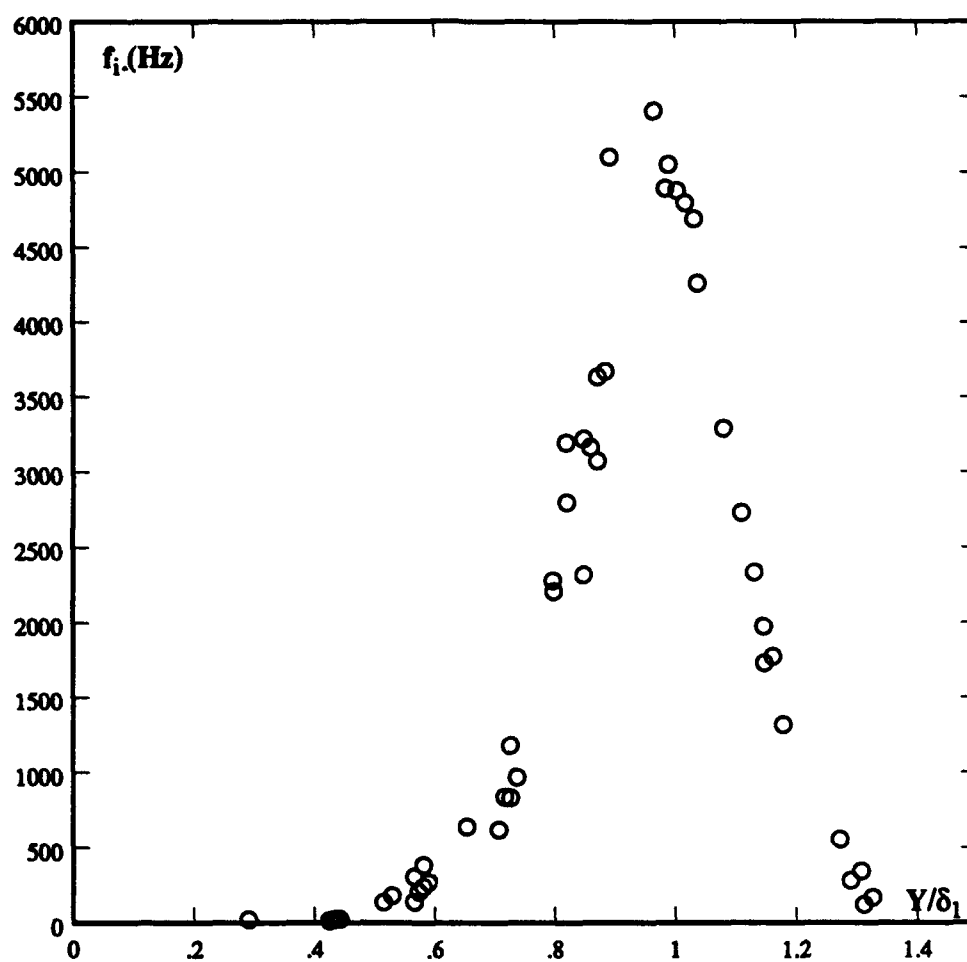


Fig. 5-16: Boundary Layer Edge Intermittency



**Fig. 5-17: Boundary Layer Edge Interface
Crossing Frequency**

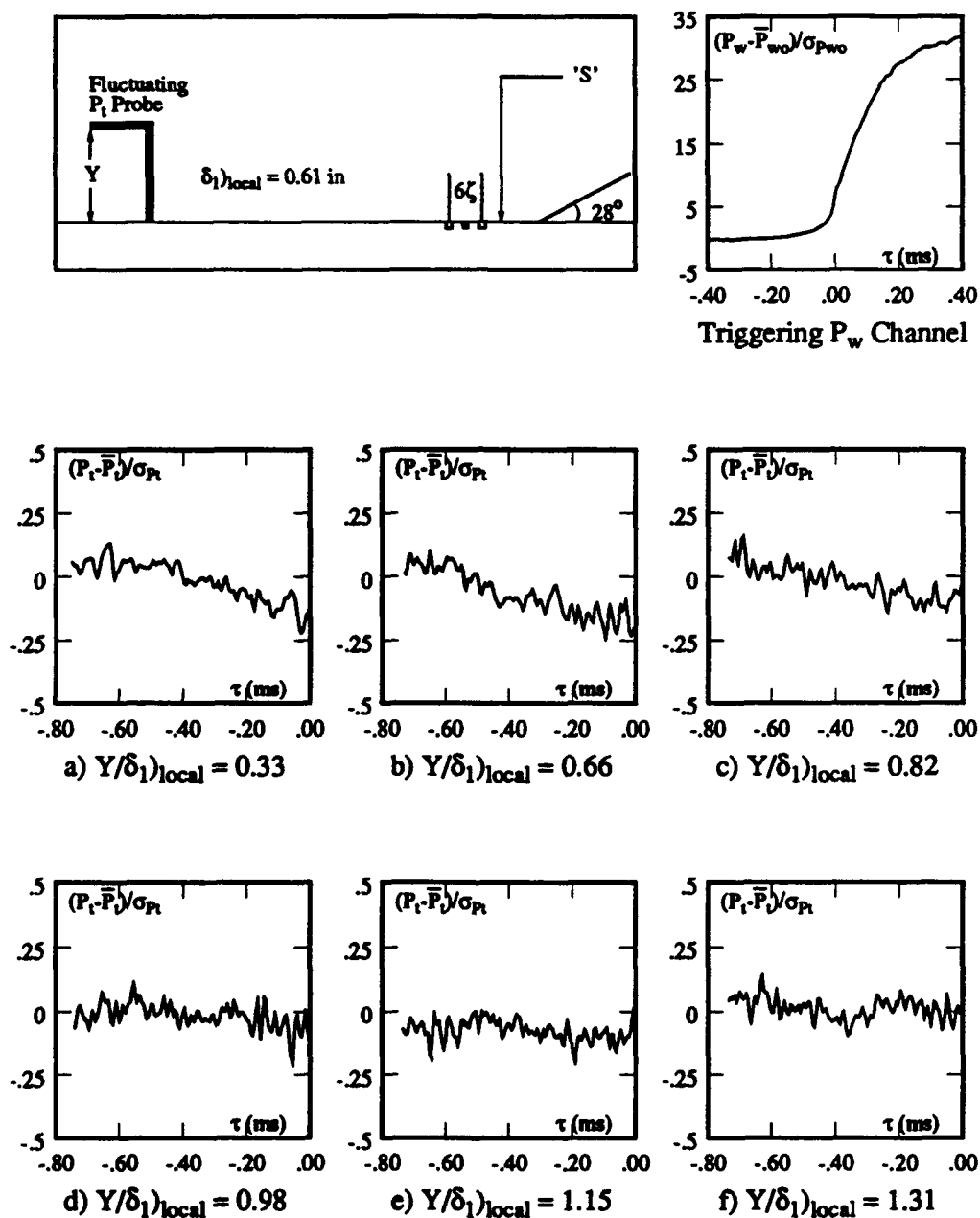


Fig. 5-18: Variation in Upstream Ensemble-Averaged Pitot Pressure Signals with Height Above the Surface - Upstream Sweep

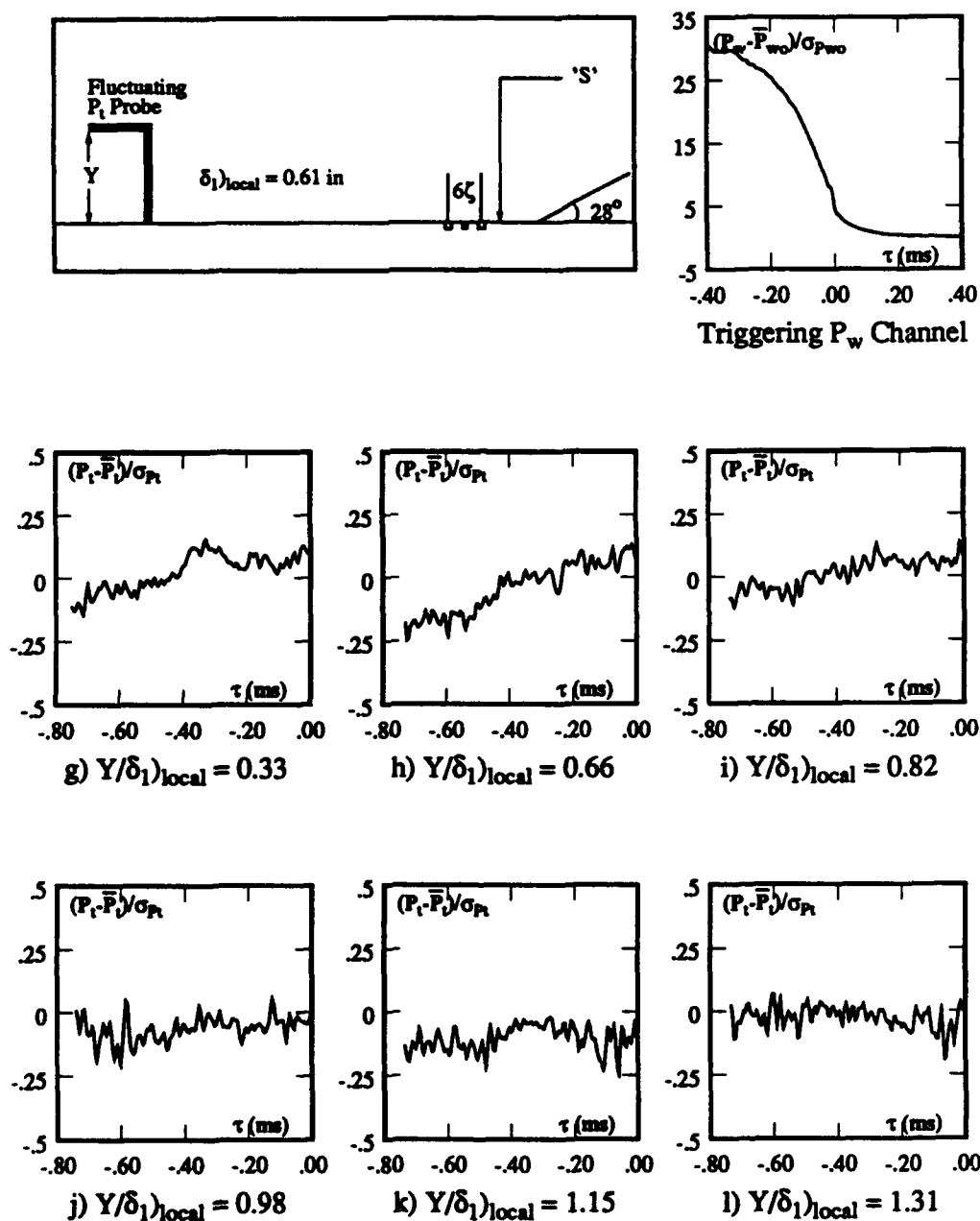


Fig. 5-18: Variation in Upstream Ensemble-Averaged Pitot Pressure Signals with Height Above the Surface -Downstream Sweep (concluded)

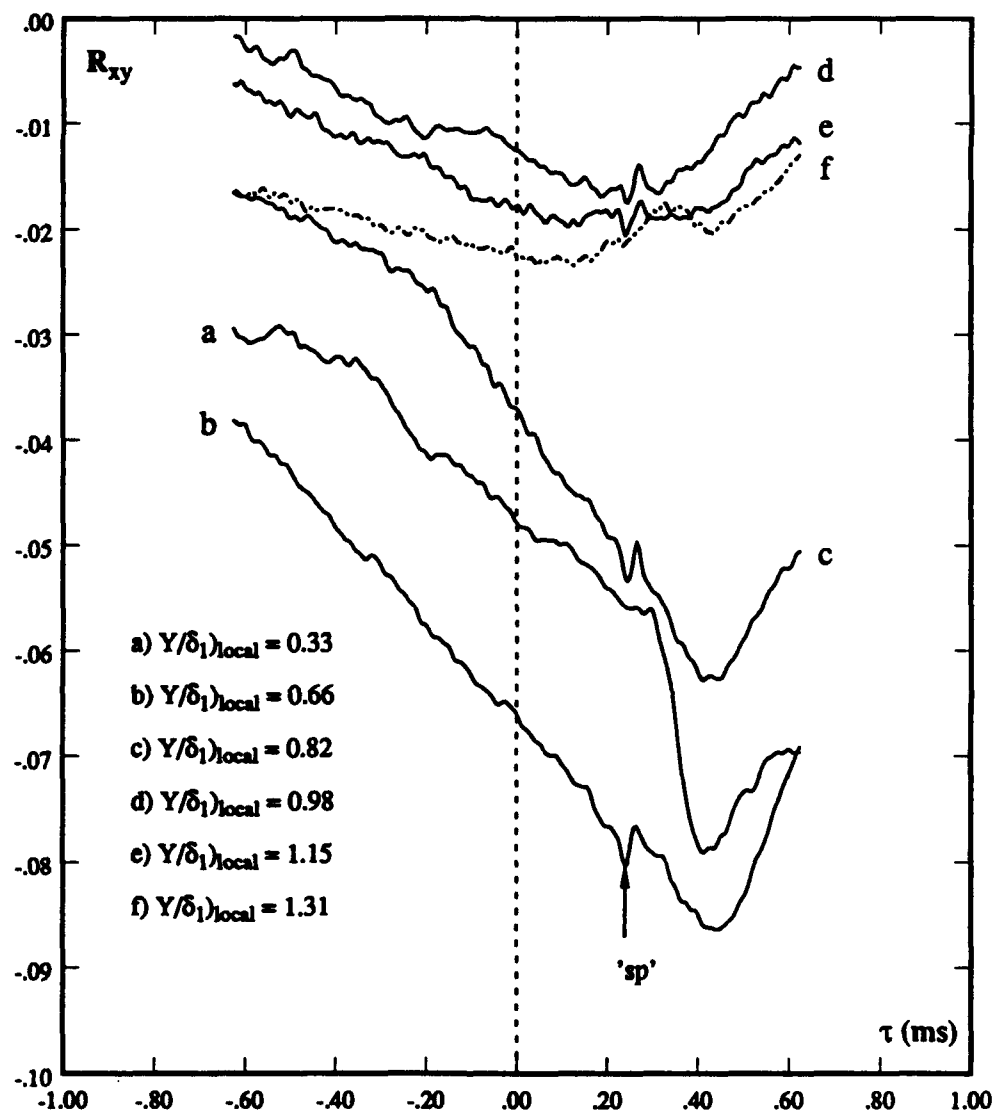


Fig. 5-19: Normalized Cross-Correlations Between Upstream Boundary Layer Pitot Pressure and Surface Pressure Beneath the Separation Shock

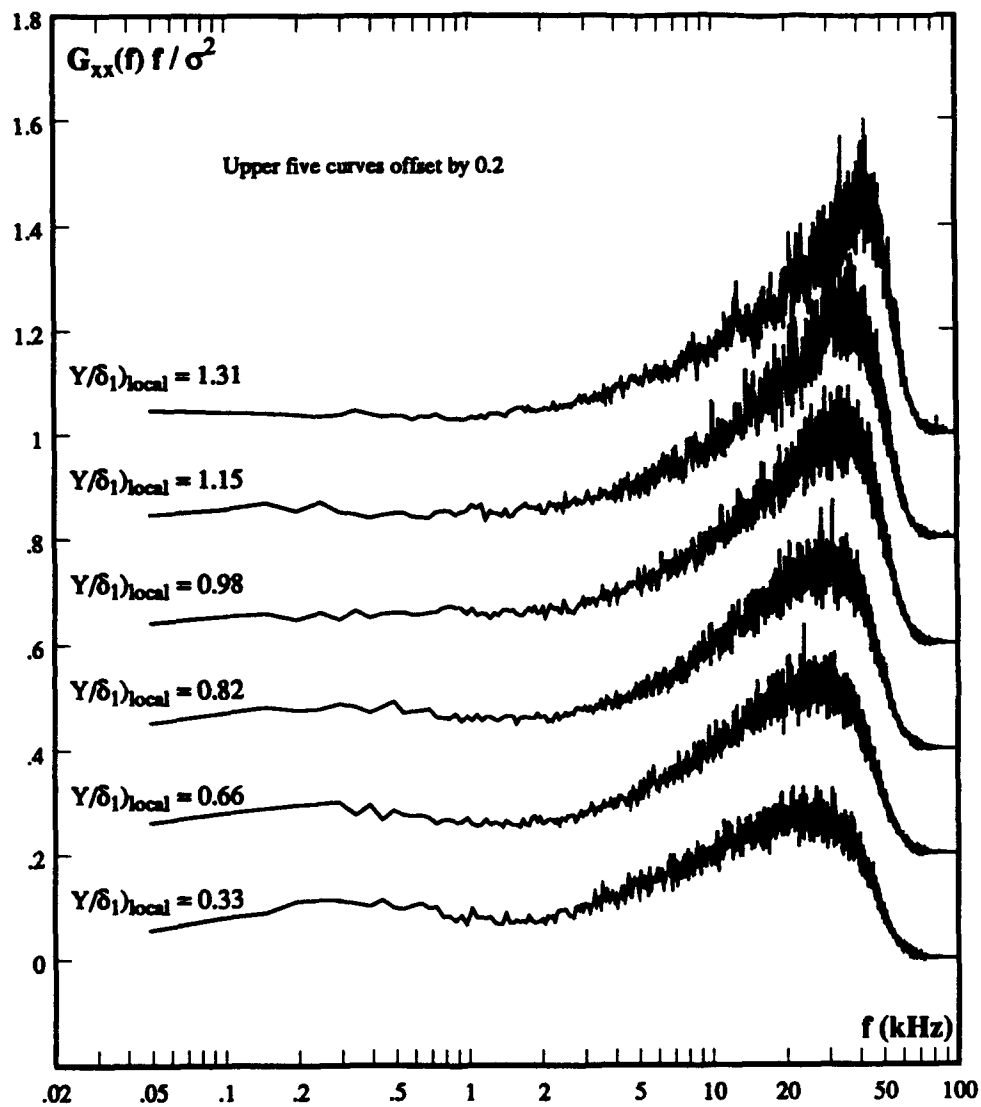


Fig. 5-20: Normalized Fluctuating Pitot Pressure Power Spectra in the Incoming Boundary Layer

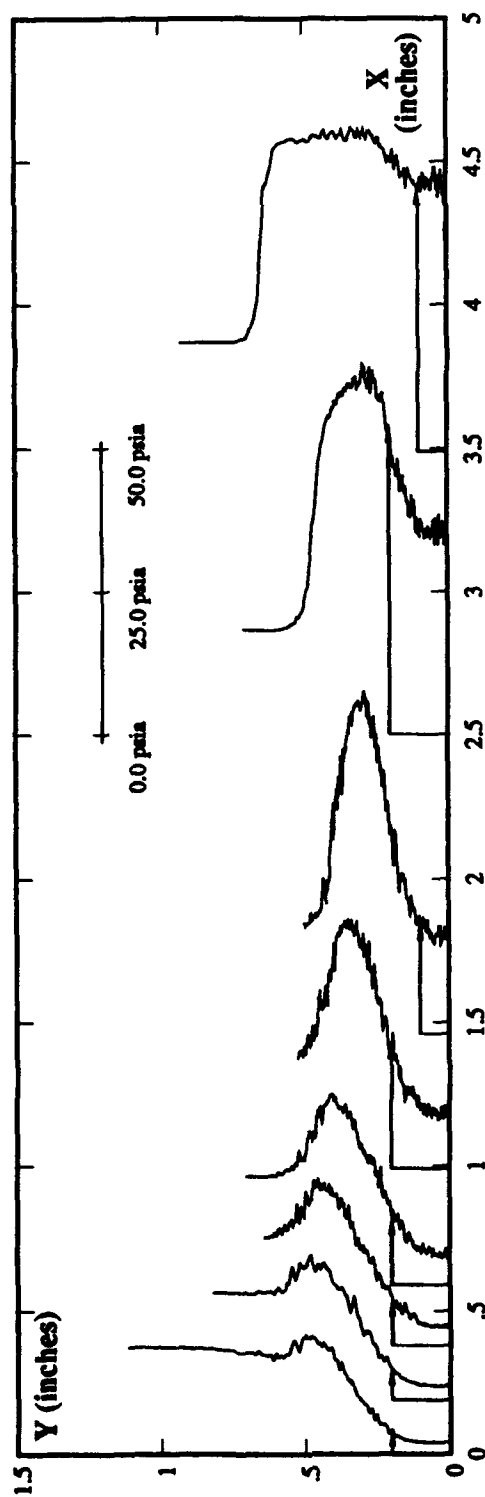


Fig. 5-21: Pitot Pressure Profiles Above Ramp Surface
-Baseline Configuration

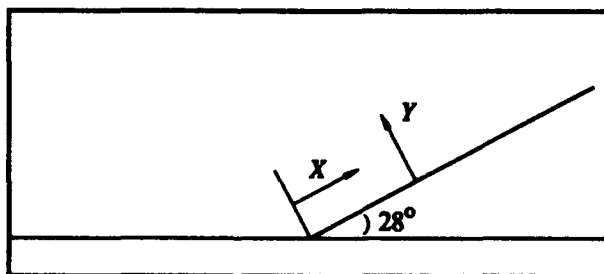
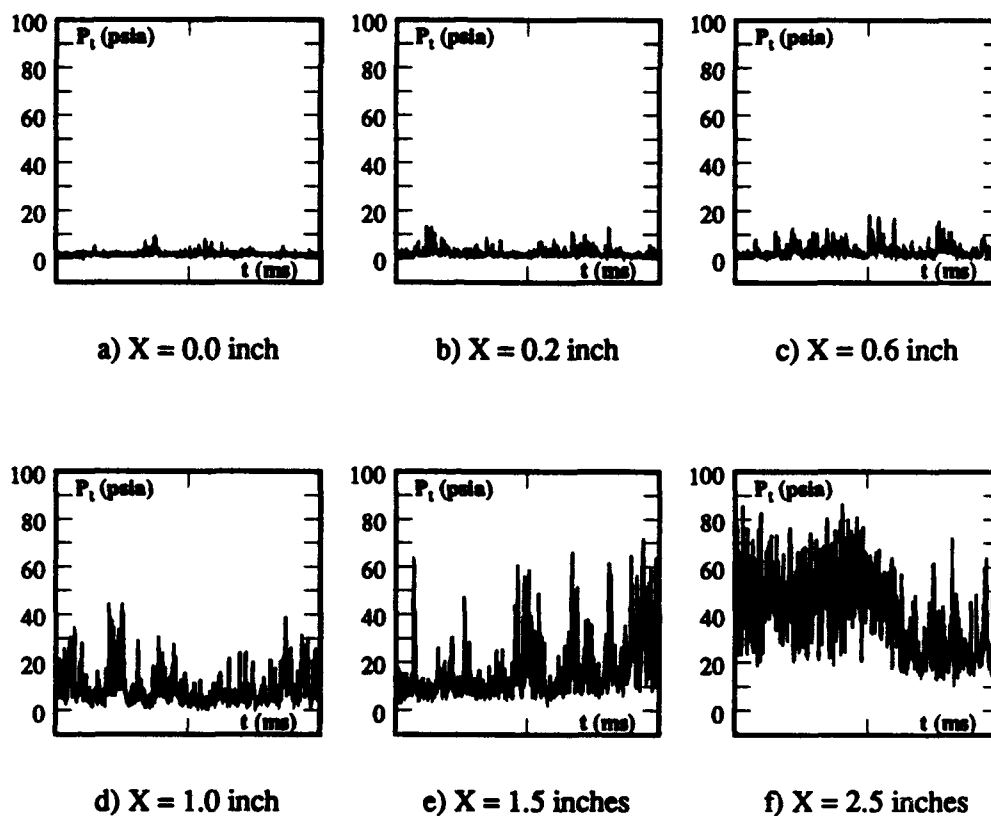


Fig. 5-22: Variation in Pitot Pressure Signals at $Y = 0.1$ inch with Distance From the Ramp Corner (Each plot contains 1 record of data)

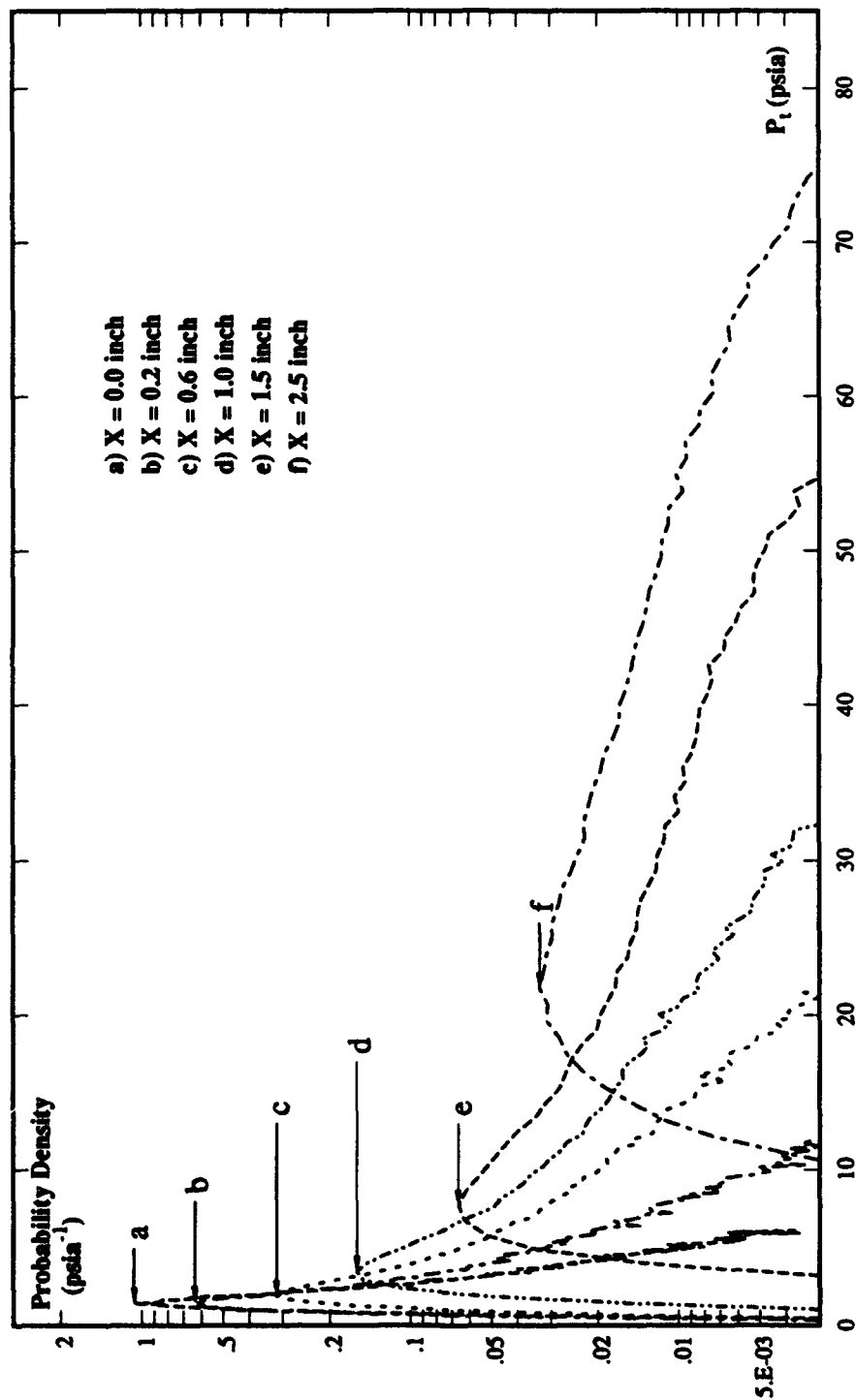


Fig. 5-23: Variation in Pitot Pressure PDD's at
Y = 0.1 inch with Distance From the Ramp Corner

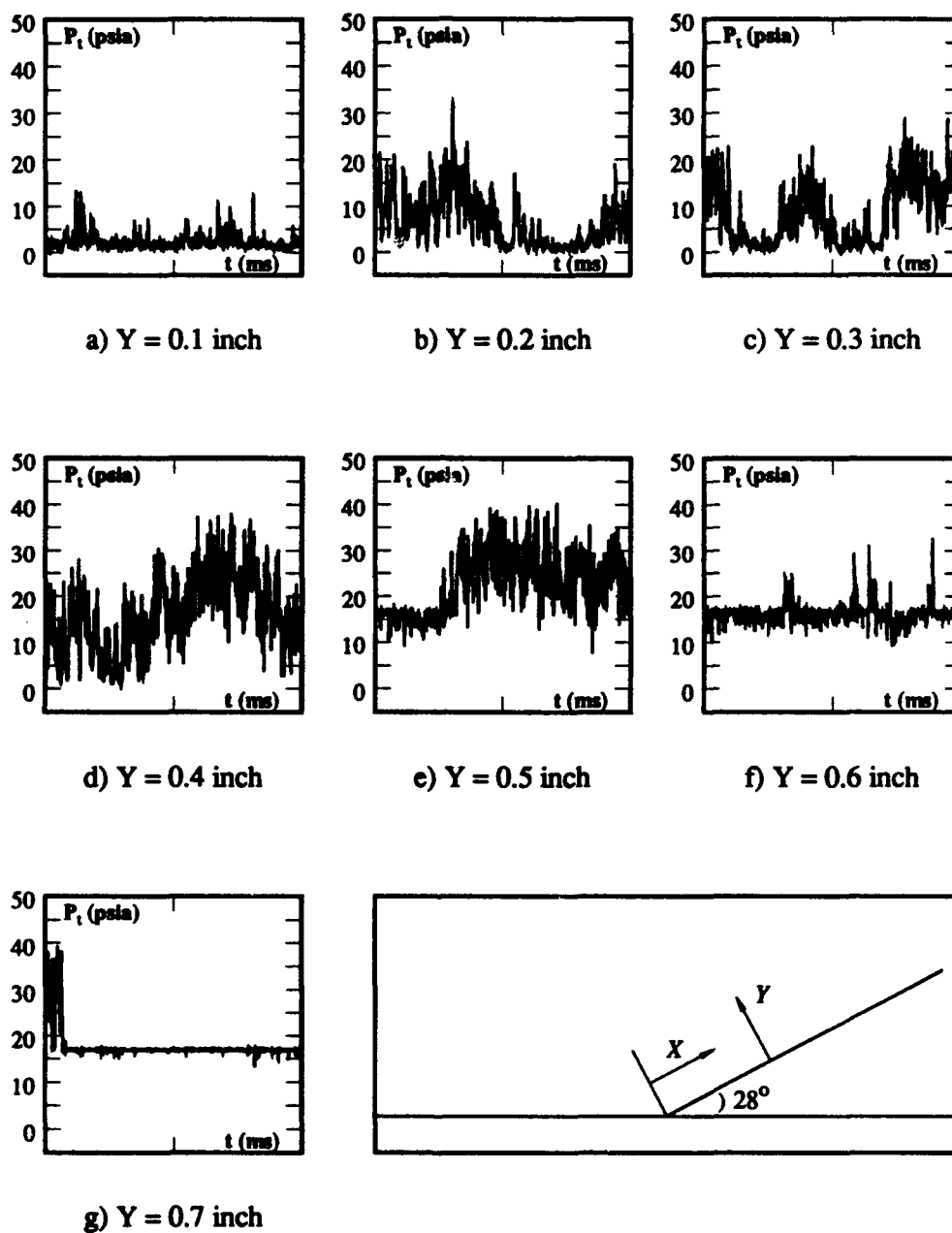


Fig. 5-24: Variation in Pitot Pressure Signals at $X = 0.2$ inch with Height Above the Ramp Surface (Each plot contains 1 record of data)

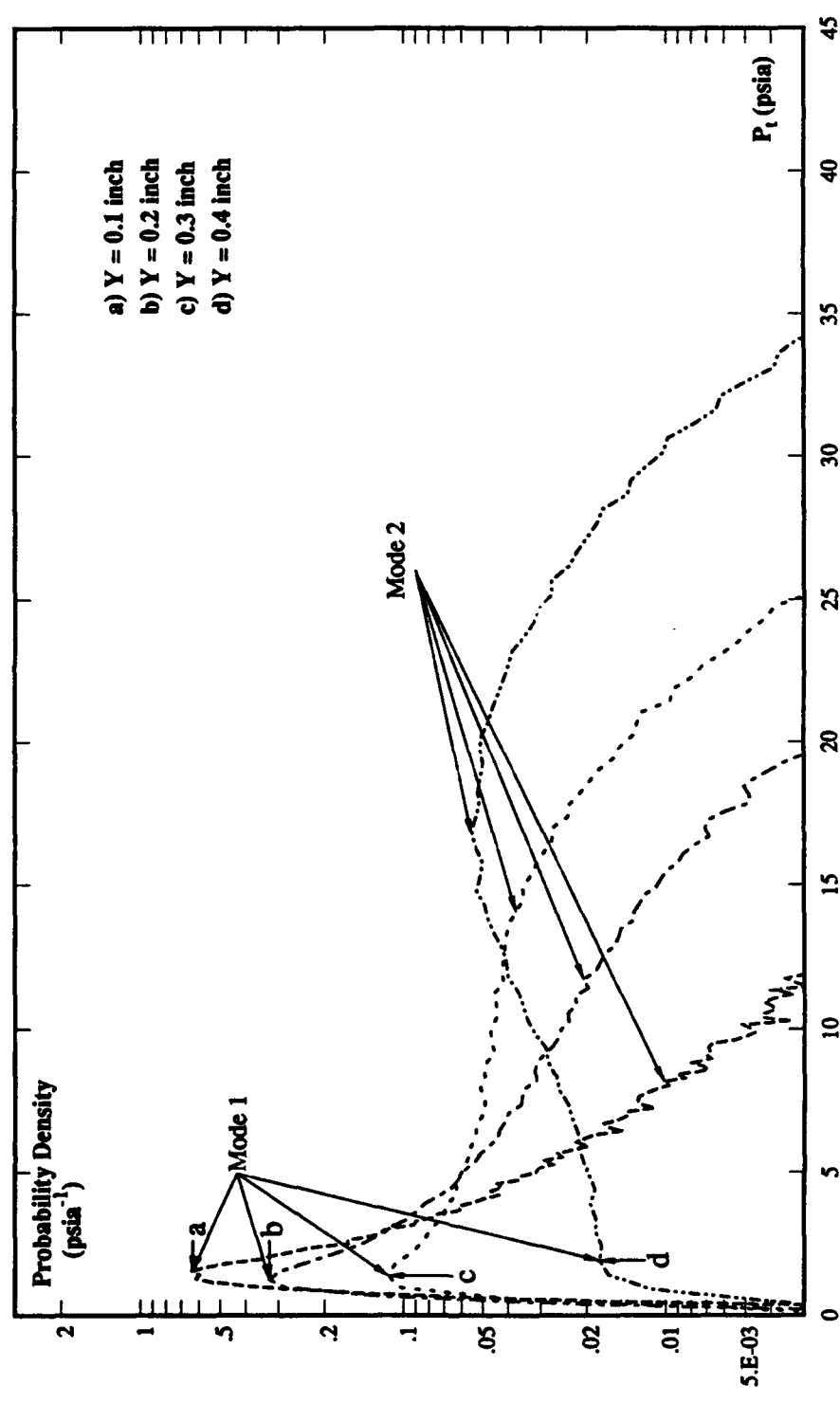
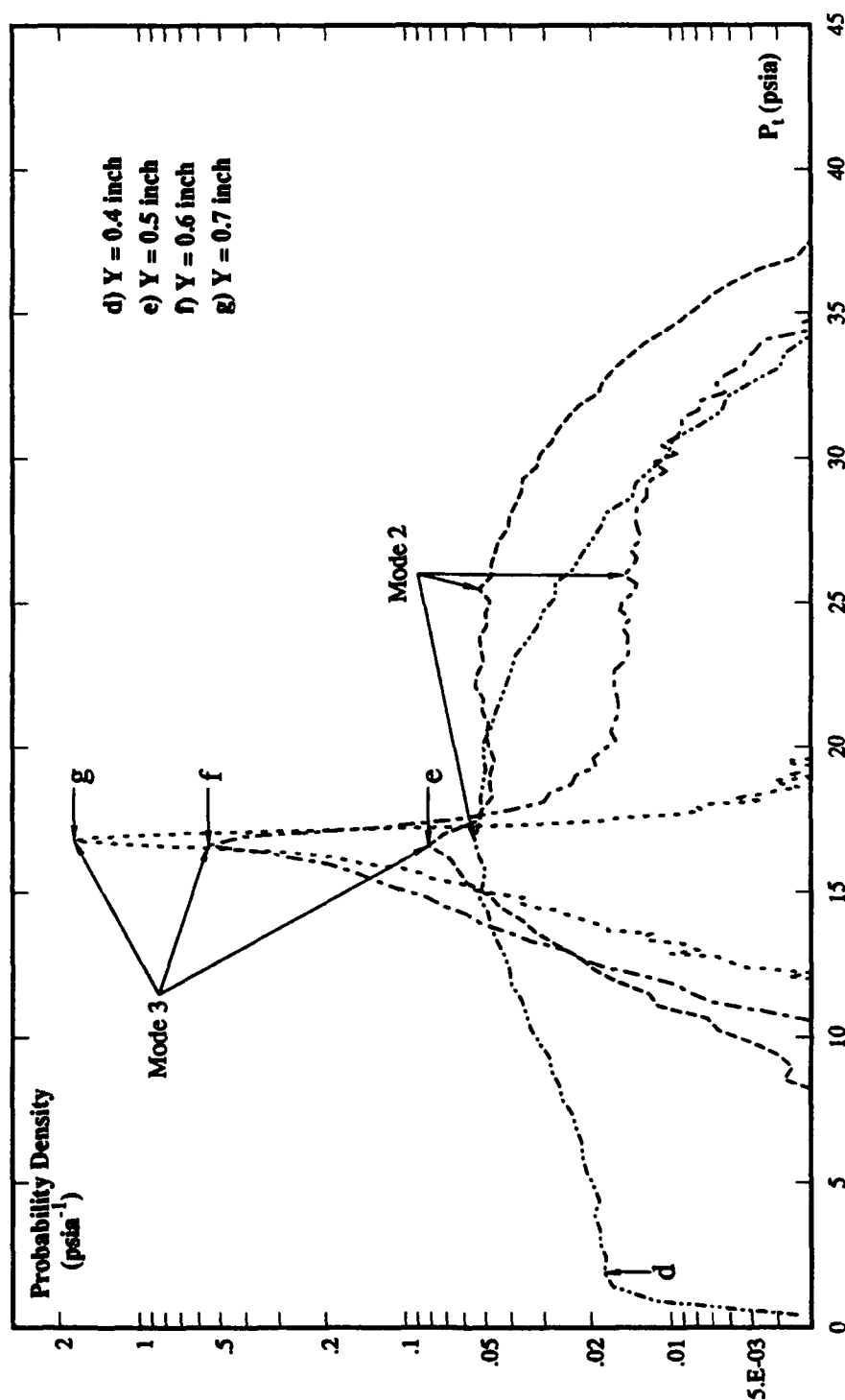


Fig. 5-25: Variation in Pitot Pressure PDD's at
 $X = 0.2$ inch with Height Above the Ramp Surface



**Fig. 5-25: Variation in Pitot Pressure PDD's at
X = 0.2 inch with Height Above the Ramp Surface
(concluded)**

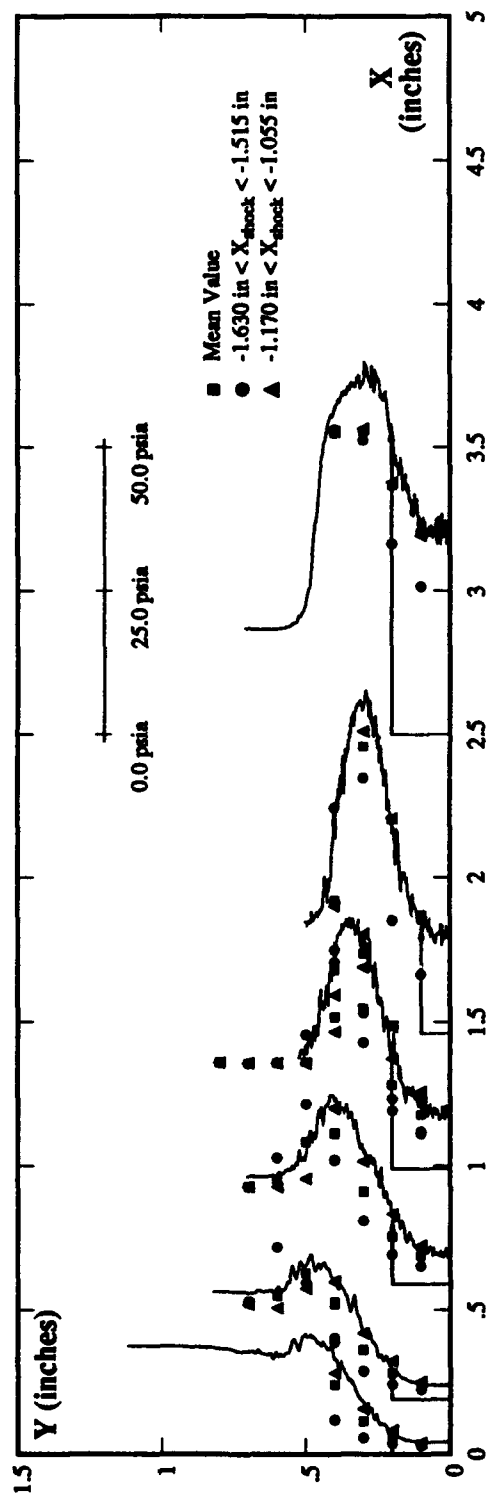
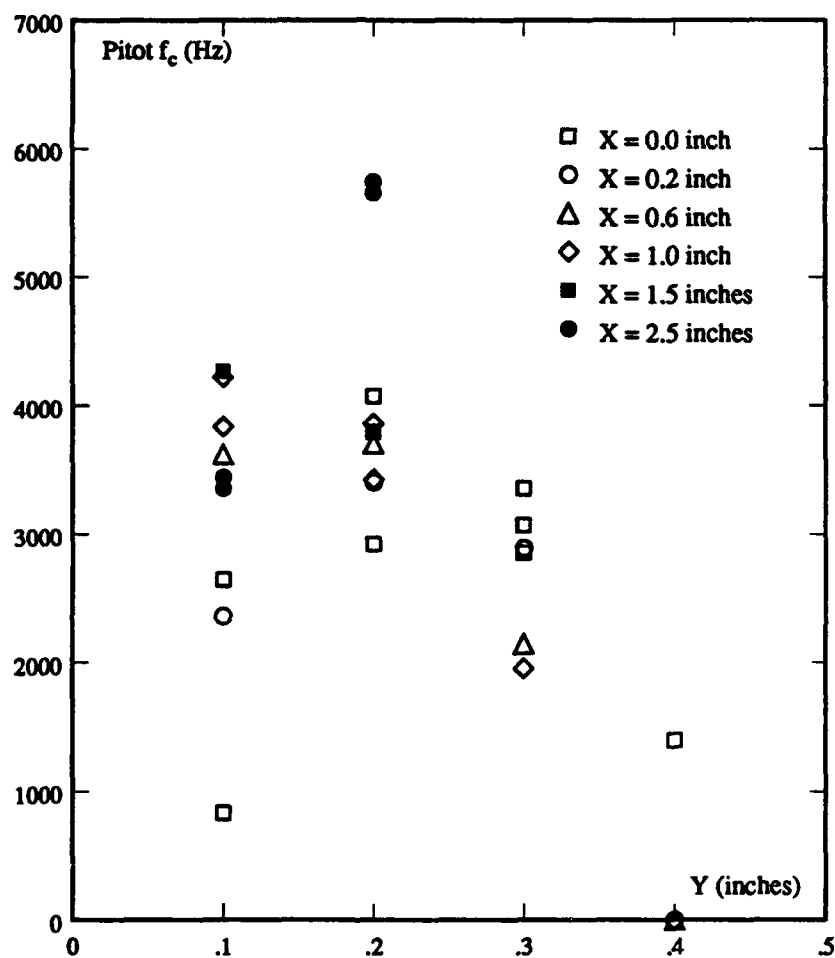


Fig. 5-26: Frozen Pitot Pressure Profiles
-Baseline Configuration



**Fig. 5-27: Shear Layer Zero-Crossing Frequency
Downstream of the Corner -
Baseline Configuration**

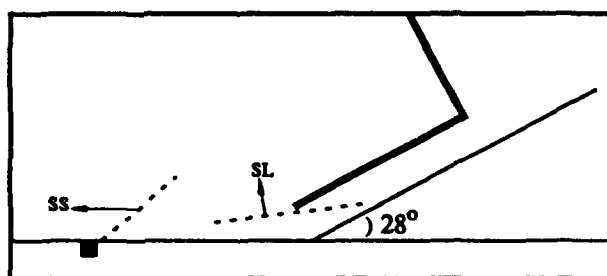
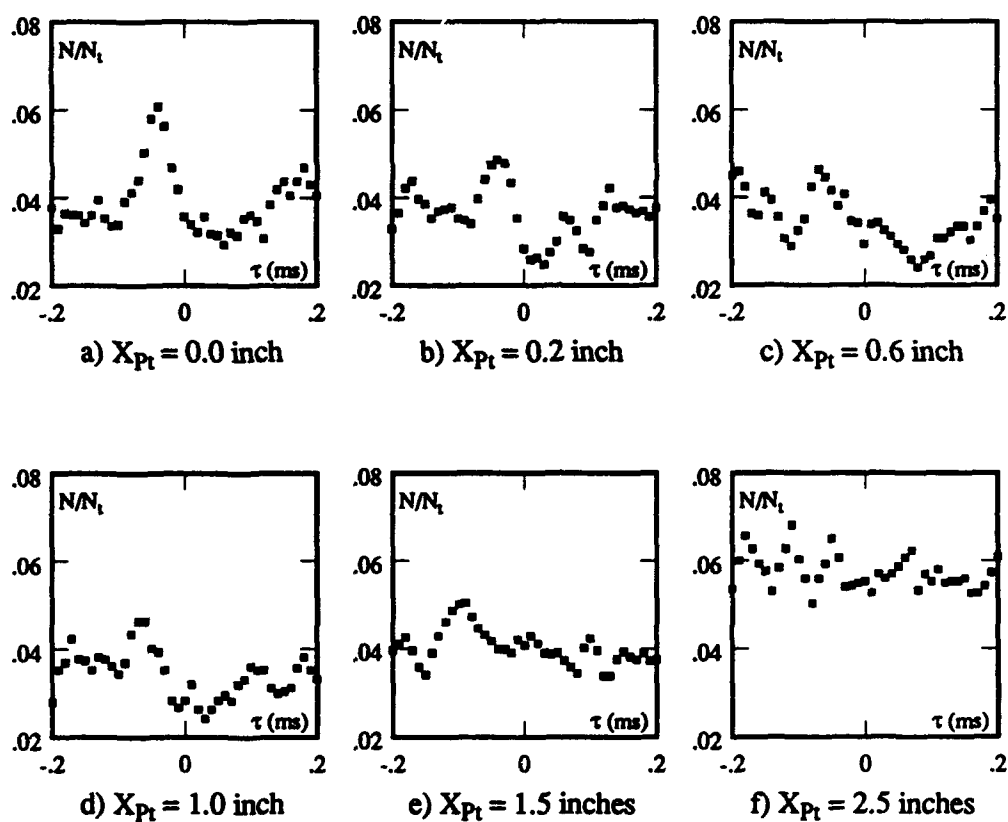


Fig. 5-28: ERTA of Separation Shock/Shear Layer Motion
 ($Y_{Pt} = 0.2$ inch, $X_{Pw} = -1.17$ inches)
 a) Event Pair = Rise_{SS} - Fall_{SL}

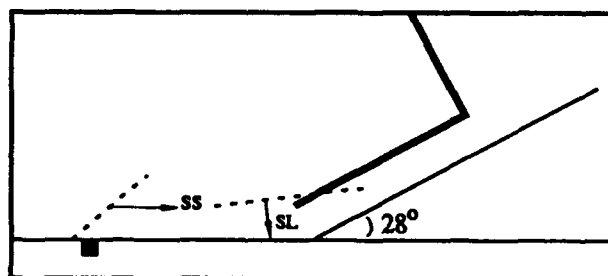
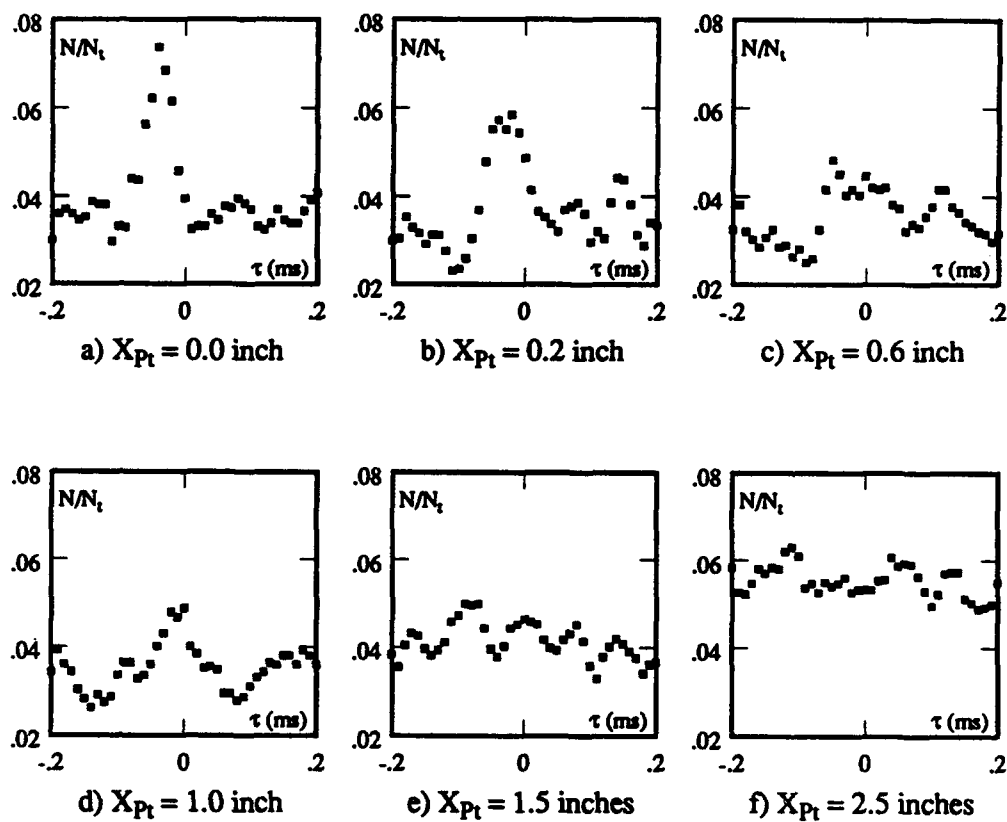


Fig. 5-28: ERTA of Separation Shock/Shear Layer Motion
 ($Y_{Pt} = 0.2$ inch, $X_{Pw} = -1.17$ inches)
 b) Event Pair = Fall_{SS} - Rise_{SL}
 (concluded)

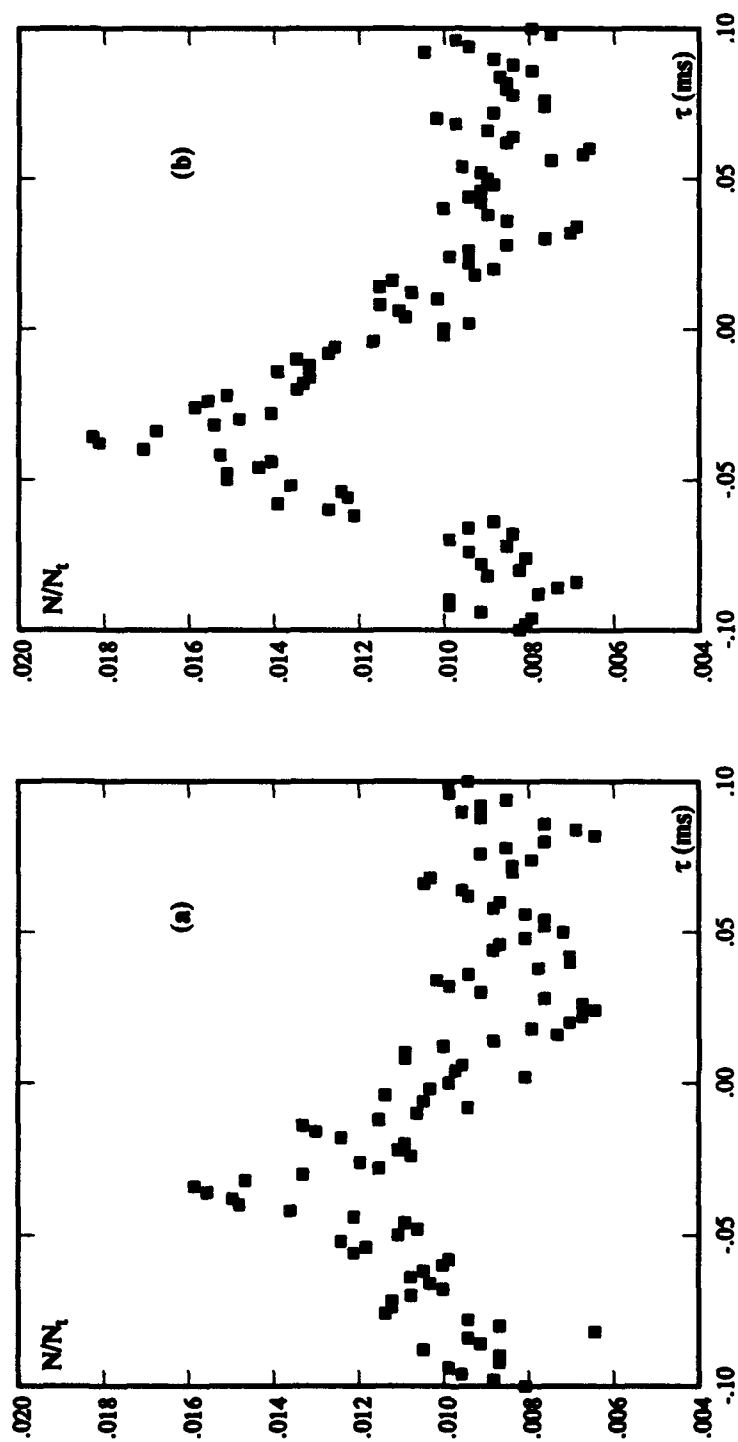
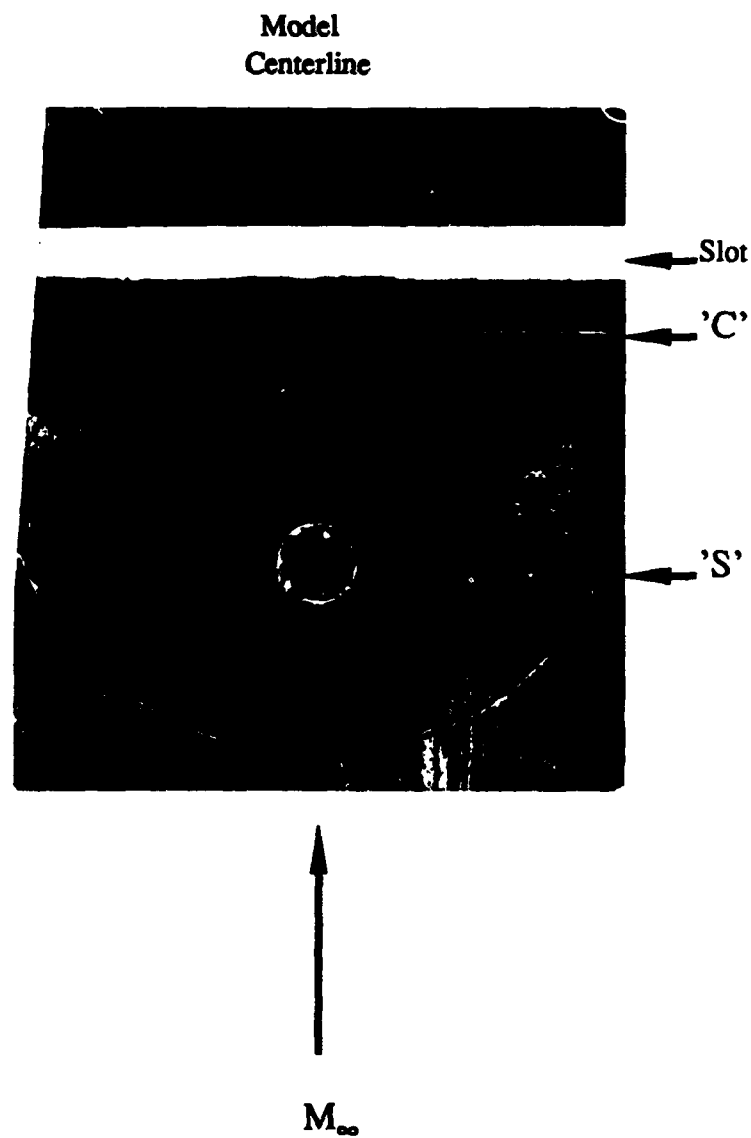
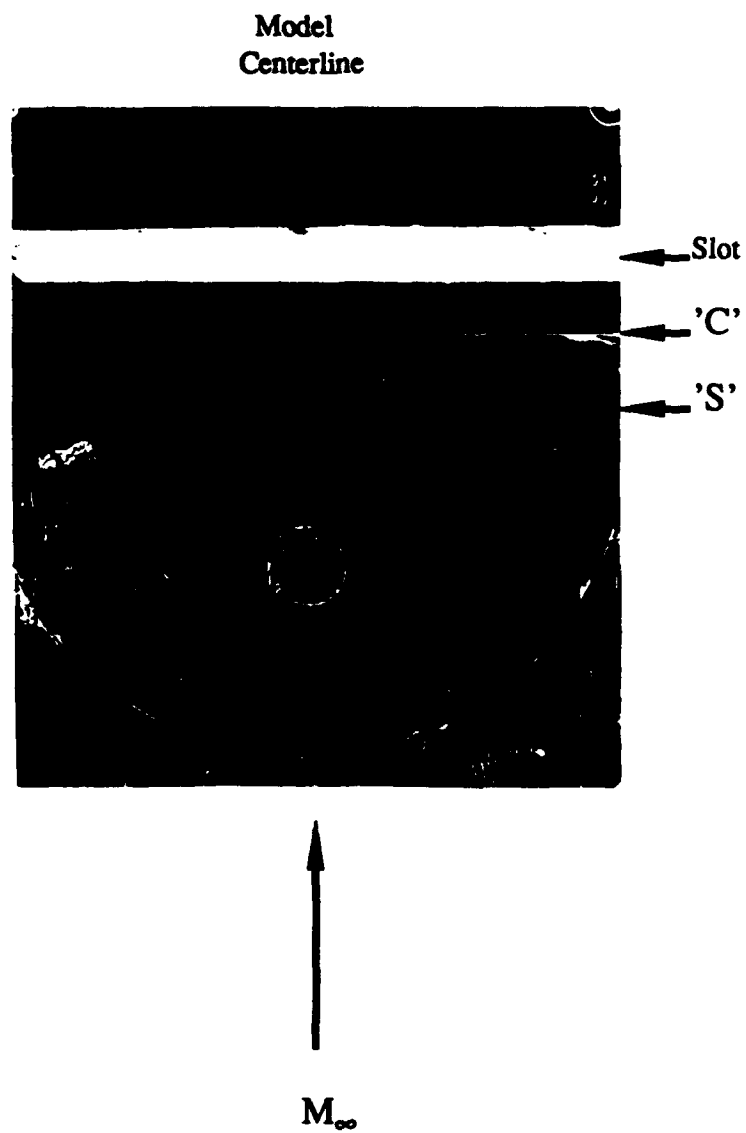


Fig. 5-29: Refined ERTA Histograms
 ($X_{Pt} = 0.0$ inch, $Y_{Pt} = 0.2$ inch, $X_{Pw} = -1.17$ inches)
 a) Event Pair = Rise_{SS}-Fall_{SL}
 b) Event Pair = Fall_{SS}-Rise_{SL}



**Fig. 6-1: Surface Flow Visualization Using
Kerosene-Lampblack Technique
(a) Slot/No Suction**



**Fig. 6-1: Surface Flow Visualization Using
Kerosene-Lampblack Technique
(b) Slot/Suction**

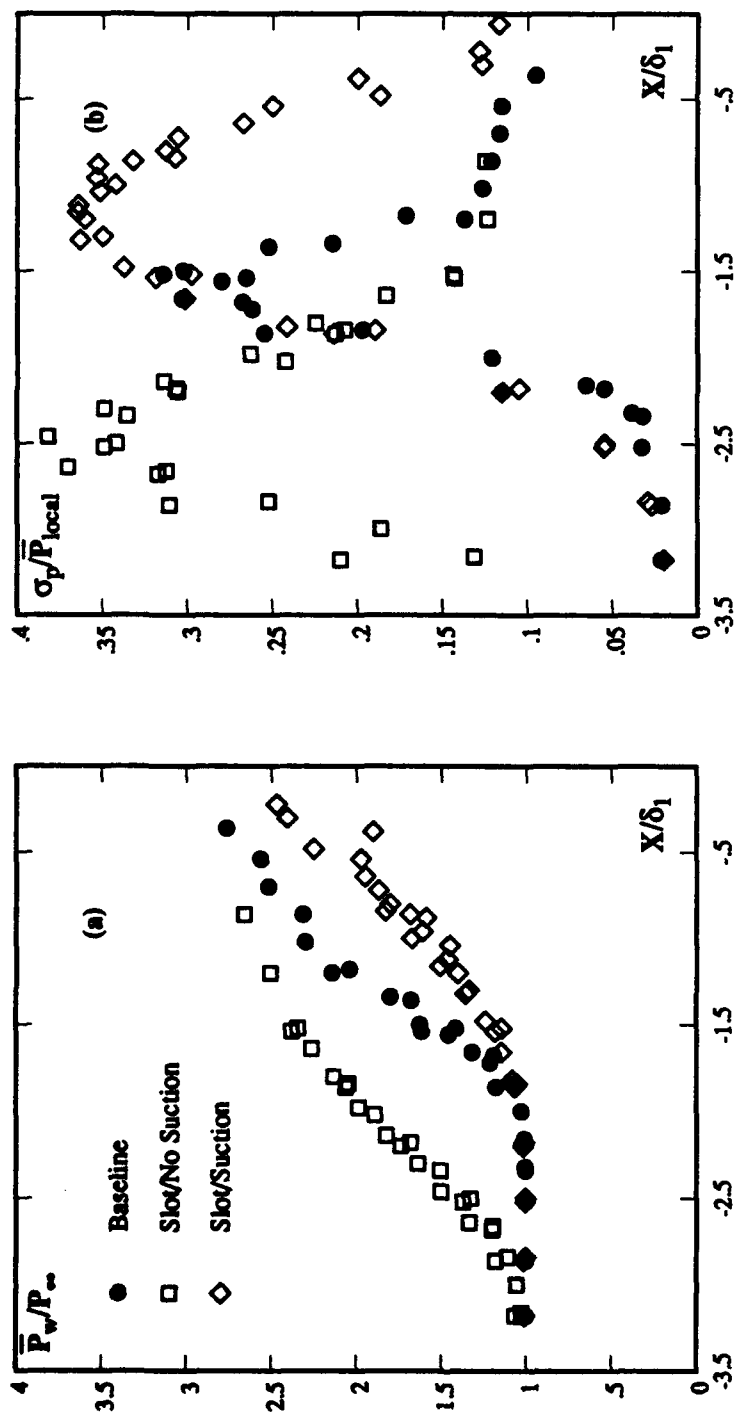


Fig. 6-2: Streamwise Surface Distributions
a) Normalized Mean Surface Pressure
b) Normalized Surface Pressure RMS

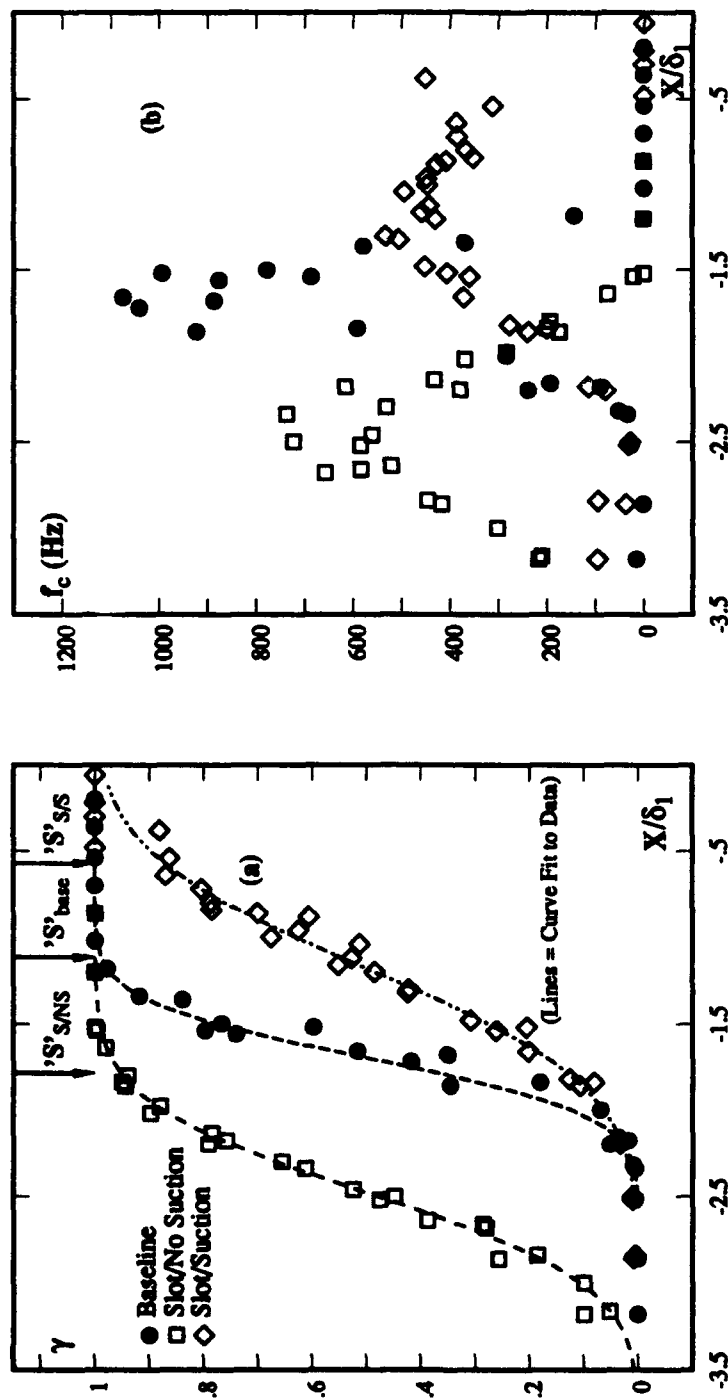


Fig. 6-3: Separation Shock Streamwise Distributions

- a) Intermittency
- b) Zero-Crossing Frequency

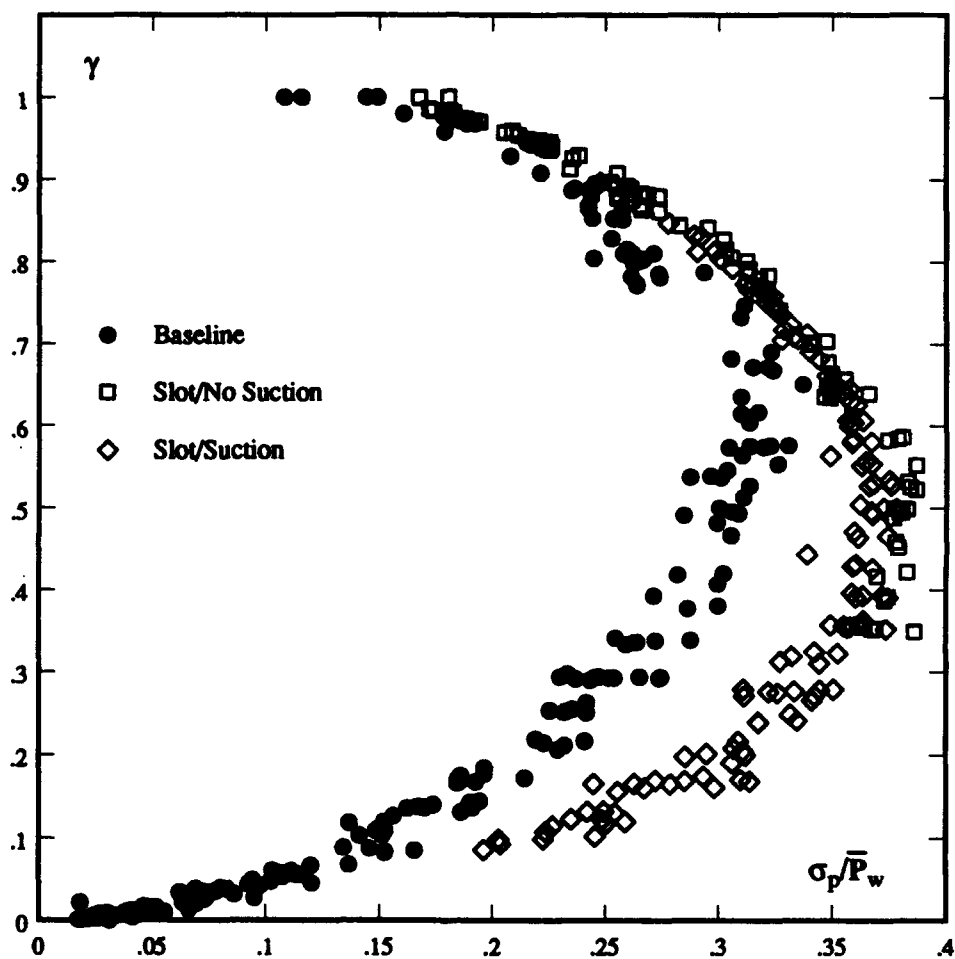


Fig. 6-4: Comparison of Surface Pressure RMS and Separation Shock Intermittency Varying Ramp Face Geometry

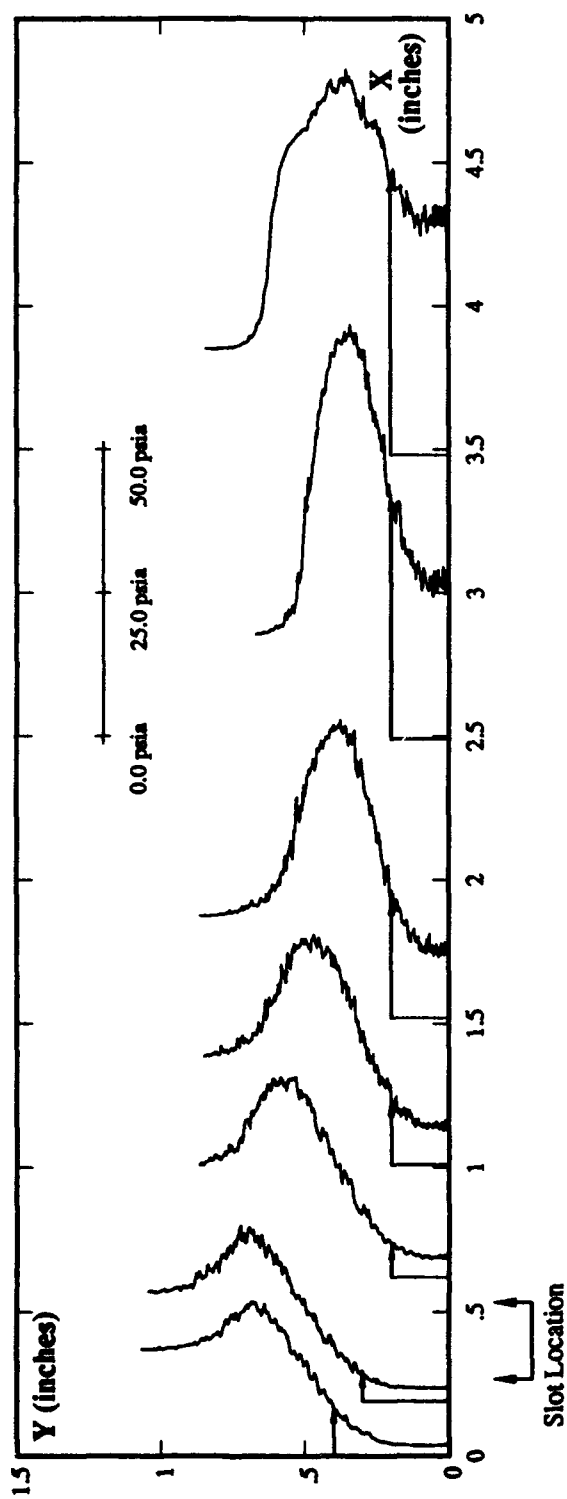


Fig. 6-5: Pitot Pressure Profiles Above Ramp Surface
(a) Slot/No Suction

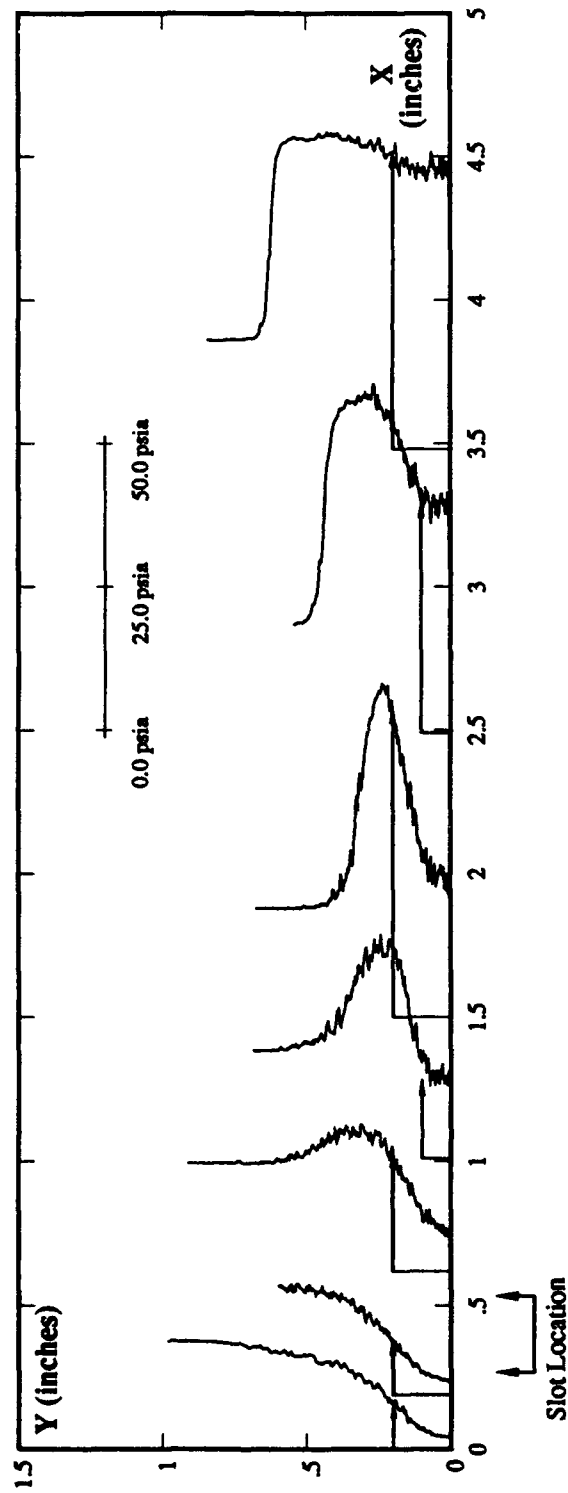


Fig. 6-5: Pitot Pressure Profiles Above Ramp Surface
(b) Slot/Suction

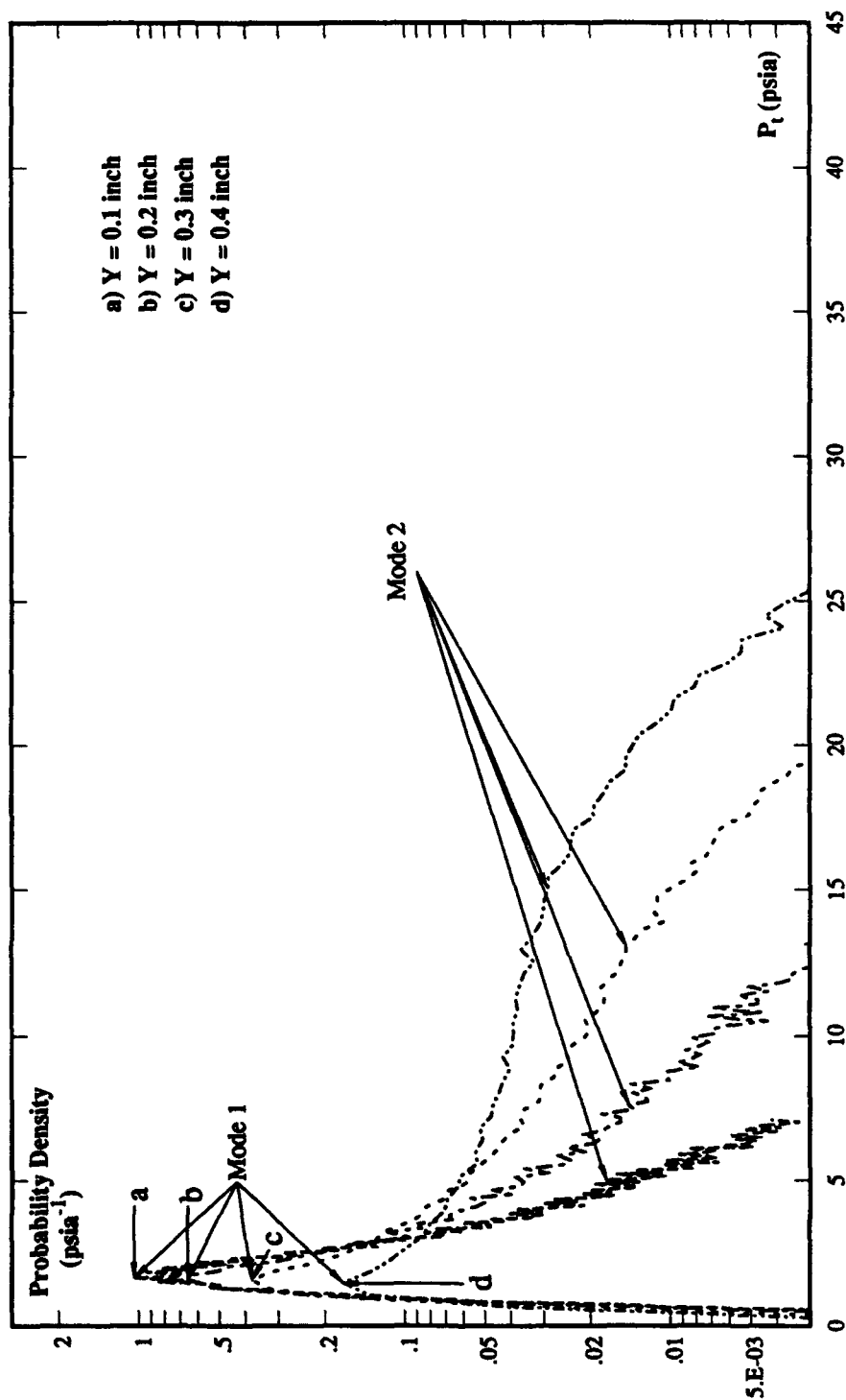
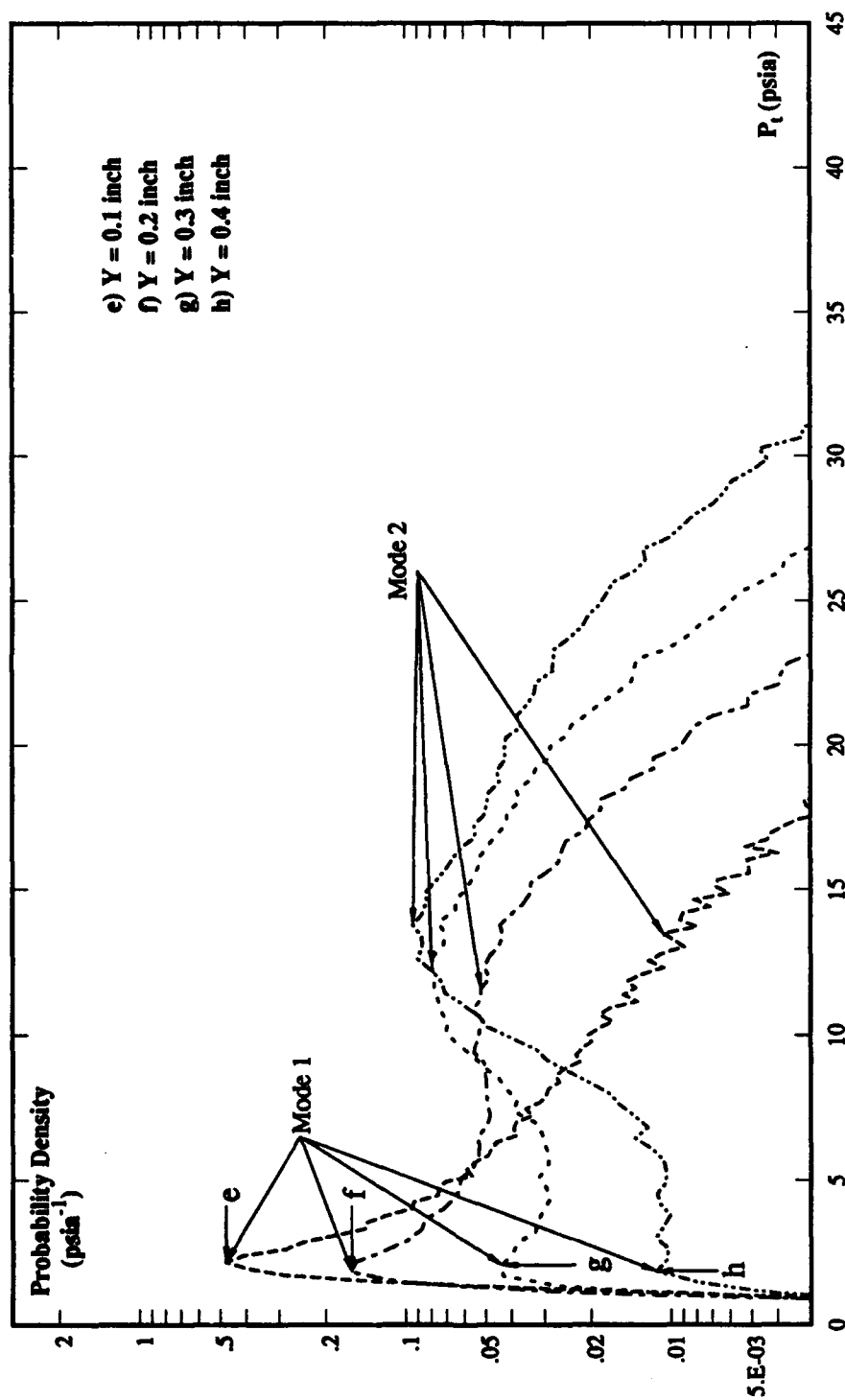


Fig. 6-6: Variation in Pitot Pressure PDD's at
 $X = 0.2$ inch with Height Above the Ramp Surface
 (a) Slot/No Suction



**Fig. 6-6: Variation in Pitot Pressure PDD's at
X = 0.2 inch with Height Above the Ramp Surface
(b) Slot/Suction**

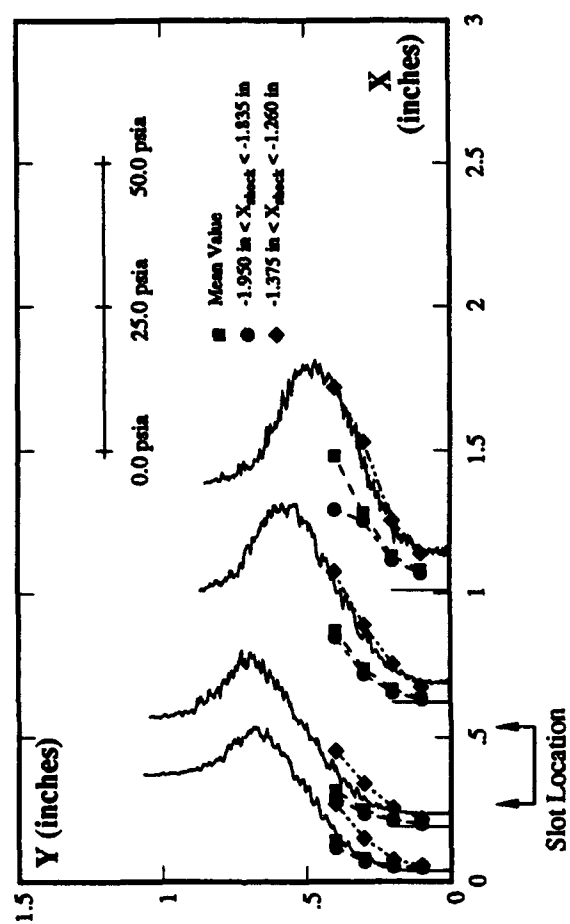


Fig. 6-7: Frozen Pitot Pressure Profiles
(a) Slot/No Suction

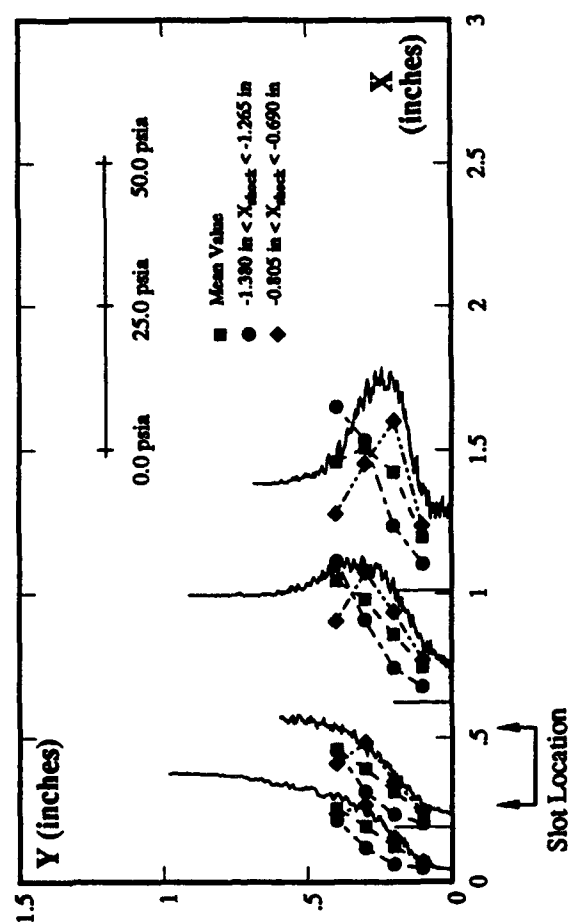


Fig. 6-7: Frozen Pitot Pressure Profiles
(b) Slot/Suction

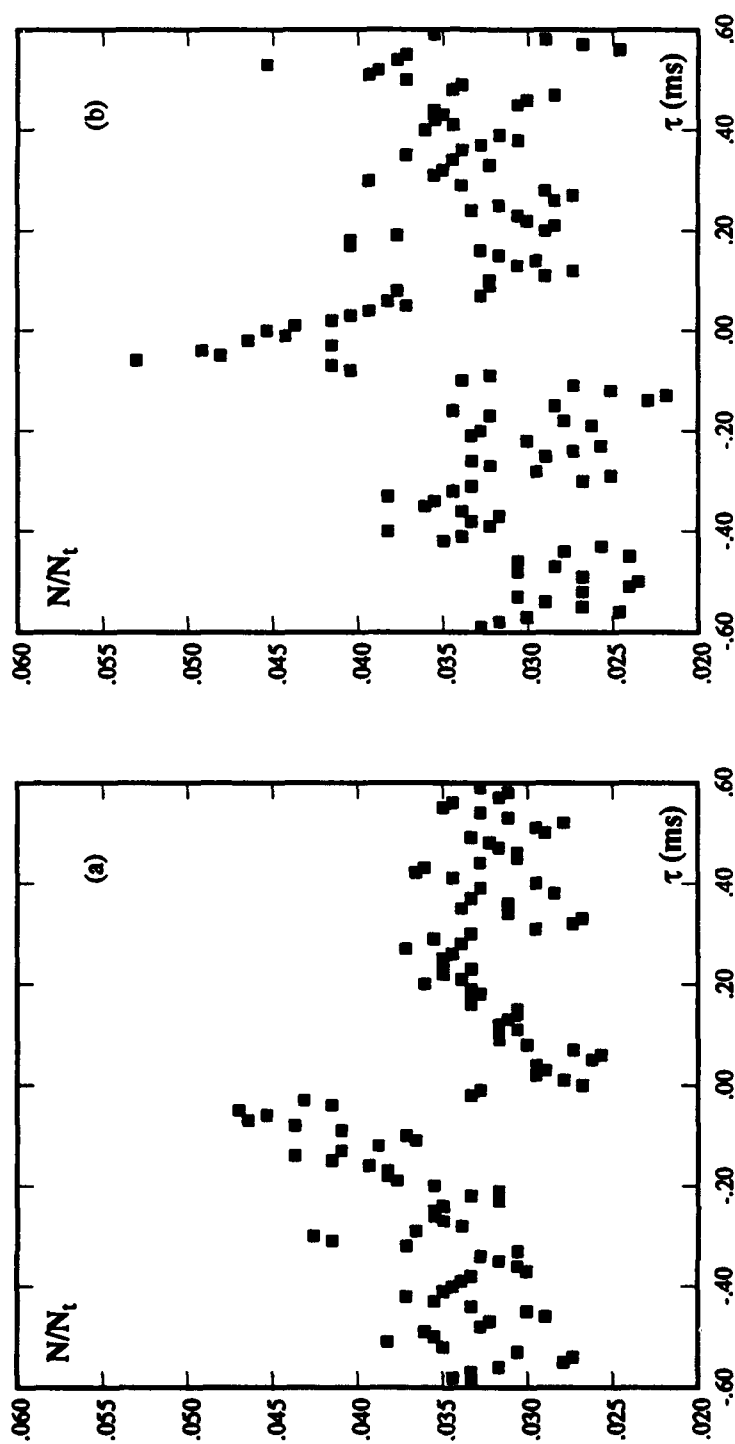


Fig. 6-8: ERTA Histograms - Slot/No Suction
 ($X_{Pt} = 0.0$ inch, $Y_{Pt} = 0.4$ inch, $X_{Pw} = -1.835$ inches)
 a) Event Pair = RiseSS-FallSL
 b) Event Pair = FallSS-RiseSL

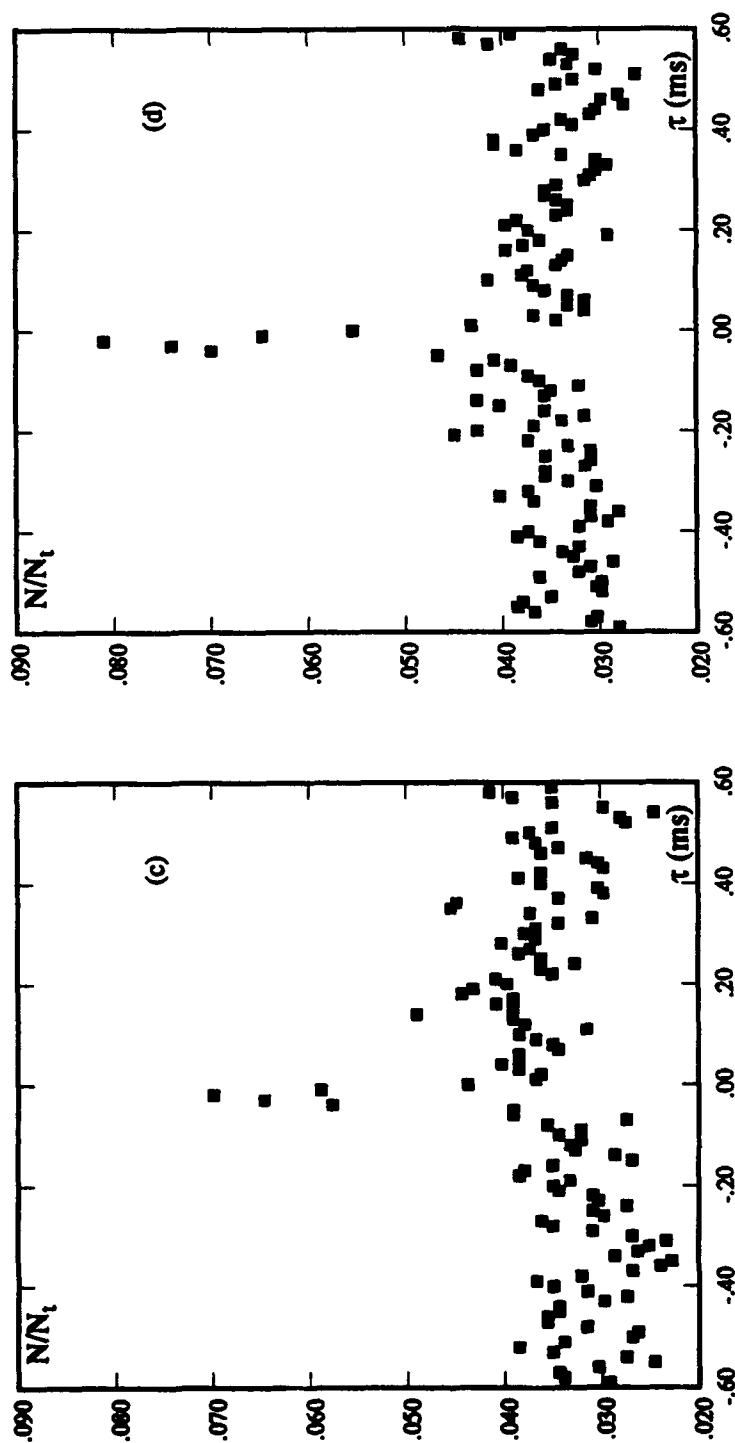
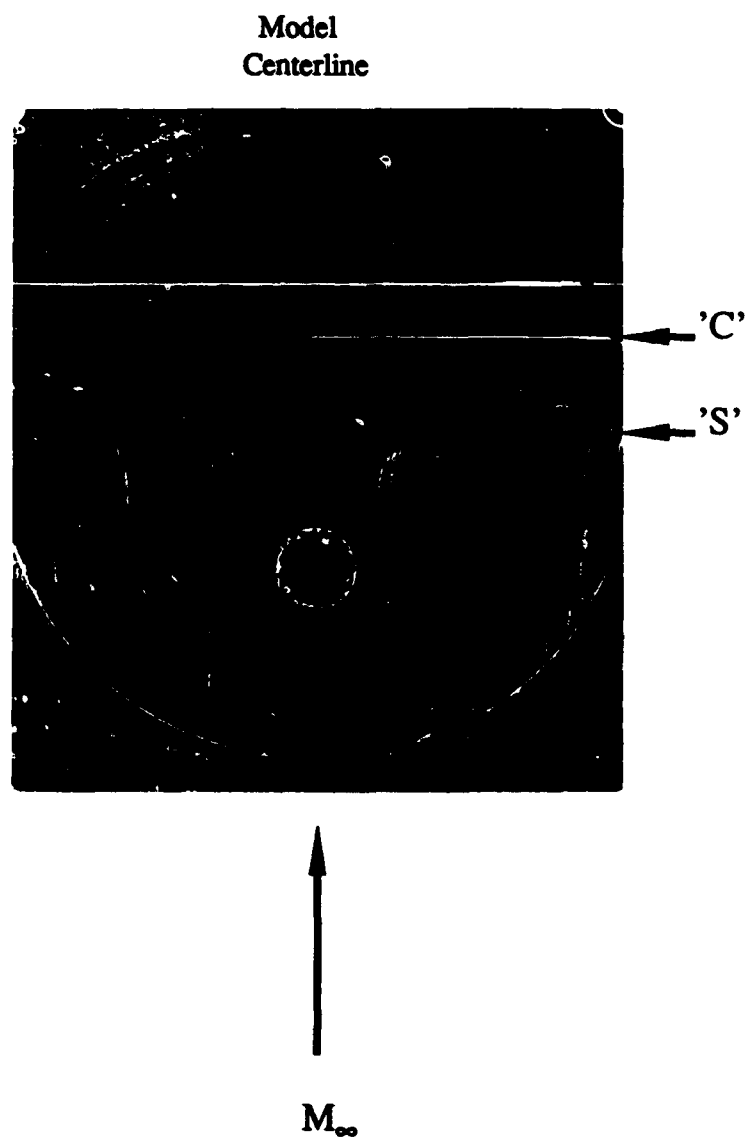


Fig. 6-8: ERTA Histograms - Slot/Suction
 ($X_{Pt} = 0.0$ inch, $Y_{Pt} = 0.1$ inch, $X_{Pw} = -0.690$ inch)
 c) Event Pair = RisesS-FallSL
 d) Event Pair = FallSS-RisesL



**Fig. 6-9: Surface Flow Visualization Using
Kerosene-Lampblack Technique
-Baseline/No Side Fences**

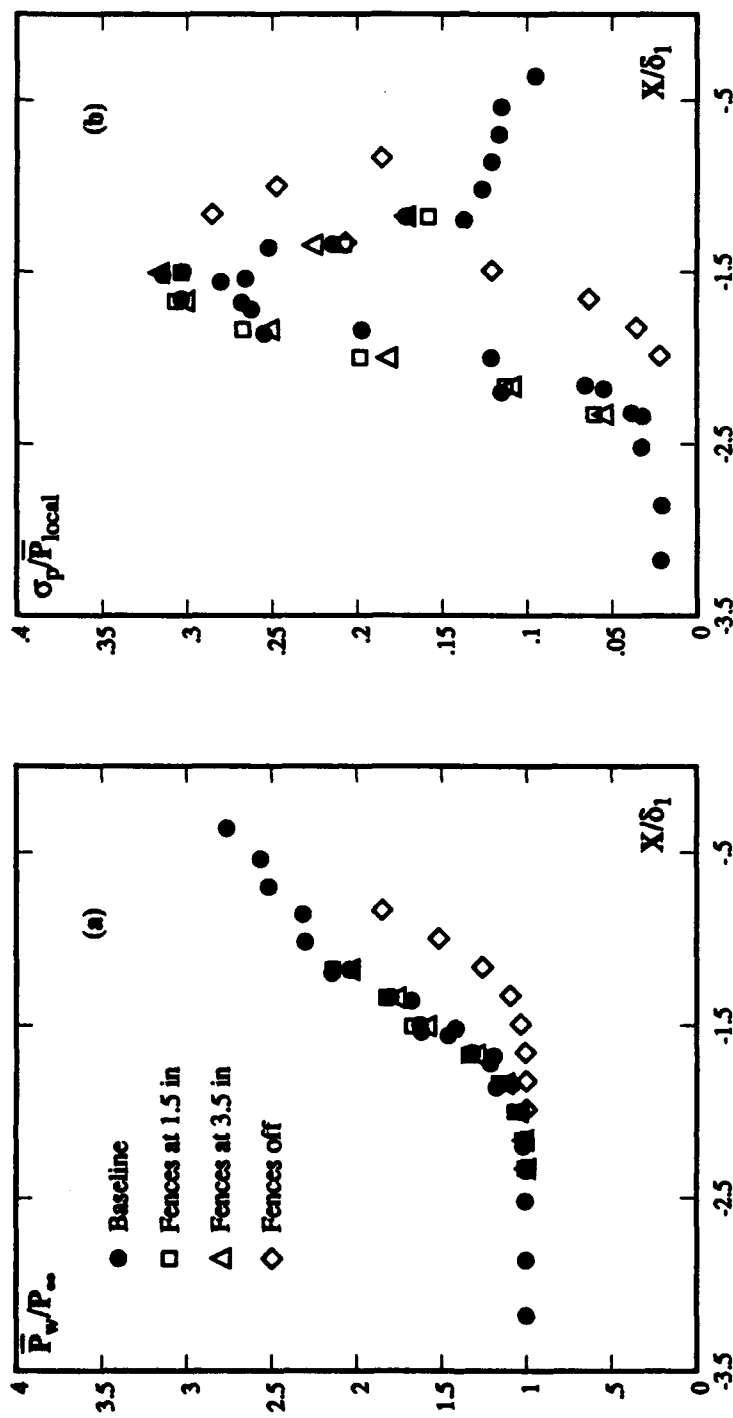


Fig. 6-10: Streamwise Surface Distributions
-Effect of End Fences
a) Normalized Mean Surface Pressure
b) Normalized Surface Pressure RMS

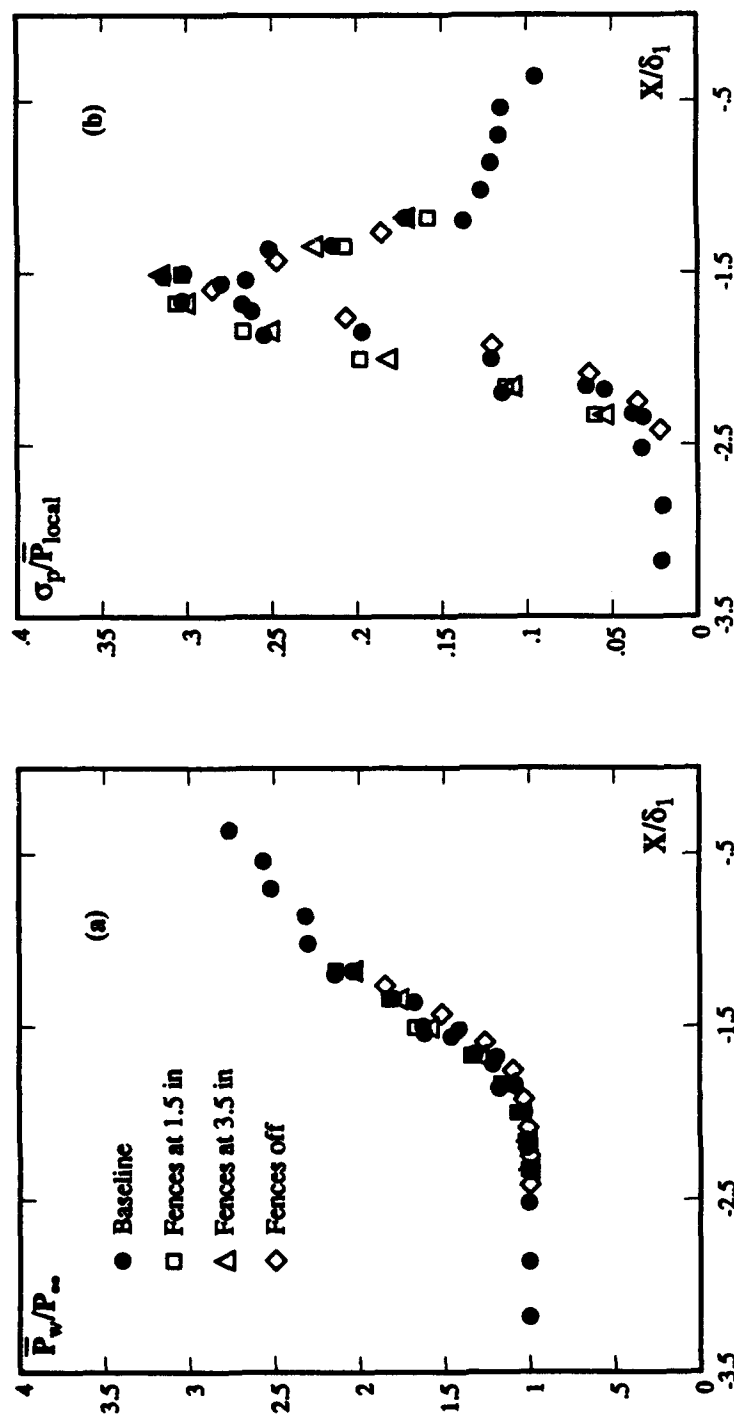


Fig. 6-11: Streamwise Surface Distributions
-Effect of End Fences (with offset)
a) Normalized Mean Surface Pressure
b) Normalized Surface Pressure RMS

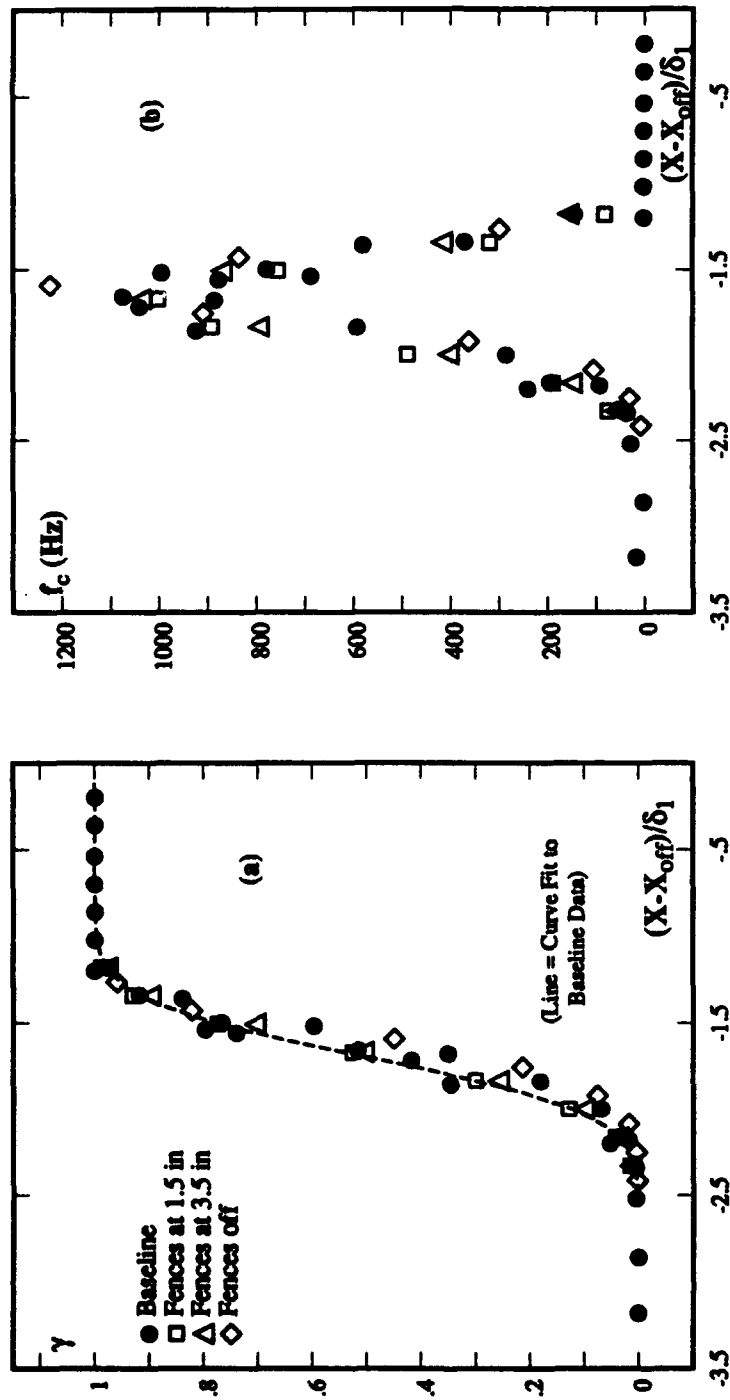


Fig. 6-12: Separation Shock Streamwise Distributions

-Effect of End Fences (with offset)

a) Intermittency

b) Zero-Crossing Frequency

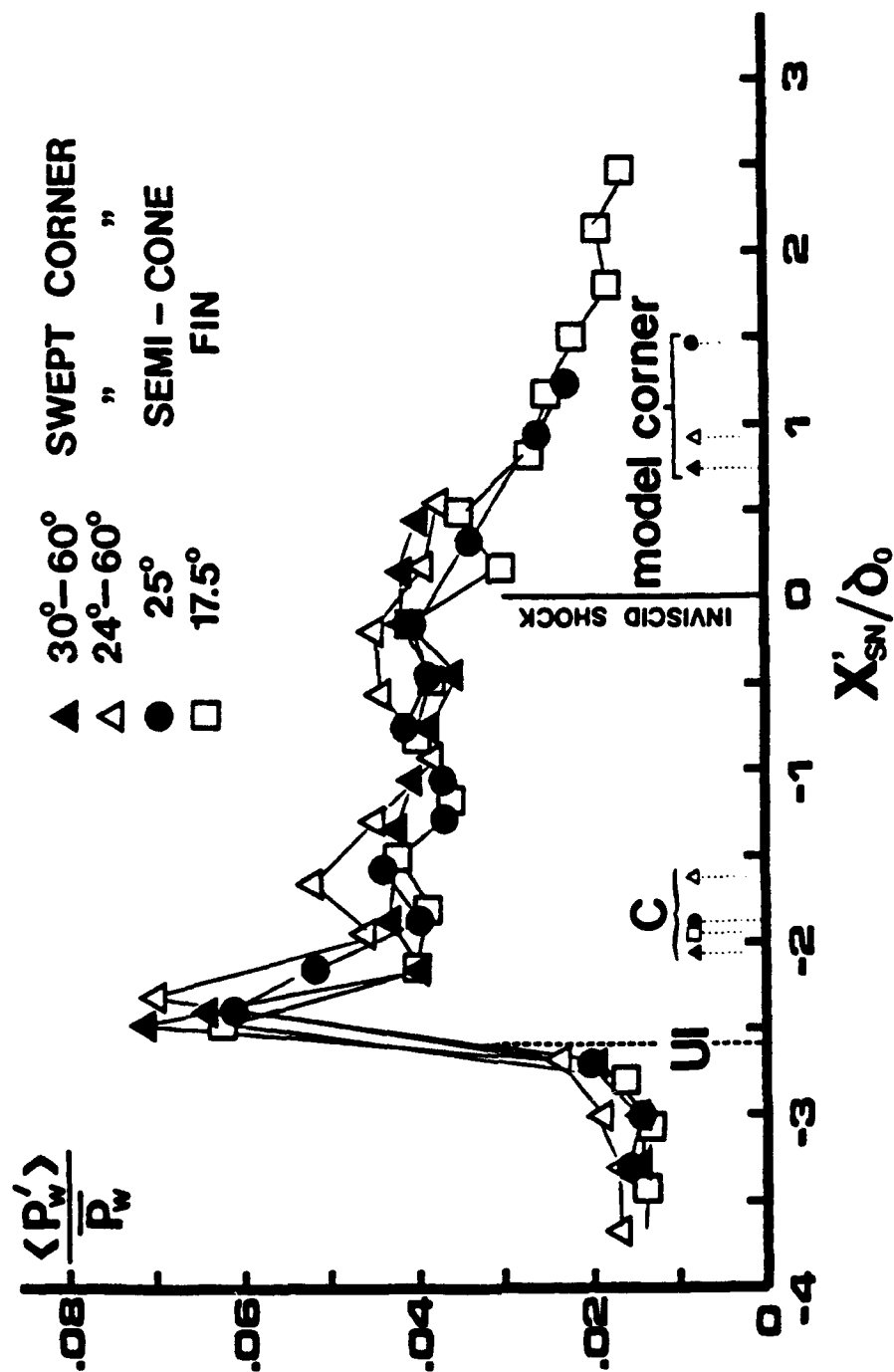
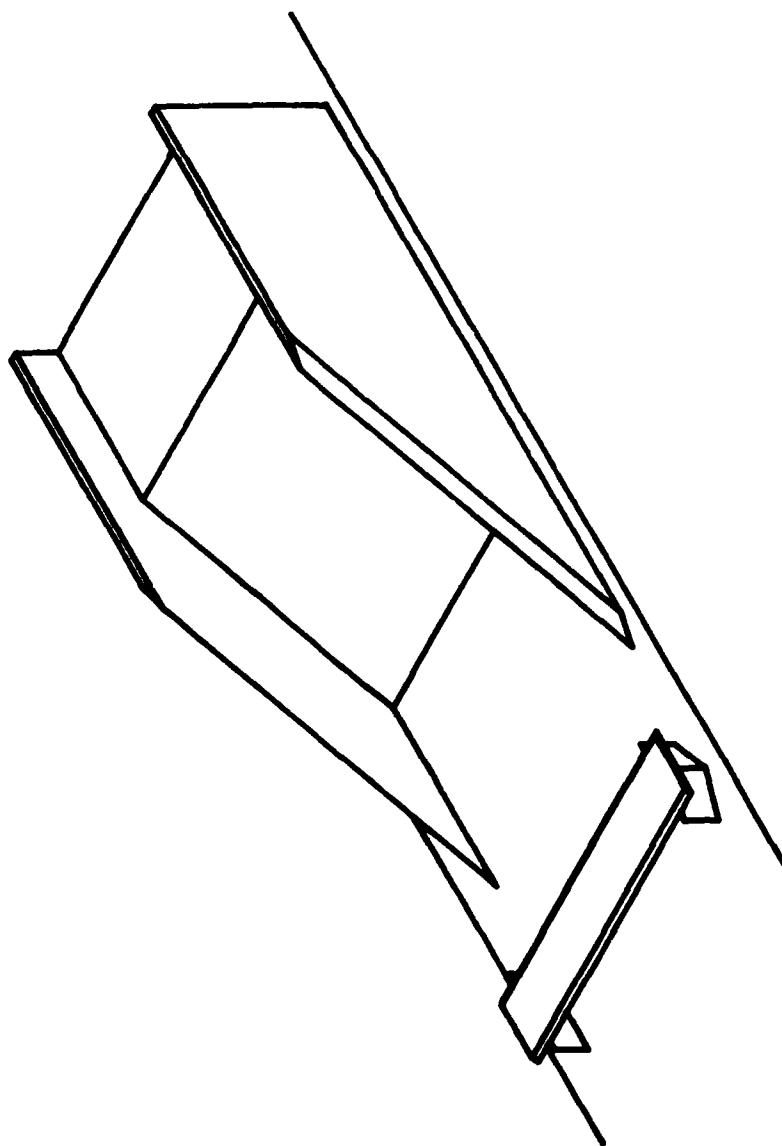
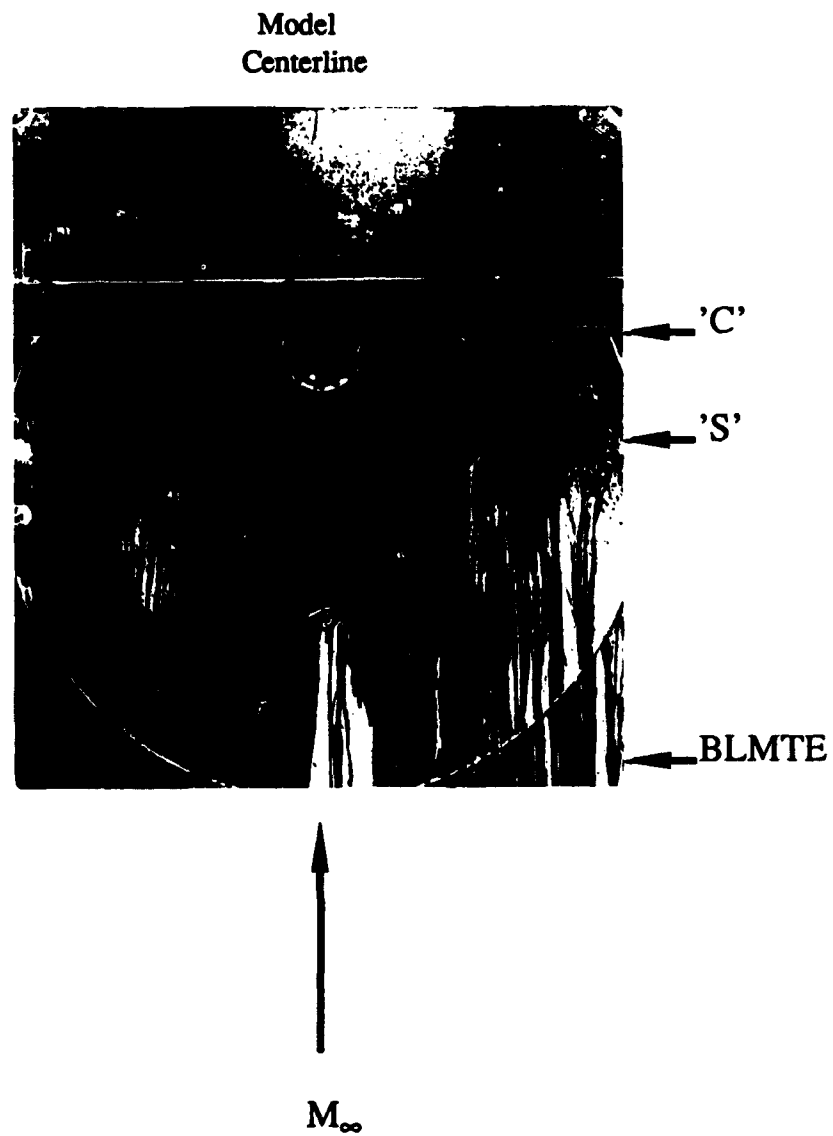


Fig. 6-13: Surface Pressure RMS Distributions Varying Shock-Generating Geometry (Tran [1987])



**Fig. 7-1: Layout of Compression Corner with
Boundary Layer Manipulator**



**Fig. 7-2: Surface Flow Visualization Using
Kerosene-Lampblack Technique
w/ Boundary Layer Manipulator**

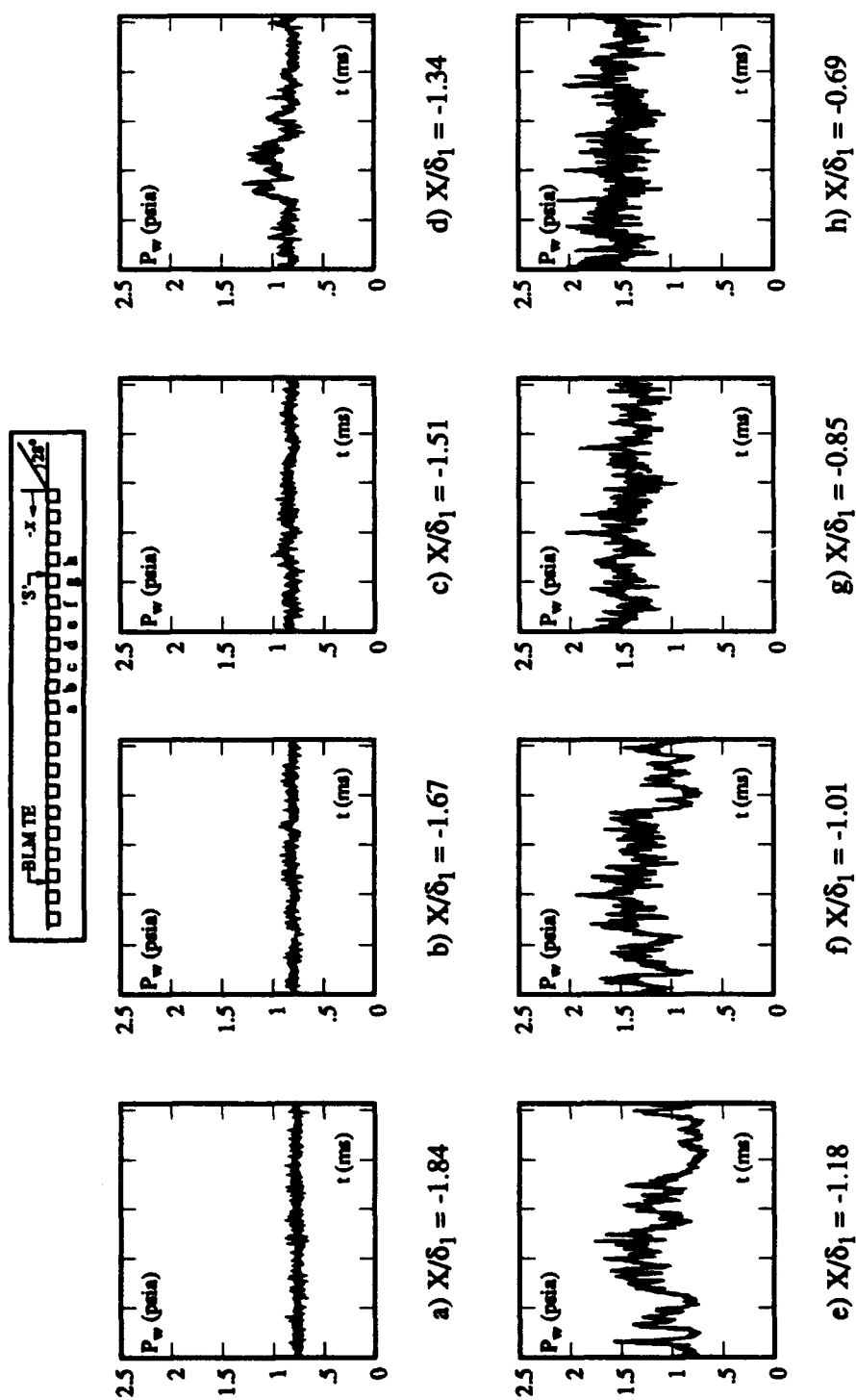
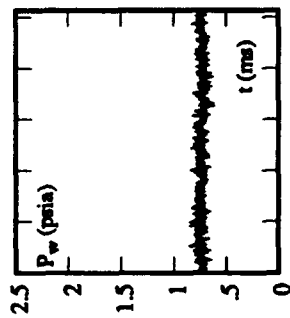
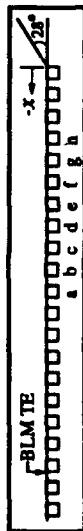
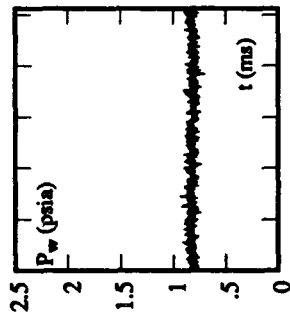


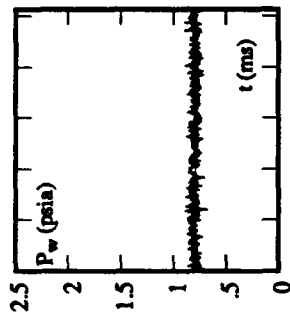
Fig. 7-3: Surface Pressure Signals Beneath the
Translating Separation Shock (15° BLM)
(1-record / 1024 data points)



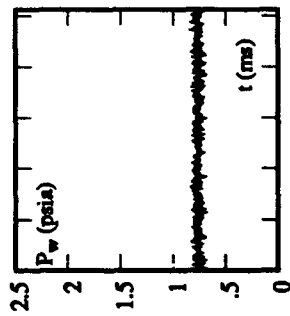
a) $X/\delta_1 = -1.84$



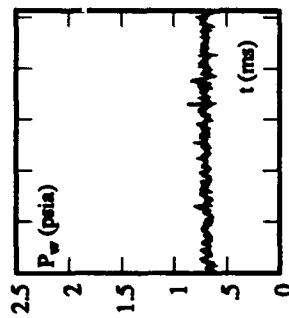
b) $X/\delta_1 = -1.67$



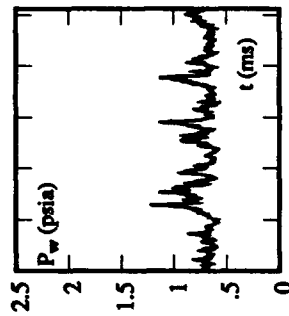
c) $X/\delta_1 = -1.51$



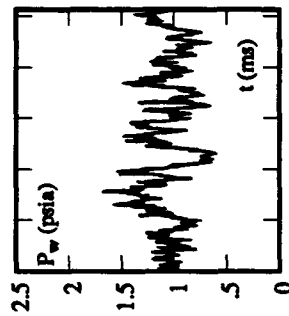
d) $X/\delta_1 = -1.34$



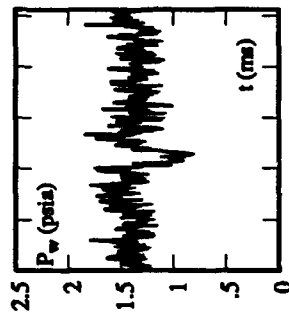
e) $X/\delta_1 = -1.18$



f) $X/\delta_1 = -1.01$



g) $X/\delta_1 = -0.85$



h) $X/\delta_1 = -0.69$

Fig. 7-4: Surface Pressure Signals Beneath the Translating Separation Shock (35° BLM) (1-record / 1024 data points)

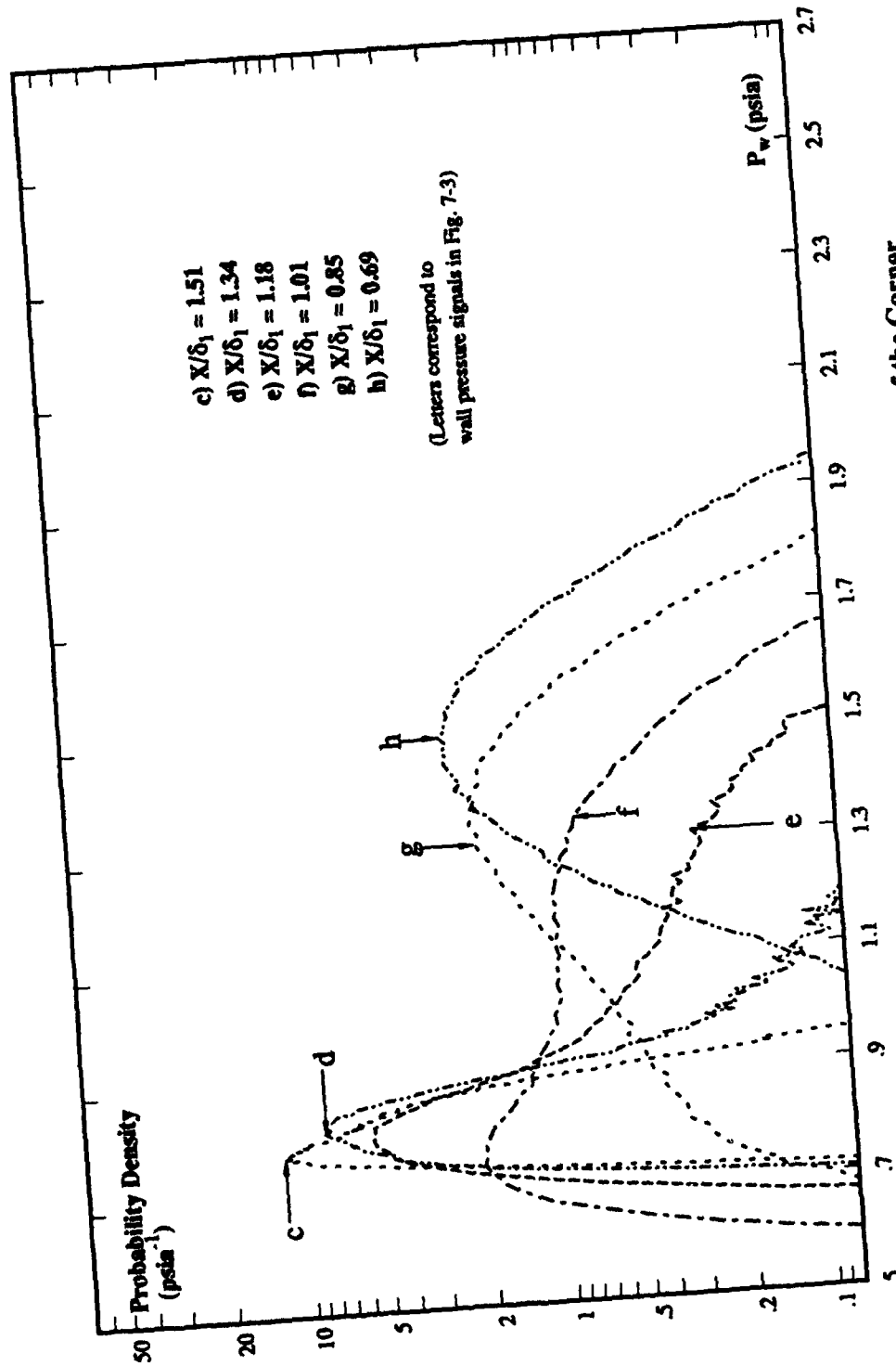


Fig. 7-5: Surface Pressure PDD's Upstream of the Corner
- 15° BLM

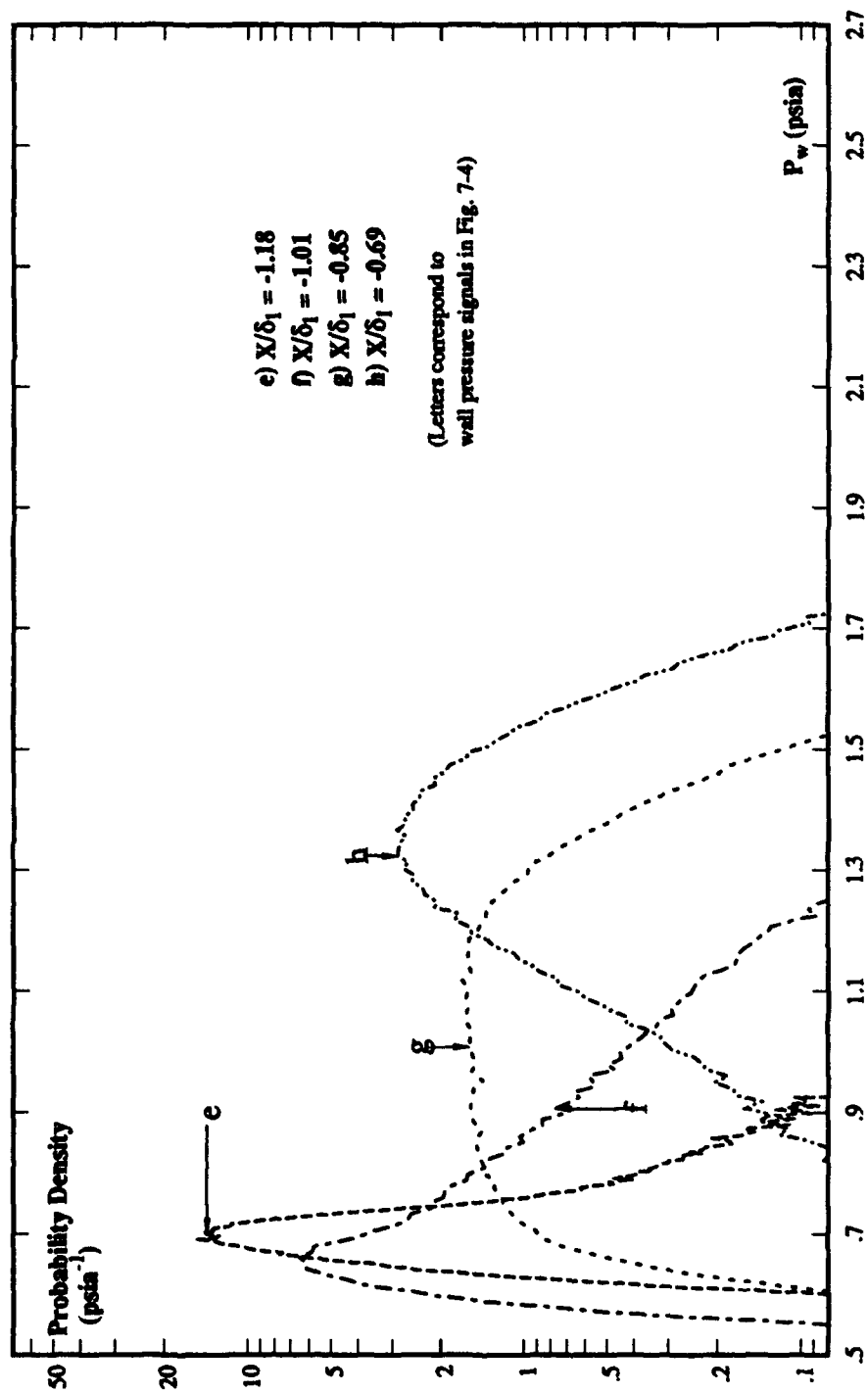
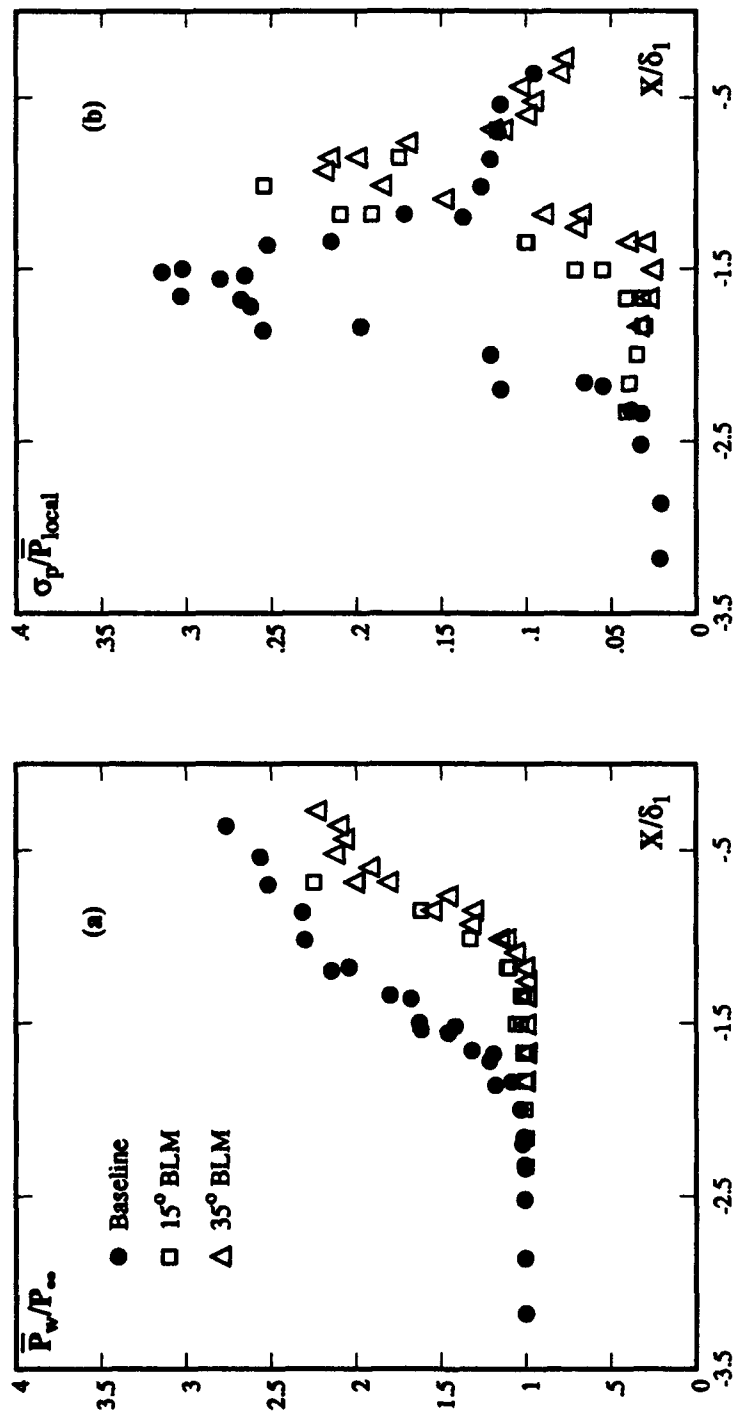


Fig. 7-6: Surface Pressure PDD's Upstream of the Corner
- 35° BLM



**Fig. 7-7: Streamwise Surface Distributions
-Effect of BLM**
a) Normalized Mean Surface Pressure
b) Normalized Surface Pressure RMS

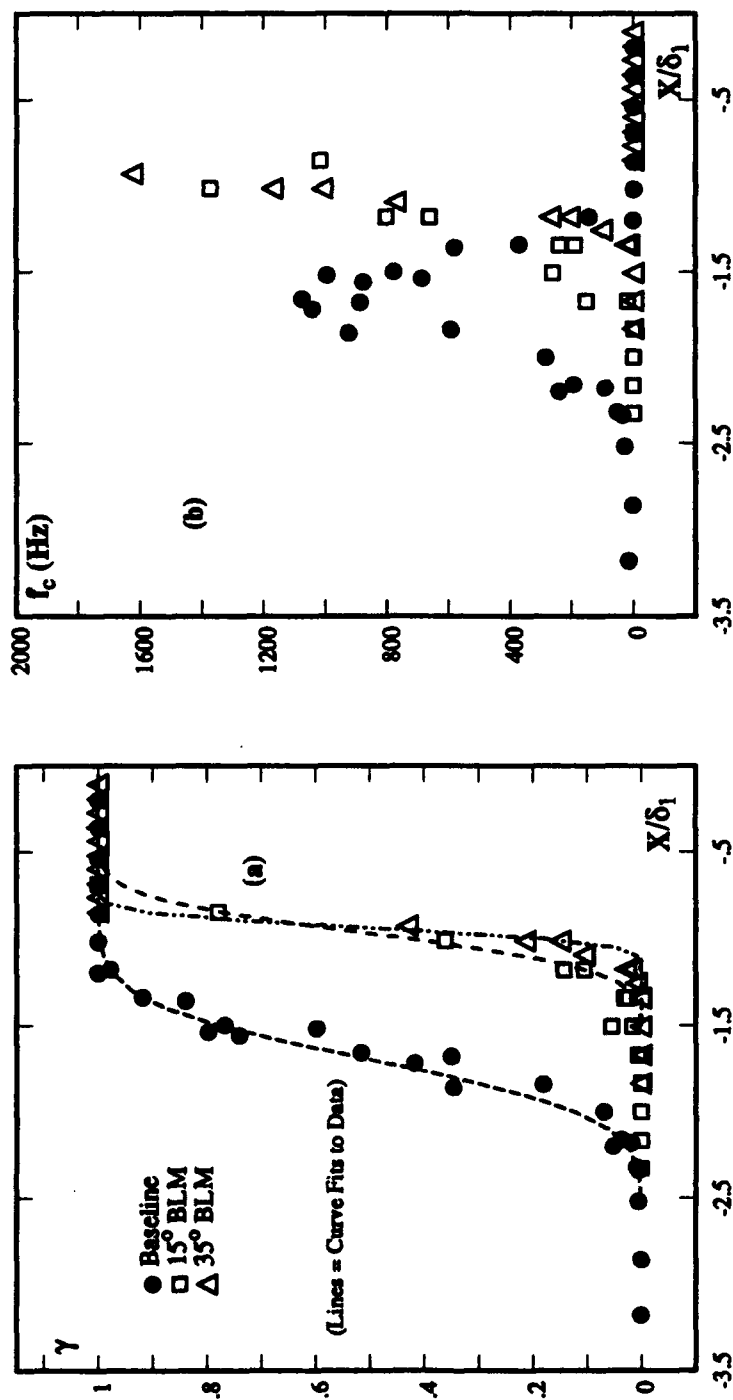


Fig. 7-8: Separation Shock Streamwise Distributions

-Effect of BLM

a) Intermittency

b) Zero-Crossing Frequency

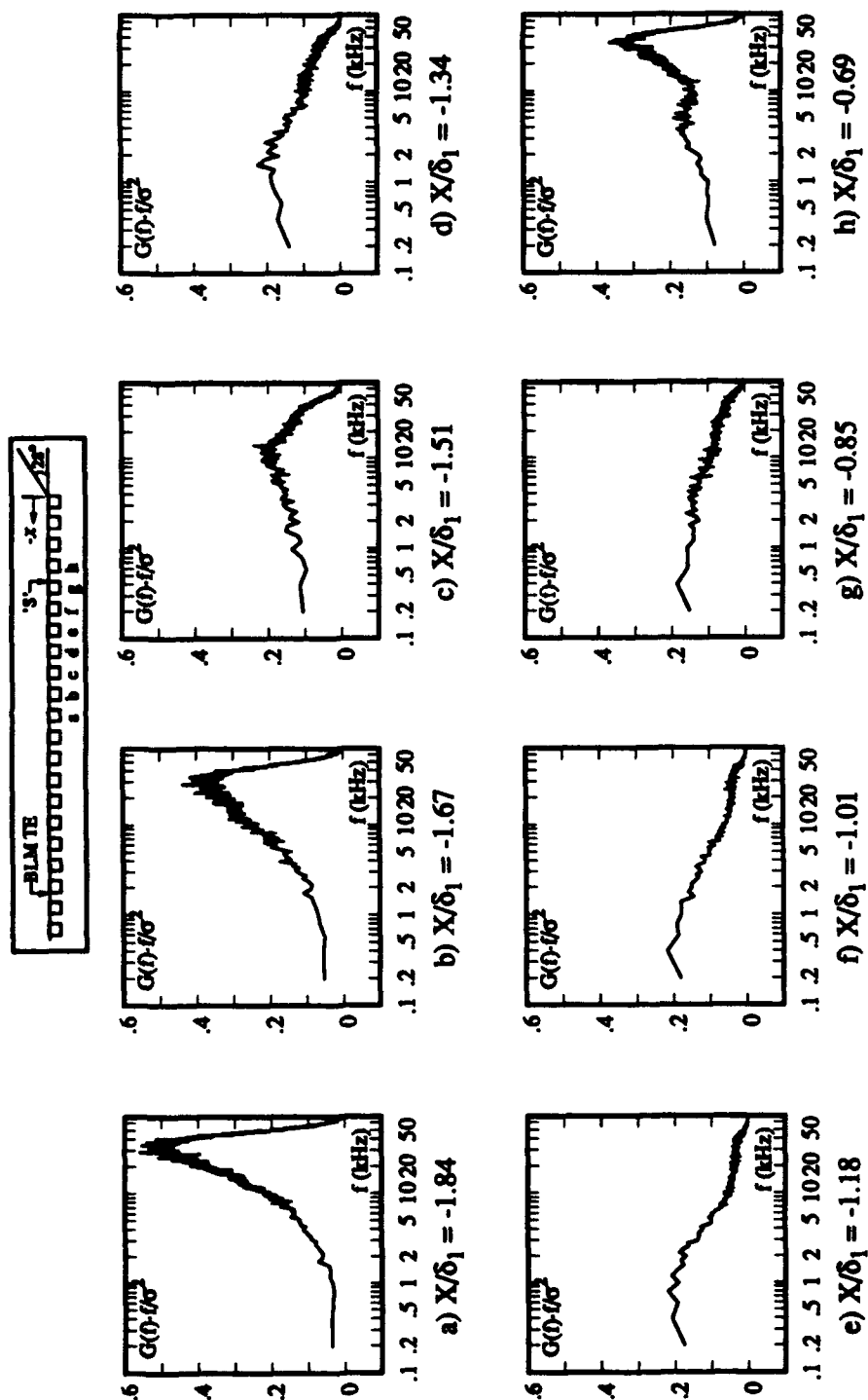


Fig. 7-9: Surface Pressure Power Spectra in the
15° BLM/Compression Corner Interaction
(Sampling Frequency = 200 kHz)

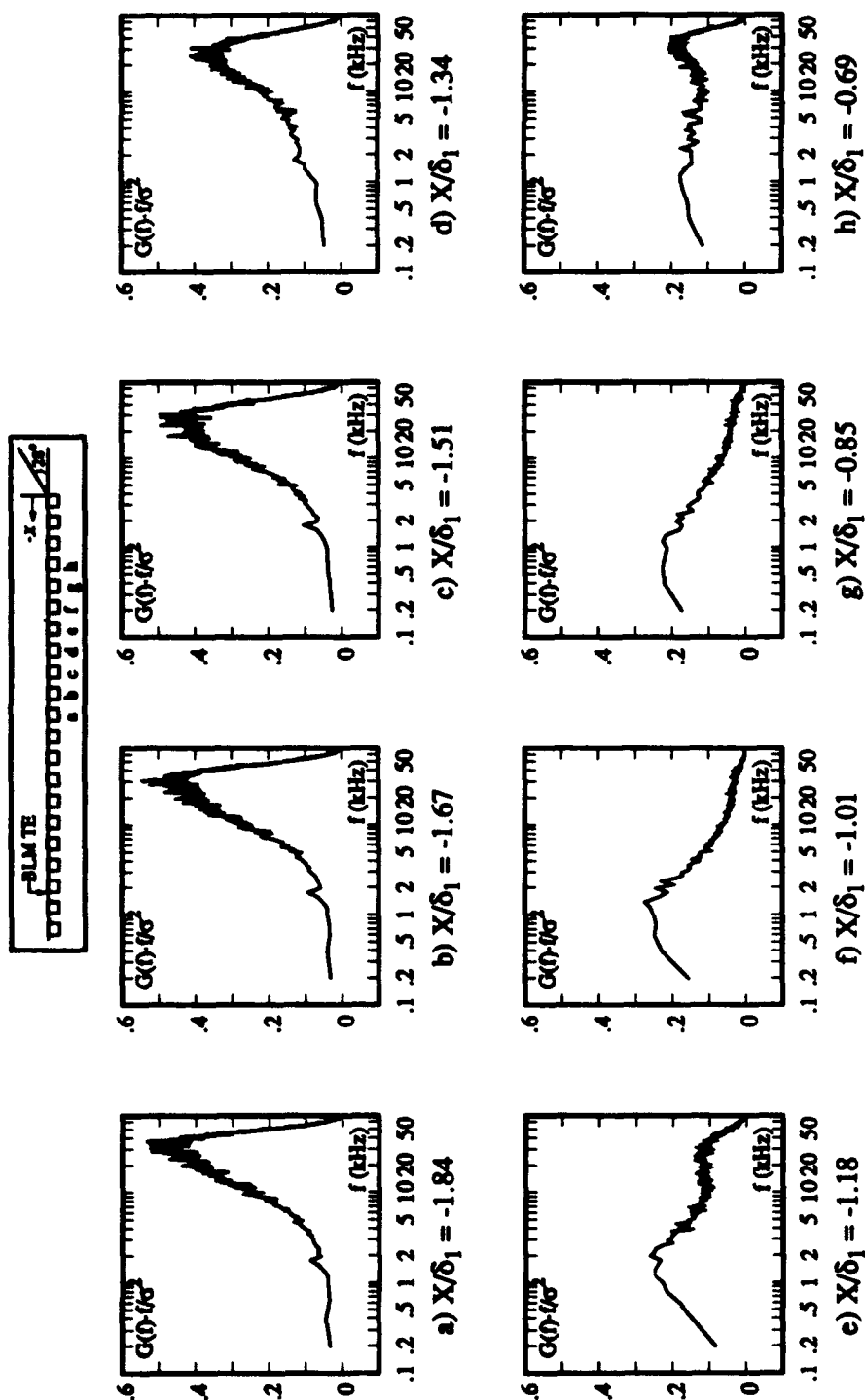


Fig. 7-10: Surface Pressure Power Spectra in the 35° BLM/Compression Corner Interaction (Sampling Frequency = 200 kHz)

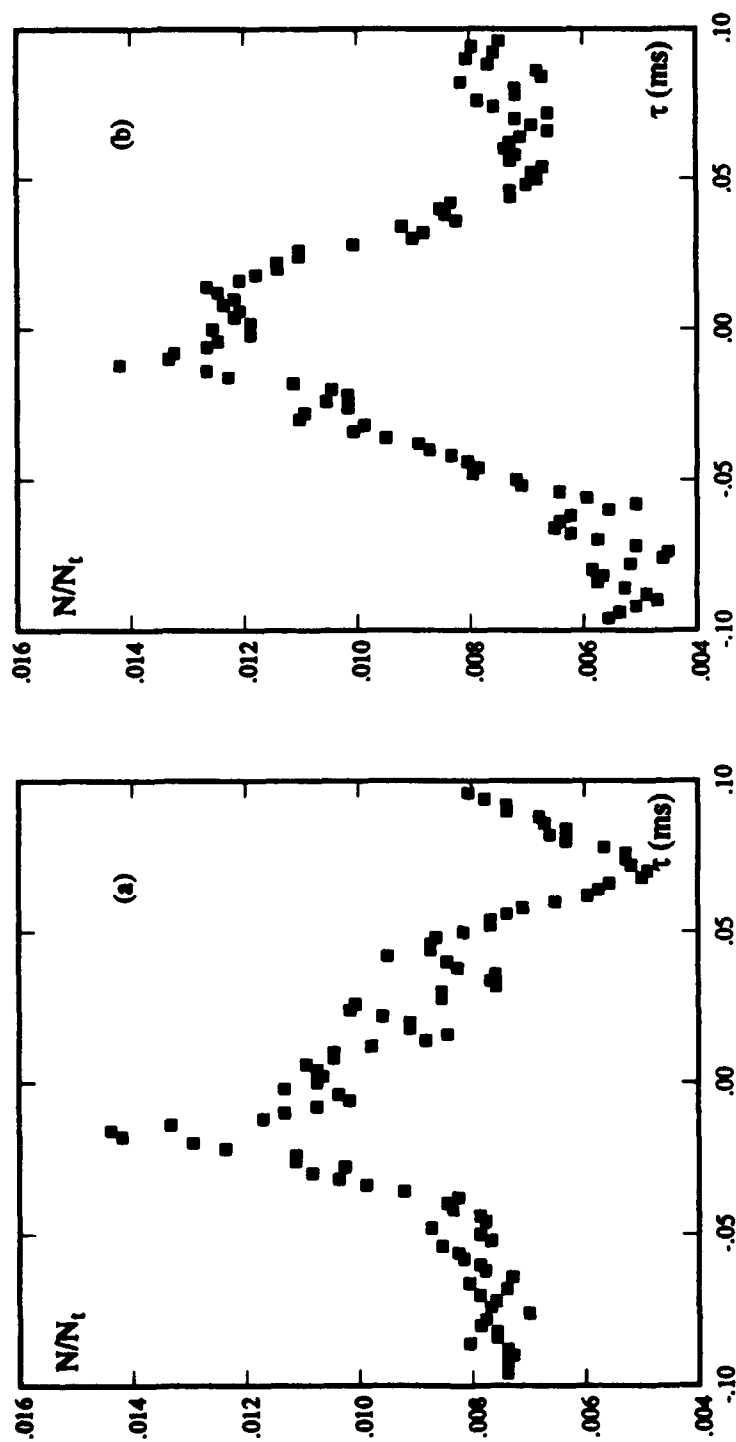


Fig. 7-11: ERTA Histograms - 15° BLM
 ($X_{Pt} = 0.0$ inch, $Y_{Pt} = 0.2$ inch, $X_{Pw} = -0.825$ inch)
 a) Event Pair = Risess-FallSL
 b) Event Pair = FallSS-RisessL

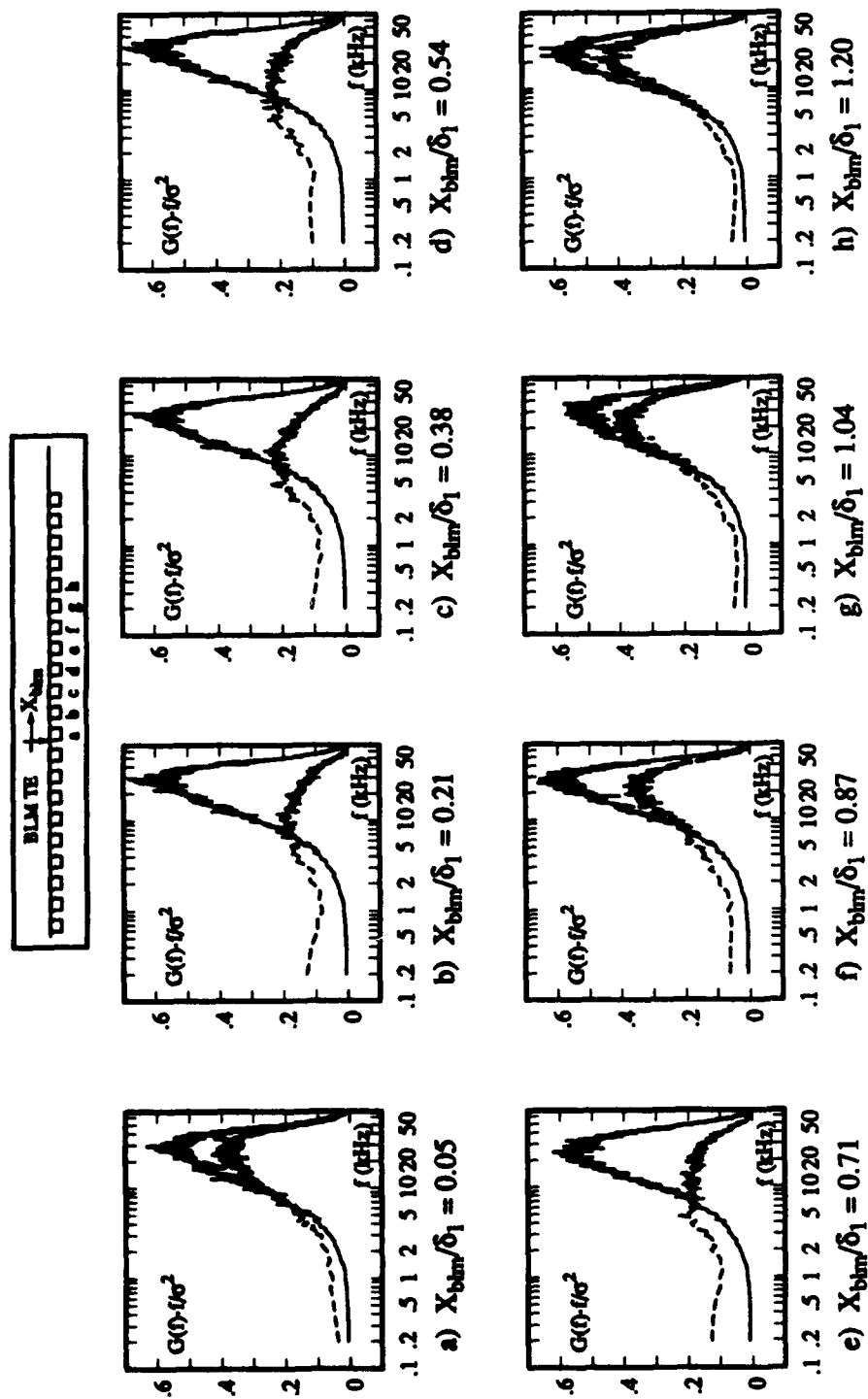
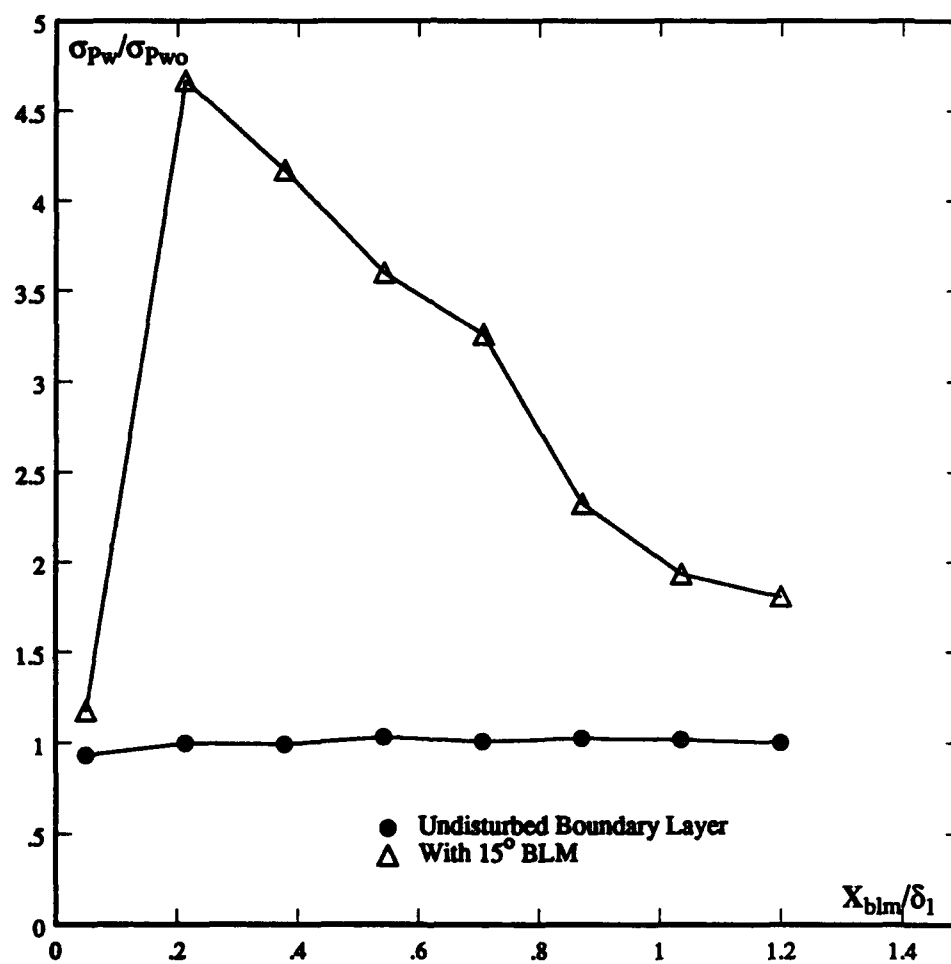


Fig. 7-12: Surface Pressure Power Spectra Downstream
of the 15° BLM Trailing Edge
(Solid Line = without BLM / Dashed Line = with BLM)



**Fig. 7-13: Comparison of Surface Pressure RMS
with and without BLM**

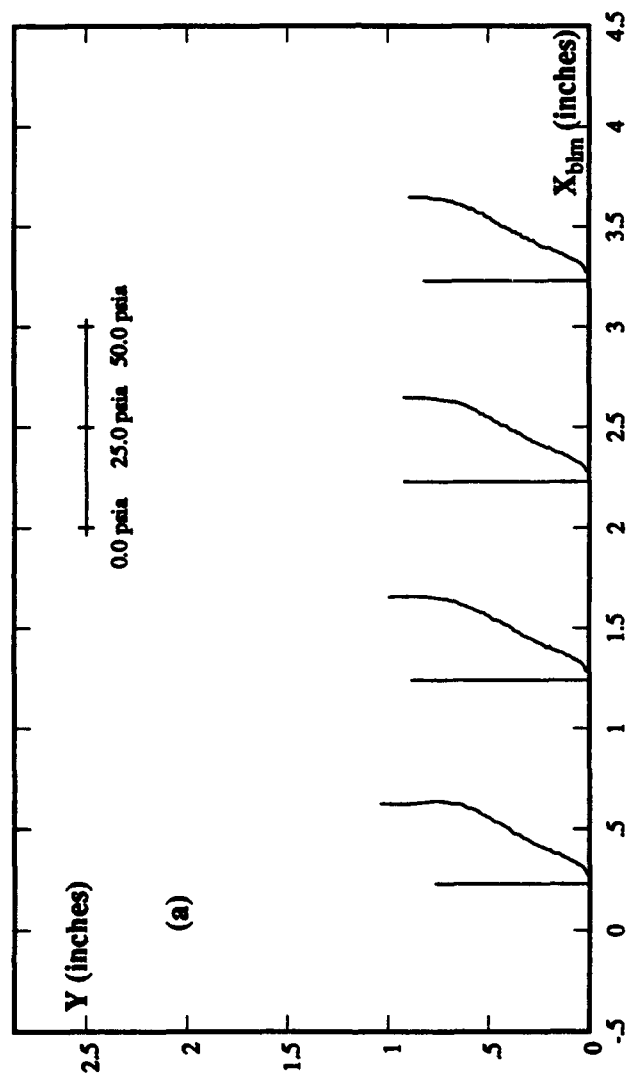


Fig. 7-14: Pitot Pressure Profiles - Undisturbed Boundary Layer

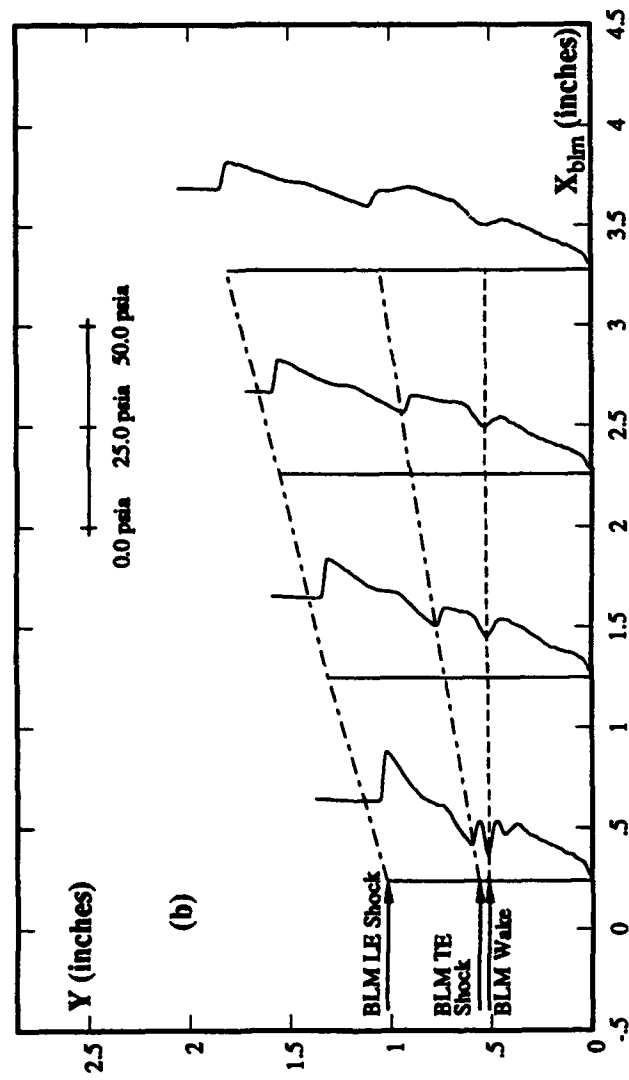


Fig. 7-14: Pitot Pressure Profiles - 15° BLM
(continued)

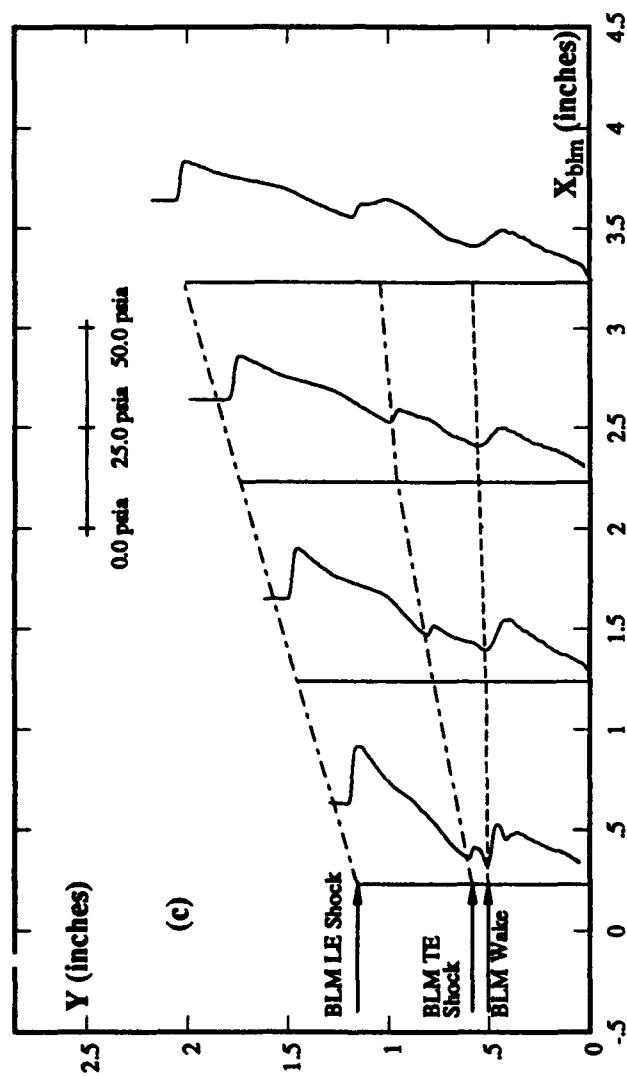


Fig. 7-14: Pitot Pressure Profiles - 35° BLM
(concluded)

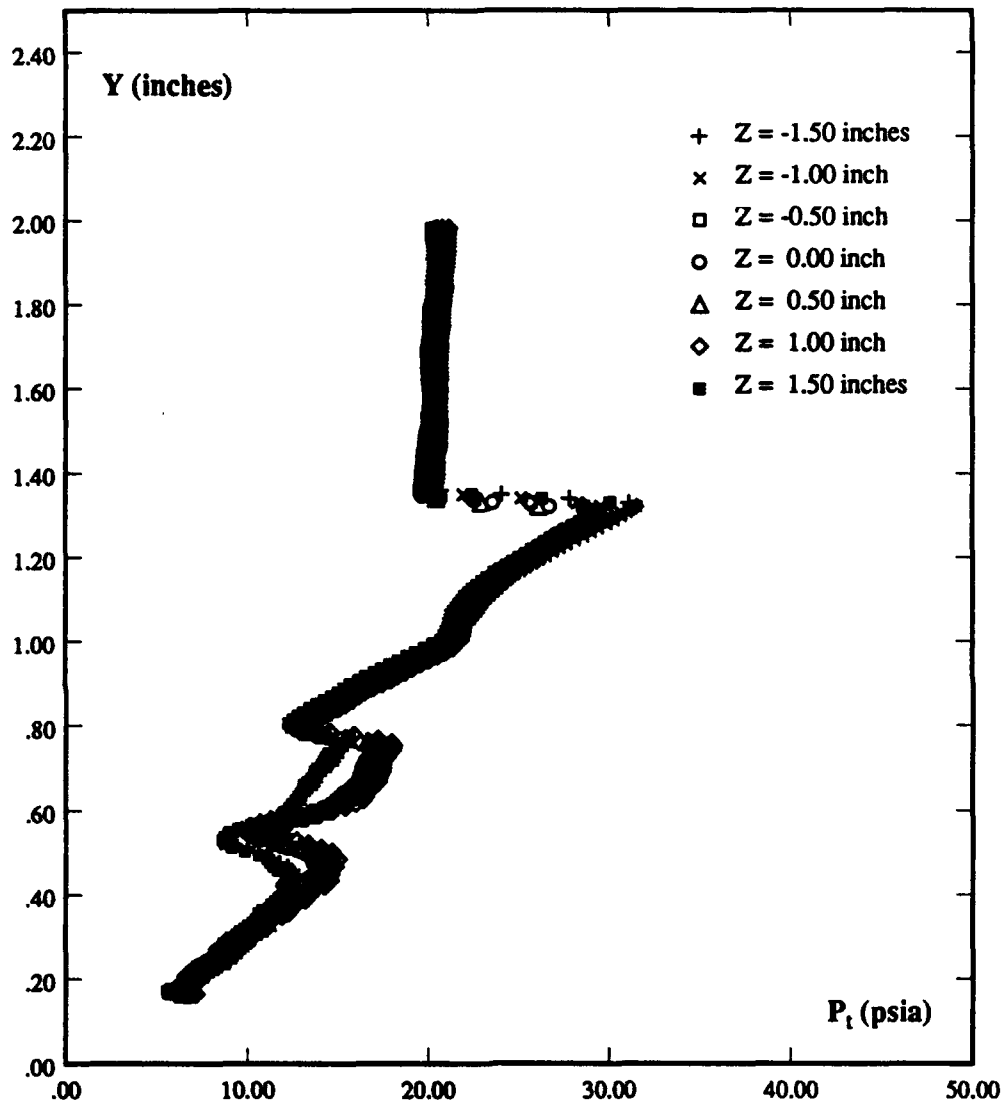
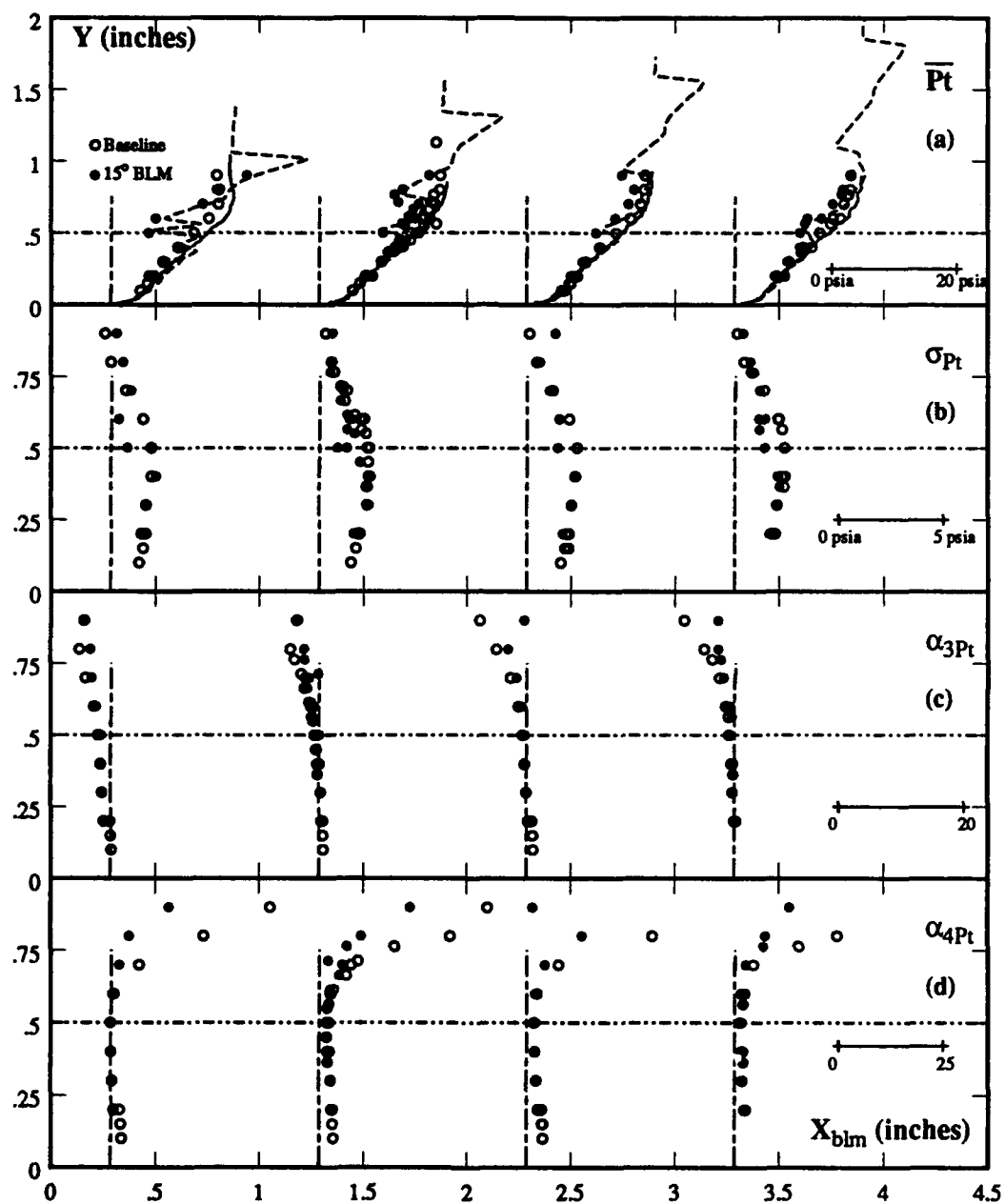


Fig. 7-15: Spanwise Variation of Pitot Pressure Profiles
 $X_{blm} = 1.28$ inches - 15° BLM



**Fig. 7-16: Pitot Pressure Statistical Moments
with and without BLM**

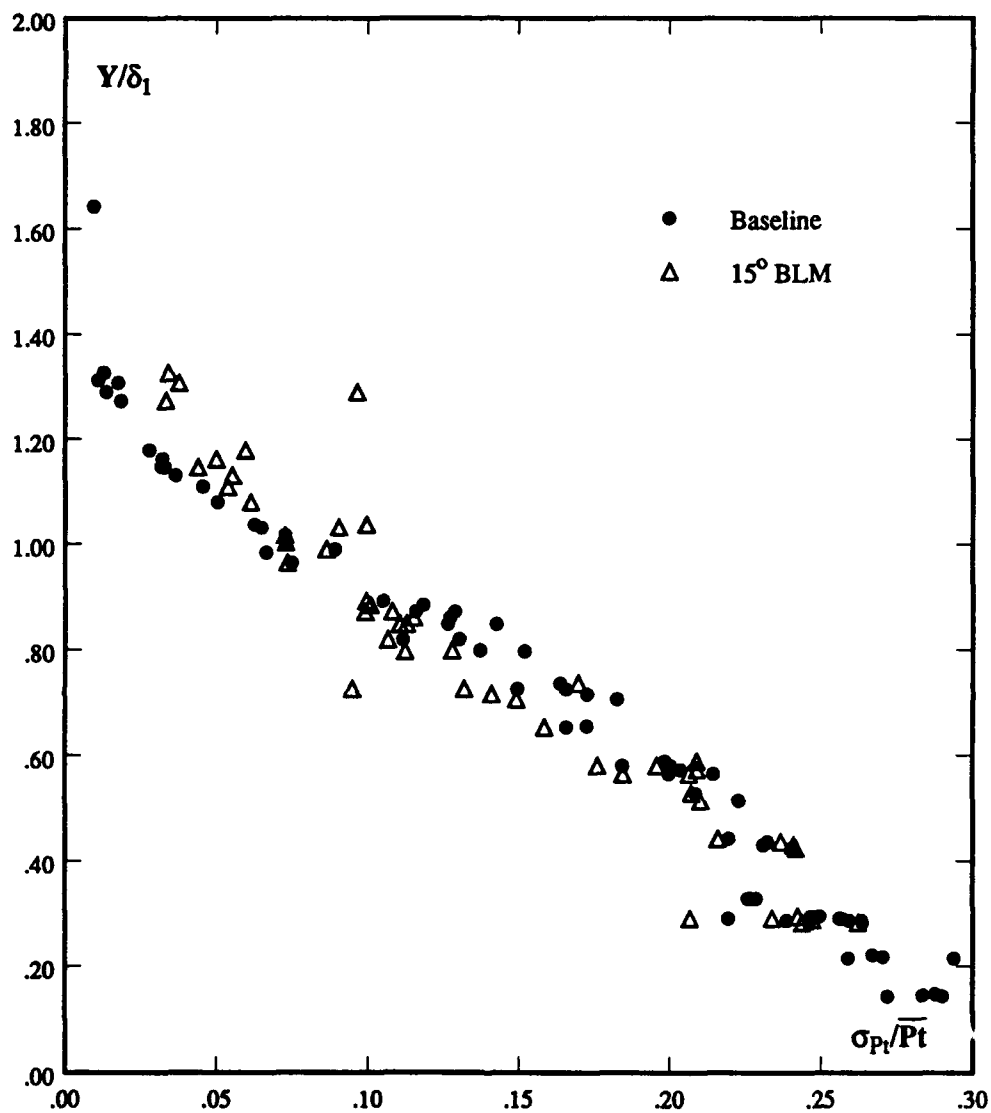


Fig. 7-17: Normalized Pitot Pressure RMS Distributions in Boundary Layer with and without BLM

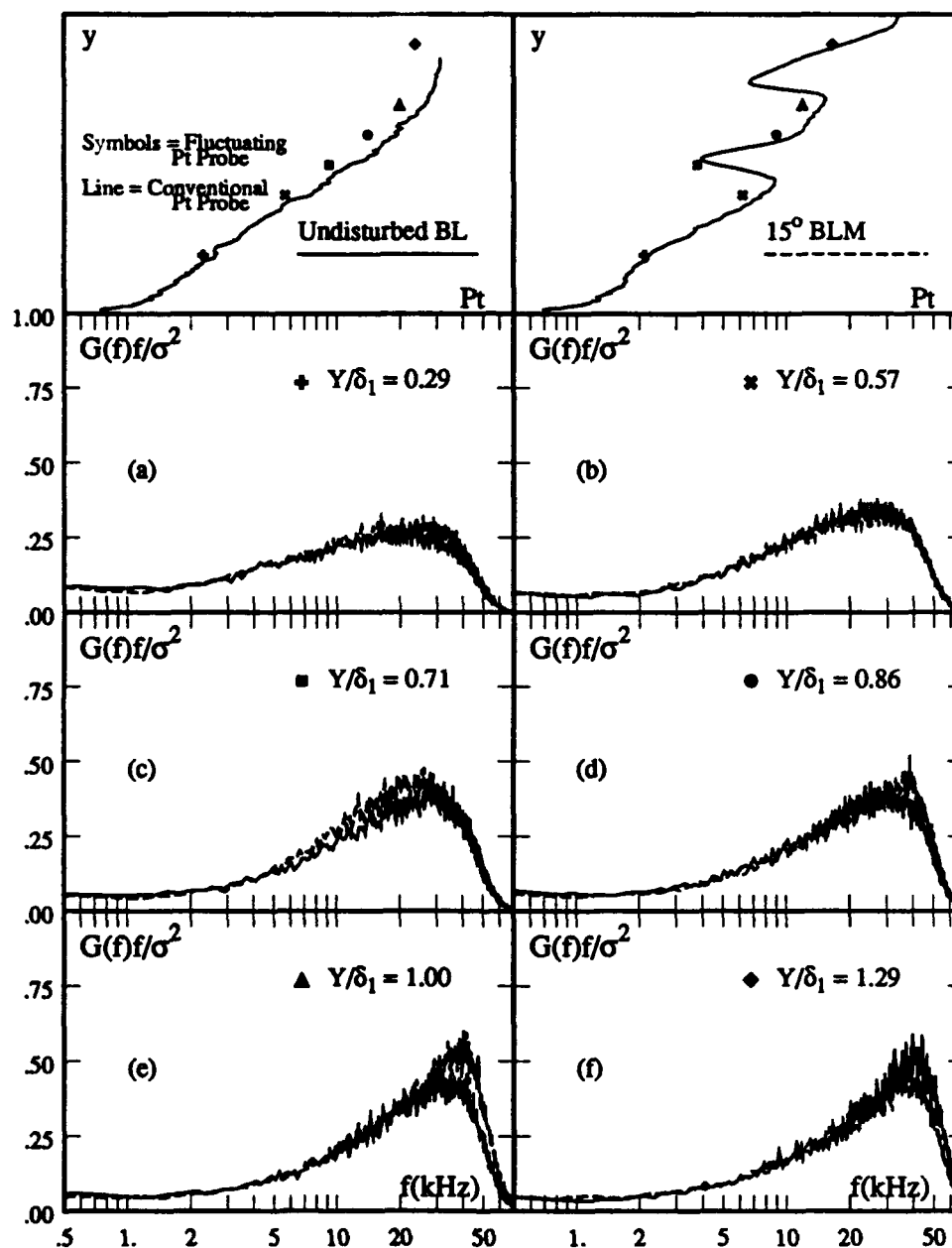


Fig. 7-18: Normalized Pitot Pressure Power Spectra
 $X_{blm} = 1.25$ inches

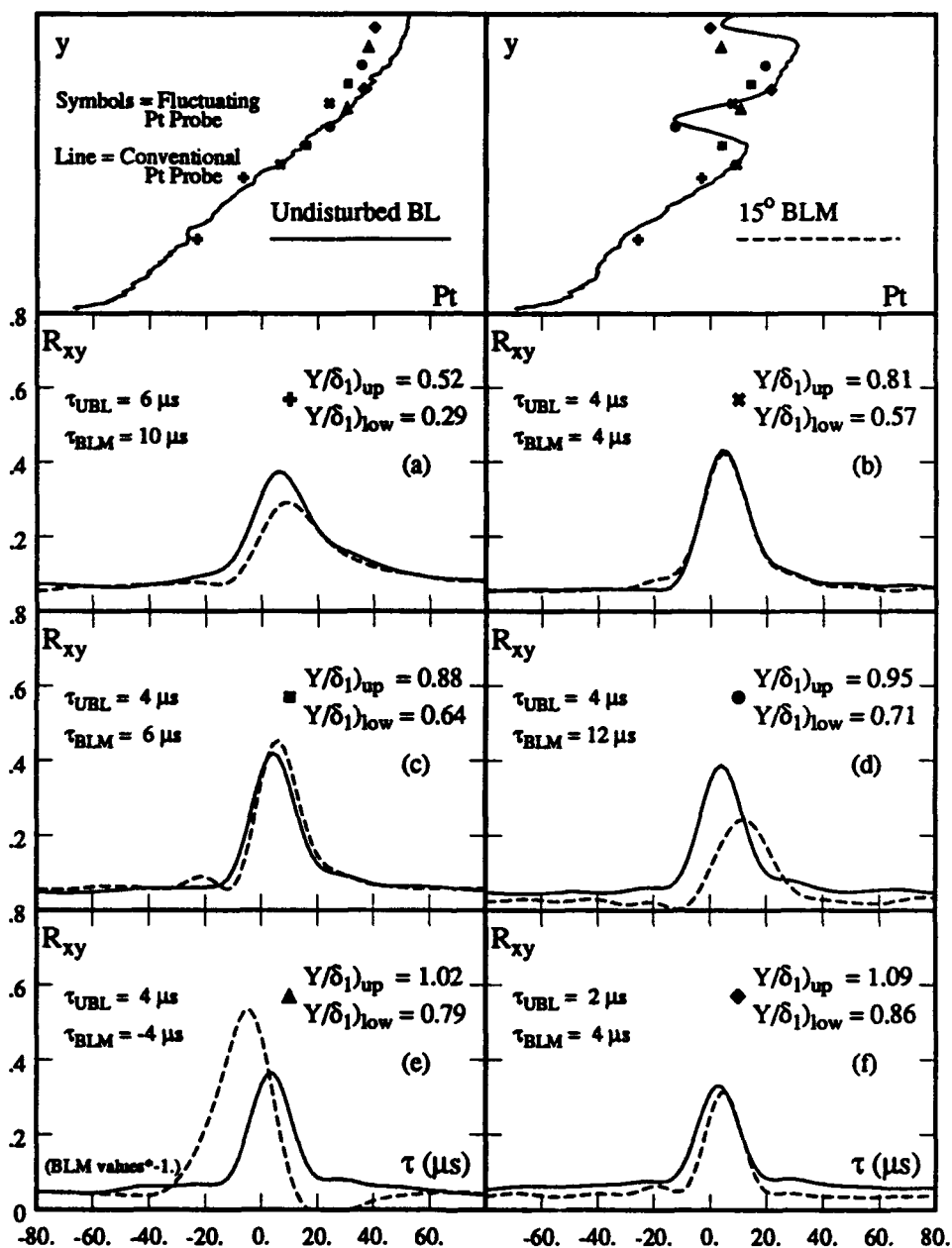


Fig. 7-19: Pitot Pressure Cross Correlations
 $X_{blm} = 1.25$ inches
 (Upper Probe = First Channel)

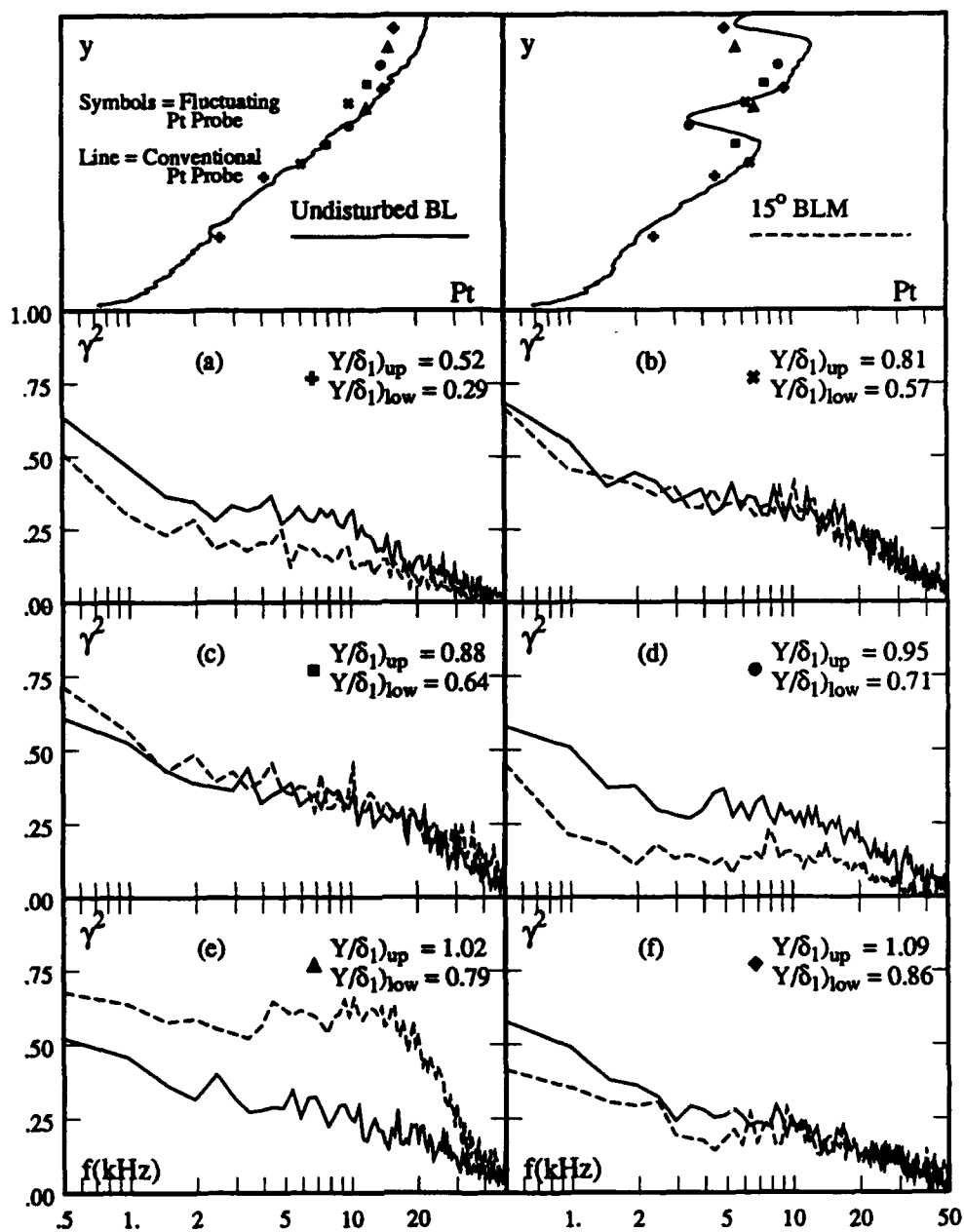


Fig. 7-20: Pitot Pressure Coherence Spectra

$X_{blm} = 1.25$ inches

(Upper Probe = First Channel)

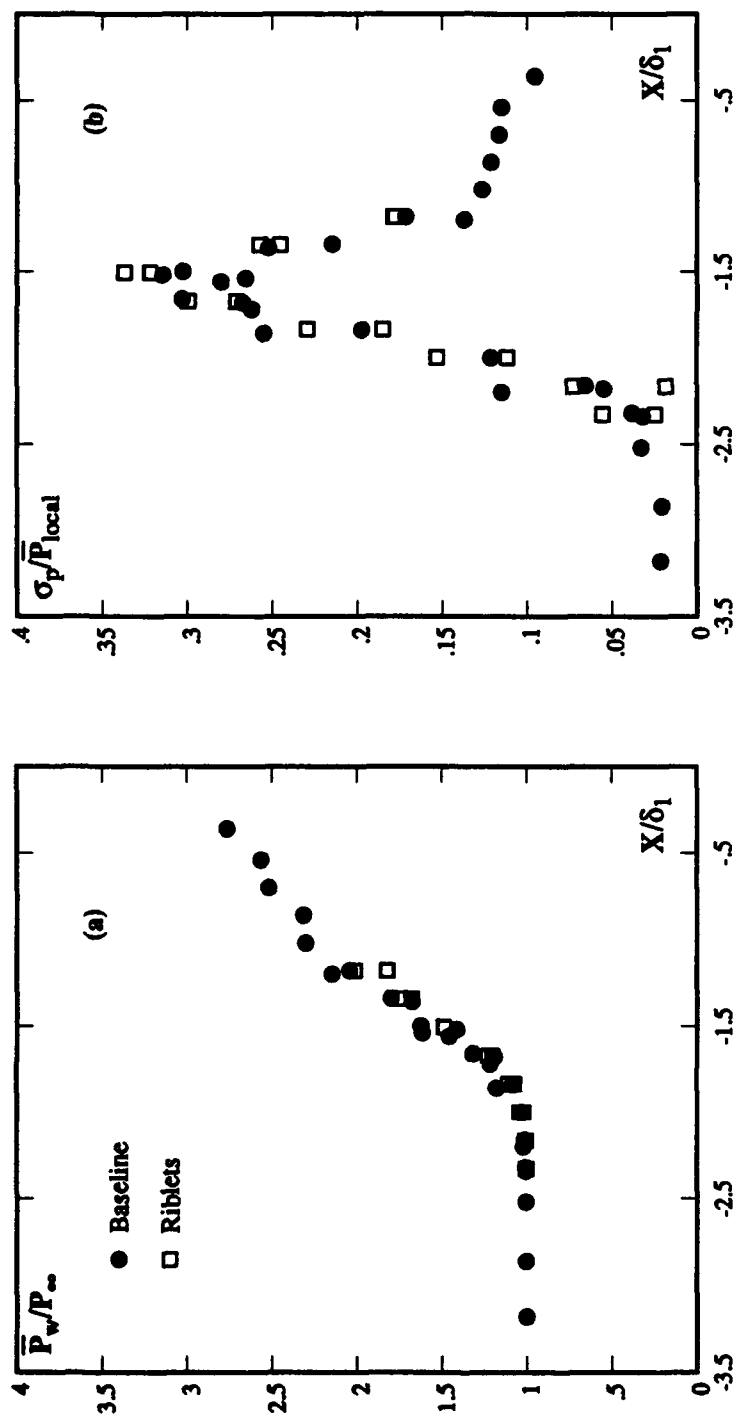


Fig. 7-21: Streamwise Surface Distributions
-Effect of Riblets
 a) Normalized Mean Surface Pressure
 b) Normalized Surface Pressure RMS

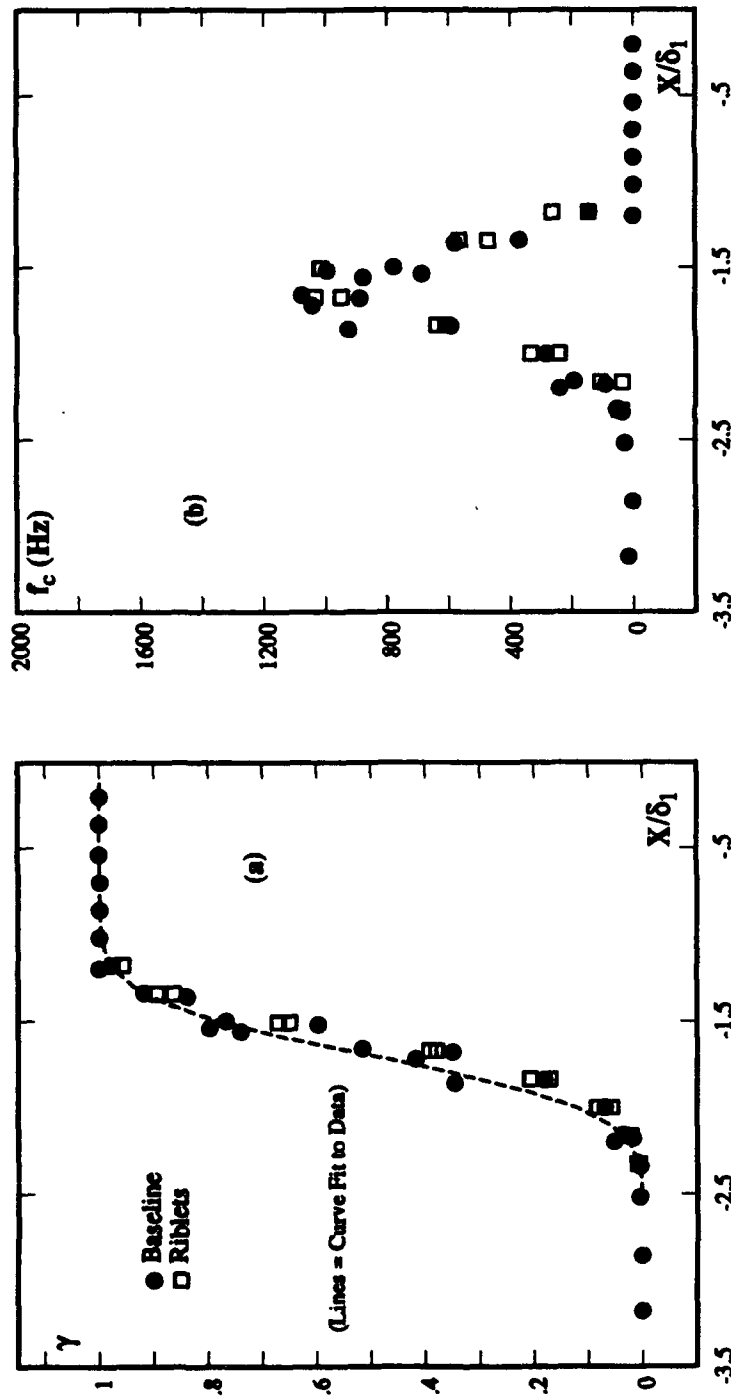


Fig. 7-22: Separation Shock Streamwise Distributions

-Effect of Riblets

a) Intermittency

b) Zero-Crossing Frequency

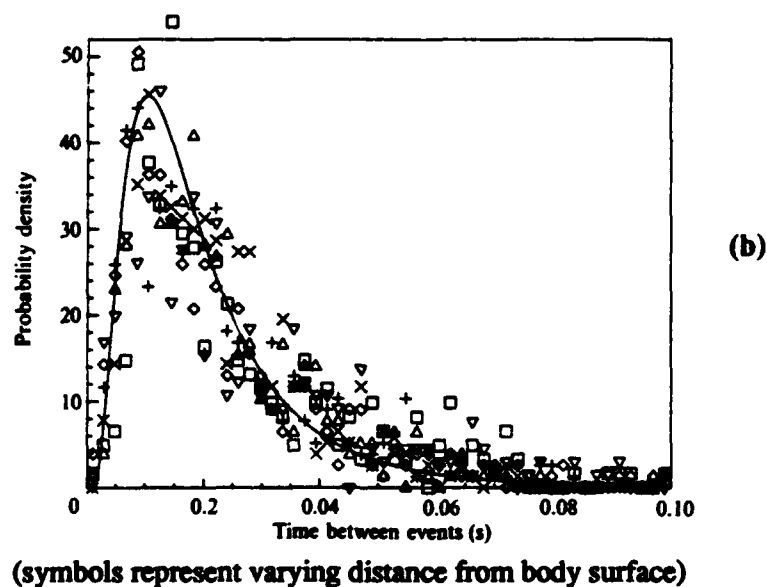
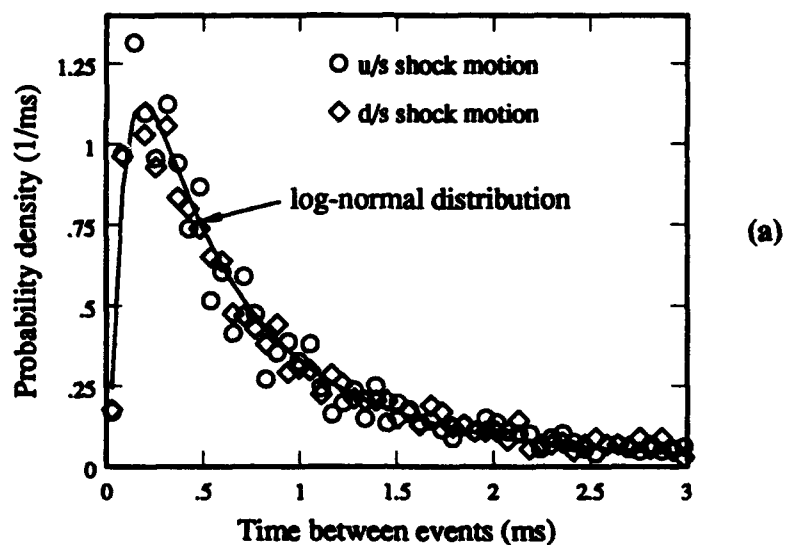


Fig. 8-1: Comparison of Event Histograms
(a) Shock Crossings in Compression Corner Interaction
(b) Transitions Between Back- and Zero-Flow
in a Wing-Body Interaction
(Devenport and Simpson [1990])

REFERENCES

- Anders, J.B., Jr (1990), "Outer-Layer Manipulators for Turbulent Drag Reduction," in AIAA Progress in Astronautics and Aeronautics: Viscous Drag Reduction in Boundary Layers, edited by Bushnell, D.M. and J.N. Hefner, Vol. 123, AIAA, New York, pp. 263-284.
- Andreopoulos, J. and K.C. Muck (1987), "Some New Aspects of the Shock-Wave/Boundary-Layer Interaction in Compression-Ramp Flows," *Journal of Fluid Mechanics*, Vol. 180, pp.405-428.
- Ardonceau, P.L. (1984), "The Structure of Turbulence in a Supersonic Shock-Wave/Boundary Layer Interaction," *AIAA Journal*, Vol. 22, No. 9, pp. 1254-1262.
- Ball, K.O.W. and R.H Korkegi (1968), "An Investigation of the Effect of Suction on Hypersonic Laminar Boundary-Layer Separation," *AIAA Journal*, Vol. 6, No. 2, pp. 239-243.
- Ball, K.O.W. (1970), "Further Results on the Effects of Suction on Boundary-Layer Separation," *AIAA Journal*, Vol. 8, No. 2, pp. 374-375.
- Bendat, J.D. and A.G. Piersol (1986), Random Data: Analysis and Measurement Procedures, Second Edition, John Wiley and Sons, New York.
- Bibko, V.N., B.M. Efimtsov, V.G. Korkach, and V.B. Kuznetsov (1990), "Oscillations of a Shock Wave Induced by Boundary Layer Separation," *Izvestiya Akademii Nauk SSSR, Mekhanika Zhidkosti i Gaza*, Vol. 25, No. 4, pp. 168-170. (English translation in *Fluid Dynamics*, January 1991)
- Blackwelder, R.F. and R.E. Kaplan (1976), "On Wall Structure of the Turbulent Boundary Layer," *Journal of Fluid Mechanics*, Vol. 76, pp. 89-112.
- Bradshaw, P. (1977), "Compressible Turbulent Shear Layers," *Annual Review of Fluid Mechanics*, Vol. 9, pp. 33-54.
- Brusniak, L. (1991), Private Communication.
- Chang, S. and R.F. Blackwelder (1990), "Modification of Large Eddies in Turbulent Boundary Layers," *Journal of Fluid Mechanics*, Vol. 213, pp. 419-442.

Chapman, D.R., D.M. Kuehn, and H.K. Larson (1958), "Investigation of Separated Flows in Supersonic Stream with Emphasis on the Effect of Transition," NACA Report 1356.

Chung, K.M. and F.K. Lu (1990), "Shock-Tube Calibration of a Fast-Response Pressure Transducer," AIAA Paper 90-1299, 16th Aerodynamic Ground Test Conference, Seattle, WA.

Coles, D. (1956), "The Law of the Wake in the Turbulent Boundary Layer," *Journal of Fluid Mechanics*, Vol. 1, pp. 191-226.

Das, D.K. (1987), "A Numerical Study of Turbulent Separated Flows," American Society of Mechanical Engineers Forum on Turbulent Flows, FED Vol. 51, pp. 85-90.

Devenport, W.J. and R.L. Simpson (1990), "Time-Dependent and Time Averaged Turbulence Structure Near the Nose of a Wing-Body Junction," *Journal of Fluid Mechanics*, Vol. 210, pp. 23-55.

Dolling, D.S. and C.T. Or (1985), "Unsteadiness of the Shock Wave Structure in Attached and Separated Compression Corner Flowfields," *Experiments in Fluids*, Vol.3, pp. 24-32.

Dolling, D.S. and L. Brusniak (1991), "Correlation of Separation Shock Motion in a Cylinder-Induced Interaction with Pressure Fluctuations Under the Separated Region," AIAA Paper 91-0650, 29th Aerospace Sciences Meeting, Reno, Nevada.

Dolling, D.S. and L. Brusniak (1989), "Separation Shock Motion in Fin, Cylinder, and Compression Ramp-Induced Turbulent Interactions," *AIAA Journal*, Vol. 27, No. 6, pp. 734-742.

Dolling, D.S. and M.T. Murphy (1983), "Unsteadiness of the Separation Shock Wave in a Supersonic Compression Ramp Flowfield," *AIAA Journal*, Vol. 21, No. 12, pp. 1628-1634.

Dolling, D.S. (1990), "Unsteadiness of Supersonic and Hypersonic Shock-Induced Turbulent Boundary Layer Separation," in Special Course on Three-Dimensional Supersonic/Hypersonic Flows Including Separation, AGARD-R-764.

D.S. Dolling and D.R. Smith (1989), "Unsteady Shock-Induced Separation in Mach 5 Cylinder Interactions," *AIAA Journal*, Vol. 27, No. 12, pp. 1098-1706.

Dolling, D.S., T. Boitnott, and M.E. Erengil (1991), "Effects of Moderate Sweepback on the Separation Shock Wave Dynamics in a Mach 5 Compression Ramp Interaction," AIAA Paper 91-0254, 29th Aerospace Sciences Meeting, Reno, Nevada.

Drougge, G. (1953), "An Experimental Investigation of the Influence of Strong Adverse Pressure Gradients on Turbulent Boundary Layers at Supersonic Speeds," Aeronautical Research Institute of Sweden, Stockholm, Rep. No 46.

Erengil, M.E. and D.S. Dolling (1991b), "Correlation of Separation Shock Motion with Pressure Fluctuations in the Incoming Boundary Layer," *AIAA Journal*, Vol. 29, No. 11, pp. 1868-1877.

Erengil, M.E. and D.S. Dolling (1992), "Effects of Sweepback on Unsteady Separation in Mach 5 Compression Ramp Interactions," AIAA Paper 92-0430, 30th Aerospace Sciences Meeting, Reno, Nevada.

Erengil, M.E. and D.S. Dolling (1991a), "Unsteady Wave Structure Near Separation in a Mach 5 Compression Ramp Interaction," *AIAA Journal*, Vol. 29, No. 5, pp. 728-735.

Gartling, D.K. (1971), "Test of Vortex Generators to Prevent Separation of Supersonic Flow in a Compression Corner," M.S. Thesis, Dept. of Aerospace Engineering, The University of Texas at Austin.

Gaudet, L. (1989), "Properties of Riblets at Supersonic Speed," *Applied Scientific Research*, Vol. 34, No. 3, pp. 245-254.

Gibson, B. and D.S. Dolling (1991), "Wall Pressure Fluctuations Near Separation in a Mach 5, Sharp Fin-Induced Turbulent Interaction," AIAA Paper 91-0646, 29th Aerospace Sciences Meeting, Reno, Nevada.

Glotov, G.F., and I.U. Korontsvit (1983), "An Investigation of a Method for Controlling a Three-Dimensional Separation Zone," *TsAGI, Uchenye Zapiski*, Vol. 14, No. 2, pp. 126-131. In Russian.

Goldberg, U.C. (1991), "Derivation and Testing of a One-Equation Model Based on Two Time Scales," *AIAA Journal*, Vol. 29, No. 8, pp. 1337-1340.

Gramann, R.A. and D.S. Dolling (1992), "A Preliminary Study of Turbulent Structures Associated with Unsteady Separation Shock Motion in a Mach 5 Compression Ramp Interaction," AIAA Paper 92-0744, 30th Aerospace Sciences Meeting, Reno, Nevada.

Gramann, R.A. and D.S. Dolling (1990), "Dynamics of Separation and Reattachment in a Mach 5 Unswept Compression Ramp Flow," AIAA Paper 90-0380, 28th Aerospace Sciences Meeting, Reno, NV.

Gramann, R.A. (1989), "Dynamics of Separation and Reattachment in a Mach 5 Unswept Compression Ramp Flow," PhD Dissertation, Dept. of Aerospace Engineering and Engineering Mechanics, The University of Texas at Austin.

Green, J. E. (1970), "Interactions Between Shock Waves and Boundary Layers," Progress in Aerospace Sciences, Vol. 11., Pergamon Press, New York, pp. 235-340.

Grin, V.T. (1967), "Experimental Study of Boundary-Layer Control by Blowing on a Flat Plate at $M=2.5$," *Izvestiya Akademii Nauk SSSR, Mekhanika Zhidkosti i Gaza*, Vol. 2, No. 6, pp. 115-117. (English translation in *Fluid Dynamics*, 1967)

Hamed, A. and J. Shang (1989), "Survey and Assessment of Validation Data Base for Shock Wave Boundary Layer Interactions in Supersonic Inlets," AIAA Paper 89-2939, 25th Joint Propulsion Conference, Monterey, California.

Hayashi, M., A. Shigeru, and A. Tan (1989), "Fluctuation of Heat Transfer in Shock Wave/Turbulent Boundary-Layer Interaction," *AIAA Journal*, Vol. 27, No. 4, pp. 309-404.

Hinze, J.O. (1975), Turbulence, Second Edition, McGraw-Hill, New York.

Horstman, C. C., G. S. Settles, I. E. Vas, S. M. Bogdonoff, and C. M. Hung (1977), "Reynolds Number Effects on Shock-Wave Turbulent Boundary-Layer Interactions," *AIAA Journal*, Vol. 15, pp.1152-1158.

Jackson, L.R., S.C. Dixon, D.R. Tenney, A.L. Carter, and J.R. Stephens (1987), "Hypersonic structures and materials: a progress report," *Aerospace America*, pp. 24-30.

Keefe, L.R. and D. Nixon (1991), "Shock Loading Predictions from Application of Indicical Theory to Shock-Turbulence Interactions," AIAA Paper 91-1777, 22nd Fluid Dynamics, Plasma Dynamics, and Lasers Conference, Honolulu, Hawaii.

Kistler, A. L. (1964), "Fluctuating Wall Pressure under a Separated Supersonic Flow," *Journal of the Acoustical Society of America*, Vol. 36, pp. 543-550.

Klebanoff, P.S. (1954), NACA Technical Note No. 3178.

Krishnamurthy, V. (1973), "Suppression of Shock Induced Separation Using Tangential Fluid Injection, Part I," Dept. of Aerospace Engineering, Indian Institute of Science, Bangalore, M.E. Project Report.

Kulite, "Kulite Miniature IS Silicon Diaphragm Pressure Transducer Catalog," Kulite Bulletin KS-1000D, Kulite Semiconductor Products, Inc.

Kuntz, D.W., V.A. Amatucci, and A.L. Addy (1987), "Turbulent Boundary-Layer Properties Downstream of the Shock- Wave/Boundary-Layer Interaction," *AIAA Journal*, Vol. 25, No. 5, pp. 668-675.

Kussoy, M.I., J.D. Brown, J.L. Brown, W.K. Lockman, and C.C. Horstman (1987), "Fluctuations and Massive Separation in Three-Dimensional Shock-Wave/Boundary-Layer Interactions," 2nd International Symposium on Transport Phenomena in "Turbulent Flows," Tokyo, Japan.

Law, C. H. (1974), "Supersonic Turbulent Boundary-Layer Separation," *AIAA Journal*, Vol. 12, pp. 794-797.

MacKay, J.D. (1991), Private Communication.

MacKay, J.D. (1992), Private Communication.

Manjunath, A.R. (1973), "Suppression of Shock Induced Separation Using Tangential Fluid Injection, Part II," Dept. of Aerospace Engineering, Indian Institute of Science, Bangalore, M.E. Project Report.

Marshall, T.A. and D.S. Dolling (1990), "Spanwise Properties of the Unsteady Separation Shock in a Mach 5 Unswept Compression Ramp Interaction," AIAA Paper 90-0377, 28th Aerospace Sciences Meeting, Reno, Nevada.

McClure, W.B. and D.S. Dolling (1991), "Exploratory Study of Effects of Suction Near Reattachment on the Unsteadiness of a Mach 5 Compression Ramp Interaction," AIAA Paper 91-1767, 22nd Fluid Dynamics, Plasma Dynamics and Lasers Conference, Honolulu, Hawaii.

Morrison, J.F., H.M. Tsai, and P. Bradshaw (1989), "Conditional-Sampling Schemes for Turbulent Flow, Based on the Variable-Interval Time Averaging (VITA) Algorithm," *Experiments in Fluids*, Vol. 7, pp. 173-189.

Muck, K.C., J. Andreopoulos, and J.P. Dussauge (1988), "Unsteady Nature of Shock-Wave/Turbulent Boundary-Layer Interaction," *AIAA Journal*, Vol. 26, No. 2, pp. 179-187.

Nordyke, R.J. (1987), "Spanwise Properties of the Unsteady Separation Shock in a Mach 5 Unswept Compression Ramp Interaction," M.S. Thesis, Dept. of Aerospace Engineering and Engineering Mechanics, The University of Texas at Austin.

Raman, K.R. (1974), "Surface Pressure Fluctuations in Hypersonic Turbulent Boundary Layers," NASA CR-2386.

Robinson, S.K. (1988), "Effects of Riblets on Turbulence in a Supersonic Boundary Layer," AIAA Paper 88-2526, 6th Applied Aerodynamics Conference, Williamsburg, Virginia.

Schmisser, J.D. and D.S. Dolling (1992), "Unsteady Separation in Sharp Fin-Induced Shock Wave/Turbulent Boundary Layer Interaction at Mach 5," AIAA Paper 92-0748, 30th Aerospace Sciences Meeting, Reno, Nevada.

Selig, M.S. and A.J. Smits (1991), "Effect of Periodic Blowing on Attached and Separated Supersonic Turbulent Boundary Layers," *AIAA Journal*, Vol. 29, No. 10, pp. 1651-1658.

Selig, M.S. (1988), "Unsteadiness of Shock Wave/Turbulent Boundary-Layer Interactions with Dynamic Control," M.S.E. Thesis 1801-T, Dept. of Mechanical and Aerospace Engineering, Princeton University.

Selig, M.S., J. Andreopoulos, K.C. Muck, J.P. Dussauge, and A.J. Smits (1989), "Turbulence Structure in a Shock Wave/Turbulent Boundary-Layer Interaction," *AIAA Journal*, Vol. 27, No. 7, pp. 862-869.

Settles, G.S. and D.S. Dolling (1986), "Swept Shock Wave/Boundary-Layer Interaction," in AIAA Progress in Astronautics and Aeronautics: Tactical Missile Aerodynamics, edited by Hemsch, M. and J. Nielsen, Vol. 104, AIAA, New York, pp.297-379.

Settles, G.S. and D.S. Dolling (1990), "Swept Shock/Boundary-Layer Interactions - Tutorial and Update," AIAA Paper 90-0375, 28th Aerospace Sciences Meeting, Reno, Nevada.

Settles, G.S. and H.Y. Teng (1982), "Flow Visualization of Separated 3-D Shock Wave/Turbulent Boundary Layer Interactions," AIAA Paper 82-0229, 20th Aerospace Sciences Meeting, Orlando, Florida.

Settles, G. S., I. E. Vas, and S. M. Bogdonoff (1976), "Details of a Shock-Separated Turbulent Boundary Layer at a Compression Corner," *AIAA Journal*, Vol. 14, pp.1709-1715.

Settles, G.S., J.J. Perkins, and S.M. Bogdonoff (1981), "Upstream Influence Scaling of 2D & 3D Shock/Turbulent Boundary Layer Interactions at Compression Corners," AIAA Paper 81-0334, 19th Aerospace Sciences Meeting, St. Louis, Missouri.

Settles, G.S., T.J. Fitzpatrick, and S.M. Bogdonoff (1979), "Detailed Study of Attached and Separated Compression Corner Flowfields in High Reynolds Number Supersonic Flow," *AIAA Journal*, Vol. 17, No. 6, pp. 579-585.

Shau, Y.R. and D.S. Dolling (1990), "Exploratory Study of Turbulent Structure in Compressible Shear Layers Using Fluctuating Pitot Pressure Measurements," presented at the Symposium on Turbulence, University of Missouri at Rolla.

Shau, Y.R. (1990), "Experimental Study of Growth Rate Enhancement and Structure of Compressible Turbulent Free Shear Layers," PhD Dissertation, Dept. of Aerospace Engineering and Engineering Mechanics, The University of Texas at Austin.

Shau, Y.R. (1991), Private Communication.

Shen, Z.H., D.R. Smith and A.J. Smits (1990), "Wall Pressure Fluctuations in the Reattachment Region of a Supersonic Free Shear Layer," AIAA Paper 90-1461, 21st Fluid Dynamics, Plasma Dynamics and Lasers Conference, Seattle, Washington.

Spina, E.F. (1988), "Organized Structures in a Supersonic Turbulent Boundary Layer," PhD Dissertation, Dept. of Mechanical and Aerospace Engineering, Princeton University.

Sun, C.C. and M.F. Childs (1973), "A Modified Wall-Wake Velocity Profile for Turbulent Compressible Boundary Layers," *AIAA Journal of Aircraft*, Vol. 10, No. 6, pp. 381-383.

Tanner, L.H. and S.L. Gai (1967), "Effects of Suction on the Interaction Between Shock Wave and Boundary Layer at a Compression Corner," ARC CP no. 1087.

Thomas, F.O., C.M. Putnam, and H.C. Chu (1991), "Measurement of the Nonlinear Spectral Dynamics Characterizing a Shock Wave/Turbulent Boundary Layer Interaction," AIAA Paper 91-0653, 29th Aerospace Sciences Meeting, Reno, Nevada.

Tran, T.T. (1987), "An Experimental Investigation of Unsteadiness in Swept Shock Wave/Turbulent Boundary Layer Interactions," PhD Dissertation, T-1763, Dept. of Mechanical and Aerospace Engineering, Princeton University.

Unalms, O.H. (1991), Private Communication.

Viegas, J.R. and C.C. Horstman (1979), "Comparison of Multiequation Turbulence Models for Several Shock Boundary-Layer Interaction Flows," *AIAA Journal*, Vol. 17, No. 8, pp. 811-820.

Viswanath, P.R. (1988), "Shock-Wave-Turbulent-Boundary-Layer Interaction and its Control: A Survey of Recent Developments," in Developments in Fluid Mechanics and Space Technology, edited by Narasimha, R. and A.P.J. Abdul Kalam, Indian Academy of Sciences, Bangalore, India, pp. 143-202.

Viswanath, P.R., L. Sankaran, P.M. Sagdeo, R. Narasimha and A. Prabhu (1983), "Injection Slot Location for Boundary-Layer Control in Shock-Induced Separation," *AIAA Journal of Aircraft*, Vol. 20, pp. 726-732.

Walsh, M.J. (1990), "Riblets," in AIAA Progress in Astronautics and Aeronautics: Viscous Drag Reduction in Boundary Layers, edited by Bushnell, D.M. and J.N. Hefner, Vol. 123, AIAA, New York, pp. 203-261.

Walsh, M.J., and A.M. Lindemann (1984), "Optimization and Application of Riblets for Turbulent Drag Reduction," AIAA Paper 84-0347, 22nd Aerospace Sciences Meeting, Reno, Nevada.

White, F.M. (1991), Viscous Fluid Flow, Second Edition, McGraw-Hill, New York.

Wilcox, D.C. (1990), "Supersonic Compression-Corner Applications of a Multiscale Model for Turbulent Flows," *AIAA Journal*, Vol. 28, No. 7, pp. 1194-1198.

Zorumski, W.E. (1987), "Fluctuating Pressure Loads Under High Speed Boundary Layers," NASA TM 100517.

Vita

William Berton McClure was born in Atlanta, Georgia on August 25, 1959, the son of George Richard and Thyrza Frances McClure. He graduated from Mount Pleasant High School, Wilmington, Delaware, in 1977 and entered the United States Air Force Academy. In May 1981, he received his Bachelor of Science in Aeronautical Engineering and entered Princeton University under a Guggenheim Fellowship. He received his Master of Science in Engineering degree in June, 1983. In January 1983, he was assigned to Aeronautical Systems Division, Wright-Patterson Air Force Base, Ohio, and in December 1986 joined the faculty of the Department of Aeronautics at the U. S. Air Force Academy. He began his doctoral program at the University of Texas at Austin in August, 1989.

**Permanent Address: 702 Naudain Avenue,
Claymont, Delaware, 19703**

This dissertation was typed by the author.